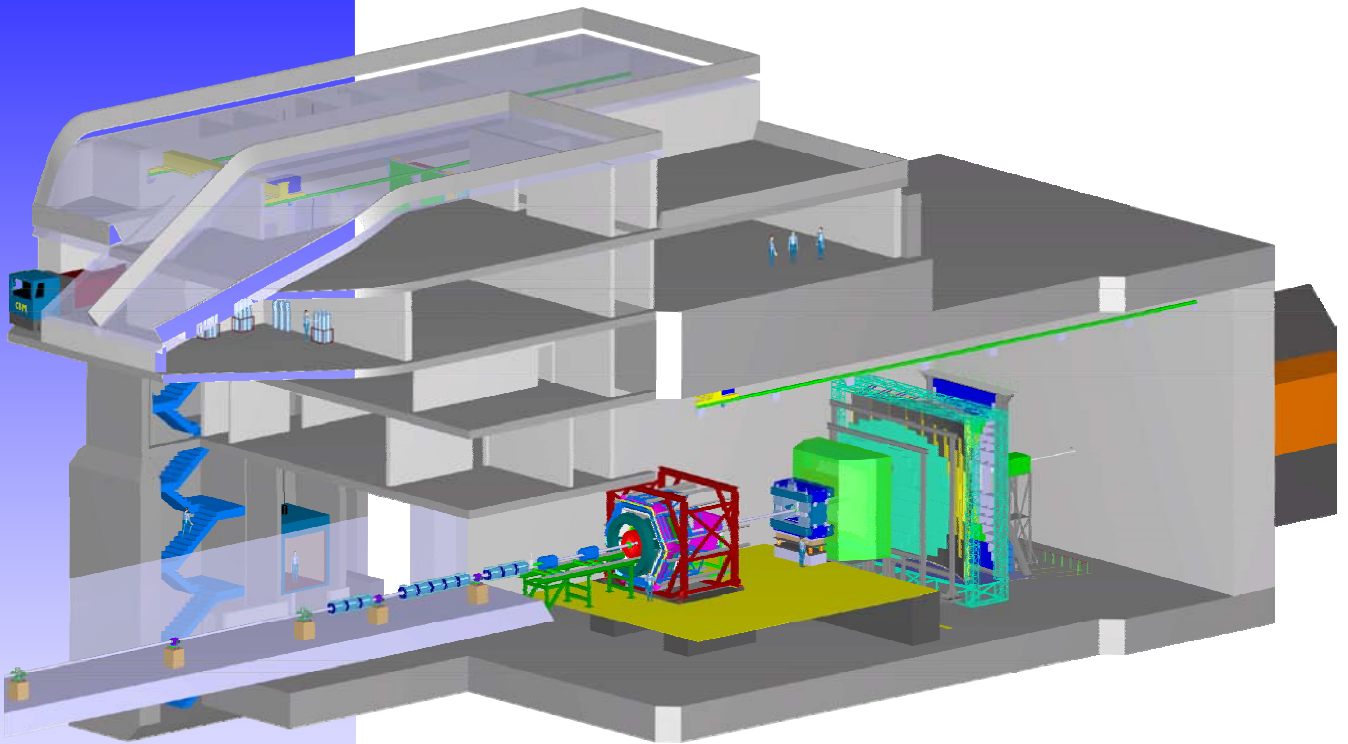


CBM

Compressed Baryonic Matter
experiment at FAIR

PROGRESS REPORT



2010

CBM Progress Report 2010

ISBN 978-3-9811298-8-5

Editors: Volker Friese and Christian Sturm
v.friese@gsi.de c.sturm@gsi.de

©2011 GSI Darmstadt, D-64291 Darmstadt, Germany
<http://www.gsi.de>

Printed in Darmstadt by GSI Darmstadt

This work was supported by the EU Integrated Infrastructure Initiatives EUNET (FP6), HadronPhysics (FP6) and HadronPhysics2 (FP7), the EU-FP7/HP2-WP18 Grant No 227431, the EU-FP7 Marie Curie Initial Training Network for Particle Detectors (MC-PAD), the Hessian LOEWE initiative through the Helmholtz International Center for FAIR (HIC for FAIR), the H-QM Helmholtz Research School, the GSI Helmholtzzentrum für Schwerionenforschung GmbH, the Bundesministerium für Bildung und Forschung (06FY173I, 06FY90991, 06WU91951, 06DR9059D, 06HD9121I, 06HD9117I) the Bundesministerium für Wirtschaft und Technologie (INNO-KOM-Ost), the Federal Agency of Russia for Atomic Energy (Rosatom), the Romanian NASR/CAPACITATI-Modul III contract nr. 42., the NASR/NUCLEU Project, and the the National Natural Science Foundation of China (10875120).

Front cover: Engineering drawing of the experimental site for HADES and CBM. The two detector setups are shown in the underground hall of 37 m length, 27 m width and 17 m height. Above ground are service buildings including control room and assembly hall. Construction permit is expected in 2011.

News

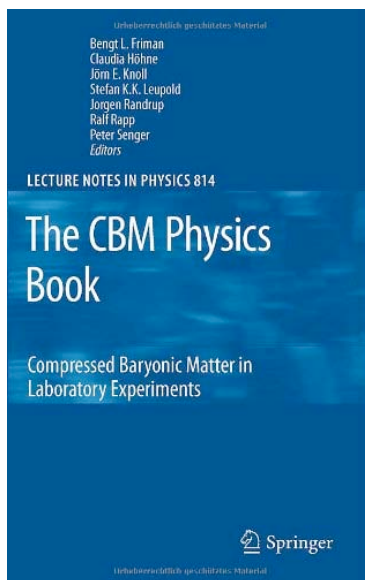
Status of FAIR

In 2010 the FAIR project made a big step towards realization. The FAIR convention was finally signed on Oct. 4 by 9 countries (Finland, France, Germany, India, Poland, Romania, Russia, Sweden, and Slovenia), and 6 countries became shareholders (Germany, India, Romania, Russia, and the Finnish/Swedish consortium). More countries will join in the coming years. As a first step the so called modularized FAIR Start version will be built, including basic experimental setups for the four scientific pillars APPA, CBM, NuSTAR and PANDA. According to the actual planning the FAIR civil construction will start in 2012, and the buildings will be ready for installation of accelerators and experiments in 2017.

Experiment Funding

Within the current FAIR budget a total amount of 78 Mio Euro is foreseen for the experiments. It is quite obvious that this money is not sufficient to build all the detectors. Consequently, the experimental collaborations have to acquire additional funding. Germany will provide financial support for the FAIR experiments on top of the FAIR contribution, and hopefully the other FAIR partner countries will follow. In any case, in order to receive construction funds the experiment collaborations have to submit Technical Design Reports on the detector systems in the near future.

The CBM Physics Book



The CBM Physics book is available now:

Springer Series: Lecture Notes in Physics, Vol. 814
1st Edition., 2011, 960 p., Hardcover
ISBN: 978-3-642-13292-6

This exhaustive survey is the result of a four year effort by many leading researchers in the field to produce both a readable introduction and a yardstick for the many upcoming experiments using heavy ion collisions to examine the properties of nuclear matter.

The book explicitly addresses everyone working or planning to enter the field of high-energy nuclear physics.

Contents

News	i
Overview	1
P. Senger and the CBM Collaboration: <i>Status of the CBM experiment at FAIR</i>	1
Micro-Vertex Detector	3
M. Winter: <i>Development of high-precision pixel sensors for the CBM vertex detector</i>	3
D. Doering <i>et al.</i> : <i>Annealing studies on X-ray and neutron irradiated CMOS MAPS</i>	4
T. Tischler <i>et al.</i> : <i>Status of the mechanical design of the CBM-MVD</i>	5
C. Schrader <i>et al.</i> : <i>Status of the CBM-MVD prototype readout</i>	6
S. Seddiki <i>et al.</i> : <i>Expected data rates of the CBM-MVD at SIS-100 based on realistic beam intensity fluctuations</i>	7
Silicon Tracking System	8
A. Kotynia and J. M. Heuser: <i>Performance simulations with a realistic model of the CBM Silicon Tracking System</i>	8
J. M. Heuser <i>et al.</i> : <i>Development of microstrip detectors for the CBM Silicon Tracking System</i>	10
M. Merkin <i>et al.</i> : <i>First Russian double-sided silicon strip sensors for CBM</i>	11
S. Chatterji, M. Singla and J. M. Heuser: <i>Simulation study on the radiation tolerance of microstrip detectors for the CBM Silicon Tracking System</i>	12
D. Karmanov <i>et al.</i> : <i>Radiation hardness tests of silicon strip detectors at the cyclotron-based neutron irradiation station of the V. G. Khlopin Radium Institute</i>	13
J. M. Heuser <i>et al.</i> : <i>Development of low-mass readout cables for the CBM Silicon Tracking System</i>	14
D. Severin, M. Bender and J. M. Heuser: <i>Radiation hardness of low-mass readout cables for the CBM experiment</i>	15
S. N. Igolkin, Y. A. Murin and J. M. Heuser: <i>Conceptual design of mechanics for the CBM Silicon Tracking System</i>	16
V. M. Borshchov <i>et al.</i> : <i>Prototyping of the CBM STS module</i>	17
J. M. Heuser <i>et al.</i> : <i>Development of a quality assurance system for CBM-STS detector modules</i>	18
J. M. Heuser <i>et al.</i> : <i>Test of prototype modules of the CBM Silicon Tracking System in a proton beam at COSY</i>	19
V. M. Borshchov <i>et al.</i> : <i>Modeling the thermal operation of CBM-STS stations</i>	20
T. Balog <i>et al.</i> : <i>Simulation study of n-XYTER front-end electronics in overflow situations for early prototyping of detectors in the CBM experiment</i>	21
K. Kasinski, R. Szczygiel and P. Grybos: <i>Evolution of a prototype silicon strip detector readout ASIC for the STS</i>	22
E. Atkin <i>et al.</i> : <i>Development of a data-driven readout ASIC for microstrip detectors</i>	23
Ring Imaging Cherenkov Detector	24
J. Eschke <i>et al.</i> : <i>Single Cherenkov photon measurements with multi-anode photomultipliers for performance studies of the CBM-RICH photodetector</i>	24
C. Pauly <i>et al.</i> : <i>Single-photon and magnetic field measurements on H8500 MAPMTs</i>	26
J. Kopfer <i>et al.</i> : <i>Quantum efficiency and gain homogeneity measurements of H8500 MAPMTs for the development of a CBM-RICH prototype camera</i>	27
J. Eschke and F. Meyer: <i>Investigation of crosstalk in multi-anode photomultipliers for the CBM-RICH photodetector</i>	28
I. Wehl, A. Sienerth and M. Dürr: <i>Wet-chemical application of wavelength-shifting films for the use on RICH-PMTs</i>	29

D. Kresan and C. Höhne: <i>Design studies for a CBM-RICH prototype</i>	30
L. Kotchenda <i>et al.</i> : <i>A gas system for the CBM-RICH prototype</i>	31
P. Kravtsov <i>et al.</i> : <i>A slow-control system for the CBM-RICH gas system</i>	32
E. Vznuzdaev <i>et al.</i> : <i>Mirror mount design for the CBM RICH detector</i>	33
Muon System	34
P. Bhaduri, A. Prakash and S. Chattopadhyay: <i>MUCH layout optimization for SIS-100</i>	34
A. Prakash <i>et al.</i> : <i>Segmentation optimization for MUCH detector at CBM</i>	35
A. K. Dubey <i>et al.</i> : <i>Update on GEM development at VECC</i>	36
J. Saini <i>et al.</i> : <i>Development of PCBs for readout plane and front-end boards for MuCH</i>	37
A. Zinchenko, D. Peshekonov and V. Peshekonov: <i>Performance evaluation of the CBM muon system for a $\omega \rightarrow \mu\mu$ trigger</i>	38
Transition Radiation Detectors	39
P. Reichelt, M. Hartig and H. Appelshäuser: <i>Study on electron-pion discrimination with the CBM Transition Radiation Detector</i>	39
T. P. Akishina, O. Y. Denisova and V. V. Ivanov: <i>Study of the optimal structure of the TRD radiator</i>	40
W. Yu, H. Appelshäuser and M. Hartig: <i>Performance studies on the CBM-TRD using J/ψ</i>	41
D. Emschermann and C. Bergmann: <i>First common beam test of the CBM STS, RICH and TRD subsystems at the CERN Proton Synchrotron</i>	42
M. Petris <i>et al.</i> : <i>Two-dimension position sensitive Transition Radiation Detector in beam- tests using new Fast Analog Signal Processor (FASP)</i>	43
W. Yu <i>et al.</i> : <i>First beam test of the Frankfurt prototype for the CBM-TRD</i>	44
T. Armbruster, P. Fischer and I. Perić: <i>CBM-TRD readout with the SPADIC amplifier / digitizer chip</i>	45
A. Caragheorghopol <i>et al.</i> : <i>Front-end electronics for high counting rate TRD</i>	46
S. Chernenko <i>et al.</i> : <i>Development and test of fast readout chambers for the CBM-TRD</i>	47
Time-of-Flight Detectors	48
M. Petris <i>et al.</i> : <i>High granularity, symmetric differential readout - timing multigap RPC</i>	48
D. Gonzalez-Diaz, H. Chen and W. Yi: <i>Crosstalk free multi-strip Resistive Plate Chambers?</i>	49
Y. Wang <i>et al.</i> : <i>Performance of low-resistive glass</i>	50
Y. Sun <i>et al.</i> : <i>Performance test of MRPC with different pad size</i>	51
L. Naumann <i>et al.</i> : <i>Development of ceramics RPC for high rate capability timing detector application</i>	52
I. Deppner <i>et al.</i> : <i>Performance of a differential CBM-TOF demonstrator</i>	53
J. Frühauf <i>et al.</i> : <i>Status of the CBM-TOF readout chain</i>	54
P.-A. Loizeau <i>et al.</i> : <i>Status of the analysis chain for CBM-TOF demonstrator data</i>	55
Calorimeters	56
I. Korolko <i>et al.</i> : <i>CBM calorimeter located at 1.5 meters from the target</i>	56
Magnet and Infrastructure	57
E. A. Matyuhevskiy <i>et al.</i> : <i>SC dipole magnet for CBM</i>	57
S. Belogurov, A. Chernogorov and A. Semennikov: <i>Design justification of the STS section of the CBM beam pipe</i>	58
DAQ and Online Event Selection	59
J. de Cuveland and V. Lindenstruth: <i>A First-level Event Selector for the CBM experiment</i>	59
F. Lemke, S. Schenk and U. Bruening: <i>Demonstrator beam time results for the clock distribution and synchronization of the CBM-DAQ system</i>	60
J. Adamczewski-Musch, B. W. Kolb and S. Linev: <i>DABC data acquisition input for slow control variables</i>	61
N. Abel <i>et al.</i> : <i>Radiation tolerance of the Universal Read Out Controller</i>	62
N. Abel <i>et al.</i> : <i>Design and implementation of an object-oriented framework for dynamic partial reconfiguration</i>	63
S. Linev, J. Adamczewski-Musch and J. Frühauf: <i>DABC as data acquisition framework for CBM</i>	64
A. Wurz <i>et al.</i> : <i>Memory kernel development of the Active Buffer</i>	65

Software and Algorithms	66
R. Frühwirth <i>et al.</i> : <i>A SIMD implementation of the Deterministic Annealing Filter for the CBM experiment</i>	66
I. Kisel <i>et al.</i> : <i>CA-based track finder with STS detector inefficiency</i>	67
I. Rostovtseva <i>et al.</i> : <i>L1 CA track finder with realistic STS clusterization</i>	68
I. Kisel and I. Kulakov: <i>Scalability of the CA-based track finder in the CBM experiment</i>	69
I. Kisel <i>et al.</i> : <i>Towards parallel track reconstruction with Intel ArBB</i>	70
C. Bergmann <i>et al.</i> : <i>A New cluster-based CbmRoot reconstruction chain for the TRD</i>	71
A. Lebedev <i>et al.</i> : <i>Status of tracking in the TRD and MUCH detectors of the CBM experiment</i>	72
S. Lebedev, C. Höhne and G. Ososkov: <i>Status of the electron identification algorithms for the RICH and TRD detectors in the CBM experiment</i>	73
V. Friese and E. Kryshen: <i>First steps towards a time-based simulation and reconstruction for the CBM experiment</i>	74
F. Uhlig: <i>Software development infrastructure for the FAIR experiments</i>	75
Physics Performance	76
V. P. Ladygin, A. I. Malakhov and T. A. Vasiliev: <i>Study of high p_T pion emission in central Au+Au collisions at CBM</i>	76
V. P. Ladygin, A. I. Malakhov and T. A. Vasiliev: <i>Study of $C_2(\Delta\phi)$ azimuthal correlation in Au+Au central collisions at CBM</i>	77
I. Vassiliev and V. Akishina: <i>Fast Ξ^- reconstruction in Au+Au collisions at 10A GeV with the CBM experiment</i>	78
I. Vassiliev, I. Kisel and V. Akishina: <i>Feasibility study of Ω^- reconstruction with the CBM experiment at SIS-300</i>	79
I. Vassiliev and I. Kisel: <i>D^0, D^+ and Λ_c decay feasibility study in the CBM experiment</i>	80
I. Vassiliev and I. Kisel: <i>D^\pm decay reconstruction in p+C collisions at SIS-100 energies with CBM</i>	81
S. Kiselev: <i>Reconstruction of Σ^+ in p+C collisions at 30 GeV with ECAL</i>	82
S. Kiselev: <i>Reconstruction of ω in p+C collisions at 30 GeV with ECAL</i>	83
A. Kiseleva <i>et al.</i> : <i>Subthreshold J/ψ production in Au+Au collisions at SIS-100 studied with a start version of the CBM muon detector</i>	84
Publications	85
Activities	87
Collaboration	94

Status of the CBM experiment at FAIR

P. Senger for the CBM Collaboration

GSI Darmstadt

Observables

The Compressed Baryonic Matter (CBM) experiment is designed to explore the QCD phase diagram in the region of high net-baryon densities using rare diagnostic probes. The layout of the CBM detectors is driven by the corresponding experimental requirements concerning reaction rates, radiation tolerance, particle densities, and selectivity. The experimental challenges are illustrated in Fig. 1, which depicts the yield of various particle species produced in central Au+Au collisions at 25A GeV. The yield is defined as the product of particle multiplicity times branching ratio for the decay products under consideration, e.g. the di-leptonic decay of vector mesons (ρ , ω , ϕ , J/ψ) and the hadronic decay of open charm (D mesons). Note that the particle yield per collision spans 13 orders of magnitude with leptons and hadrons in the exit channel, embedded in about 800 charged particles. Multi-strange hyperons, vector mesons and charmed particles will be measured for the first time at FAIR energies with CBM, which therefore has a substantial discovery potential.

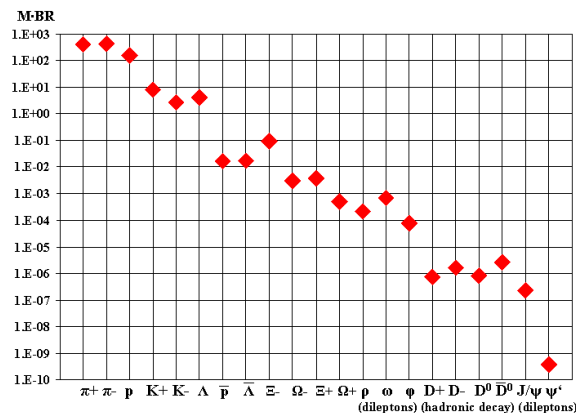


Figure 1: Particle multiplicities times branching ratio for central Au+Au collisions at 25A GeV as calculated with the HSD transport code and the statistical model. For the vector mesons (ρ , ω , ϕ , J/ψ), the decay into lepton pairs was assumed, for D mesons the hadronic decay into kaons and pions.

Selected R&D activities for CBM

The **CBM SC dipole magnet** has a large aperture (gap height 130 cm, gap width 160 cm) in order to host the Sil-

icon Tracking System (STS). The last STS station exhibits a height of about 120 cm including its front-end boards and the thermal enclosure. In beam direction, the magnet yoke is very compact (length 100 cm) in order to achieve a polar angle acceptance of $\pm 25^\circ$. The engineering design of the magnet is in progress.

The precise determination of the secondary decay vertices of charmed particles requires a highly-granulated, fast, radiation-hard, and low-mass detector system. The **CBM Micro-Vertex Detector (MVD)** consists of silicon pixel stations, which are based on ultra-thin Monolithic Active Pixel Sensors (MAPS). In 2010, sensors could be produced with a high-resistivity CMOS process, resulting in a high signal-to-noise value even after irradiation with an integrated neutron dose of $10^{13} n_{eq}/cm^2$. Further improvements are expected with smaller feature size. A prototype read-out-system and a mechanical detector design were developed.

The **CBM Silicon Tracking System (STS)** is based on double-sided micro-strip sensors. Large-area prototype detectors with outer dimensions of 6.2 cm by 6.2 cm and 1024 AC-coupled strips per side were produced. The front and back side strips are inclined by a stereo angle of 15° . Short strips in the sensor corners are interconnected to a strip in the opposite corner via a second metallization layer. The sensors will be used to build a demonstrator ladder. Further double-sided micro-strip test sensors with new radiation tolerant structures were designed.

The sensors are read out via low-mass cables of up to 50 cm length in order to keep the active area of the detector free of electronics. The cables consist of micro-line-structured aluminium layers on polyimide carrier foils.

Two prototype Silicon tracking stations consisting of double-sided silicon micro-strip sensors, ultra-thin readout cables, and self-triggering readout electronics were successfully tested at COSY with a 3 GeV proton beam. Detailed simulations were performed in order to understand the expected radiation damage in the sensors. The layout of the detector stations, i.e. the number and size of the sensors mounted on the vertical ladder structures, was optimized to reduce the number of spare parts while preserving the tracking performance.

The **RICH photo-detector** exhibits an active area of $2.4 m^2$, which is covered by multi-anode photomultipliers (MAPMTs). Beam tests at GSI and CERN and measurements with LEDs in the laboratory demonstrated that the Hamamatsu H8500 with 64 pixels is very well suited for the detection of single Cherenkov photons. Properties like the quantum efficiency (with and without wavelength shift-

ing films), crosstalk and the performance of MAPMTs in the presence of magnetic fields were successfully studied. The MAPMT signals were read out by the self-triggered electronics of the nXYTER chip. The results were very promising, also in view of the possible use of a future CBM ASIC for the RICH photo detector. The RICH gas system was designed and is presently being built. The reflectivity of different mirrors was investigated.

The **CBM Transition Radiation Detector (TRD)** has to provide electron identification and pion suppression by a factor of the order of 100 for momenta above 1 GeV/c at hit rates of 100 kHz/cm². Such a high pion suppression factor (corresponding to a pion efficiency of 1%) together with an electron efficiency of better than 90% can only be achieved with 9 - 12 layers of TRD chambers, resulting in an overall detector area of almost 1000 m². Several prototype detectors were developed to fulfill the requirements. One approach is to use fast multi-wire chambers with a thin amplification region with and without drift section. These detectors were read out by a newly developed self-triggered SPADIC chip, which both amplifies and digitizes the pulses from the CBM-TRD. Another option is a two-dimension position sensitive prototype TRD with diagonally split rectangular (i.e. triangular) read-out pads, which allow a position determination both across and along the pads. This detector is read out by a new Fast Analogue Signal Processor (FASP). The various prototype TRDs were successfully tested at CERN using a mixed beam of electrons and pions with momenta of 1 - 5 GeV/c.

In order to identify the soft muons from vector meson decays in a large combinatorial background, the **CBM muon detector** is designed as an instrumented hadron absorber. The detection system comprises six iron slabs of different thickness (20 cm - 100 cm) with detector triplets behind each iron absorber (18 detector layers in total). The development of the muon tracking detectors concentrates on the construction and test of prototype gaseous detectors based on different technologies. The detector layers behind the first and second hadron absorber (particle density up to 500 kHz/cm²) will be based on GEM technology or on hybrid detectors combining different technologies. Various prototype detectors were built and tested with radioactive sources and particle beams: double and triple thin GEMs, double thick GEMs, and thin and thick GEMs with Microegas. We investigated the use of single-mask GEM foils, which can be produced in large size at moderate costs. In the third and fourth absorber gap (particle density up to 5 kHz/cm²), we may either use hybrid detectors or Microegas with a resistive strip layer suppressing the sparks. The latter technology allows to build large-area detectors. For the last detector layers where the occupancy is low, we foresee multiple-layer straw tubes. Prototype triple GEM detectors read out by a free-streaming FEE and DAQ system were successfully tested at COSY with a 3 GeV proton beam. The hybrid detectors were successfully tested with 5 GeV proton and pion beams at CERN.

A start version of the muon detection system was devel-

oped with three absorber layers and three detector triplets only. This system would allow to identify J/ψ mesons in Au+Au collisions at SIS-100, i.e. at beam energies below the J/ψ production threshold in nucleon-nucleon collisions, which is 11.3 GeV.

Time-of-flight measurements in CBM require a large-area, highly granulated and fast detector, which will be based on Multigap Resistive Plate Chambers (MRPC). Hit rates of up to 20 kHz/cm² are expected to occur in the inner part of the **CBM-TOF wall**. Prototype MRPCs were built with electrodes made of special glass with a resistivity of the order of 10¹⁰ Ω/cm. With a 10-gap MRPC, a time resolution of about 70 ps was achieved at a rate of 20 kHz/cm². In order to cope with the high particle density per event at small emission angles, a high-granularity MRPC was developed. This prototype exhibits a symmetric structure with 2 × 8 glass electrodes and a read-out electrode with short strips (46 mm long). The resulting time resolution is 57 ps. A MRPC with electrodes made of low-resistivity ceramics was built and tested at rates up to 200 kHz/cm². At large polar emission angles, i.e. in most of the active area of the CBM-TOF detector, the hit rate is of the order of 1 kHz/cm². At such low rates, a conventional MRPC in multi-strip configuration with thin standard float glass can be used. For this application, a fully differential prototype MRPC was built and tested successfully at COSY with a proton beam, together with a high-granularity prototype MRPC with low-resistivity glass electrodes. In the test experiment, both detectors were read out with self-triggered front-end electronics.

The free-streaming **CBM data read-out system** sends the hit information of each detector together with time stamps into the data acquisition chain. The hits have to be associated to physical events by the reconstruction algorithms. A software package was developed which allows the generation of Monte-Carlo data consisting of hits with individual time stamps, and removing the correlation of detector hits with events. The next step is to develop "4-dimensional" event reconstruction algorithms, which take the time information into account for track reconstruction and pattern recognition.

Development of high-precision pixel sensors for the CBM vertex detector

M. Winter for the IPHC team

IPHC, Strasbourg, France

The physics program of the CBM experiment translates into stringent constraints on its Micro-Vertex Detector (MVD). CMOS sensors, which are granular and thin enough, are developed since several years to adapt them to the high hit rate expected. An important step was achieved in 2010 with a high-resistivity CMOS process, which was investigated with two sensors.

The first full-scale sensor featuring fast readout with integrated zero suppression, called MIMOSA-26 [1], was manufactured in 2008/2009 in a $0.35\ \mu\text{m}$ CMOS technology based on a standard, low-resistivity epitaxial layer. More recently, high-resistivity epitaxial layers became available, reducing the thermal diffusion of the signal charges, for the benefit of the SNR and thus the radiation tolerance. MIMOSA-26 was re-fabricated with a $400\ \Omega\cdot\text{cm}$ resistivity, 10, 15 or $20\ \mu\text{m}$ thick, epitaxial layer. Laboratory measurements were performed by illuminating these sensors with ^{55}Fe and ^{106}Ru sources [2]. The SNR obtained with the high-resistivity epitaxial layer ($\sim 35\text{-}40$) was about twice higher than with the standard one (~ 20).

Sensors were tested with a $\sim 100\ \text{GeV}$ particle beam at the CERN-SPS. The results are summarised in Fig. 1. The detection efficiency remains close to 100 % for high discriminator threshold values, indicating that even after a potential increase of the noise, consecutive e.g. to irradiation, a threshold value should still be found with a detection efficiency well above 99% and an affordable fake hit rate.

The sensitivity to non-ionising radiation was investigated for a fluence of $10^{13}\ \text{n}_{\text{eq}}/\text{cm}^2$. The sensor performances were measured at the CERN-SPS for a temperature of 0°C (see Fig. 1). A threshold of 5-6 mV allows keeping the fake hit rate below 10^{-4} with a detection efficiency of nearly 100 %.

In order to optimise the detection performances of the sensor in this new, high-resistivity process, a dedicated prototype was manufactured in spring 2010. By sub-dividing the sensitive area in sub-arrays, each equipped with different pixels, alternative amplification schemes were investigated as well as a larger pitch ($20.7\ \mu\text{m}$ instead of 18.4) and enclosed transistor designs. The sensor detection performances were assessed in the laboratory and with a test beam as already mentioned for MIMOSA-26.

Beam tests were in particular performed at a temperature of $+30^\circ\text{C}$ with pixels featuring a $20.7\ \mu\text{m}$ pitch read out in $125\ \mu\text{s}$, irradiated with 1 MeV neutrons (fluence of $3\cdot 10^{12}\ \text{n}_{\text{eq}}/\text{cm}^2$) and 10 keV X-Rays (150 kRad). A detection efficiency of 99.8 % was still observed for a 5 mV threshold, with a fake hit rate well below 10^{-4} . One may derive from these results that for typical CBM-MVD run-

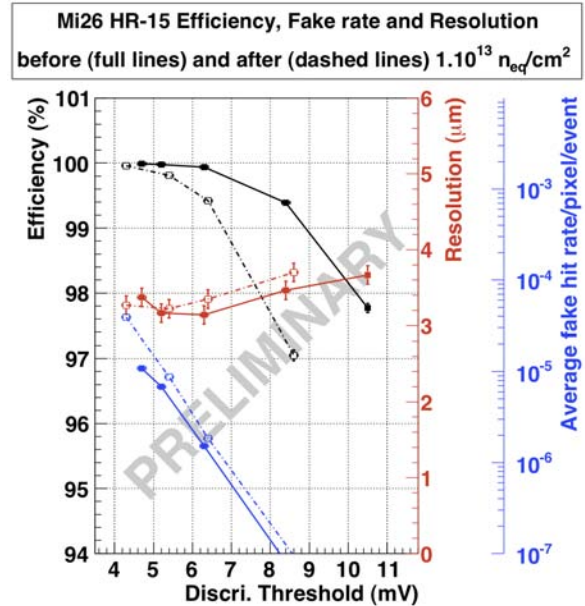


Figure 1: MIMOSA-26 beam test results for a $15\ \mu\text{m}$ thick high-resistivity epitaxy. The detection efficiency (black), fake hit rate (blue) and spatial resolution (red) are shown as function of the discriminator threshold. They are displayed at 20°C before irradiation (full lines) and after an equivalent dose of $10^{13}\ \text{n}_{\text{eq}}/\text{cm}^2$ at 0°C (dashed lines).

ning conditions ($20\text{-}40\ \mu\text{s}$ integration time and negative operating temperature), a substantially larger irradiation level would still be affordable. This study is under way.

The next step of the development will consist in moving from the coarse $0.35\ \mu\text{m}$ technology used up to now to a substantially smaller feature size, i.e. $0.18\ \mu\text{m}$. This translation is expected to benefit several aspects of the sensor, in particular the ionising radiation tolerance. A first prototype (MIMOSA-27) was fabricated in such a technology in 2010. Its tests at the CERN-SPS are foreseen in spring 2011.

References

- [1] M. Winter and M. Deveaux, *CBM Progress Report 2009*, Darmstadt 2010, p. 5
- [2] M. Deveaux *et al.*, *Radiation tolerance of a column parallel CMOS sensor with high resistivity epitaxial layer*, accepted for publication by JINST

Annealing studies on X-ray and neutron irradiated CMOS MAPS

D. Doering, M. Deveaux, C. Dritsa, M. Domachowski, I. Fröhlich, M. Koziel, C. Müntz, and J. Stroth
Goethe University, Frankfurt, Germany

Monolithic Active Pixel Sensors (MAPS) are proposed as sensor technology for the vertex detector of the CBM experiment [1]. The development of MAPS towards the radiation hardness required by CBM is the matter of a joint research programme of IPHC Strasbourg, the University of Frankfurt and GSI Darmstadt.

It is a known fact that the lifetime of silicon-based sensors might be extended by recovering radiation damage by means of annealing [2]. A prominent example of this annealing is the recovery of surface and bulk defects. The past studies on MAPS have shown that a thermal treatment may reduce the leakage current of X-ray irradiated diodes [3]. We therefore considered annealing as an interesting method to recover the performances of irradiated sensors. However, it had to be studied if the benefits of annealing would eventually be cancelled by a potential reverse annealing of bulk damage, when defects create a complex defect cluster. Thus we performed a systematic study on the annealing of MAPS.

The annealing studies were carried out with the MIMOSA-19 prototype sensors received from IPHC Strasbourg. The chips were irradiated with 10^{13} n_{eq}/cm² unmoderated fission neutrons [4]. Consecutive to the neutron irradiation, the chips were bonded, characterized and stored for one year at room temperature. Another characterization was then performed to identify potential long-term room temperature annealing, which was not observed. Once those studies were completed, several of the neutron irradiated samples and some not irradiated ones were exposed to 200 kRad of 10 keV X-rays at room temperature and their characterization started three hours later. The measurements were regularly repeated in order to study room temperature annealing. As shown later, this effect went mostly into saturation after ~ 280 h. The sensors were then heated up to $+80$ °C in order to search for the consequences of annealing at this temperature. This thermal treatment was regularly interrupted in order to perform further measurements. To magnify the radiation-induced leakage current, which was the point of interest, the sensors were kept at $+20$ °C during the measurements.

The results of our measurements are shown in Fig. 1, which displays the leakage current of the differently irradiated sensors as function of the annealing time. The left part of the plot represents the annealing time at room temperature, the right part the annealing time at $T = +80$ °C. Note that in the second part, the time needed for measurements and the time of room temperature storage are neglected. This explains the step at $t = 290$ h, which was caused by few days of room temperature annealing. After

X-ray irradiation, an exponential room-temperature annealing occurred, reducing the leakage current by $\sim 20\%$. At $T = +80$ °C, we observed a more pronounced effect. After keeping the sensor in hot atmosphere for 75 h, the leakage current of the pixels was observed to decrease to 30% of the pre-annealing value. For sensors irradiated only with neutrons, the leakage current decreased by $\sim 10\%$. This may be attributed to an annealing of the ionizing damage caused by the γ -background of the neutron beam. The annealing behavior of the sensors irradiated with both X-ray and neutron radiation is mostly determined by the annealing of the ionizing damage.

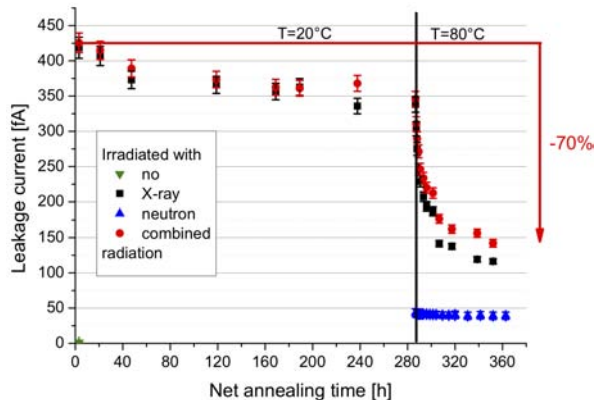


Figure 1: Results of the annealing study

The observed decrease of the leakage current after annealing is likely specific for the chosen sensor prototype. However, the trend which was found should be representative for the general case, and therefore it can be concluded that annealing might be a helpful tool to reduce the effects of ionizing radiation damage in CMOS Monolithic Active Pixel Sensors.

References

- [1] M. Deveaux *et al.*, Pos(VERTEX 2008)028 (2008)
- [2] G. Lindström *et al.*, Nucl. Instrum. Meth. A **466** (2001) 308
- [3] G. Deptuch, *A New Generation of Monolithic Active Pixel Sensors for Charged Particle Detection*, Dissertation, IPHC Strasbourg 2002
- [4] H. Breitkreutz *et al.*, Nucl. Instrum. Meth. A **593** (2008) 466

Status of the mechanical design of the CBM-MVD

*T. Tischler, S. Amar-Youcef, M. Deveaux, I. Fröhlich, M. Koziel, C. Müntz, C. Schrader, and J. Stroth
for the CBM-MVD Collaboration*

Goethe University, Frankfurt am Main, Germany

For the design of the Micro-Vertex Detector (MVD) for the CBM experiment, we are following two approaches. The first approach uses advanced technologies regarding sensor integration and interconnections. The second one is a more conventional approach with well defined building blocks (sensor, carrier, cooling, readout cables, FEE), which however incorporates advanced materials and concepts under the aspects of minimisation of the material budget as well as vacuum operation. The latter will be discussed here.

The sensor technology we will use in the MVD is based on Monolithic Active Pixel Sensors (MAPS). The sensor for the final MVD will be MIMOSIS-1, which will be thinned down to a thickness of 50 μm . As this sensor is still to be developed, we are currently working with a precursor named MIMOSA-26[1]. The form factor of this precursor does not fit the one of the final sensor, which will be adapted during the development phase.

The support material in the active area of the MVD will be CVD diamond with a thickness of 300 μm , adding only a small amount to the material budget. An effective cooling is mandatory because of the operation in vacuum. The CVD diamond covers this part by providing an outstanding heat conductivity of about $2000 \text{ WK}^{-1}\text{m}^{-1}$ at low temperatures.

Outside of the active area of the MVD, copper plates are currently discussed to be used for cooling of the CVD diamond (and sensors) and readout electronics. The diamond on which the MIMOSIS-1 sensors are mounted is cooled via cooling the copper plates. The interconnections ensuring an optimal heat transfer between CVD diamond and copper heat sinks as well as between cooling fluid and copper heat sinks are key points, which are still subject of detailed studies.

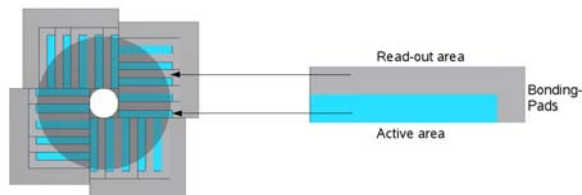


Figure 1: Double-sided sensor arrangement of the first MVD station, acceptance of the first station (grey disk) and MIMOSIS-1 sensor with subdivision into active and passive parts

The design of the MVD, worked out with Autodesk [2], is constrained by the requirements of the CBM experiment. For the first station, a disk featuring an inner radius of 5.5 mm and an outer radius of 25 mm has to be covered with sensors; for the second station, the inner radius is 5.5 mm and the outer radius 50 mm. Based on the form factors of the sensors, which are still under consideration and are not necessarily the same for both stations, this acceptance translates to 40 double-sided arranged sensors for the first and 76 double-sided arranged sensors for the second station (see Fig. 1 for the first station). Figure 2 shows the preliminary concept of the vacuum vessel housing both MVD stations, comprising the support structures, heat sinks for the readout electronics, readout electronics, FPCs, readout cables and cooling tubes (both not in proper numbers). The dimensions of this vacuum vessel are $800 \times 600 \times 200 \text{ mm}^3$.

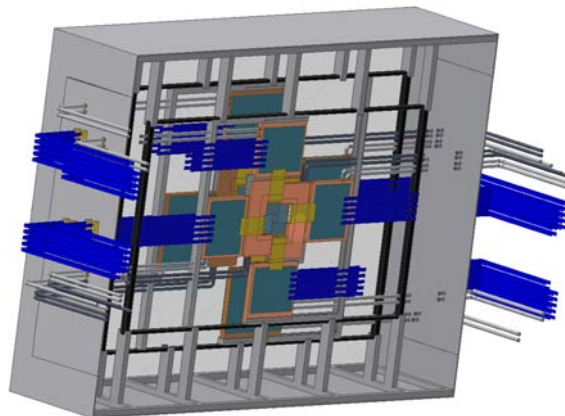


Figure 2: Complete vacuum vessel housing the MVD

For the ongoing physics simulations, a simplified model of the first MVD station containing the support material, the sensors (which were explicitly divided into active and passive areas), the heat sink for the sensors and for the electronics was successfully transformed from CAD to ROOT geometry with a converter provided by the Panda Collaboration [3].

References

- [1] MIMOSA-26, IPHC, Strasbourg, France, <http://www.iphc.cnrs.fr>
- [2] Autodesk Inventor 2010, <http://www.autodesk.de>
- [3] Panda CAD-Converter, <http://panda-wiki.gsi.de>

Status of the CBM-MVD prototype readout

C. Schrader, N. Bialas, S. Amar-Youcef, M. Deveaux, I. Fröhlich, M. Koziel, J. Michel, C. Müntz, B. Neumann, S. Schreiber, T. Tischler, and J. Stroth for the CBM-MVD Collaboration

Goethe University, Frankfurt am Main, Germany

The readout system of the prototype of the CBM-MVD is intended to form a flexible software and hardware solution, which provides the bandwidth and scalability needed for a use in the final MVD. It will be developed based on the state-of-the-art prototype sensor MIMOSA-26 [1]. Despite the readout speed of this sensor not yet being optimised for the final MVD, MIMOSA-26 provides already today the full architecture foreseen for the final MVD and may therefore serve as a useful model of the final sensor.

The MIMOSA-26 sensor handles 570 hits per frame and provides a digital output data stream of 160 Mbit/s sent via two digital output lines. The data stream holds addresses of the pixels containing hits, and frame numbers. A firmware update of our MAPS readout board allowed us to read out the MIMOSA-26 sensors. Furthermore, we were able to reduce the data stream to 80 Mbit/s by removing redundant information.

The future sensors equipping the first generation CBM-MVD will presumably handle a several times higher occupancy than MIMOSA-26, likely ranging up to 800 Mbit/s [2].

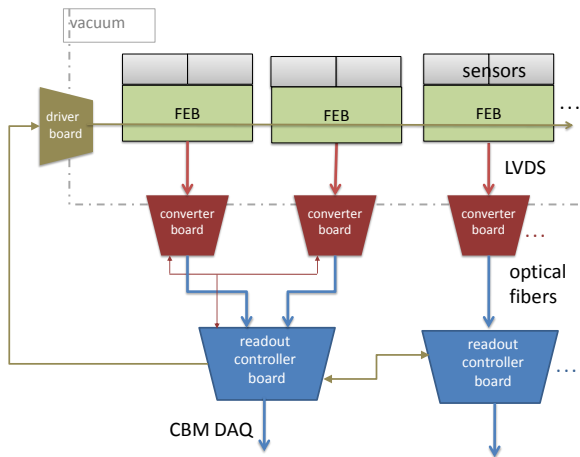


Figure 1: The prototype readout chain

The concept of the readout system of the MVD-prototype is designed accordingly. Figure 1 shows a sketch of the envisaged architecture of the prototype readout chain. Two sensors will be bonded on a flex-print cable, which transfers the data via a fine pitch connector to a front-end board. The future radiation environment requires the use of a radiation-tolerant, passive board. This board serves as an interface between the flex-print cables

and conventional copper wires. Moreover, it distributes the sensor clock and the slow-control signals. The data of the two digital output channels of each sensor are transferred via LVDS cables to a converter board. Currently we consider two functionalities for this board. By embedding it into a vacuum flange, we aim to use the board to pass the cables out of the vacuum of the combined MVD and target chamber. The second task is the data conversion from LVDS to 8 bit/10 bit encoded, 1 Gbit/s, optical signals (see Fig. 2 for details).

A readout controller board receives the optical signals. It hosts an FPGA which controls the data acquisition and allows using on-line data reduction and filtering algorithms.

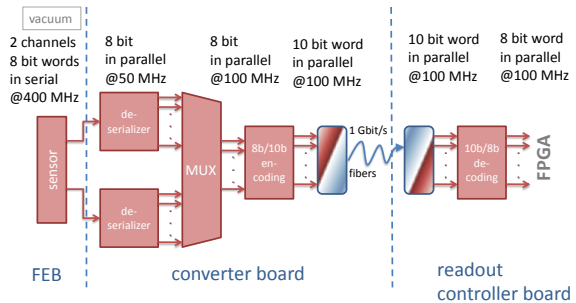


Figure 2: Data flow with the different conversion steps

Slow control will be done by JTAG boundary scan which allows accessing the internal register of the individual sensors. The slow control ensures also latch-up handling and monitoring of on-line temperature and current.

The boards are submitted for production and will be assembled and tested in the next months. In parallel to the hardware developments, the related FPGA firmware is being developed.

References

- [1] C. Hu-Guo *et al.*, Nucl. Instrum. Meth. A **623** (2010) 480
- [2] S. Seddiki *et al.*, *Expected data rates of the CBM-MVD at SIS-100 based on realistic beam intensity fluctuations*, this report

Expected data rates of the CBM-MVD at SIS-100 based on realistic beam intensity fluctuations

S. Seddiki^{1,2}, M. Deveaux¹, C. Drita^{1,2}, C. Müntz¹, and J. Stroth^{1,3}

¹Goethe University, Frankfurt am Main, Germany; ²IPHC, Strasbourg, France; ³GSI, Darmstadt, Germany

The Micro-Vertex Detector (MVD) of the CBM experiment will be located close to the collision point and exposed to very high track densities from heavy-ion collisions at high interaction rates. The design of the MVD requires a detailed knowledge of the detector occupancies and the corresponding data rates, which were simulated in this work.

The first step of the study was to determine typical beam intensities for standard collision systems foreseen at SIS-100, i.e. p+Au collisions at 30 GeV and Au+Au collisions at 10A GeV bombarding energy. Two main constraints on the beam intensity were considered: the hit densities and the radiation dose in the first MVD station placed 5 cm downstream of the target. First, studies demonstrated that a maximal hit density of $\sim 17.5 \text{ mm}^{-2}$ per readout cycle can be accepted in the MVD [1]. Secondly, simulations of the radiation dose received by the MVD indicated that it could tolerate $\sim 5 \times 10^{13}$ p+Au and $\sim 5 \times 10^{12}$ Au+Au collisions [2], assuming a non-ionizing radiation hardness of $10^{14} \text{ n}_{\text{eq}}\text{cm}^{-2}$. This last value might be in reach for the future sensor at SIS-100, according to measurements performed with MIMOSA-25 featuring a highly resistive epitaxial layer [3].

Simulations of the occupancies in the MVD stations located at 5, 10 and 15 cm from the target were performed using UrQMD + GEANT 3.21, as discussed in [4]. These simulations accounted for the δ electrons knocked out of the target by the Au ions (they could be neglected for p+Au collisions). The geometry of the MVD sensors and stations located at 5 and 10 cm from the target was chosen according to [6]. The third station was extrapolated at 15 cm from the target to satisfy the CBM acceptance. The simulations suggest that in the case of p+Au collisions, the beam intensity is limited by the radiation hardness of the MVD to a mean value of $\sim 10^9$ protons/s. For Au+Au collisions, the beam intensity is limited by the high hit densities caused by the δ electrons to a maximal value of $\sim 2 \times 10^7$ ions/s.

The second step is to estimate the amount of data provided by the MVD sensors during their $30 \mu\text{s}$ long readout cycle. To account for the beam fluctuations of SIS-100, we assumed a factor of three for the ratio between the maximal and the average beam intensity. This number was motivated by observations made with the HADES beam diagnostics at SIS-18 [5]. We simulated 10^3 readout cycles which contained in average 3×10^4 protons or ~ 200 Au ions passing through the target. The number of nuclear collisions was computed using a Poisson distribution considering a 1% interaction target.

The data volume was estimated based on the data for-

mat of MIMOSA-26 [7], since this chip integrates the binary readout and sparsification circuits foreseen for the final sensor of the MVD. The left panel of Fig. 1 shows the data volume per readout cycle in the sensor exposed to the highest track densities. For Au+Au collisions the data flow is dominated by the δ electrons (red curves) and amounts up to $\sim 3 \text{ kB}$ per readout cycle. Consequently, the memory of the final chip should be increased by a factor of ~ 3 and the output clock frequency by a factor of ~ 7 with respect to MIMOSA-26. The right panel presents the data flow per station for p+Au collisions. As in the absence of hot spots driven by δ electrons, a higher average occupancy can be reached, data flows as high as 7 GB/s for 3 MVD stations are obtained.

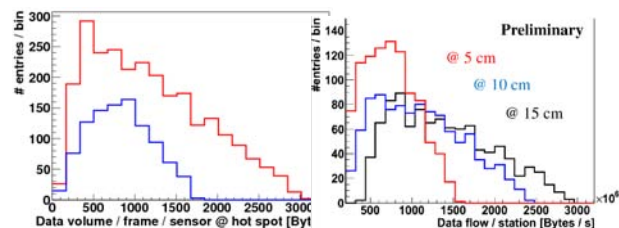


Figure 1: (Left) Data volume per readout cycle in the sensor exposed to the highest track densities, in case of p+Au (blue) and Au+Au collisions (red). (Right) Data flow per station for p+Au collisions.

References

- [1] C. Drita, *Feasibility studies of open charm reconstruction with pile-up*, CBM collaboration meeting, Darmstadt, April 2010
- [2] D. Bertini, *Radiation dose simulations*, CBM collaboration meeting, Darmstadt, March 2009
- [3] W. Dulinski, VIPS-2010, Workshop, Pavia, April 2010
- [4] S. Seddiki, *CBM Progress Report 2008*, Darmstadt 2009, p. 3
- [5] P. Forck *et al.*, *GSI Scientific Report 2005*, Darmstadt 2006, p. 107
- [6] T. Tischler *et al.*, *Status of the mechanical design of the CBM Micro-Vertex Detector*, this report
- [7] A. Himmi, *Mimosa 26 User Manual*, V.1.0, December 2008

Performance simulations with a realistic model of the CBM Silicon Tracking System

A. Kotynia¹ and J. M. Heuser²

¹Goethe University, Frankfurt, Germany; ²GSI, Darmstadt, Germany

Efficient charged-particle tracking and high momentum resolution are central performance requirements of the CBM Silicon Tracking System (STS). The aim of the ongoing layout studies is to design a highly granular and low-mass detector system which can track up to 1000 charged particles that are typically generated in one central Au+Au collision at 25 GeV/nucleon projectile energy.

Detector layout

The STS comprises eight tracking stations located at 30, 35, 40, 50, 60, 75, 95 and 100 cm downstream of the target (Fig. 1). The stations have a modular structure and are constructed from 300 μm thick double-sided silicon micro-strip sensors. Groups of sensors (sectors) are individually read out with electronics located at the perimeter of the stations. The number, position and segmentation of the layers are optimized for efficient track reconstruction and high momentum resolution. On the other hand, from the point of view of mass production and logistic, it is highly desirable to limit the number of different sensors and ladders to the minimum possible.

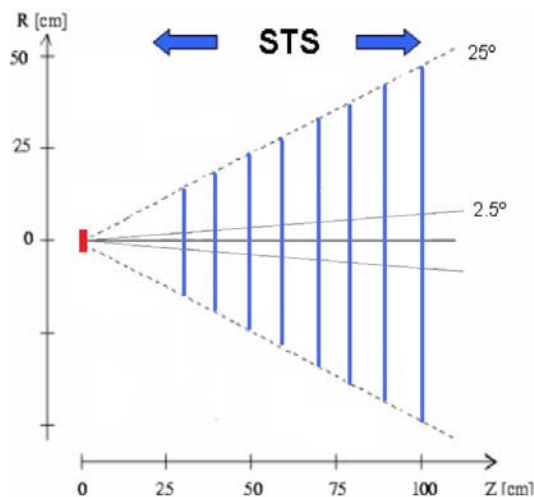


Figure 1: Schematical side view of the STS system

Material budget

The silicon detector is designed minimizing the total amount of material: the silicon sensors have the minimum

thickness capable to provide a good signal-to-noise ratio, namely 300 μm . The simulated amount of material for the STS corresponds to 0.3% X_0 for the silicon sensors; a comparable effective thickness is added by the cables, where the simulated amount of material is equivalent to 70 μm silicon, giving 0.08% X_0 for every cable layer. A maximum value of approximately 1% X_0 is reached in the outer parts of every station, where eight layers of cables overlap. Adding the cable material into the simulation worsens the momentum resolution from 1.1% to 1.5%.

Silicon sensors

The full STS will use only four types of silicon sensors. In the innermost parts of the first three stations, where the particle occupancy is expected to reach 5%, 2 cm long strips were chosen to minimize the number of ghost hits. However, to reduce the material budget in the regions where the occupancy is lower than 5%, it is possible to use up to three 6 cm long sensors chained together, thus creating an effective strip length of up to 18 cm.

The expected strip occupancies and the required spatial resolution suggest a strip pitch of 60 μm . A value of 58 μm was chosen here, because it allows to divide the sensitive width of the sensor into 1024 strips, corresponding to 8 read-out chips of 128 input channels each. On either side of the double-sided sensor the strips are tilted by $+7.5^\circ$ or -7.5° with respect to the vertical edge, creating 15° stereo angle between the opposite sides. This allows to reconstruct multiple hits from the same sensor at the expense of a poorer spatial resolution in the vertical direction, keeping high resolution in horizontal direction for better reconstruction of the particle momenta in the 1 T dipole field.

Station layout

For all stations the full height of the sensitive area can be covered by vertical ladders of ten sectors (see Fig. 2). Neighboring ladders overlap by 5 mm in order to avoid dead space caused by the guard ring structures of the sensors. The number of ladders was chosen to cover 25° acceptance as closely as possible, the outer parts of stations 2-8 are equipped with ladders from previous stations. The presented layout allows to construct the full STS with only eight types of ladders. The total number of sensors, ladders and read-out channels are summarized in Table 1.

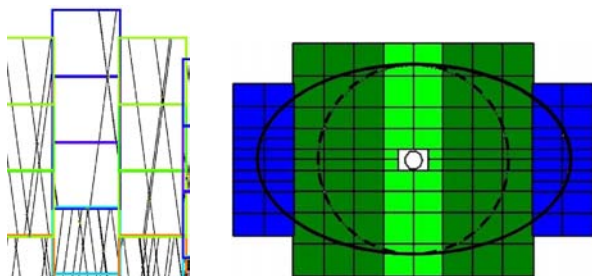


Figure 2: Left: Event display showing active strips in one of the STS stations; the stereo angle between front and back strips is 15° . Right: Second STS station, placed at 40 cm downstream from the target. Different colors represents different ladder types. Each ladder is built from ten sensors. The dashed circle corresponds to 25° geometrical acceptance, the solid ellipse to a horizontally extended acceptance in order to provide efficient reconstruction of low-momentum electrons.

Table 1: Summary of STS components

Station	Ladders	Sectors	Sensors	R/O chips	Channels
1	8	80	80	1280	164k
2	12	120	120	1920	247k
3	12	120	120	1920	247k
4	14	136	172	2176	279k
5	14	136	156	2176	279k
6	14	136	192	2176	279k
7	16	156	220	2496	319k
8	16	156	232	2496	319k
Total	106	1040	1292	16640	2133k

For comparison, a purely geometric estimate of the minimal number of read-out channels required to cover the geometrical acceptance of $2.5^\circ - 25^\circ$ at a maximal sensor occupancy of 5% yields 12k read-out chips. The difference between this estimate and the number of r/o chips quoted for the proposed layout is mainly due to the necessity to limit the number of different sensors and ladders to the minimum possible.

Performance studies

The layout presented above was used to implement the STS in the CBM simulation framework. This implementation includes the complete chain of physical processes caused by a charged particle traversing the detector from charge creation in the silicon to the digital output signals. The first step of STS hit reconstruction is performed by an algorithm called cluster finder. A cluster is a group of signals caused by a particle traversing a portion of the detector. A signal has to pass a threshold to be taken into account, otherwise it is rejected. In the STS case, the threshold is constant for every channel and equals $4000 e^-$. The accepted signals coming from adjacent strips of a sensor side are grouped together in a cluster. The total charge of a cluster is defined as the sum of the single strip signals. The

cluster position is given by the center-of-gravity [1] equation

$$X_{COG} = \frac{\sum_{cluster} S_i x_i}{\sum_{cluster} S_i} \quad (1)$$

where x_i is the position of the i^{th} strip included in the cluster and S_i the signal on this strip; the sums runs over all strips included in the cluster.

In the next step, the association of two clusters lying on the opposite sides of the double-sided sensor is performed. The last step defines the hits and their properties.

Applying realistic detector response functions [2] such as:

- ▷ signal sharing between strips
- ▷ charge collection inefficiency
- ▷ Lorentz shift due to presence of the magnetic field
- ▷ channel dead time
- ▷ random noise added to the charge signal

together with a Cellular Automaton for track finding and a Kalman Filter for track fitting, results in a track finding efficiency of 97% for fast primary tracks and 75% for secondary tracks, with a momentum resolution of 1.1%. These results were obtained with a noise width of 0.5k electrons and a charge threshold level of 4k electrons.

Since the granularity of the detector changed in comparison to the one presented in [3], the time for track reconstruction of central Au+Au collisions decreased from 3.6 to 2.3 seconds per event on a single-core CPU. The STS granularity has also a strong impact on number of combinatorial hits. It was possible to reduce the number of ghost hits by 10%.

Conclusions

The simulations described in this report take into account the properties of the STS detector. The results obtained with our algorithm indicate a preference for a detector geometry with high granularity. As far as the predictions of realistic cable thickness are correct, the results obtained clearly show that the solution with a minimum number of different ladders is the preferred one from the point of view of performance and maintenance. However, the external constraints that define the size of STS stations are not yet finally defined. Consequently, details of the layout may be subject to change.

References

- [1] V. Bartsch *et al.*, Nucl. Instrum. Meth. **A 497** (2003) 389
- [2] A. Kotynia, J. M. Heuser and W. F. J. Müller, *CBM Progress Report 2009*, Darmstadt 2010, p. 7
- [3] A. Kotynia and J. M. Heuser, *CBM Progress Report 2009*, Darmstadt 2010, p. 6

Development of microstrip detectors for the CBM Silicon Tracking System

J. M. Heuser¹, L. Long², H. G. Ortlepp², S. Chatterji¹, A. Lymanets^{3,4}, I. Sorokin^{3,4}, M. Singla³,
C. J. Schmidt¹, V. Kleipa¹, C. Simons¹, W. Niebur¹, L. Xu⁵, and A. Hastir⁶

¹GSI, Darmstadt, Germany; ²CiS Forschungsinstitut für Mikrosensorik und Photovoltaik GmbH, Erfurt, Germany;
³Goethe University, Frankfurt, Germany; ⁴Kiev Institute for Nuclear Research, Kiev, Ukraine;
⁵University of Science and Technology of China, Hefei, China; ⁶Guru Nanak Dev University, Amritsar, India

The second prototype of a full-size microstrip detector for the CBM Silicon Tracking Detector System was developed in cooperation with CiS [1]. It will be used for the construction of a demonstrator ladder, the building block of the silicon tracking stations. A batch of 24 wafers was produced in July 2010, and first detectors were characterized at GSI. A further achievement in the cooperation with CiS was the design and fabrication of double-sided test detectors with novel radiation tolerant structures.

The design CBM03 [2] was realized on 4" masks and was produced on high-resistivity n-type float-zone wafers of 300 μm thickness. It includes one large double-sided microstrip detector, several small double-sided detectors and other test structures. The large-area detector has outer dimensions of $6.2 \times 6.2 \text{ cm}^2$ and comprises 1024 AC-coupled strips per side forming a stereo angle of 15° between the front and back side strips. Short strips in the detector corners are interconnected to a strip in the opposite corner via a second metallization layer. The strips are biased with both poly-silicon resistors and punch-through structures. Both detector sides have the same segmentation and contact pattern, which limits the complexity of the microcables for their connection to the readout electronics.

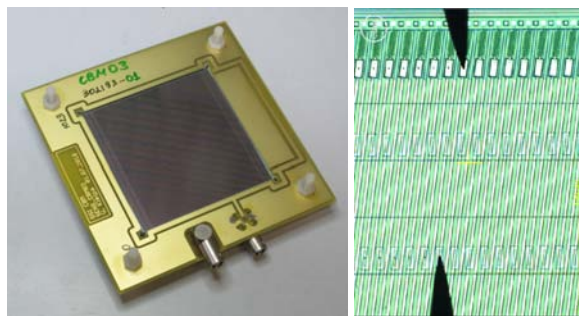


Figure 1: (Left) A CBM03 microstrip detector mounted on a test board for characterization under bias voltage; (right) microscope photograph of a CBM03 detector on a probe station for testing individual strips.

For the characterization of the detectors, new infrastructure was developed and set up at GSI. This includes a program-controlled voltage-scan test station and a wafer prober Süss-PA300. The bulk current-voltage (I-V) and capacitance-voltage (C-V) behaviour can serve as primary acceptance criteria. For this test, every detector is installed

in a simple fixture, shown in Fig. 1-left. The sandwich of two identical printed circuit boards has a square opening with a thin balcony structure milled in that accepts the detector. Bias is provided to the detector through two wire bonds. The scan is then run with a program-controlled precision source-measure unit and a LCR meter. Results of the characterization are shown in Fig. 2. Individual strips are characterized on the probe station. Fine needles can be brought into contact with the readout or bias pads as shown in Fig. 1-right. One important inspection concerns the insulation between the implanted strip and the metal electrode. It is formed by an about 0.2 μm thin SiO_2 layer. This layer is prone to defects that short the capacitor. A strip-by-strip investigation showed that the current CBM03 detectors exhibit such defects. The reason for the shorts is being investigated. Further characterization of the sensor will involve measurement of interstrip parameters, e.g. resistance and capacitance, and their alteration after exposure to radiation.

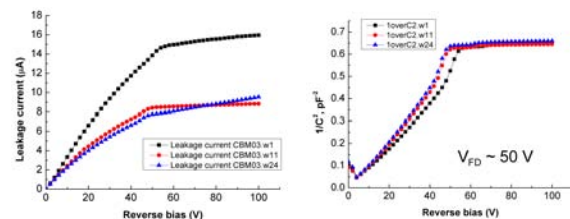


Figure 2: Characterization of CBM03 detectors. Plots of I vs. V (left) and $1/C^2$ vs. V (right) allow extracting the full depletion point, here around 50 V.

Prototypes of double-sided microstrip detectors with new radiation-tolerant structures were designed and manufactured by CiS. The test detectors comprise Schottky barriers between the strips to increase their charge collection after irradiation. GSI is research partner for the evaluation of these detectors before and after irradiation, to be performed in 2011.

References

- [1] <http://www.cismst.de>
- [2] J. M. Heuser *et al.*, *CBM Progress Report 2009*, Darmstadt 2010, p. 10

First Russian double-sided silicon strip sensors for CBM

M. Merkin¹, N. Baranova¹, D. Karmanov¹, N. Egorov², S. Golubkov², A. Yu. Murin^{3,4}, and the CBM-MPD STS Consortium

¹Skobeltsyn Institute of Nuclear Physics of Moscow State University (SINP MSU), Moscow, Russia; ²Research Institute of Material Science and Technology (RIMST), Zelenograd, Russia; ³Joint Institute for Nuclear Research (JINR), Dubna, Russia

In July 2010, the first pilot batch of Russian silicon double-sided sensors with double metallization was produced at RIMST by the topology especially developed for the CBM experiment. Of the 20 wafers manufactured, 14 were made on Wacker Siltronic HighReflection (HiRef) wafers, and 6 on double-sided, polished FZ wafers.

The sensors were tested and certified at SINP MSU. The yield of the sensors made on the HiRef material as estimated from the total leakage currents was around 20%. Further measurements of these sensors revealed numerous other faults such as broken-through coupling capacitors (on both p- and n-sides) caused by surface scratches on the wafers, from which it became clear that using the HiRef wafers for production of double-sided detectors is not practical. The yield of the sensors produced from the FZ material was about 50%; their quality significantly surpassed that of the sensors made on the HiRef wafers. Fig. 1 shows the $1/C^2-V$ dependencies for the sensors made on the FZ wafers. From these curves, the depletion voltage can be estimated as the voltage at which the measured capacitance becomes nearly constant. Determined this way, depletion voltages for the sensors made on the FZ wafers turn out to be lower than those of the HiRef sensors.

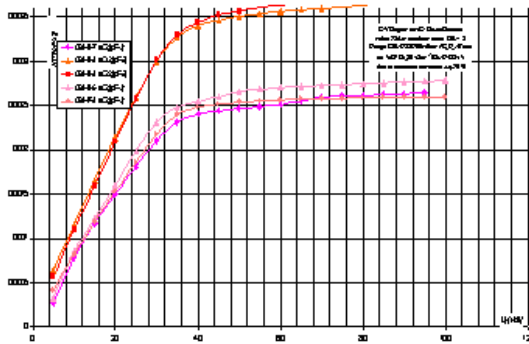


Figure 1: Total bulk capacitance of sensors on FZ wafers

To characterize the sensors more precisely and for a probable correction of the detector topology, we measured the capacitances and quality of coupling capacitors on the n- and p-sides of the sensors. The results obtained for the p-side are shown in Fig. 2.

The proportion of short-circuit capacitors for the p-side is less than 0.5%, but there exist a few short-circuit ones with twofold and threefold capacitances. The total proportion of broken-through and short-circuit capacitors is less

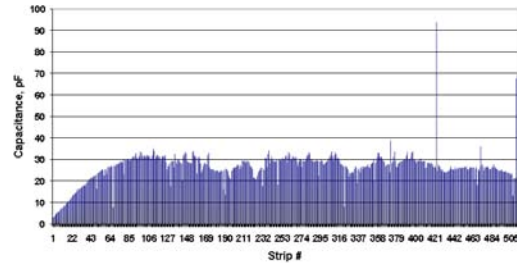


Figure 2: Capacitances of coupling capacitors at the p-side

than 1%. The results obtained for the n-side of the sensors suggest high enough etching quality of aluminium: no short-circuit strips were observed. The proportion of broken-through capacitors (with capacitances below 20pF) is less than 1%.

Among the most important characteristics of double-sided sensors is the quality of the n-strip isolation. This characteristic was selectively investigated on the sensors made on the FZ wafers. Figure 3-left shows the strip current as a function of bias voltage. The sharp drop of strip current at 34-35 V is an evidence of the separation of strips by p-stops. This value of separation voltage agrees well with the measurements of the full depletion voltage.

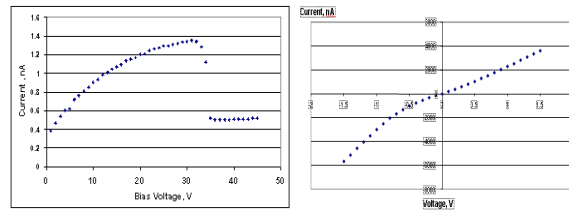


Figure 3: (left) Strip current on the n-side of a sensor as a function of bias voltage; (right) measurement of a bias resistor on the p-side of the sensor (right)

Figure 3-right shows the values of polysilicon biasing resistors measured on the p-sides of the sensor. The resistance falls within the tolerable range and is fairly linear. The measured values of the resistors are 0.5 MΩ and 2.5 MΩ for p- and n-sides, respectively.

The topology and production technology developed and used for manufacturing the first Russian double-sided Silicon strip detectors may be considered as well suited for further use.

Simulation study on the radiation tolerance of microstrip detectors for the CBM Silicon Tracking System

S. Chatterji¹, M. Singla², and J. M. Heuser¹

¹GSI, Darmstadt, Germany; ²FIAS, Goethe University, Frankfurt, Germany

We are using the three-dimensional TCAD simulation package from Synopsys [1] to simulate double-sided silicon strip detectors (DSSDs) for the CBM Silicon Tracking System (STS). The STS will consist of eight stations of DSSDs at a distance of 30-100 cm from the target. The expected neutron fluence will vary from $1 \times 10^{13} \text{ n}_{eq} \text{ cm}^{-2}$ to $1 \times 10^{15} \text{ n}_{eq} \text{ cm}^{-2}$ depending on the location of the sensors. Hence we performed detailed simulations to understand the expected radiation damage in DSSDs and to foresee if these DSSDs will be able to survive the expected lifetime of the CBM experiment. We have simulated two types of DSSDs, one having orthogonal strips and other having a stereo angle of $\pm 7.5^\circ$. Fig. 1 shows a zoom on the n-side of the simulated detector.

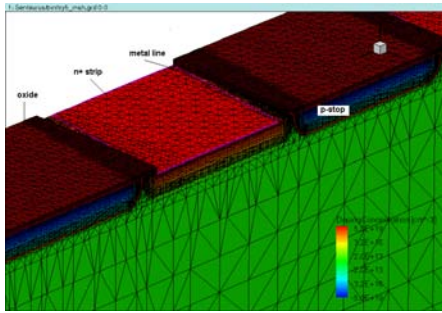


Figure 1: Zoomed frontal view of the simulated DSSD

We simulated the impact of irradiation by varying the effective doping concentration (N_{eff}) and minority carrier lifetime (τ) with fluence (ϕ) using the Hamburg model [3]. The effect of surface damage was also studied by varying the oxide charge density (Q_F) at the Si-SiO₂ interface. The values of integrated fluence and the corresponding values of N_{eff} and τ are listed in Table 1. The University of Perugia trap model [2] was applied. The time line assumes CBM operating at highest interaction rates ($10^7/\text{s}$).

Fig. 2 shows the simulated versus the measured current-

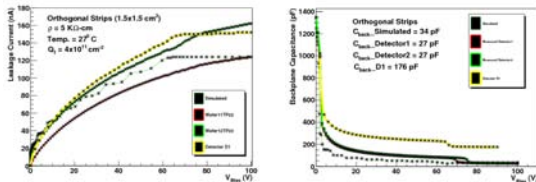


Figure 2: Simulated I-V and C-V curves compared with measurements of several CBM01/02 prototype detectors

voltage (I-V) and backplane capacitance-voltage (C-V) behaviour before irradiation for a DSSD with orthogonal strips of size $1.5 \times 1.5 \text{ cm}^2$. The simulation results are comparable with the measurements. Fig. 3 shows the leakage current density versus the fluence for DSSDs with a stereo angle of $\pm 7.5^\circ$. The simulated values of the damage constant (α) for DSSDs with orthogonal strips and with stereo angle of $\pm 7.5^\circ$ are $3.6 \times 10^{-17} \text{ A/cm}$ and $4.0 \times 10^{-17} \text{ A/cm}$, respectively, while the experimental value is $\alpha = (3.99 \pm 0.03) \times 10^{-17} \text{ A/cm}$ [4]. We will compare the simulated α with our detectors after irradiations in 2011.

Table 1: Fluence profile of neutrons as expected for CBM

Year	Int. Fluence [$10^{14} \text{ n/cm}^{-2}$]	$N_{eff} * 10^{11}$ [cm^{-3}]	$\tau_{electron}$ [μsec]	τ_{hole} [μsec]
0	0	9	1000	300
0.05	0.05	7.41	4.98	4.92
0.3	0.3	-1.72	0.833	0.831
1	1.0	-34.3	0.250	0.250
2	2.0	-89.9	0.125	0.125
3	3.0	-150	0.083	0.083
4	4.0	-214	0.062	0.062
5	5.0	-278	0.05	0.05
6	6.0	-343	0.041	0.041

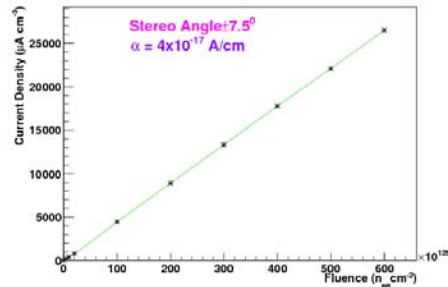


Figure 3: Variation of leakage current density with neutron fluence for the silicon microstrip detector with stereo angle

References

- [1] <http://www.synopsys.com/home.aspx>
- [2] M. Petasecca *et al.*, IEEE Trans. Nucl. Sci. **53** (2006) 2971
- [3] M. Moll, E. Fretwurst and G. Lindström, Nucl. Instrum. Meth. A **439** (2000) 282
- [4] M. Moll, *Radiation damage in silicon particle detectors-microscopic defects and macroscopic properties*, Dissertation, Universität Hamburg 1999

Radiation hardness tests of silicon strip detectors at the cyclotron-based neutron irradiation station of the V G. Khlopin Radium Institute

D. Karmanov¹, N. Baranova¹, M. Merkin¹, L. Lebedev², V. Jakovlev², S. Lashaev², Yu. Murin^{2,3}, J. M. Heuser⁴, and the CBM-MPD STS Consortium

¹Skobeltsyn Institute of Nuclear Physics of Moscow State University (SINP MSU), Moscow, Russia;

²V. G. Khlopin Radium Institute (KRI), St. Petersburg, Russia; ³Joint Institute for Nuclear Research (JINR), Dubna, Russia; ⁴GSI, Darmstadt, Germany

Five double-sided silicon strip detectors manufactured by CiS, Germany, were irradiated at the MGC-20 cyclotron-based neutron irradiation station of KRI, St.-Petersburg, and tested at SINP MSU, Moscow, Russia. The detectors were irradiated with mono-energetic neutrons generated in the deuterium gas target in the D(d,n) reaction. The energy of the deuterium beam was determined by irradiating nickel foils with a thickness of 100 μm and using interpolated data on the yield of the $^{nat}\text{Ni}(d,X)^{61}\text{Cu}$ reaction. The neutron spectrum calculated from the measured deuteron energy was then used (with the data on reactions' cross sections) to determine the neutron fluxes and reduce them to the 1 MeV equivalent neutrons. The neutron fluxes were monitored by irradiating aluminium foils and measuring the activity of ^{27}Mg and ^{24}Na from the $^{27}\text{Al}(n,p)^{27}\text{Mg}$ and $^{27}\text{Al}(n,\alpha)^{24}\text{Na}$ reactions. The samples were exposed to the neutron fluences (reduced to 1 MeV) of 2.06×10^{12} , 3.03×10^{12} , 3.93×10^{12} , 11.2×10^{12} , and 2.6×10^{13} n/cm^2 . Prior to and after irradiation, the following detector parameters were determined at SINP MSU: total leakage current (I_{bias}), resistance of the FOXFET biasing resistors at the working biasing voltage (R_{FOXNET}), inter-strip resistance between adjacent strips at the working bias ($R_{\text{interstrip}}$), depletion voltage of the p-n junctions of strips (V_{op}), leakage currents of p- and n-strips at depletion voltage or exceeding it by 10 V (I_{str}), and the leakage currents of the AC capacitors at depletion voltage or exceeding it by 10 V (I_{AC}).

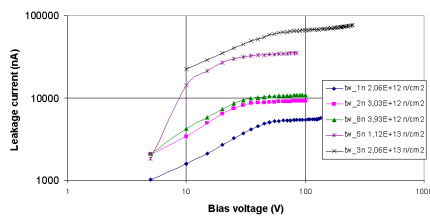


Figure 1: Total leakage current (n side, normalised to 20°C) as a function of bias voltage for different neutron fluences

The total leakage current of all strips of the irradiated samples as a function of bias voltage is shown in Fig. 1. The flat parts of the I(V) curves give an indication of the bulk volume thermal generation current as the main component of the total leakage current. Some typical inter-strip resistance - bias voltage relationships for separate strips of all irradiated samples which were used to determine the galvanic separation voltage are shown in Fig. 2-top. After

irradiation, the voltage drop across the bias (FOXFET) resistors significantly increases, which results from the rapid increase of the leakage current coupled with the slow resistance increase of the resistors. This means that for detectors with the FOXFET resistors used in harsh radiation environment, the working voltage depends not only on the full depletion voltage but even more on the leakage current. The full depletion voltage V_{fd} as a function of neutron fluence is shown in Fig. 2-bottom. In the same figure, values obtained in 2009 from the capacitance - voltage relationship for CiS sample pad test structures are shown. The 10^{13} n/cm^2 fluence is interpreted as a conductivity type inversion point. We observe a similar dependence of full depletion voltage on neutron fluence for double-sided microstrip sensors and for sample pad structures produced by the same manufacturer and measured using different procedures.

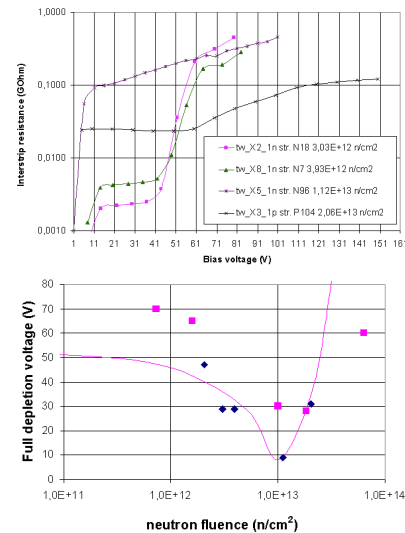


Figure 2: (top) Resistance between adjacent strips as a function of bias voltage; (bottom) full depletion voltage as a function of neutron fluence. The squares denote the strip detectors, the diamonds the CiS test structures.

The procedures developed for irradiation and measuring parameters of double-sided detectors provide results conforming to the expected values and to the results obtained using other procedures. This makes it possible to use the developed procedures in further radiation tests of such detectors.

Development of low-mass readout cables for the CBM Silicon Tracking System

J. M. Heuser¹, V. Borshchov², S. Chatterji¹, M. Singla³, and W. F. J. Müller¹

¹GSI, Darmstadt, Germany; ²State Enterprise Scientific Research Technological Institute of Instrumental Engineering (SE SRTIIE), Kharkov, Ukraine; ³Goethe University, Frankfurt, Germany

Low-mass readout cables are of critical importance in the Silicon Tracking System (STS) under development for the CBM experiment. The aperture of the tracking stations is planned to be kept free of readout electronics that is arranged at the perimeter of the fiducial area instead. The signals from the double-sided silicon microstrip detectors are routed through multi-line fine-pitch cables to those readout boards, bridging distances of up to around 50 cm. Prototype cables are being developed in cooperation with SE SRTIIE of the State Space Agency of Ukraine [1].

The cable is based on microline-structured aluminum layers on polyimide carrier foils. Line pitches down to a few tens of micrometers are feasible depending on the length of the cable to be realized. The electrical connection of the lines to both the detectors and the readout electronics are laid out as tab bonds through openings in the polyimide foil.

Demonstrators of a fine-structured single-layer cable tab-bonded to prototype microstrip detectors CBM02 were realized in the year 2008. The aluminum signal lines are 14 μm thick, 20 μm wide and have 50 μm pitch at the detector. The objects were used in the recent STS beam test [2]. Further optimized specimen, shown in Fig. 1, were produced in 2010 to complete a reference tracking system for forthcoming in-beam tests of STS components.

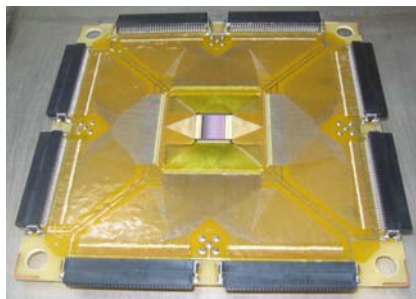


Figure 1: Demonstrator board 2b-4 with a CBM02 detector

High line densities up to 50 μm pitch can only be produced in short cables. From about 7 cm length on, the signal paths must be arranged staggered across two signal layers at e.g. double line pitch. Demonstrators of such multi-layer cables were produced already last year [3]. In the first approach, they yielded non-symmetric capacitive load to the readout electronics. This is shown in Fig. 2, obtained with the simulation package RAPHAEL of Synopsis TCAD. An improved cable design is shown in Fig. 3. It is being used in the demonstrator module shown in Fig. 4 with three daisy-chained microstrip detectors and a multi-layer readout cable of 1024 signal lines. Measurements of

the line capacitances yield close values for the upper and lower layer, about 0.3 pF per cm. The material budget of the cable is between 0.1% and 0.17% radiation length.

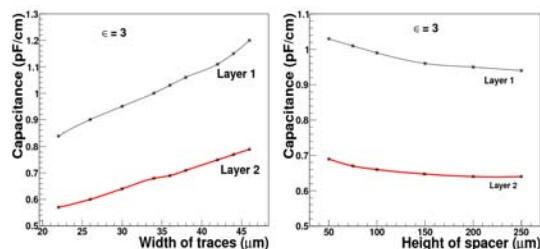


Figure 2: Line capacitance in the upper and lower signal layers as a function of the width of the traces (left) and the thickness of the spacer (right)

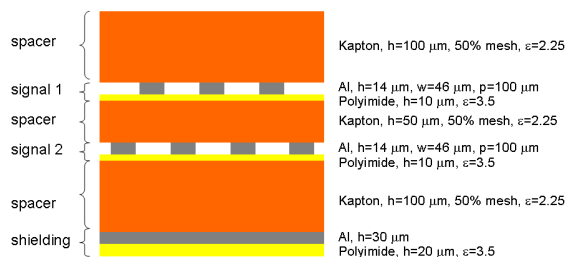


Figure 3: Cross section of the readout cable

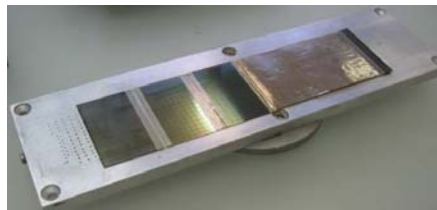


Figure 4: Demonstrator 2a with ISTC03/CBM03 detectors

Further electrical parameters, e.g. the line resistivity as a source of noise, are being addressed together with the designers of the front-end electronics. Also the radiation hardness of the polyimide material is being studied [4].

References

- [1] <http://www.nkau.gov.ua/nsau/nkau.nsf/indexE>
- [2] J. M. Heuser *et al.*, *Test of prototype modules of the CBM Silicon Tracking System in a proton beam at COSY*, this report
- [3] V. M. Borshchov *et al.*, *CBM Progress Report 2009*, Darmstadt 2010, p. 15
- [4] D. Severin *et al.*, *Radiation hardness of low-mass readout cables for the CBM experiment*, this report

Radiation hardness of low-mass readout cables for the CBM experiment

D. Severin, M. Bender, and J. M. Heuser

GSI, Darmstadt, Germany

For the fixed-target heavy-ion experiment CBM at FAIR, a low-mass silicon tracking detector system is being developed that can track at high rates the hundreds of charged particles that will be created when an intense beam of heavy nuclei interacts with the target [1]. The detector is based on silicon microstrip technology. Fast self-triggering front-end electronics will be located at the periphery of the tracking system. The distance between the detectors and the electronics will be bridged with thin long aluminium cables structured into microstrip lines and insulated with polyimide. In the CBM environment, the exposure to ionizing radiation is estimated to be about 100-200 kGy in several years of operation. For reliable operation, radiation-induced changes of the bulk and/or surface conductivity of the dielectric material have to be excluded.

Several cable prototypes with lengths between 10 and 30 cm, shown on Fig. 1, were manufactured at SE SRTIIE, Kharkov, Ukraine [2]. A cable consists of two signal layers, a shielding layer, and a mesh spacer. Each signal layer is structured into 64 aluminium lines ($14\ \mu\text{m}$ thick, $20\ \mu\text{m}$ wide, at $100\ \mu\text{m}$ pitch, on $10\ \mu\text{m}$ thick FDI-A-24 dielectric).



Figure 1: Different prototypes of microstrip line cables

For a first radiation hardness test, a 10 cm long multi-layer flat-wire of the CBM detector demonstrator was mounted on an aluminium plate and irradiated with 4.8 MeV/u Au ions at the M3-beamline of the UNILAC. The size of the beam spot was about $1\ \text{cm}^2$. Three single-circuit paths were connected to a charge-frequency converter (IFC). The IFC records charges down to 100 fC and is triggered by the beam pulse. On-line measurements thus allow us to monitor beam-induced currents passing through the device.

In stage A of the experiment, the beam spot was set besides the flat-wire lines to check any indirect radiation ef-

fect (section A in Fig. 2). Comparing the ion-beam flux and the signal during the irradiation of the test device clearly shows that no additional electric current appears in the back plate. During stage B, the middle part of the flat-wire was irradiated on a length of 1 cm with a flux of 2.5×10^7 ions/cm²s. The IFC recorded a signal of 22 pC which follows synchronously the beam flux signal. Even small flux variations are visible.

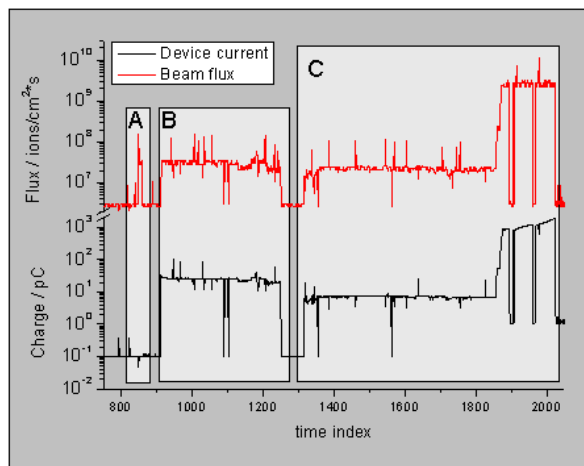


Figure 2: Device signal (black, bottom) and flux of the ion beam (red, top) during different irradiation tests A-C (see text for details)

In stage C, only one single wire (instead of three) was measured. At a fixed flux of 2.3×10^7 ions/cm²s, the measured charge for three contacted wires was 21.9 pC compared to 7.2 pC for a single wire, confirming a linear scaling behaviour. In the last phase of experiment C, the flux was increased by two orders of magnitude. Under this high-flux condition, the current increased significantly with time, indicating either a serious temperature increase or a pronounced change of the electrical properties.

This demonstrator device, which has been exposed in total to 1.56×10^{12} ions/cm², will be tested off-line especially with respect to loss of insulation properties due to radiation damage of polyimide [3].

References

- [1] J. M. Heuser, PoS(VERTEX 2008)017 (2008)
- [2] V. M. Borshchov *et al.*, *CBM Progress Report 2009*, Darmstadt 2010, p. 15
- [3] D. Severin *et al.*, Nucl. Instrum. Meth. **B 236** (2005) 456

Conceptual design of mechanics for the CBM Silicon Tracking System

S. N. Igolkin¹, Yu. A. Murin^{1,3}, J. M. Heuser², and the CBM-MPD STS Consortium

¹V. G. Khlopin Radium Institute (KRI), St. Petersburg, Russia; ²GSI, Darmstadt, Germany; ³Joint Institute for Nuclear Research (JINR), Dubna, Russia

The mechanics of the STS was designed in accordance with the requirements of the CBM experiment, with the extensive use of the experience gained in creating similar installations for other experiments, including ALICE at LHC. The tracker consists of eight stations of silicon detectors positioned along the beam axis. A general view of the tracker is shown in Fig. 1.

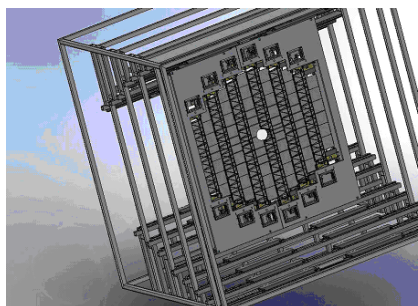


Figure 1: Front view of the tracker with detector station 4

The detectors used in the tracking system are either single double-sided silicon strip detectors or, at the periphery of the stations, complex detectors composed of two or three daisy-chained sensors. Single or composite detectors connected to the end cap electronics with analogue cables make up detector modules, which can be tested separately and stored as spares. The modules are mounted on lightweight space frames with end supports to form ladders. The supporting structure of the ladder is a three-edged space frame made of the M55JB high-modulus carbon fiber impregnated with a hot polymerization epoxy binder. Depending on the station number and on the ladder position, the lengths of the frames vary from 280 mm to 1060 mm. The frames were optimized in calculations using the ANSYS software package. Their mass can be minimized by placing them vertically to reduce the gravitation sagging. The calculated specific mass of the frames is 14 g / 1000 mm. An optimized version of the ladder is shown in Fig. 2.

The fabrication technique for the production of lightweight carbon-fiber space frames is based on a one-cycle polymerization process at 125°C in a metallic mold. The ladders are assembled with the use of a dedicated machine. They are mounted on flat bearing plates made of carbon plastic. The accurate positioning of the ladders with minimum stress is ensured by pins with ruby spheres. A block of ladders is shown in Fig. 3-left. The stations are built from these blocks.

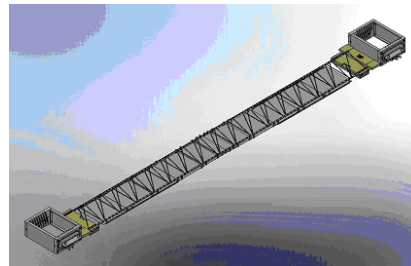


Figure 2: Optimized version of the ladder (without cables and front-end electronics)

The eight stations of the tracking system are arranged in four two-station modules. The main supporting unit of the module is a rectangular frame made of carbon composite tubes. Each frame is equipped with a precision linear bearing and two carriages joined together by a U-shaped bar thus forming a movable block. This block can be moved along the rail of a linear bearing and even outside of the module with the use of a supplementary rail. The U-shaped bars have landing pins for precision mounting of the ladders. The stations in the module are placed 110 mm apart, but the two-station modules themselves are placed 200 mm apart, which makes it possible to freely place on the vertical tubes of the main supporting frame such service components as fittings, electrical and optical connectors and manifolds of the liquid cooling system. The frames with the linear bearings provide accurate relative positioning of the stations. A half station is shown in Fig. 3-right.



Figure 3: (Left) A block of ladders. (Right) Half-station of a two-station module with two blocks mounted.

The design presented above provides

- accurate mounting/replacement of ladder blocks using a removable supplementary rail,
- realization of detector overlaps in the vertical plane by slightly shifted front and rear blocks,
- possible movement of blocks to the sides during beam tuning to avoid radiation damage to the detectors.

Prototyping of the CBM STS module

V. M. Borshchov¹, Yu. A. Murin², M. A. Protsenko¹, I. T. Tymchuk¹, O. M. Listratenko¹, S. Bazylev², V. Rogov², A. V. Tsenner¹, A. M. Steblina¹, L. V. Klimova¹, and the CBM-MPD STS Consortium

¹State Enterprise Scientific Research Technological Institute of Instrumental Engineering (SE SRTIIE), Kharkov, Ukraine;

²Joint Institute for Nuclear Research (JINR), Dubna, Russia

For the prototyping of CBM-STS module, a unit of Demonstrator 2-a and front-end board (FEB) with flexible chip commutation were developed by the participants of the CBM-MPD STS Consortium and manufactured using aluminium-polyimide commutation elements and “Chip-on-Flex” assembly technology in SE SRTIIE, Kharkov, Ukraine.

Each prototype of the Demonstrator 2a detector modules, shown in Fig. 1, comprises one or three thin, double-sided silicon sensors measuring 42 mm by 62 mm (CBM03/ISTC) or 62 mm by 62 mm (CBM03/CiS), multi-layer connecting boards as shown in Fig. 2, pitch adapters, and mechanical holding elements. The demonstrator prototypes are designed for modeling the space position of the module components, for developing fabrication methods of the components, procedures of assembling module units and the module in whole, as well as for measuring parameters of the sensors.

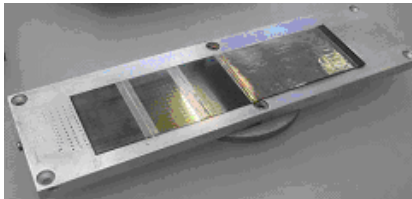


Figure 1: Demonstrator 2a

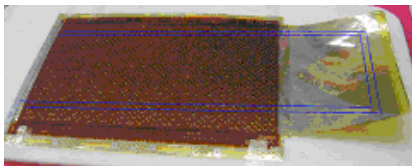


Figure 2: Multilayer readout cable

The design of the multilayer analogue connecting cable was optimized to improve the capacitive parameters. The suggested design of the optimized board is shown in Fig. 3. The total length of lines on the measured samples was approximately 24-26 cm, indicated in blue colour in Fig. 2. The measured inter-trace capacitances are presented in Table 1. An assembly sequence of the demonstrators was developed, using methods like ultrasonic bonding, gluing, and soldering. Since the number of bondings for the 2a Demonstrators is as high as 40,000, the bonding regimes were studied, and it was decided to bond the connecting boards on the automated EM-4370 machine.

Table 1: Measurement of inter-trace capacitances

	M1, pF	M2, pF	Mean, pF	pF/cm
C12	6,80	7,10	6,95	0,29
C13	3,90	4,10	4,00	0,17
C34	8,00	8,30	8,15	0,34
C1G	5,80	5,90	5,85	0,24
C3G	7,00	7,10	7,05	0,29

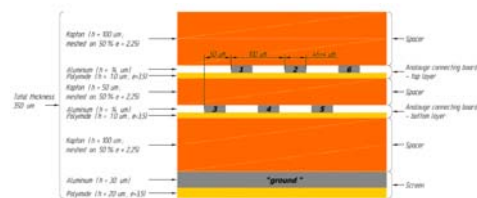


Figure 3: Structure of an analogue multi-layer cable

A further double-layer micro-cable was developed for the connection of the chip to the FEB (Fig. 4). The proposed cable design reduces the number of output contacts on the board to nearly one half. Later on, such cables will make it possible to test the chips after bonding to the cable, prior to mounting them on the board, i.e. to have on the board the indubitably operable chip. Five front-end boards with application of the n-XYTER-v01 chip and chip-cables were assembled.

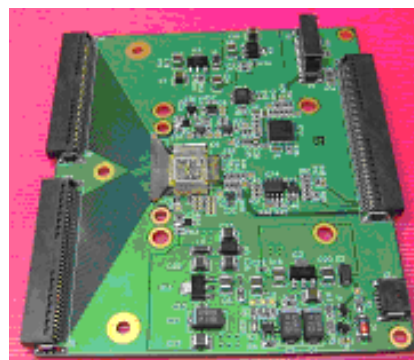


Figure 4: FEB with a cable-connected chip

The development outlined above allow us to gain experience which will be applied in future for the manufacturing of the CBM STS detector modules by the CBM-MPD STS Consortium.

Development of a quality assurance system for CBM-STS detector modules

J. M. Heuser², V. Kyva¹, A. Lymanets^{1,3}, H. Malygina¹, V. Militsiya¹, Y. Panasenko¹, V. Pugatch¹, and I. Sorokin^{1,3}

¹KINR, Kyiv, Ukraine; ²GSI, Darmstadt, Germany; ³FIAS, J.W. Goethe University, Frankfurt, Germany

The quality assurance system for the evaluation of the CBM STS detector modules equipped by silicon microstrip detectors and readout electronics is under development at KINR [1]. This year an essential progress was achieved by replacing the discrete electronics with the n-XYTER microchip and related infrastructure. The n-XYTER readout chip was used to characterize double-sided microstrip detectors of *CBM02* type. To operate the n-XYTER electronics, a front-end board (FEB) was designed at GSI as a general purpose board. We used two FEBs of revision C and D. Before connecting a sensor to the n-XYTER board, their CV as well as IV characteristics were measured. A sensor with good behaviour (*CBM02-B2*) was selected for further evaluation with the n-XYTER electronics. After connection, we inspected the IV-characteristic of the chosen sensor and found that it changed w.r.t. the unconnected sensor (Fig. 1, stars).

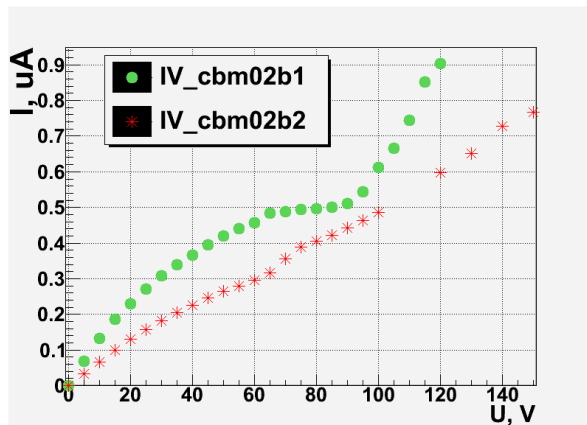


Figure 1: IV-curves measured for the *CBM02-B1* and the *CBM02-B2* sensors. For sensor *B1*, full depletion is at 65 V.

The FEB was connected to 128 channels on the p-side of a *CBM02-B2* sensor, mounted in a demonstrator 1-b assembly produced in Kharkov [2]. The n-XYTER board was operated together with a readout controller (ROC) developed at GSI.

Since double-sided detectors will be used in the future experiment, the n-XYTER must be configured for the proper polarity of the signal depending on the detector side where the chip will be connected. It was found that the baselines have different shapes for different polarities.

The dispersion (standard deviation) of the baseline position relative to the averaged one is larger for FEB D (170 ADC channels) than for FEB C (110 ADC channels).

The bent shape as well as the position dispersion reduce the effective dynamical range.

The investigation showed that half of the readout channels exhibit high noise, which complicates their usage for detector investigation. This behavior is due to the way of connecting the sensor to the nXYTER using a two-layer micro-cable. One of the layers has a considerable capacitance. Fig. 2 shows the baseline width observed with both FEBs. The noise broadens the baseline by a factor of two for strips connected by a micro-cable with large capacitance.

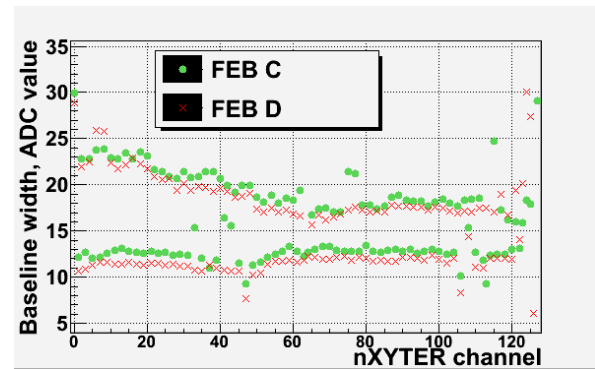


Figure 2: Baselines widths of both FEBs. The bias voltage is 70 V.

The sensor response to different types of radiation was studied (α -source ^{226}Ra , β -source ^{90}Sr , X-ray-source ^{241}Am). We tried to calibrate the detector system using X-rays (^{241}Am), but the activity of the source was insufficient (10^4 Bq) to acquire sufficient statistics. The low activity of the source requires a long exposition time. Since the current n-XYTER chip demonstrated a temperature instability, the baseline position drifts considerably with temperature and time. We used a fan for cooling; in the future we plan to use a water cooling system.

In the nearest future we will calibrate the detector module with X-rays using a 10 MBq source. Next studies will be related to the n-XYTER + *CBM02-B2* setup response to MIPs triggering on ^{90}Sr β -particles ($E_\beta > 2$ MeV).

References

- [1] V. Pugatch *et al.*, *CBM Progress Report 2009*, Darmstadt 2010, p. 12
- [2] V. M. Borshchov *et al.*, *CBM Progress Report 2009*, Darmstadt 2010, p. 15

Test of prototype modules of the CBM Silicon Tracking System in a proton beam at COSY

J. M. Heuser¹, W. Niebur¹, W. Müller¹, S. Linev¹, J. Adamczewski-Musch¹, V. Friese¹, B. W. Kolb¹, S. Chatterji¹, T. Balog^{1,3}, A. Lymanets^{2,4}, I. Sorokin^{2,4}, and M. Singla²

¹GSI, Darmstadt, Germany; ²Goethe University, Frankfurt, Germany; ³Comenius University, Bratislava, Slovakia;

⁴Kiev Institute for Nuclear Research, Kiev, Ukraine

In December 2010, prototypes of CBM's silicon tracking detector system, the muon detection system, and readout electronics were tested in a 3 GeV/c proton beam at COSY, Forschungszentrum Jülich, Germany [1]. The experimental area "Jessica" was equipped with newly prepared infrastructure from GSI, shown in Fig. 1, foreseeing forthcoming CBM in-beam tests there on a regular basis.

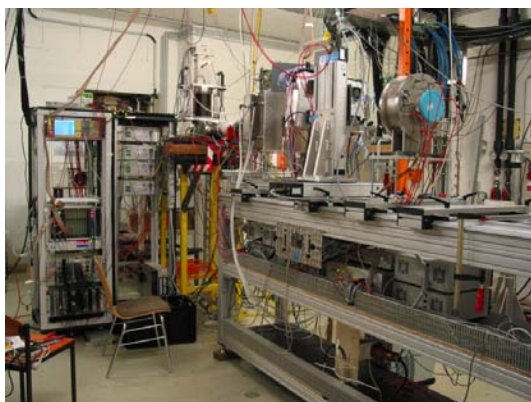


Figure 1: Test beam stand in the Jessica cave at COSY

The prototype Silicon Tracking System comprised two stations based on double-sided silicon microstrip detectors, ultra-thin readout cables, and self-triggering readout electronics (Fig. 2-left). The detectors SPID-CBM02 originate from a cooperation with CiS, Erfurt, and have 256 orthogonal strips per side with 50 μm strip pitch. The detectors were assembled into boards at SE SRTIIE, Kharkov, Ukraine. The readout boards developed at GSI are based on the self-triggering n-XYTER chip. Numerous improvements as compared to the in-beam test of 2009 [2] were introduced on hardware and software levels.

By implementing proper shielding and grounding techniques, the electronic noise was reduced to about $600 e^-$, which is now dominated by the preamplifier noise. The n-XYTER temperature was stabilized with water cooling, which abated the problem of the baseline drift significantly. In addition, an automatic baseline calibration was implemented in the data acquisition software and run between the beam spills. A detector control application based on the EPCIS [3] framework was developed and ran on a dedicated PC. All the auxiliary hardware, including power supplies, stepping motors for the GEM and the beam monitor-

ing detectors, water cooling units and temperature sensors were operated and monitored remotely. Some of the measured process variables (STS bias voltages, GEM detector position, temperatures) were periodically inserted into the data stream to study the detector response as a function of those values and to allow for temperature and high-voltage corrections in the on-line and off-line data analyses.

The amplitude response of the silicon detector system was measured as a function of the bias voltage and of the beam incidence angle. Landau-like spectra were clearly seen on the p-side at all bias voltages (50 V – 90 V) and on the n-side starting from 60 V. A cluster analysis of the charge collected in adjacent strips shows peaks at around 140 ADC units corresponding to the most probable signal from the minimum ionizing particles (Fig. 2-right). The signal-to-noise ratio was about 20 in this point. According to a previous calibration of the n-XYTER gain [4], it seems that only 60% of the expected charge was collected on either side of the detector. The reason for the apparently low collection efficiency is to be investigated.

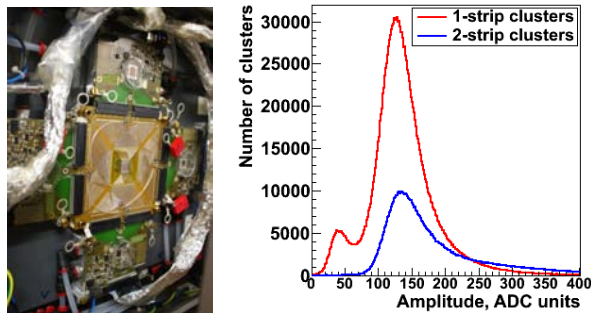


Figure 2: (Left) Opened STS station with the silicon detector board surrounded by readout electronics. (Right) Typical amplitude response spectra, here from the detector n-side, at 70 V bias and normal beam incidence.

References

- [1] <http://www.fz-juelich.de/ikp/cosy/en/>
- [2] V. Friese *et al.*, *CBM Progress Report 2009*, Darmstadt 2010, p. 9
- [3] <http://www.aps.anl.gov/epics>
- [4] C. J. Schmidt *et al.*, *CBM Progress Report 2009*, Darmstadt 2010, p. 50

Modeling the thermal operation of CBM-STS stations

V. M. Borshchov¹, Yu. A. Murin², O. M. Listratenko¹, M. A. Protsenko¹, I. T. Tymchuk¹,
L. V. Klimova¹, A. M. Steblina¹, S. V. Vlasenko¹, and the CBM-MPD STS Consortium

¹State Enterprise Scientific Research Technological Institute of Instrumental Engineering (SE SRTIIE), Kharkov, Ukraine; ²Joint Institute for Nuclear Research (JINR), Dubna, Russia

For the estimation of the temperature behaviour of the STS stations, thermal demonstrators of silicon micro-strip detectors were developed and are under production in SE SRTIIE, with participation of the CBM-MPD STS Consortium. Four types of simulators were developed on the basis of mono-crystalline silicon. Their dimensions are the same as the sensors that are foreseen to be applied in the STS detector modules:

- type 1: 62 mm by 62 mm (with beam hole);
- type 2: 62 mm by 62 mm;
- type 3: 42 mm by 62 mm;
- type 4: 22 mm by 62 mm.

The thickness of the simulators also corresponds to the thickness of silicon sensors for the modules and amounts to 300 μm .

The technical solution chosen for the realization of the simulators utilizes a heating element placed on the oxidized silicon wafer (Fig. 1). The heating elements are made from adhesiveless nickel-polyimide foiled dielectric EFN-7-type (thickness of the nickel layer: 7 μm , polyimide layer: 10 μm). The application of this material and the design of the simulators simplify the assembly of the simulators into the station by soldering (nickel is more preferable for soldering than aluminium which is used e.g. for contact pads of diffusion resistors). For this purpose, the contact pads of the heating elements are tinned. The heating elements are realized in a “meander”-type structure. The technological process for the manufacturing of the heating elements was developed as well as procedures of thinning of silicon wafers and gluing of heating elements.

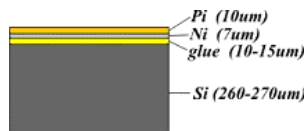


Figure 1: Structure of the thermal simulator

Several experimental samples of the thermal simulators were produced and investigated. A sample of type 4 is shown in Fig. 2. Fig. 3 shows results of a temperature cycle on the silicon wafer surface.

For the investigation of thermal operating modes of the stations, it is foreseen to manufacture sensor simulators arranged into a demonstrator of STS station 4 as shown in

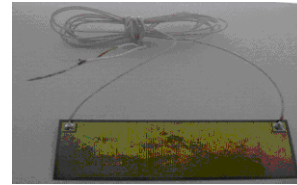


Figure 2: A manufactured demonstrator of type 4

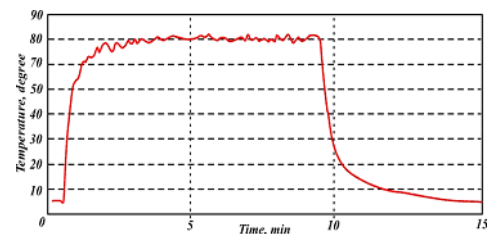


Figure 3: Temperature cycle on the silicon wafer

Fig. 4: 4 \times type 1, 86 \times type 2, 16 \times type 3 and 4 \times type 4.

The thermal simulators of sensors which were developed and are being produced will allow to perform investigations of the temperature operating modes of the CBM-STS stations and of the STS as a whole. The obtained results will be used in future for the construction of the Silicon Tracking System by the CBM-MPD STS Consortium.

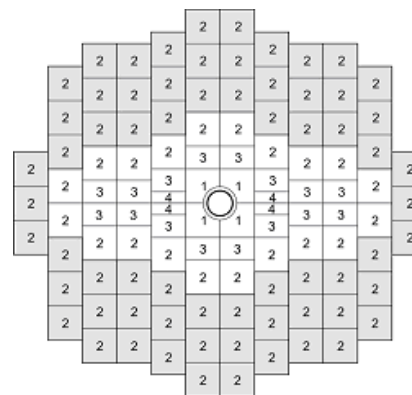


Figure 4: Arrangement of thermal simulators in configuration of STS Station 4 (right)

Simulation study of n-XYTER front-end electronics in overflow situations for early prototyping of detectors in the CBM experiment

T. Balog^{1,2}, C. J. Schmidt¹, W. F. J. Müller¹, and J. M. Heuser¹

¹GSI, Darmstadt, Germany; ²Comenius University, Bratislava, Slovakia

In high interaction rate experiments, a situation can occur when the data rate temporarily exceeds the available bandwidth. In a conventionally triggered system, these overload situations are handled with common dead time mechanisms which discard the affected fraction of the events. With self-triggering front-end electronics, such overload situations would lead, without further measures, to uncontrolled data losses and a potentially large number of incomplete events. Thus mechanisms are needed to control data losses and to ensure that complete events are recorded at least part of the time in case of overload.

The self-triggering n-XYTER chip, originally developed for neutron physics experiments, is used for early prototyping of CBM detectors [1]. This study investigates possible modifications of the n-XYTER chip architecture to control data losses. The simulations were performed using the hardware description language SystemC, which is built on the C++ standard extended with class libraries and a run-time system [2]. SystemC addresses the need for a system design and verification language that spans multiple hardware and software platforms.

We simulated the behavior of systems with one, ten, hundred and thousand chips. Each chip has 128 channels comprising a fast shaper, a pile-up rejector and a FIFO. The selection of the FIFO in which the data has to be written is made according to the Uniform distribution. The frequency of data reading by the Token Ring is 32 MHz for every n-XYTER chip. The Token Ring is able to read only one data from one FIFO in one period. We investigated the behavior of the chip with data incoming at average frequencies of 64 MHz, 52 MHz, 40 MHz, 32 MHz, 16 MHz, 8 MHz and 2 MHz. The dead time for each channel was assumed to be 30 ns, which is the recovery time needed by the fast shaper to see the next incoming hit. Furthermore, pile-ups can occur. The time window for pile-up after incoming data is assumed to be 300 ns, which is the shaping time of the slow shaper. For all the modules after the Token Ring, we assumed that no data loss occurred.

To introduce controlled data losses a counting module was added. Every channel has its own counter, which increments by one with incoming data in the FIFO. The FIFO is closed when the number of counts reaches its depth. All FIFOs are opened again and counters are set to zero after the epoch period has elapsed. An epoch period is defined as the time needed for reading all cells from all FIFOs in one chip by the Token Ring.

Fig. 1 shows that the data losses do not significantly change with the size of the system. With increasing frequency, there are also no significant losses until the aver-

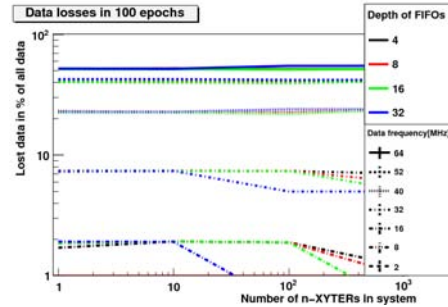


Figure 1: Data losses of the simulated system with respect to system size and average frequency of incoming data

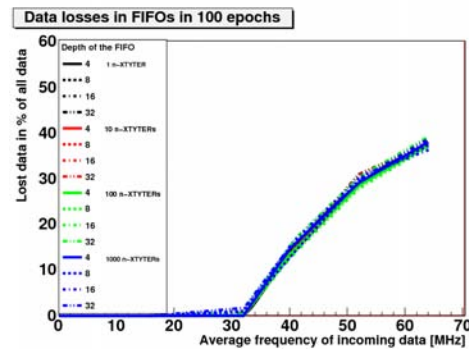


Figure 2: Data losses at the FIFO of the simulated system with respect to the average frequency of incoming data

age frequency of incoming data is same as the frequency of the Token Ring, as shown in Fig. 2. The biggest losses in the investigated range of data rate occur at the FIFOs. This is due to the reading frequency of the Token Ring which is approximately 250 kHz per channel while the average frequency of incoming data is also 250 kHz (500 kHz for 64 MHz average data rate) but with statistical fluctuations.

Another investigation was made to find out how data losses depend on the depth of the used FIFOs (4, 8, 16 and 32 cells). The result shows no significant changes within the investigated frequency range.

References

- [1] C. J. Schmidt *et al.*, *CBM Progress Report 2009*, Darmstadt 2010, p. 50
- [2] <http://www.systemc.org>

Evolution of a prototype Silicon strip detector readout ASIC for the STS

K. Kasinski, R. Szczygiel, and P. Gryboś

AGH University of Science and Technology, Krakow, Poland

The TOT01 prototype readout ASIC for the CBM STS detector was manufactured and tested in 2010. Its purpose was to test the usability of the time-over-threshold method in this application [1]. The tests revealed a significant potential of the TOT architecture. It is able to provide a low-noise, low-power and simple solution for energy measurement [2]. Since it is possible to smoothly adjust the chip's noise vs. speed characteristic to meet the application-specific requirements, its performance was evaluated for two arbitrary, opposite settings called "fast" and "slow". The performance of the TOT01 ASIC is summarized in Table 1.

GBW	1.2 GHz	power/ch	1.2 mW
gain	1600 [V/V]	ENC ^{C_{det}=28pF}	700 e ⁻
CSA gain	≈ 13 mV/fC	ENC ^{fast}	162 e ⁻
		ENC ^{slow}	162 e ⁻

Table 1: Performance of the TOT01 ASIC

TOT02, an upgraded version of this ASIC (Fig. 1), was submitted, fabricated and preliminarily tested. The chip consists of 16 channels, improved ToT-based CSA and discriminator in a radiation-hard layout and a digital back-end.

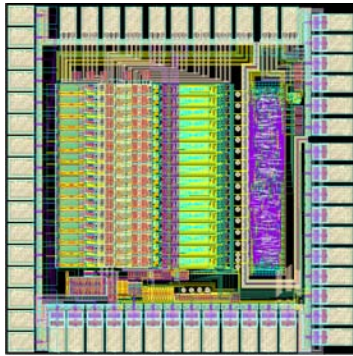


Figure 1: TOT02 ASIC layout

The analogue part contains enhanced charge-sensitive amplifier (CSA) architecture (folded cascode with booster) and modified constant-current, complementary discharge circuits (Fig.2). These changes were to minimize the pulse tail, which for lower threshold caused deterioration in energy resolution. The CSA is followed by a discriminator supplied with a 6-bit DAC for the DC level spread correction. The pulse stretchers added between the discriminator and the digital back-end prevent from short glitches which could corrupt the operation of the latches. The digital back-end implements timestamp latches triggered by the discriminator output pulse edges, token ring and serializer

(Fig. 3). Each channel is supplied with two latches triggered by the consecutive edges of the discriminator. The timestamp value latched first is the event time, while the difference between two latches represents the pulse length and should directly translate to the deposited energy.

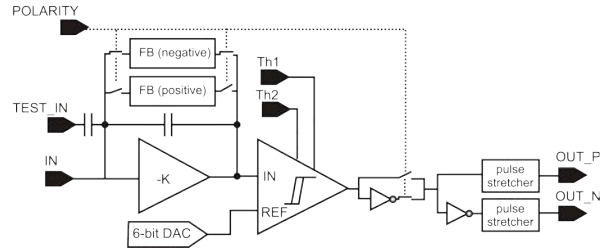


Figure 2: Analog part of the ASIC channel

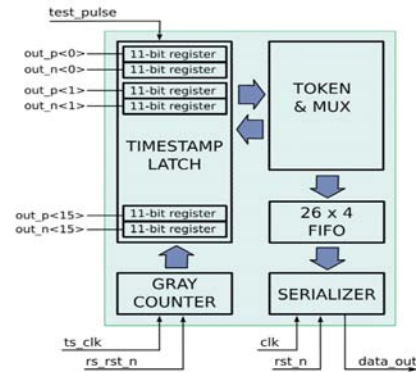


Figure 3: Digital back-end

The test setup of the TOT02 ASIC consists of the main test board incorporating an independent power supply and biasing circuitry with many debugging features. The board supports both direct detector placement and remote detector connection through an ERNI connector (standard connector for STS detectors). The configuration and read-out is performed by a National Instruments DAQ card interfaced to the ASIC through fast level translators for read-out and shift registers for slow control. The tests are ongoing; we expect to receive results soon.

References

- [1] K. Kasinski and R. Szczygiel, *CBM Progress Report 2009*, Darmstadt 2010, p. 44
- [2] K. Kasinski, R. Szczygiel and P. Gryboś, 2011 JINST 6 C01026

Development of a data-driven readout ASIC for microstrip detectors

E. Atkin, Yu. Bocharov, V. Butuzov, A. Klyuev, D. Osipov, V. Shumikhin, A. Simakov, and A. Voronin
National Research Nuclear University "MEPhI", Moscow

We present the current status of the development of an asynchronous data-driven architecture for multichannel silicon tracker system experiments. The known event statistics in multichannel equipment permits to use new variants of architecture synthesis with the use of analog de-randomizing blocks. The requirements of the silicon tracking system of the CBM experiment were used in the design.

The ASIC, which has been under development for the last few years, consists of two parts: the front-end readout and the data processing ones. The readout chain contains a charge-sensitive amplifier, followed by shaper and comparator. The data processing channel includes a peak detector and an ADC (one for all the channels for this prototype run). The block diagram was presented in [1, 2, 3]; a more detailed description is given in [4].

The de-randomization of analog signals is provided by an analog key array, controlled by a logical unit that analyzes the random appearance of input signals in the readout channels and the possibility of their transfer to the free processing ones. The de-randomizer logic is based on the facts that the pulse shape is known and the number of processing channels is chosen such that the number of occupied readout channels equals the number of processing channels under maximum load, wherat the average hit period in the channel equals the processing time of a hit (Fig. 1).

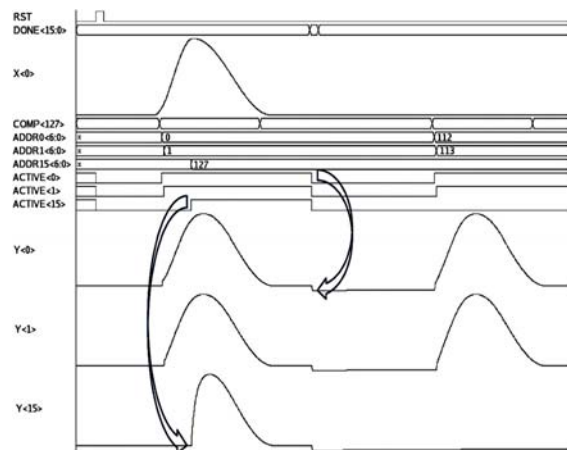


Figure 1: Switching diagram

To avoid distortion of the amplitude information, it is necessary to switch all channels in a time not exceeding a certain peaking time of the signal. Given that every act of switching the readout channel to a processing one occurs at the front of a clocking signal, it is sufficient to establish its frequency such that the duration of a number of cycles equal to the number of processing channels will be less than

the peaking time of the input signals.

The basic task in 2010 was to develop a prototype version of the de-randomizing ASIC and to implement a high-speed analog switching circuit of the 128 to 16 structure. One of the aims for the design was to improve the arbitration logic used and supplement the ASIC by both an input analog part and an output ADC. The principal feature of the ASIC is a low power consumption within 2 mW/channel at a maximum average channel hit rate not less than 150kHz.

The analog part includes a DC CSA with a circuit of detector leakage current compensation (up to 1 μ A) and a CR-RC shaper (100 ns peaking time), both designed according to the STS specifications [5]. The de-randomizing part consists of an asymmetrical analog switch array and arbitration logic. The number of readout chains was reduced down to 24 and provides a cost-effective approach at prototyping.

The ASIC was manufactured using the UMC 0.18 μ m CMOS process. The ASIC layout is shown in Fig. 2; its area occupied on chip is $1525 \times 3240 \mu\text{m}^2$ (double mini-asic). The chips were encapsulated in PGA144 cases, and a test setup is being developed.

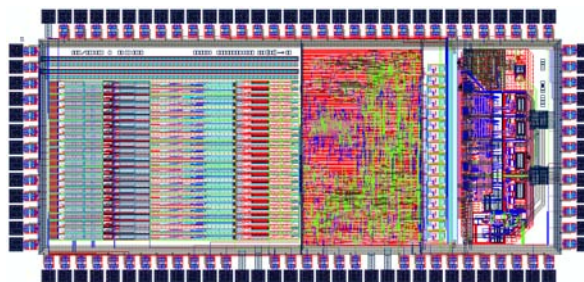


Figure 2: The ASIC layout

The prototyping via Europractice (April 2010 run No. 2537 of UMC) was paid by GSI. We use this opportunity to thank Dr. W. Müller and Dr. H. Flemming for their help.

References

- [1] E. Atkin *et al.*, *CBM Progress Report 2009*, Darmstadt 2010, p. 45
- [2] E. Atkin *et al.*, *Instrum. Exp. Tech.* **53** (2010) 524
- [3] E. Atkin *et al.*, *Development of the data-driven readout ASIC for microstrip detectors*, Proc. IEEE EWDTS, St. Petersburg (2010), p. 374
- [4] A. Klyuev, Ph.D. thesis, MEPhI, Moscow, 2010
- [5] E. Atkin *et al.*, *Instrum. Exp. Tech.* **53** (2010) 520

Single Cherenkov photon measurements with multi-anode photomultipliers for performance studies of the CBM-RICH photodetector

J. Eschke¹, C. Höhne², K.-H. Kampert³, J. Kopfer³, D. Kresan², and C. Pauly³

¹GSI, Darmstadt, Germany; ²Justus Liebig University, Giessen, Germany; ³Bergische Universität, Wuppertal, Germany

In November 2010 the CBM-RICH group together with other CBM groups took part in a test beam time at the CERN PS target area T10. We report on first results from the analysis of the obtained data.

Our goal for this beamtime was to further study the Cherenkov photon detection with Hamamatsu H8500 multi-anode PMTs using a proximity focusing test setup. This test provided valuable experience for the preparation of a full-scale gas Cherenkov prototype setup [1] to be tested at CERN in autumn 2011.

Setup and data analysis

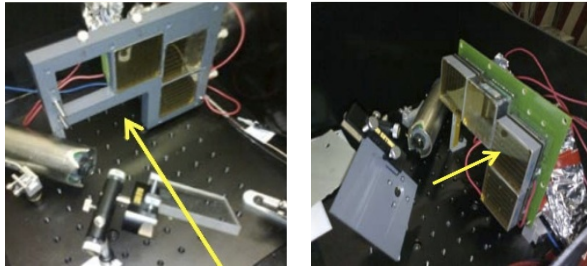


Figure 1: Proximity focusing setup with Plexiglas radiator (left) and quartz radiator with pin hole mask (right)

The experiment was set up inside a light-tight box, similar to earlier tests at GSI [2]. This time, 4 MAPMTs were mounted in a L-shaped arrangement in front of a Cherenkov radiator, covering roughly 25% of the generated Cherenkov cone. Two alternative kinds of radiator were used: an 8 mm thick Plexiglas sheet and a 4 mm thick quartz radiator. Both were oriented such that the plane normal pointed towards the PMTs in order to minimize ring distortion due to refraction at the radiator surface. Two different kinds of PMT mountings were tested (see Fig. 1): During the first runs, the PMTs were held by a plastic frame and connected directly via ribbon cables to the readout electronics. Later, the PMTs were plugged on a special PCB board, allowing for a better positioning and good shielding of the PMTs. Such a solution is foreseen to be used for the full detector and was tested here for the first time. Each pair of two PMTs was connected via attenuator boards to individual nXYTER frontend boards (FEB) each providing 128 readout channels.

A secondary beam of mixed pions and electrons in the momentum range between 1 and 6 GeV/c was used for the experiment, entering the box through a light-tight en-

trance window. After crossing the radiator, it passed the PMT plane with the beam centre a few cm away from the PMT cathodes. The Cherenkov cone at these momenta has a nearly fixed opening angle of 46.6° for both radiators. The projected ring image, however, is smeared out because of the large beam spot of several cm. A pinhole mask of ≈ 1 cm diameter on top of the radiator was used in some of the runs to limit the origin area of photons in order to nevertheless obtain a sharp ring image.

A coincidence condition of several scintillating finger detectors before and behind the setup provided a trigger signal used for normalization of the data. All obtained data, together with the trigger signal and data from the silicon tracking station (STS) in front of our setup, were synchronized and stored in ROOT trees for later analysis.

Results

First results from the data analysis are shown in Fig. 2 and Fig. 3. The time distribution of MAPMT hits in relation to the trigger (Fig.2 left) shows a clear coincidence peak with background below the peak on the permille level. A cut on these coincident hits is applied for all later analysis. The amplitude sum spectrum (Fig. 2 right) is dominated by the peak corresponding to single photon response, a small peak around ADC values of 1700 is induced by signal overflow. These high amplitudes are mainly caused by direct hits of charged beam particles.

Integrated hit distributions are shown in Fig. 3 for three different setups, together with their corresponding hit multiplicity distributions. Data obtained with the Plexiglas radiator without pinhole mask show a broad structure because of the large size of the beam. Applying a coincidence condition on ≥ 1 hit in the STS limits the acceptance range significantly and leads to a less smeared ring

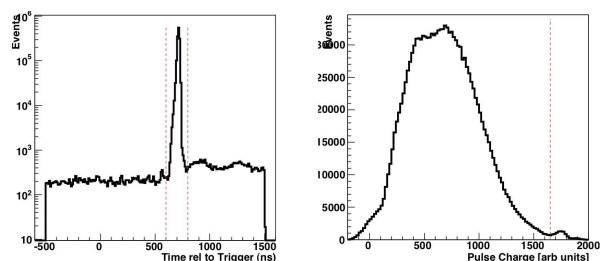


Figure 2: Time and amplitude distributions for individual hits. The dotted lines visualize cuts applied in the further data analysis.

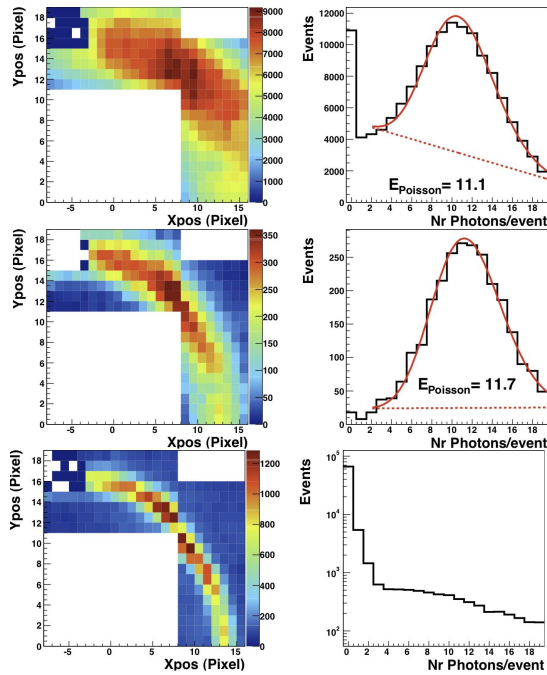


Figure 3: (Top row) Integrated image of Cherenkov ring and hit multiplicity for data with Plexiglas radiator without pin hole. (Middle row) Same data including an additional cut on ≥ 1 hit in STS. (Bottom row) Data obtained with quartz radiator using 1 cm pin hole. The full line in the multiplicity distributions represent a Poisson fit plus a linear background.

image. Missing hits in the upper left corner are caused by a broken cable. In both cases, the hit multiplicity nicely reflects a Poisson-shaped distribution on some linear background. A χ^2 fit yields an average multiplicity of 11-12 Cherenkov photons per event. In case of the quartz radiator with pinhole mask, the observed ring image is well focused. However, the acceptance area is now much smaller than the trigger corridor, which causes many events without Cherenkov photons. The multiplicity distribution in this case is dominated by background and does not show any Poisson-shaped peak structure, probably because of partial shadowing by the pinhole mask. An average photon number cannot be extracted for this configuration so far; a full Monte Carlo simulation is being prepared to understand this distribution quantitatively.

Expected photon yield

The total number N of produced Cherenkov photons per incident charged particle is

$$N = \int_{\lambda_1}^{\lambda_2} \frac{1}{\lambda^2} d\lambda \cdot L \cdot 2\pi\alpha \cdot z^2 \sin^2\theta_C \quad (1)$$

with the low wavelength end of the radiator transmission λ_1 , the high wavelength end of the photocathode quantum efficiency λ_2 , the radiator length L , the fine-structure

constant α , the charge of the incident particle z in units of the electron charge, and the Cherenkov angle θ_C . The number of expected Cherenkov photons in the photodetector is lower than the number of produced photons. Limiting factors are the finite transmittance of the radiators (80% above 390 nm for Plexiglas, 85% above 200 nm for quartz), the geometrical coverage of the MAPMTs (89% for the H8500 series), the wavelength-dependent quantum efficiency of the photodetector. Considering refraction of photons at the radiator-air interface and dead MAPMT pixels due to the broken cable leads to a geometrical acceptance of 21.5 % for the Plexiglas radiator and 20 % for the quartz according to a simple geometry simulation shown in Fig. 4. For the above analyzed runs, MAPMTs with alkali photocathode and UV glass window were used. The number of photons detected by the photodetector is then expected to be 8.0 for the Plexiglas radiator and 15.5 for the quartz.

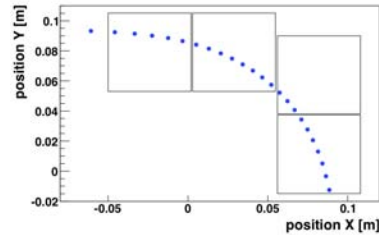


Figure 4: Geometrical acceptance of the photodetector. The dots display the expected position of Cherenkov photons on the photodetector plane. The ring is distorted because of refraction.

Summary and conclusion

For data taken with the Plexiglas radiator, the measured number of Cherenkov photons per event exceeds the theoretical expectation of 8 photons/event significantly. This might be partly attributed to crosstalk between neighbouring pixels (see [3]), which would increase the observed hit multiplicities. Another possible contribution could be an underestimation of the transmittance of Plexiglas for UV photons. In any case, the high photon yield demonstrates the good single-photon detection capabilities of H8500 PMTs. A full Monte Carlo simulation of the setup is being prepared to further improve the quantitative understanding of the data.

References

- [1] D. Kresan and C. Höhne, *Design studies for a CBM RICH prototype*, this report
- [2] J. Eschke, K. Todoroki and C. Höhne, *CBM Progress Report 2009*, Darmstadt 2010, p. 21
- [3] J. Eschke and F. Meyer, *Investigation of cross talk in multi-anode photomultipliers for the CBM RICH photodetector*, this report

Single-photon and magnetic field measurements on H8500 MAPMTs

C. Pauly, K.-H. Becker, K.-H. Kampert, J. Kopfer, J. Pouryamout, and J. Rautenberg

Bergische Universität, Wuppertal, Germany

The CBM-RICH photon detector will use photomultiplier tubes for the detection of Cherenkov photons, with the current design focusing on the H8500 multi-anode PMT from Hamamatsu. We measured and compared the single-photon spectra of three different tubes, namely the H8500C (12-stage, standard cathode), the H8500C-MOD8 (8-stage, SBA cathode), and, for comparison, the R8900 (single channel version, SBA cathode), which is a tube explicitly recommended for single-photon detection. All tubes were illuminated with single photons from a pulsed LED light source about 1 m away from the photocathode in a fixed setup in order to ensure constant and homogeneous illumination. Signals were read out via an 8-channel charge-sensitive preamplifier (Mesytec MSI-8) coupled to a sampling ADC, the readout being triggered from the pulse generator.

The obtained single-photon spectra are shown in Fig. 1. The best peak-to-valley ratio is obtained with the R8900 tube from Hamamatsu; however, also the H8500C 12-stage tube shows a clearly pronounced single-photon peak in all 64 channels. In contrast, the tested 8-stage version does not show a clear single-photon peak, even if the supply-voltage is increased to 1100V (maximum rating).

A quantitative comparison of detection efficiency is obtained by normalizing the number of registered photons (signal above threshold indicated in Fig. 1) to the active cathode area for a fixed number of 100k LED pulses. This test yields 19.4 registered photons per mm^2 for the R8900, 14.1/ mm^2 for the 12-stage H8500, and 14.1/ mm^2 for the 8-stage version. Despite the increase in quantum efficiency by 30% due to the SBA cathode, the 8-stage version H8500C-MOD8 does not register significantly more photons than the 12 stage version. The increased photon yield for the R8900 tube (SBA) in comparison to the 12-stage H8500C directly matches the higher quantum efficiency due to the SBA cathode, which we measured to be 28%

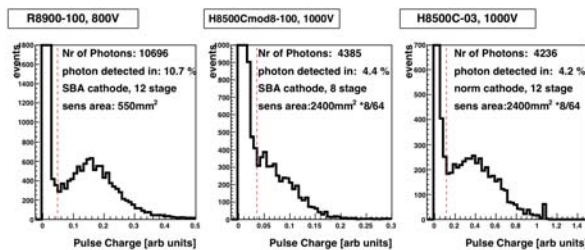


Figure 1: Single-photon spectra for R8900-100 (left), H8500C-100-MOD8 (centre), and H8500C-03 (right). For the multi-anode PMs, the sum spectrum of all diagonal elements is shown.

for the R8900 and 20% for the H8500C at $\lambda = 470$ nm (see [1] for details). These results show that the H8500-12stage is well suited for single-photon detection; a significantly higher detection efficiency can only be obtained with SBA cathodes, which are not (yet) available for the H8500C. The increased quantum efficiency due to the SBA cathode of the H8500C-MOD8, however, does not pay off in terms of photon yield because of the poor single-photon spectrum.

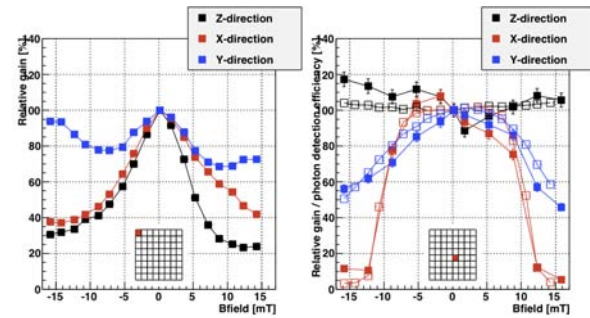


Figure 2: Gain variation for light pulses of ≈ 50 photons as function of magnetic field for two selected pixels of a H8500C. The open symbols on the right side show the normalized variation of single-photon efficiency.

The effect of magnetic fields on gain and detection efficiency of the designated MAPMTs is another important issue in view of stray fields of up to 25 mT in direct vicinity to the CBM dipole magnet. In order to study these effects, we mounted different H8500 MAPMT tubes inside a Helmholtz coil pair generating a homogeneous field up to ± 15 mT. Again, a pulsed LED was used to generate multi-photon pulses to study the variation of overall gain as function of the magnetic field. In a second step, the amplitude was reduced to the single-photon level in order to determine single-photon detection efficiencies. The results are summarized in Fig. 2 for two selected MAPMT pixels (H8500C 12-stage) and three different field orientations. In particular the outer pixels show a significant drop in gain and detection efficiency for fields as low as a few mT. The drop in gain seems to be mainly caused by the deflection of the first photo-electron as suggested by the very similar behaviour of gain and detection efficiency. Additional shielding will be necessary to operate these tubes at the foreseen position.

References

- [1] J. Kopfer *et al.*, *Quantum efficiency and gain homogeneity measurements of H8500 MAPMTs for the development of a CBM-RICH prototype camera*, this report

Quantum efficiency and gain homogeneity measurements of H8500 MAPMTs for the development of a CBM-RICH prototype camera

J. Kopfer, K.-H. Becker, K.-H. Kampert, C. Pauly, J. Pouryamout, and J. Rautenberg

Bergische Universität, Wuppertal, Germany

The camera of the RICH detector in the CBM experiment is foreseen to consist of approximately 860 Hamamatsu H8500 multi-anode photomultiplier tubes (MAPMTs). A RICH prototype is currently being built. Knowing the MAPMT characteristics is crucial for understanding the expected detector performance. Gain homogeneity and spectral response in terms of quantum efficiency (QE), i.e. the number of generated electrons per incident photon, were measured at Bergische Universität Wuppertal.

The QE of a PMT is mainly determined by the materials of the photocathode and the window. MAPMTs with bialkali (BA) and superbialkali (SBA) photocathodes as well as borosilicate and UV glass windows were tested.

The QE was measured by operating the PMT as a photocell, i.e. shortening all dynodes and applying a voltage of ≈ -100 V between the photocathode and the dynode system. The photocathode was illuminated with monochromatic light from a deuterium and tungsten-halogen lamp in the wavelength range between 200 nm and 800 nm using a double grating monochromator. For spatially resolved measurements, the light was coupled to a light fibre connected to a x-y stage. The photocurrent was measured by a picoamperemeter, and the QE was determined using a calibrated photodiode as a reference.

Figure 1 (top) shows the wavelength-dependent QE for MAPMTs with different types of photocathode and window materials. The maximal QE is $\approx 35\%$ for SBA cathodes and $\approx 25\%$ for BA cathodes. UV glass windows are transparent down to the deep UV, resulting in a QE of $\approx 5 - 10\%$ at 200 nm, whereas borosilicate blocks the light below about 300 nm. Folding these QE curves with the $1/\lambda^2$ -spectrum of Cherenkov light leads to 89.6% of detected Cherenkov photons for BA + UV glass and 83.2% for SBA + borosilicate when compared to SBA + UV glass which exhibits the maximal yield. As the difference of QE between SBA and BA cathode vanishes towards UV, and because of the $1/\lambda^2$ dependence of the Cherenkov spectrum, the benefit of using SBA instead of BA is just 10%.

Spatially resolved QE measurements reveal relative inhomogeneities of $\approx 25\%$ over the photocathode surface. A gradient from down right to top left as well as a circular structure are visible (Fig.1 bottom).

The gain was measured using a pulsed LED emitting at 470 nm. A voltage of -1000 V was applied between cathode and anode. The charges of the pulses were sampled by VME-based 100 MHz flash ADCs [1]. Using the x-y stage, MAPMTs were scanned with a resolution of < 1 mm. The average values of each MAPMT pixel normalized to the

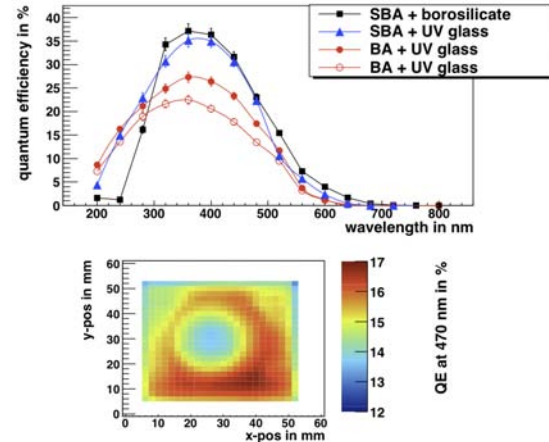


Figure 1: QE as function of wavelength for H8500 MAPMTs (top) and spatially resolved at 470 nm for a MAPMT with BA cathode and UV window (bottom)

maximum are shown in Fig. 2 for a SBA (left) and a BA cathode (right). The ratio between minimal and maximal charge is 1:1.4 for SBA and 1:1.3 for BA, slightly better than stated by the manufacturer.

These results demonstrate that MAPMTs are suitable for the construction of the CBM-RICH detector. They will thus be implemented in prototype simulations [2].

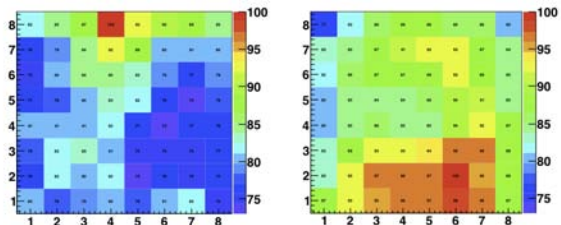


Figure 2: Normalized gain distribution (in % of the maximum) of a MAPMT with SBA (left) and BA cathode (right)

References

- [1] K.-H. Becker *et al.*, *CBM Progress Report 2009*, Darmstadt 2010, p. 24
- [2] D. Kresan and C. Höhne, *Design studies for a CBM-RICH prototype*, this report

Investigation of crosstalk in multi-anode photomultipliers for the CBM-RICH photodetector

J. Eschke¹ and F. Meyer²

¹GSI, Darmstadt, Germany; ²University of Bielefeld, Bielefeld, Germany

A key item of the CBM physics programme is the precise measurement of low-mass vector mesons and charmonium in their leptonic decay channel. In CBM, electrons will be identified using a gaseous RICH detector combined with several TRD detectors positioned behind a system of silicon tracking stations [1]. The concept of the RICH detector foresees an array of multi-anode photomultipliers (MAPMTs) for the photodetector covering an area of 2.4 m².

Beam tests at GSI (2009) and CERN (2010) and measurements with LEDs in the laboratory could demonstrate that the Hamamatsu H8500 with 64 pixels with a pixel size of 5.8×5.8 mm² is very well suited for the detection of single Cherenkov photons and therefore very likely will be used for the CBM RICH photodetector [2, 3]. In all these tests, the signals of the MAPMT were attenuated by a factor of 50 in order to be compatible with the self-triggered readout electronics based on the n-XYTER ADC chip.

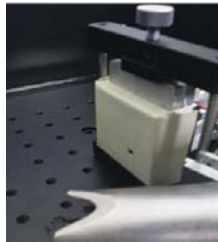
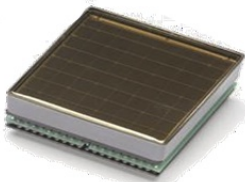


Figure 1: Single-photon illumination of a single pixel of the MAPMT with a LED

An important feature of H8500 MAPMT to be investigated is the crosstalk between neighbouring pixels. For its determination, a light-emitting diode (LED) with a wavelength of 350 nm was pulsed with ≈10 ns signals of ≈4.5 V amplitude. The distance between the LED and the MAPMT of ≈20cm in combination with the voltage at the operating threshold of this particular LED assured that not more than one photon per pulser signal reached one MAPMT pixel. Figure 1 shows the Hamamatsu H8500 covered by an aperture with a 3×3 mm² hole. Only the central part of a single pixel was illuminated at a time.

A clear separation of uncorrelated, low-amplitude noise events from signals of single photons with higher amplitude was achieved by a cut on the time difference between the pulser signal and the hits in the MAPMT. Figure 2 shows the event-integrated yield of MAPMT hits in linear and logarithmic scale. The uncovered pixel shows the largest number of hits. However, the 8 direct neighbour pixels, but also the 16 second neighbour pixels, exhibit an

non-negligible signal yield, even though they could not be directly excited by photons.

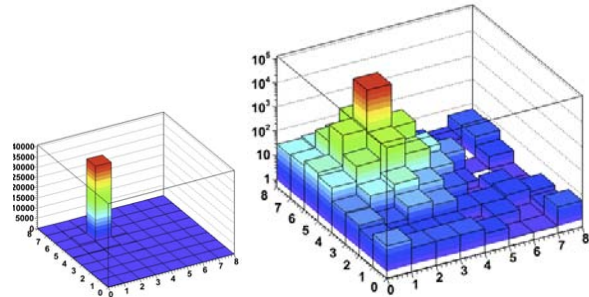


Figure 2: Yield of fired MAPMT cells from single-photon illumination of one pixel

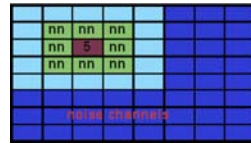


Figure 3: Calculation of average noise (\bar{n})

For a quantitative determination of this crosstalk, the average noise level in the 39 non-neighbouring MAPMT pixels was calculated (see Fig. 3) and subtracted. The fraction of cross talk in the 8 direct neighbour pixels

$$x = \frac{\sum N_{hits} - 8\bar{n}}{N_{central} - \bar{n}}$$

compared to the central, illuminated pixel was determined by measurements on four different pixels of this MAPMT to be 7.7% on average. The measurement will be repeated by single-photon illumination with a template of the same size as the MAPMT pixels. It is expected that these measurement will reveal a crosstalk of more than 10%.

References

- [1] C. Höhne, *CBM Progress Report 2007*, Darmstadt 2008, p. 17
- [2] J. Eschke, K. Todoroki and C. Höhne, *CBM Progress Report 2009*, Darmstadt 2010, p. 21; J. Eschke *et al.*, this report
- [3] J. Kopfer *et al.*, *Quantum efficiency and gain homogeneity measurements of H8500 MAPMTs for the development of a CBM RICH prototype camera*, this report

Wet-chemical application of wavelength-shifting films for the use on RICH-PMTs

I. Wehl, A. Sienerth, and M. Dürr

Hochschule Esslingen, 73728 Esslingen, Germany

High sensitivity for photon detection in the UV region is an important quality criterium for the photomultiplier tubes (PMTs) used in the CBM Ring Imaging Cherenkov (RICH) detector. In order to increase the sensitivity of standard PMTs, application of wavelength shifting (WLS) films on top of the photomultiplier window is an established method [1, 2, 3, 4]. These WLS films typically consist of organic molecules absorbing light in the UV region and re-emitting fluorescence photons at a longer wavelength, ideally at the maximum of spectral sensitivity of common photocathodes.

In agreement with literature [1, 3, 4], p-terphenyl (PT) was identified as a most promising molecule in an earlier study on evaporated WLS films [5, 6]. In order to facilitate the application procedure, wet-chemical application methods such as dip-coating and spin-coating, have now been tested [4, 7]. For example, different binders were evaluated, and both paraloid as well as PMMA were shown to exhibit good transmission in the interesting wavelength region. Whereas dip-coating results in films with lower homogeneity, spin-coating can lead to very smooth films. Besides the spinning frequency, the ratio between PT, binder, and solvent is most important for the film quality. As depicted in Fig. 1, both scattering and transparent films can be realized depending on the binder concentration.

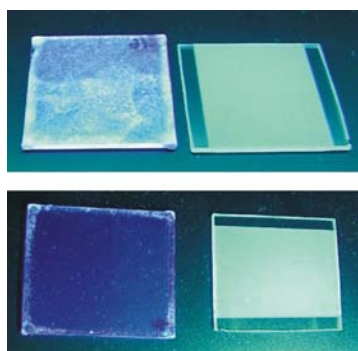


Figure 1: Influence of the concentration of binder on the morphology of spin-coated WLS films. The films are illuminated with UV-light at 254 nm. On the right hand side, an evaporated layer of $50 \mu\text{g}/\text{cm}^2$ PT is shown as reference. Top: low concentration of binder leads to more scattering layers (1 g PT, 1 g PMMA, 41.5 mL dichloro methane). Bottom: high concentration of binder leads to transparent films (0.5 g PT, 18 g paraloid, 5.4 mL chloroform, 36 mL toluene). In both cases, the blue fluorescence of PT can be observed.

In order to check the efficiency of the wet-chemically applied WLS films, fluorescence spectra were measured of the films which were applied by means of dip-coating. The overall results are comparable to the evaporated reference layer when excited at the absorption maximum of PT at 280 nm (Fig. 2); however, some variation from sample to sample or even on one sample is observed. Similar results but with stronger variation are obtained for excitation at 230 nm, the absorption minimum of PT. Most likely, the observed variation is due to the above mentioned lower homogeneity of these films, which leads to reduced absorption in areas with lower thickness.

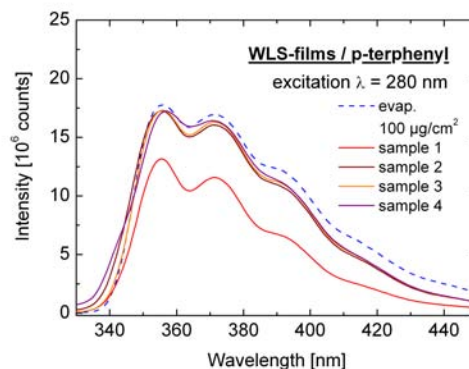


Figure 2: Fluorescence spectra of dip-coated WLS films (PT, paraloid, dichloro methane). The fluorescence intensity of the wet-chemically applied films is comparable to the evaporated reference layer. Stronger variations from sample to sample are observed, e. g. for sample 1.

References

- [1] E. L. Garwin, Y. Tomkiewicz and D. Trines, Nucl. Instrum. Meth. **107** (1973) 365
- [2] M. A. F. Alves *et al.*, Nucl. Instrum. Meth. **119** (1974) 405
- [3] P. Baillon *et al.*, Nucl. Instrum. Meth. **126** (1975) 13
- [4] G. Eigen and E. Lorenz, Nucl. Instrum. Meth. **166** (1979) 165
- [5] P. Koczoń *et al.*, *CBM Progress Report 2009*, Darmstadt 2010, p 19
- [6] C. Höhne *et al.*, Nucl. Instrum. Meth. A (in print)
- [7] V. Körstgens *et al.*, Appl. Phys. Lett. **93** (2008) 041916

Design studies for a CBM-RICH prototype

D. Kresan and C. Höhne

Justus Liebig University, Giessen, Germany

A RICH prototype is being planned in order to verify the concept of the CBM-RICH detector. This prototype will be scalable to the full detector, and results of the prototype test will be used to evaluate the simulations in the *CbmRoot* framework including tests of ring finding and fitting algorithms on real data. Concepts for the photodetector plane, including the integration of readout electronics, and mirror adjustment and alignment can also be tested. Finally, the results will provide all necessary information for the Technical Design Report.

First tests are foreseen in October 2011 at the T9 test-beam line of the CERN-PS. Here, a secondary beam of hadrons and electrons in the momentum range 1-10 GeV/c is available offering ideal conditions for understanding the electron-pion suppression capability of the RICH detector in the relevant momentum range for CBM. For the simulations shown in this report, the beam conditions were included following the characterization in [1] (polar angle spread, momentum range). The beam focal point in the simulation was placed 1 m in front of the detector; the azimuthal angle is uniformly distributed; the beam in the simulation consists of 50% electrons and 50% negative pions.

In order to have approximately the same amount of Cherenkov photons per electron or pion track, the length of the radiator (1.7 m) and the gas type (CO_2) were kept as in the layout of the CBM-RICH [2]. The positioning and alignment of the mirror and the photomultiplier (PMT) plane were adjusted to achieve focusing of the light cone from Cherenkov radiation of an electron beam passing the detector.

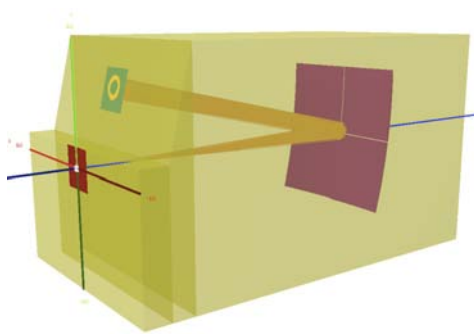


Figure 1: Schematic drawing of the prototype geometry

A schematic view of the prototype layout is shown in Fig. 1. The illustration includes the radiator (transparent yellow), the beam entrance window (left, red), the MAPMT plane (green) and four rectangular mirrors (pink). The beam axis is shown in blue. The transverse dimensions of

the gas radiator are $1.2 \times 1.2 \text{ m}^2$, its total length is 2.1 m.

In the event reconstruction, the granularity of the photodetector is implemented as an array of 4×4 MAPMTs with 64 channels each (1024 channels in total). Hits are created from projected photons by applying a tabulated quantum efficiency of the PMTs. In addition 50 channels (5%) are randomly fired in each event, simulating in this way a rather pessimistic noise level. Both the signal and the noise hits were taken as input for the ring finding algorithm [3], which is based on a standard implementation of the Hough transform finder in *CbmRoot*. As a fitter, the standard Ellipse Fitter is used. The Hough transform ring finding algorithm yields an electron ring reconstruction efficiency of 99.1%.

Applying a simple particle identification, a cut on the main axis a of the reconstructed ellipse was used: ellipses with $a > 4.4 \text{ cm}$ were identified as electrons, those with $a < 4.4 \text{ cm}$ as pions. On average this yields a pion misidentification of 3.3%. Figure 2 shows the distribution of the ellipse main axis versus momentum of the particle (left picture) and pion misidentification as a function of momentum (right picture).

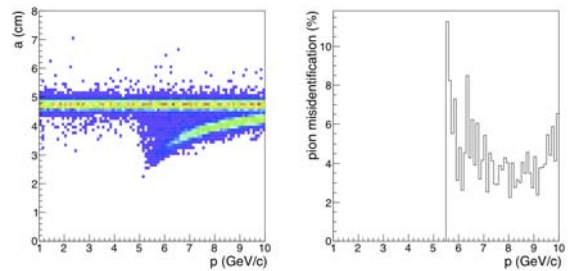


Figure 2: (Left) Distribution of the ellipse main axis versus momentum. (Right) Pion misidentification as a function of momentum.

In summary, the full RICH prototype was successfully implemented and tested in the *CbmRoot* framework. The testbeam data expected end of 2011 will allow to evaluate these simulations and the concept and performance of the CBM-RICH detector.

References

- [1] <http://ps-div.web.cern.ch/ps-div/Reports/PA9321/Tables/Table9.html>
- [2] S. Lebedev, E. Belolaptikova and C. Höhne, *CBM Progress Report 2008*, Darmstadt 2009, p. 20
- [3] S. Lebedev *et al.*, *J. Phys. Conf. Ser.* **219** (2010) 032015

A gas system for the CBM-RICH prototype

L. Kotchenda¹, P. Kravtsov¹, J. Eschke², T. Mahmoud³, and C. Höhne³

¹PNPI, Gatchina, Russia; ²GSI, Darmstadt, Germany; ³Justus Liebig University, Giessen, Germany

The primary purpose of the gas system being designed for the CBM-RICH prototype (Fig. 1) is to provide pure CO₂ gas to the prototype at the correct differential pressure. Its design is based on the gas systems for the STAR and PHENIX experiments at BNL [1, 2]. The system operates nominally as a closed-circuit gas system with the majority of the gas recirculating through the prototype. During normal operation, fresh gas is added with a Burkert 8711 mass flow controller FM1. The gas flow through FM1 is used to stabilise the differential pressure, measured by PT4, at the level of 2 mbar. The gas system can be operated in an open configuration for purging.

A bypass valve (BMV1) is manually adjusted to enable the optimum flow rate through the prototype. The purity of recirculation gas is monitored using Panametrics Oxygen (O2X1) and Humidity (MMS35) analyzers. A fraction (up to 30 %) of the recirculation gas can be passed through the purifier and dryer to remove oxygen and moisture. There is the possibility to check the gas purity with the analyzers after the purifier and dryer to determine their saturation.

The purifier is filled with active copper. Its operating and regenerating temperature is 220°C. A Temperature Indicating Controller TIC1 supports this temperature level. A mixture of CO₂ + 5% H₂ can be used to regenerate the purifier. The oxygen content after the purifier is about 2-3 ppm.

The dryer is filled with NaX (13X) molecular sieves. Its normal operating temperature is 22°C. The water content in the output flow of the dryer at this temperature is 1-2 ppm. The regeneration of the dryer is performed at 350-400°C supported with Temperature Indicating Controller TIC2.

A computer-driven data acquisition/control system monitors all of the process variables and provides differential pressure stabilization. The computer system flags quantities which fall outside of predefined limits and initiates corrective action. Using data from the TT1, PT4 and BP (barometric pressure) sensors, the computer system estimates the CO₂ refraction index.

The gas system is assembled in a single 19" rack and can be easily transported with the RICH prototype. It can also be used in the future for the complete RICH detector with minor changes.

References

- [1] L. Kotchenda *et al.*, Nucl. Instrum. Meth. A **499** (2003) 703
- [2] L. Kotchenda *et al.*, Nucl. Instrum. Meth. A **578** (2007) 172

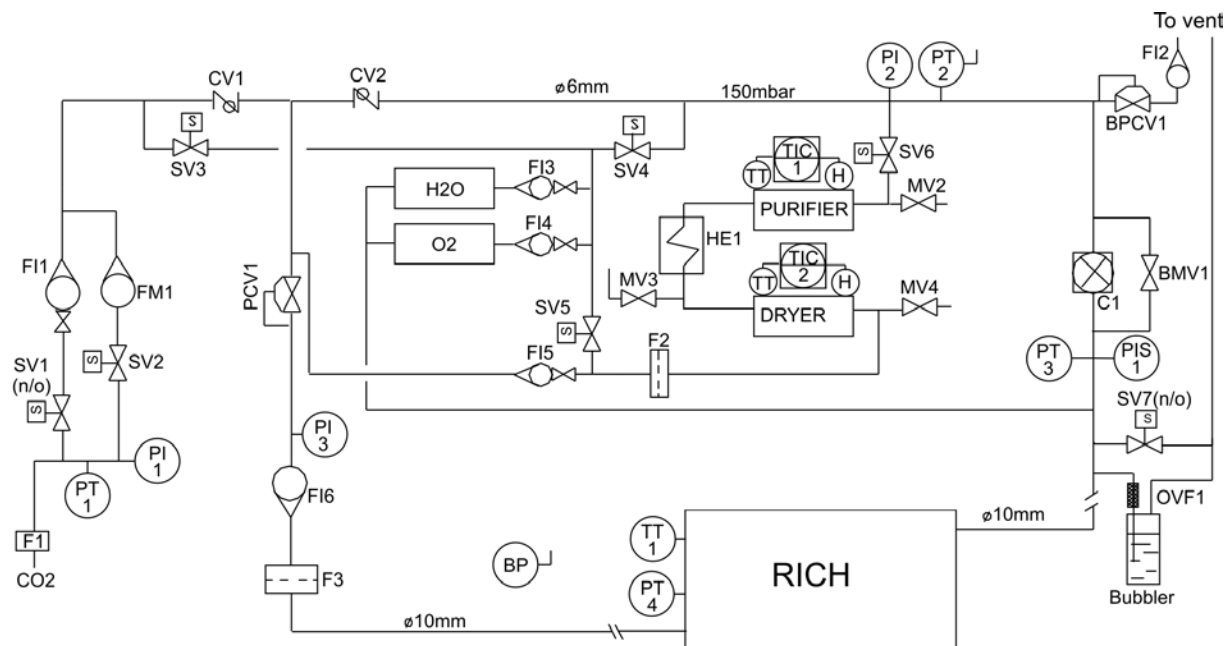


Figure 1: The gas system for the RICH prototype

A slow-control system for the CBM-RICH gas system

P. Kravtsov¹, L. Kotchenda¹, J. Eschke², T. Mahmoud³, and C. Höhne³

¹PNPI, Gatchina, Russia; ²GSI, Darmstadt, Germany; ³Justus Liebig University, Giessen, Germany

The gas system for the CBM-RICH prototype was built to provide pure CO₂ gas to the RICH prototype at a constant differential pressure of about 2 mbar. In addition it supports the necessary purity of the gas using a purification unit. A computer-driven slow control system monitors all of the process variables and provides differential pressure stabilization. Besides, the control system reacts on some gas system faults and takes care for automatic recovering.

The gas system is controlled by a custom slow-control subsystem that is based on the DAQ32 module [1]. This module (Fig. 1) was designed for controlling small cryogenic and gas supply systems. It provides reading of up to 32 sensors with industrial standard voltage or current output. The device accuracy is 0.004% of the measurement scale that can be selected from the range of +4 V, ±5 V, +10 V, ±10 V. The module is also equipped with 16 buffered digital outputs to control acting devices like solenoid valves or compressors, and 4 analog voltage output channels for flow controllers or heaters control. Such input-output channel density in a standard 100 × 160 mm² board allows using a single module to control small systems like the CBM-RICH gas system.

The variety of the data exchange interfaces simplifies a connection of the instrument to the external control system or computer. Flexible controller firmware allows implementing the necessary control algorithms, like PID regulation, directly in the firmware. Two of these modules (one working and one spare) are mounted in the gas system rack.

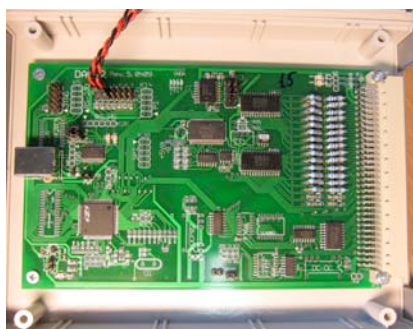


Figure 1: The DAQ32 module

The control computer software [2] was developed for the Windows platform. It provides reliable data acquisition, automated alarm condition handling and manual control of the gas system. All alarm events and system variables are logged into a database. The software is divided into multiple processes that communicate, making use of special operating system kernel objects.

The main process reads all sensor values and passes them

to other processes. In order to make the software more reliable, it was divided into two threads: one for the Graphical User Interface (GUI) and one for the data acquisition. The GUI thread shows all gas system parameters including valve states in the main window. The operator can also use the controls to manage the system manually as well as adjust alarm parameters.

The DAQ thread acquires all the process variables, writes them into shared memory and checks alarm conditions. Every alarm setting contains an alarm threshold, alarm message and control template. The template indicates alarm set and releases actions for every controlled device, e.g. valve or compressor. The system makes corrective actions automatically and alerts the operator about the trouble. Usage of the alarm control template provides the user a high degree of flexibility when setting up the system. All process variables are written into the MS Access database with specified period. In case of alarm trigger, current values are also written out of turn. All alarm events and software messages are also logged into the same database.

It is also useful to have fast access to particular data and plot the results during the gas system operation. A special tool (DBViewer) was developed to work with the gas system database. It provides visualization of the data for any gas system process variable and exports data from the database to MS Excel or a tab-delimited text file for further analysis.

Another program was designed for the visualization of the actual state of the system. This program (Charts) displays up to ten selected parameters in the time chart format. Besides, it can be used for tabular display of the process variables, with extra alarm signals for every parameter in the table. In addition, a TCP/IP client/server is implemented in the Charts software so that it can be used remotely for monitoring the system under control.

The gas system control software was successfully used in nine gas systems [3, 4] of various detectors in the STAR and PHENIX experiments at RHIC.

References

- [1] P. Kravtsov and V. Trofimov, *Multi-channel measuring instrument for slow control systems*, preprint PNPI-2723, Gatchina 2007
- [2] P. Kravtsov, *Data acquisition and control software of the STAR and PHENIX gas systems*, preprint PNPI-2593, Gatchina 2005
- [3] L. Kotchenda *et al.*, Nucl. Instrum. Meth. A **499** (2003) 703
- [4] L. Kotchenda *et al.*, Nucl. Instrum. Meth. A **578** (2007) 172

Mirror mount design for the CBM-RICH detector

E. Vznuzdaev, V. Dobyryn, N. Miftakhov, O. Tarasenkova, V. Polyakov, V. Samsonov, V. Evseev, V. Tolchin, and G. Rybakov

PNPI, Gatchina, Russia

In the CBM-RICH detector, a spherical mirror of approximately 11.8 m² will be used for Cherenkov light projection onto the photodetector plane. In the current layout, the radius of curvature is 3 m, and mirrors with glass substrate of 6 mm thickness or less and reflective Al+MgF₂ coating are foreseen [1]. In order to cover a spherical mirror wall with this comparatively small radius, trapezoid mirror tiles of approximately 400×400 mm² will be used. A mirror mount design was developed in order to mount these tiles and allow for enough degrees of freedom for mirror adjustment [2]. Using ANSYS calculations based on a minimal deformation of the mirror tile (5-6 μm along the radius of a mirror surface), positions and degrees of freedom for the mount points were chosen for a 3-point mount attachment to the mirror tile as illustrated in Fig. 1.

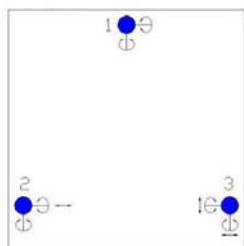


Figure 1: Layout of attachment points

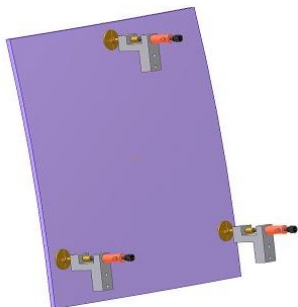


Figure 2: Three-point mirror mount attachment

The directions of possible shifts and rotations (degrees of freedom) are shown, except the rotations along the radius of the mirror tile. A three-dimensional model of the mirror mount (see Fig. 2) was designed using the Autodesk Inventor software.

The influence of the gravitational forces on the image of the reflected light spot (D_0) from a point light source was

estimated by optical simulations. A value of 0.5 mm for such an image was obtained (see Fig. 3), which is negligible compared to the required reflected spot diameter of 3 mm.

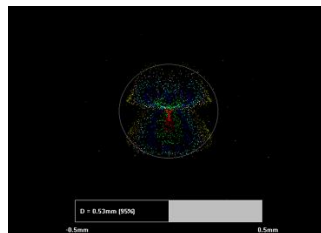


Figure 3: Optical simulation of the reflected light spot

The basic element of the mount is a cardan shaft allowing to implement all necessary degrees of freedom (shifts and rotations). A real mirror mount prototype with manual control was constructed (see Fig. 4) and preliminarily tested using a flat aluminium plate attached to the mounts.

Results of first tests show a good functionality of the developed mirror mount. More exhaustive and quantitative data can be obtained after optical tests with a spherical mirror prototype to be delivered and tested in 2011. Mirrors with these mounts will also be implemented in the CBM-RICH prototype [3].

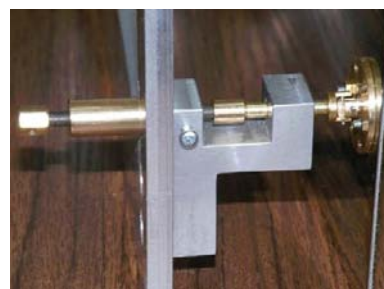


Figure 4: Prototype of the mirror mount

References

- [1] M. Dürr, A. Braem and C. Höhne, *CBM Progress Report 2008*, Darmstadt 2009, p. 21
- [2] V. Dobyryn *et al.*, *CBM Progress Report 2009*, Darmstadt 2010, p. 25
- [3] D. Kresan and C. Höhne, *Design studies for a CBM-RICH prototype*, this report

MUCH layout optimization for SIS-100

P. P. Bhaduri¹, A. Prakash², and S. Chattopadhyay¹

¹Variable Energy Cyclotron Centre, 1/AF Bidhan Nagar, Kolkata-700 064, India; ² Department of Physics, Banaras Hindu University, Varanasi-221005, India

The experimental programme of CBM includes the measurement of charmonia and low-mass vector mesons via their decay into the di-muon channel. The simulation studies done so far have already established the feasibility of such measurements, and an optimized layout of the muon detection system was found for operation at SIS-300. The aim of the present work is to search for an optimized MUCH layout for SIS-100 collision energies. As it is likely that there will be a gap between the start of operation of SIS-100 and SIS-300, we plan to have a start version of MUCH with less number of stations compared to SIS-300, in order to take advantage of emerging technologies for the full version of the detector.

The present version of the muon detection system, implemented in the cbmroot repository (DEC09) and optimized for SIS-300 collisions, is termed as standard (S) geometry. It includes 6 iron absorbers and 18 detector layers (3 behind each absorber). The total absorber length in the current design amounts to 225 cm of iron, the last absorber being 100 cm thick. This geometry is used for both charmonium and low mass vector mesons (lmvm). For the latter, hits before the last absorber are relevant. We explored the possibility to perform muon simulations with two additional geometries, namely reduced geometry (R) and intermediate geometry (I). In both cases the total effective absorber thickness for lmvm as well as for charmonia is kept the same as in the standard geometry. The reduced geometry thus consists of 3 hadron absorbers (30+95+100 cm) and 9 gas detector layers located in triplets behind each absorber. The intermediate geometry consists of 4 hadron absorbers (30+30+65+100cm) and 12 detector layers located in triplets behind each absorber.

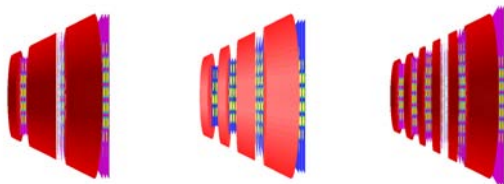


Figure 1: Schematic view of the three MUCH geometries: reduced(R) (left), intermediate(I) (middle) and standard(S) (right) as implemented in cbmroot

We simulated central Au+Au collisions for the beam energies $E_L = 8A, 25A$ and $35A$ GeV. As signal we considered the ω meson, which was generated and decayed by the PLUTO generator and embedded into background events generated with URQMD. The particles were trans-

ported through the detector setup using GEANT3. Ideal tracking [1] was used for track finding and momentum reconstruction in STS. The littrack software [2] was used for track finding in the muon system. A track was required to be reconstructed both in STS and in the Muon Chamber (MuCh) for being classified as a muon track. We segmented the detector planes into pads of varying size from 4×4 mm² to 3.2×3.2 cm² for track reconstruction. The reconstruction efficiency and the signal-to-background ratio were calculated in a $\pm 2\sigma$ window around the signal peak and are presented in Tables 1 and 2, respectively.

Table 1: Reconstruction efficiency ϵ (%) for ω in central Au+Au collisions at 8A, 25A and 35A GeV for different geometries

E_L [A GeV]	ϵ [%]		
	R	I	S
8	0.94	0.91	0.86
25	1.77	1.72	1.48
35	1.85	1.83	1.82

Table 2: Signal-to-background ratio S/B for ω in central Au+Au collisions at 8A, 25A and 35A GeV for different geometries

E_L [A GeV]	S/B		
	R	I	S
8	0.05	0.088	1.41
25	0.00098	0.003	0.49
35	0.00059	0.00162	0.34

It is evident from the tables that different geometries with same absorber thickness but varying number of detector layers give comparable values for the reconstruction efficiency. The S/B ratio, however, is drastically different for the different geometries. Reduction in the number of stations results in a huge reduction of the S/B ratio for ω mesons, even at the lowest energy. Thus our studies indicate that as far as the measurement of low-mass vector mesons is concerned, there is practically no cheaper version of the muon detection system other than the standard geometry, which effectively comprises 15 layers for lmvm detection.

References

- [1] I. Kisel, Nucl. Instrum. Meth. **A 566** (2006) 85
- [2] A. Lebedev *et al.*, *CBM Progress Report 2008*, Darmstadt 2009, p. 81

Segmentation optimization for the MUCH detector

A. Prakash¹, P P Bhaduri², B K Singh¹, and S. Chattopadhyay²

¹Department of Physics, Banaras Hindu University, Varanasi-221 005, India; ²Variable Energy Cyclotron Centre, 1/AF, Bidhan Nagar, Kolkata-700 064, India

We present a simulation for the optimization of the MUCH segmentation using the CBM simulation framework cbmroot [1]. The tools used for the simulations are the same as in [2]. We employed the 18-layer geometry as optimized in [2].

The detection procedure involves the reconstruction of the track parameters in STS and extrapolation to the muon detecting stations through the absorbers. We considered tracks passing through 15 layers as valid muon candidates from low-mass vector meson decays. The study of segmentation is important for a) the determination of occupancy, which eventually determines the feasibility of tracking and the efficiency of muon measurements; b) the total number of pads, which influences the cost; and c) the smallest pad size, important from the point of view of fabrication and signal strength.

Table 1: Minimal and maximal pad sizes and total number of pads for the different segmentation schemes

Scheme	min. size	max. size	N_{pads}
1	$4 \times 4 \text{ mm}^2$	$3.2 \times 3.2 \text{ cm}^2$	791,040
2	$2 \times 4 \text{ mm}^2$	$3.2 \times 3.2 \text{ cm}^2$	989,184
3	$5 \times 5 \text{ mm}^2$	$3.2 \times 3.2 \text{ cm}^2$	567,459

We segmented the detector into pads of varying size from $4 \times 4 \text{ mm}^2$ to $3.2 \times 3.2 \text{ cm}^2$ depending on the radial distribution of particle density. The minimal and maximal pad sizes are listed in Table 1. Figure 1 (left) shows the radial distribution of occupancy in station 1, the highest occupancy being $\approx 4.5\%$. Even though the framework provides the option to divide a layer into pads of varying size, we used a constant pad size throughout each layer. The

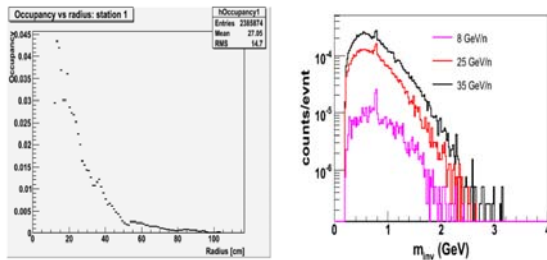


Figure 1: (Left) Occupancy in the first station (Au+Au @ 25A GeV beam energy) with segmentation option 1. (Right) Invariant-mass spectrum of muon pairs for the three different segmentation schemes.

minimal and maximal pad sizes mentioned here refer to the pad size in the first and in the last station, respectively. The reconstruction efficiency and the signal-to-background ratio (S/B) for ω mesons were calculated in a $\pm 2\sigma$ window around the signal invariant-mass peak and are presented in Tables 2 and 3 for central Au+Au collisions at 8A, 25A and 35A GeV beam energy. Normalized invariant-mass spectra for the segmentation option 1 for three different beam energies are shown in Figure 1 (right). The combinatorial background is calculated using the event mixing technique. Our studies indicate that at all energies low-mass vector mesons can be identified above the combinatorial background, which is dominated by muons from weak pion decays. The efficiency does not change significantly for the three different segmentation options, whereas the S/B is reduced by 10% to 40% when going from segmentation option 1 to 3. The increase in S/B from option 1 to option 2, however, is marginal and even reversed at 8A GeV beam energy. We therefore conclude that a minimal pad size of $4 \times 4 \text{ mm}^2$ is the preferable option, given the fact that pads of this size are relatively easy to fabricate.

Table 2: Reconstruction efficiency for ω in central Au+Au collisions at 8A, 25A and 35A GeV beam energies for different segmentations

Energy [A GeV]	Efficiency [%]		
	Seg-1	Seg-2	Seg-3
8	0.86	0.86	0.78
25	1.58	1.61	1.43
35	1.81	1.82	1.7

Table 3: S/B ratio for ω in central Au+Au collisions at 8A, 25A and 35A GeV beam energies for different segmentations

Energy [A GeV]	S/B		
	Seg-1	Seg-2	Seg-3
8	1.41	1.03	0.94
25	0.49	0.497	0.3
35	0.31	0.34	0.28

References

- [1] <http://cbmroot.gsi.de>
- [2] P. P. Bhaduri, A. Prakash and S. Chattopadhyay, *MUCH layout optimization for SIS-100*, this report

Update on GEM development at VECC

A. K. Dubey, S. Chattopadhyay, S. Singaraju, J. Saini, G. S. N. Murthy, and Y. P. Vijoyi

Variable Energy Cyclotron Centre, 1/AF, Bidhan Nagar, Kolkata 700064, India

With regard to the ongoing R&D on GEM-based detectors for the CBM-MuCH [1, 2], we discuss in this report the performance test of a triple-GEM chamber assembly mainly using cosmic rays. The aim is to determine the charged particle detection efficiency of the detector.

A triple-GEM prototype chamber was built by assembling three GEM foils (10 cm x 10 cm) made and framed by CERN. Two such chambers with 512 readout channels each were fabricated: chamber A with 3 mm x 3 mm pad size and chamber B with 4 mm x 4 mm pad size. This granularity was chosen based on realistic MuCH simulations. While the drift gap of chamber A was 5 mm, that of chamber B was 3 mm. Tests with cosmic rays were performed for chamber B.

For the efficiency estimation with cosmic rays, the readout connections from all pads were shorted together to form a single output of the GEM signal, which was coupled to conventional NIM electronics (Ortec 142 IH +572A). A timing SCA was used to produce the corresponding analog and logic signal. A suitable threshold was applied on the SCA window to suppress the noise. For all tests, a gas mixture of Ar and CO₂ (70:30) was used in the chamber.

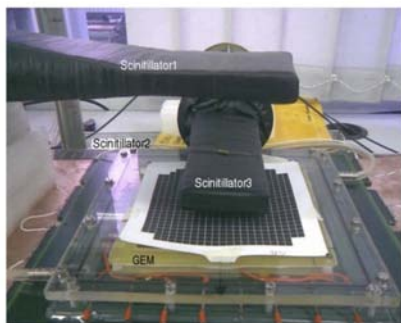


Figure 1: Test setup for cosmic rays at VECC

The cosmic ray test setup was assembled using three scintillators each coupled to a PMT via light guides. The detector was placed between the middle and the bottom scintillator as shown in Fig. 1. The middle scintillator, which was kept very close to the detector, had an area of 5 cm x 5 cm, well within the active area of the detector (10 cm x 10 cm). The cosmic muon trigger was defined as threefold coincidence of the three scintillators. The corresponding coincidence outputs were fed to a counter. The detector efficiency was estimated as the ratio of the number of detected tracks (4-fold counts) to the total number of triggers (3-fold counts).

The pulse height spectra corresponding to a MIP, fitted to Landau distributions, are shown in the left panel of Fig. 2 for two different bias voltages. The right panel shows the variation of efficiency with bias voltage. It increases with voltage because of the increase in gain. The maximal efficiency achieved is around 95% and is found to saturate around this value at $\Delta V_{GEM} \approx 425$ V for the chamber layout described above.

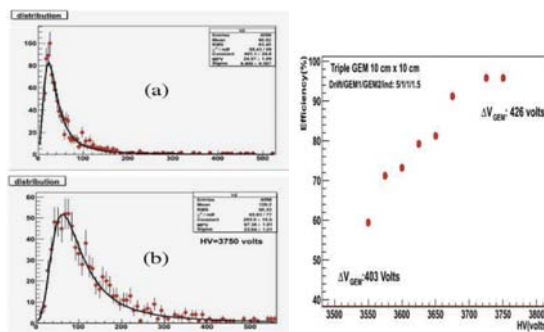


Figure 2: (Left) Pulse height spectra for cosmic ray data for two different bias voltages; (Right) Variation of efficiency with applied high voltage

The chambers were also successfully tested with proton beams at the Jessica beam line at FZ Jülich in December 2010. Fig. 3 shows the beam spot seen on-line by the two chambers with a cut of 900 ns on the time difference of chamber hit to beam trigger signal. The analysis of the data from this beam test is still ongoing.

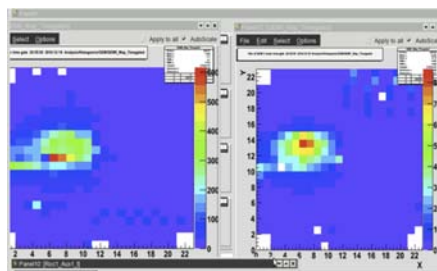


Figure 3: On-line snapshot of the proton beam as seen in the two triple-GEM chambers

References

- [1] A. Dubey *et al.*, *CBM Progress Report 2008*, Darmstadt 2009, p. 32
- [2] S. Chattopadhyay *et al.*, *CBM Progress Report 2009*, Darmstadt 2010, p. 28

Development of PCBs for readout plane and front-end boards for MuCH

J. Saini, R. N. Singraju, G. S. N. Murthy, A. K. Dubey, and S. Chattopadhyay

VECC, Kolkata, India

The MuCH layout consists of 18 layers with 6 stations. Simulations suggested that a pad size of $4 \times 4 \text{ mm}^2$ for stations 2 and 3 gives a reasonable performance. In this respect we designed PCBs of $4 \times 4 \text{ mm}^2$ and $3 \times 3 \text{ mm}^2$ pad size. For flexibility and easier fabrication of the readout PCBs, we considered a modular design which can be easily extended to larger PCBs. The basic building block as shown in Fig. 1 consists of an array of 32×8 pads (total 256 pads), and this can be extended to an array of $32 \times 32 = 1024$ pads by multiplying the basic block. The small pad size imposes severe restrictions on track widths, track-to-track distances and track-to-pad distances. The design and fabrication of such a small pad size cannot be carried out with the conventional approach of using a multilayer PCB with through hole vias only. Hence the design is done using a four-layer PCB with blind vias along with through holes. The signals from all 256 pads are brought to a 300-pin connector (SMT) with 1.27 mm pitch by using blind vias and tracks drawn through inner layers. The blind vias also help in ensuring a gas tight design. The 300-pin female connector on the detector PCB mates with another 300-pin male connector on a 2-chip front-end board (FEB). This FEB processes all 256 analog signals with two nXYTER chips, each processing 128 signals.

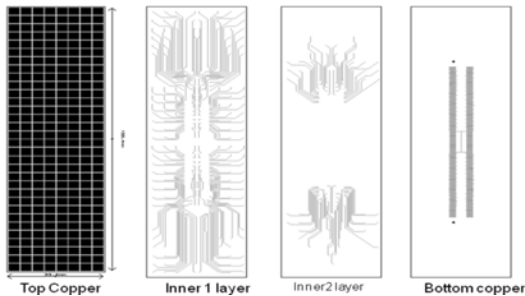


Figure 1: Basic building block for the 32×8 array

For 1024 channels, four specimen of the 2-chip FEB have to be fit into the size of the MuCh PCB, which poses immense size restrictions on the front-end PCB. This led to a PCB design with extremely thin track widths (3 mil), track to track distances as low as 3 mil, and final via sizes like 12 mil. Taking into account all these design restrictions, a prototype PCB was designed. All digital signals to the readout controller (ROC) are connected using a 80-pin connector placed on top copper. The PCB design was done on eight layers, extensively using blind vias on the top and bottom planes. The size of the front-end PCB is $112 \text{ mm} \times 31 \text{ mm}$ as shown in the right panel of Fig 2. The fabrication for this design is in process.

Figure 2 shows the schematic of the proposed readout PCB with $4 \times 4 \text{ mm}^2$ pads in a 32×32 array (1024 channels). All 1024 channels will be read by four FEBs. The left panel shows the top layer with pads while the right panel shows the bottom layer with four 300-pin connectors along with the proposed two-chip FEB boards. The inner layers are not shown.

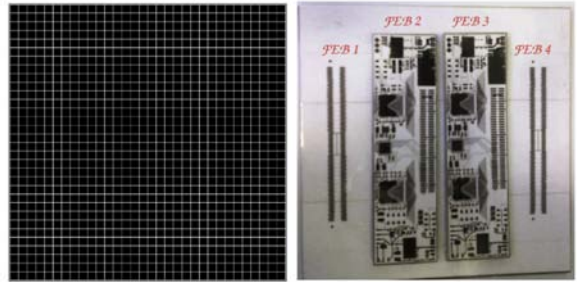


Figure 2: One readout module with 1024 channels. Left: Top view with $4 \times 4 \text{ mm}^2$ pads. Right: Bottom view with connectors and two connected FEBs.

As a first attempt towards fabricating multilayer pad-plane PCBs with blind vias for readout, two 512-channel PCBs with pad sizes $3 \times 3 \text{ mm}^2$ and $4 \times 4 \text{ mm}^2$ were prepared. A GND plane between each track was introduced in order to reduce the crosstalk between two nearby channels. These PCBs were used in the COSY test beam in December 2010.

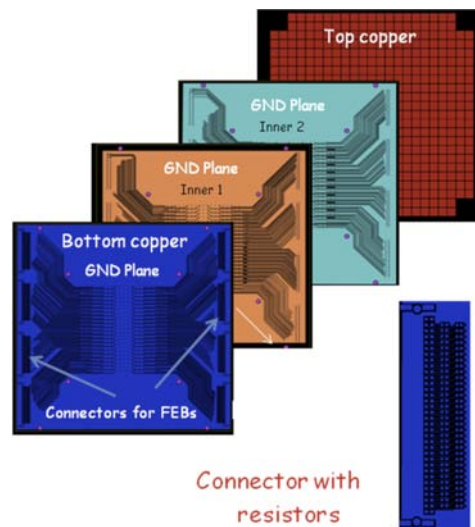


Figure 3: Layout of PCB used in the test beam at COSY

Performance evaluation of the CBM muon system for a $\omega \rightarrow \mu\mu$ trigger

A. Zinchenko, D. Peshekhonov, and V. Peshekhonov

JINR, Dubna, Russia

The emission of lepton pairs out of the hot and dense collision zone of heavy-ion reactions is a promising probe to study the electromagnetic structure of hadrons under extreme conditions. The reconstruction of vector mesons ($\rho, \omega, \phi, J/\psi, \psi'$) is one of the prime tasks of the CBM experiment. To perform this study using the di-muon decay mode, a muon system consisting of a set of absorbers and detector stations will be built.

Since the di-muon yield from vector meson decays is expected to be very low, it is essential to develop a fast and efficient trigger for such events. The muons from decays of low-mass vector mesons (LMVM), e.g. from ω , will be rather soft, making it undesirable to use the total absorber thickness. Therefore, the detector stations surrounding the last but one absorber will be used in the trigger. A similar approach was already presented in [1]. Here somewhat different aspects of this problem are addressed.

At present there are several options for a choice of detectors for the muon system. The homogeneous configuration is based on GEM detectors with pad readout in all tracking stations. The heterogeneous one contains less expensive detectors in several of the downstream stations. The final choice will be based on several considerations including the physics performance. Therefore, it was interesting to compare the ability of these two options to provide a trigger for LMVM. It was also useful to obtain a tool independent from the general tracking to compare two detector configurations, keeping in mind that the general tracking might not be fully tuned to properly handle the heterogeneous detector environment.

A possible heterogeneous muon system configuration is shown in Fig. 1, where the last three detector stations (behind absorbers 4-6) are built from straw tubes. Each sta-

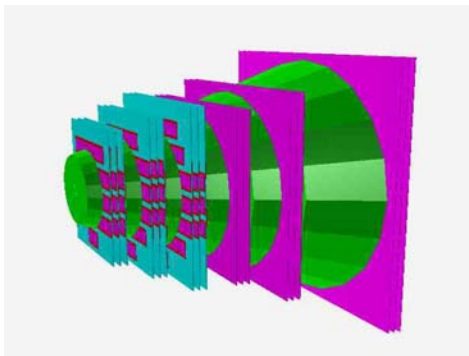


Figure 1: Heterogeneous configuration of the CBM muon system. The last three detector stations (behind absorbers 4-6) are built from straw tubes.

tion consists of three double layers (doublets), with different doublets rotated around the beam axis to create stereo views. Three doublets of the same station, separated in z by some distance, can be used to create track vectors (segments) necessary for efficient suppression of the background.

The following event selection strategy was used:

- find track segments in stations 4 and 5;
- merge track segments from different stations, taking into account multiple scattering in the absorber;
- propagate tracks to the target position using a linear extrapolation;
- apply a cut on the radial position of the extrapolated points;
- accept the event if two or more tracks pass the cuts.

In order to ensure a fair comparison of the two detector configurations, the following implementation details were considered:

- simplified (planar) GEM geometry: automatic segmentation and simple digitization and hit finding;
- 6 mm straw tubes: hit producer with hit merging (i.e. only one hit per tube is kept) and left-right ambiguity (i.e. for each “true” hit a mirror one (symmetric relative to the anode wire position) is added (no local left/right ambiguity resolution));
- track segments should include the maximum number of hits (i.e. 3 for GEMs and 6 for straws);
- segment merging: introduced multiple scattering parameters $\sigma_{\alpha\beta}$ and σ_{xy} (thick scatterer approximation) which were obtained from simulation.

The trigger efficiency and background rejection factor were estimated on Monte Carlo event samples of UrQMD central Au+Au events at 25 GeV mixed with $\omega \rightarrow \mu\mu$ decays and minimum bias events, respectively. The obtained results are presented in Table 1. Both detector configurations demonstrate a similar performance.

Table 1: Trigger efficiency for the di-muon signal and background rejection factor.

Geometry	Efficiency,%	Bkg. rejection
GEM	6.7 ± 0.4	19.8
Straws	6.7 ± 0.4	19.7

References

- [1] A. Kiseleva *et al.*, *CBM Progress Report 2009*, Darmstadt, 2010, p. 67

Study on electron-pion discrimination with the CBM Transition Radiation Detector

P. Reichelt, H. Appelshäuser, and M. Hartig

Goethe University, Frankfurt am Main, Germany

In the CBM experiment at FAIR, a Transition Radiation Detector (TRD) is foreseen for tracking and electron-pion discrimination. Up to twelve detector layers are considered, each with a thin gas volume in order to have a sufficiently fast readout for the intended high collision rates. In this report, we present a combined simulation study of the dependence of electron-pion discrimination power on the detector thickness and on two methods of combining the signals of the individual layers. The influence of the radiator performance is discussed.

For discriminating electrons from pions in the momentum region of a few GeV/c, a TRD profits from their different energy loss through ionization, but mostly from the additional transition radiation produced by electrons. A complete TRD setup should reduce the number of misidentified pions by a factor of 100 (i.e. a pion efficiency of 1%) while keeping 90% electrons in the sample (electron efficiency of 90%), whereas - because of the statistical nature of both signal contributions - a single detector cannot achieve this unless it has a very thick active volume. For a moderate electron efficiency however, even a detector of around 1 cm thickness rejects more than 90% of the pions. This is demonstrated in Fig. 1, showing the results of a stand-alone Monte Carlo simulation with TR production matched to ALICE-TRD sandwich radiator measurements and dE/dx based on Geant 3.21 [1].

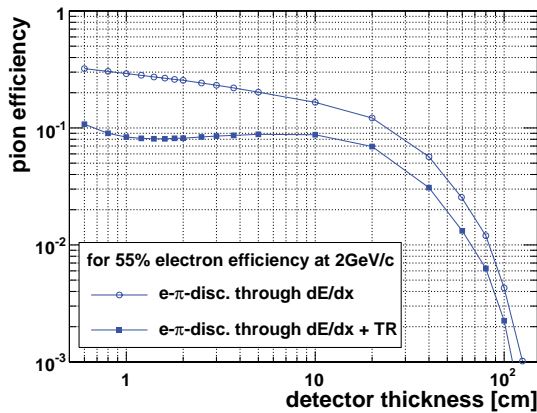


Figure 1: Pion efficiency for a single detector as function of detector thickness for 55% electron efficiency

The performance of multiple detectors depends on the method of combining their signals. For a setup of 12 layers of 1 cm and demanding 90% electron efficiency for the full

system, a pion efficiency of 3.4% can be reached by just analyzing the sum of all signals. It is more powerful, however, to decide for each layer between electron and pion and accept electrons with at least k out of n electron-like signals. Figure 2 shows that with this strategy, the lowest pion efficiency can be reached with a single-layer electron efficiency of $p = 64\%$ and demanding at least six electron-like signals. The resulting pion efficiency is 0.2%.

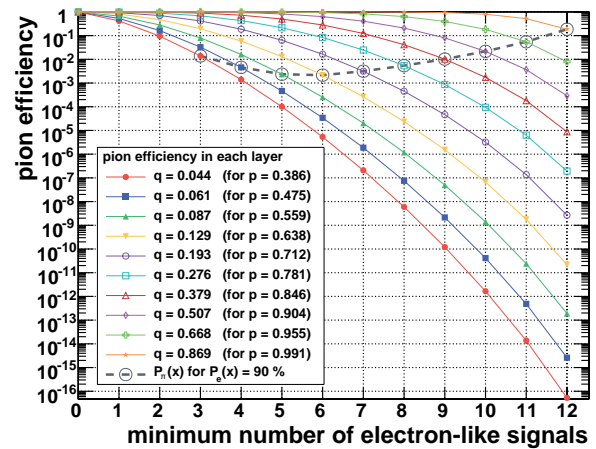


Figure 2: Pion efficiency from 12 detectors of 1 cm thickness as a function of the number of requested electron-like signals in single layers, for different single-layer pion efficiencies q . The dashed line shows values for 90% electron efficiency.

The yield of TR and its spectrum depend on the radiator type and composition. An increase in the photon yield by 20% with respect to the ALICE radiator would e.g. reduce the pion efficiency by a factor of 4 to only 0.05%. Moreover, the energy range of the TR photons is not ideal for absorption in a thin detector. The largest amount of deposited TR energy is reached with an almost 50% softer TR-spectrum (w.r.t. the ALICE radiator), having a mean of 7 keV and also resulting in 0.05% pion efficiency. On the other hand, one finds that a substantial increase of the detector thickness from 1 to 1.6 cm gives a pion efficiency of 0.09%, suggesting that the radiator offers a higher potential for improvements.

References

- [1] P. Reichelt, Master Thesis, Goethe-Universität Frankfurt, to be submitted Feb. 2011

Study of the optimal structure of the TRD radiator

T. P. Akishina, O. Yu. Derenovskaya, and V. V. Ivanov

LIT JINR, Dubna, Russia

We present results of a study aiming to find the optimal radiator for the CBM-TRD, taking into account peculiarities of the transition radiation (TR) and results of worldwide investigations on the development of optimal radiator structures.

The standard version of the CBM-TRD consists of three stations located at 5 m, 7.25 m and 9.5 m downstream of the target, respectively. Each station consists of four modules, each of which containing a layered radiator consisting of N_f alternating layers of polypropylene foils of thickness t_f and air gaps of thickness t_g for producing the transition radiation from high-energy electrons and positrons, and a multi-wire proportional chamber (MWPC) for the registration of the energy loss of charged particles (by ionization and transition radiation) and for the measurement of the coordinates of their intersection with the MWPC plane.

To estimate the quality of the TRD radiator structure, the pion rejection factor at a fixed level of electron efficiency was used. We applied different methods for the discrimination of electrons from pions: the mean value (MV) method, the likelihood functions ratio (LFR) test, the ω_n^k goodness-of-fit criterion, the modified ω_n^k test, the combined method (MV + ω_n^k), and a three-layered perceptron from the JETNET and ROOT packages [1]. Table 1 shows the pion rejection factor at 95% electron efficiency for different momenta p as obtained for the GSI-Bucharest radiator model ($N_f = 220$, $t_f = 25 \mu\text{m}$, $t_g = 250 \mu\text{m}$, total width = 6.05 cm).

Table 1: Pion rejection factor at 95% electron efficiency for different momenta, calculated for the GSI-Bucharest radiator model with different methods for electron-pion discrimination

p [GeV/c]	1.5	3	5	7
MV	10	15	18	18
ω_{12}^6	22	32	33	25
MV + ω_{12}^6	90	219	265	277
mod ω_n^6	64	240	282	254
	(n=6)	(n=6)	(n=7)	(n=7)
LFR	168	524	1075	1150
root	218	833	1212	1228
jetnet	255	1176	1290	3071

For technological and geometric considerations, we assumed the total thickness of the radiator to be ≈ 6 cm. Taking into account both this thickness and the fact that the radiator must efficiently generate and simultaneously weakly absorb the transition radiation, computations were

performed aiming to optimize the structure of the radiator. According to the recommendations in [2], we varied the foil thickness (see Fig. 1 a) and the size of the TR formation zone in the air gap of the radiator (see Fig. 1 b). As a result of this study, the optimal structure of the radiator with the total width of 6.24 cm was found to be $N_f = 320$, $t_f = 15 \mu\text{m}$ and $t_g = 180 \mu\text{m}$. The pion rejection factors obtained for this radiator are given in Table 2, demonstrating that a gain by a factor of 4 - 8 w.r.t. the GSI-Bucharest radiator model is obtained.

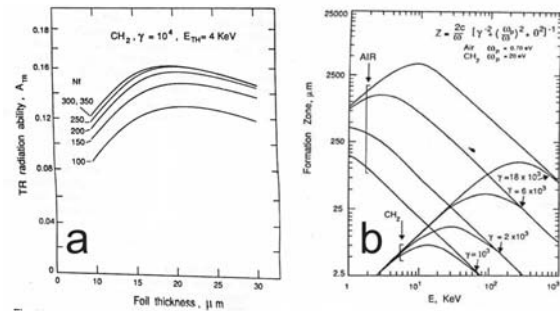


Figure 1: (a) TR radiation ability as a function of the foil thickness for different numbers of foils; (b) size of the TR formation zone in air.

Table 2: Pion rejection factor at 95% electron efficiency for different momenta, calculated for the optimized radiator model with different methods for electron-pion discrimination

p [GeV/c]	1.5	3	5	7
MV	17	21	22	22
ω_{12}^6	98	110	94	77
MV + ω_{12}^6	390	686	762	770
mod ω_7^6	521	1715	2118	2073
LFR	1143	3921	3813	3593
root	1451	1622	4516	8483
jetnet	2250	17300	10840	10180

References

- [1] E. P. Akishina *et al.*, *CBM Progress Report 2009*, Darmstadt 2010, p. 82
- [2] B. Dolgoshein, *Nucl. Instrum. Meth. A* **326** (1993) 434; T. P. Akishina, O. Yu. Derenovskaya and V. V. Ivanov, *JINR Communication P10-2009-61*, Dubna 2009

Performance studies on the CBM-TRD using J/ψ

W. Yu, H. Appelshäuser, and M. Hartig

Goethe University, Frankfurt am Main, Germany

The Transition Radiation Detector (TRD) will be one of the key components of the CBM experiment. It will be used for particle tracking and for the identification of electrons and positrons [1]. J/ψ production in the di-electron channel is a unique physics process to study the performance of the TRD. We here derive a limit on the TRD coordinate resolution, which provides useful information to determine the size of readout pads, using the ratio of reconstructed J/ψ signal to background as performance figure.

Simulations are performed in the cbmroot software framework. The TRD is implemented with three stations at 450 cm, 675 cm and 900 cm downstream of the target, respectively. In this geometry configuration, each station has four layers. Each layer has a 29 mm thick radiator followed by a 6 mm thick gas detector. J/ψ signals are produced by the HSD code for central Au+Au collision at 25A GeV and forced to decay into electron-positron pairs. Background events are generated using the UrQMD event generator for the same collision system. Electron-positron pairs decaying from J/ψ and background events are subsequently mixed together. This mixed sample is then used as input for the detector simulation. A global tracking method which uses spatial hits from the TRD and the silicon tracking system (STS) is applied for track reconstruction. To focus on the TRD performance, only idealized digitisation is used for the STS. Monte-Carlo generated hits from the TRD are smeared with different values to simulate the detector resolution. The transverse momentum p_t of electrons and positrons is required to be larger than 1 GeV/c. Figure 1 shows the invariant-mass spectrum of reconstructed electron-positron pairs from this simulation.

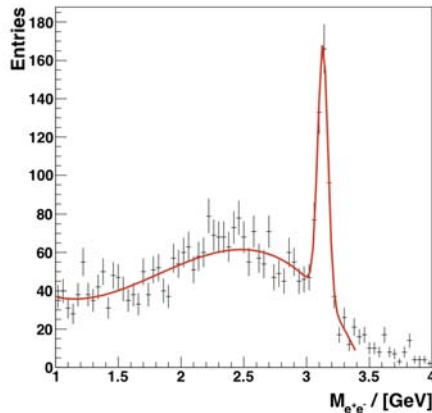


Figure 1: Invariant-mass spectrum of reconstructed e^+e^- pairs

The ratio of signal to background from the invariant-mass spectrum of e^+e^- provides a useful way to check the detector performance. However, this ratio cannot be directly extracted from Figure 1, since the proportion of J/ψ signals to background events in this simulation (1 : 1) is far from reality. Experimentally, J/ψ is a very rare physics process. Thus, the combinatorial background formed by one of the decay daughters and one electron or positron from the background events is significantly enhanced compared to the reality. This distorts the background in the e^+e^- invariant mass spectrum dramatically. A reliable ratio of signal to background can be obtained by removing this distorted combinatorial background source in the simulation. Figure 2 shows the ratio of signal to background extracted from the e^+e^- invariant-mass spectrum for different position smearing of the TRD hits. Here, the above mentioned combinatorial background was removed. the S/B ratio is found to stay constant when the hit resolution is less than 1 mm.

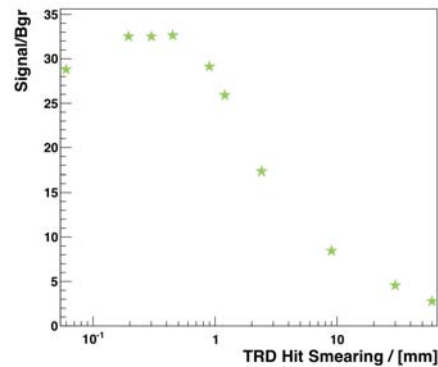


Figure 2: Ratio of signal to background for J/ψ as a function of smearing of TRD hits

In summary, studies on a mixed sample of J/ψ and UrQMD events provide a limit on the coordinate resolution of the TRD. The signal-to-background ratio is found to drop significantly when the hit resolution is worse than 1 mm. Further studies need to be carried out on the MC data with more realistic detector digitisation and clustering. A feasibility study on the TRD online trigger for J/ψ can also be performed using a standalone TRD tracking method developed by M. Krauze, A. Bubak and W. Zipper.

References

- [1] B. Friman *et al.*, *The CBM Physics Book*, Springer Series: Lecture Notes in Physics, Vol. **814**, 2011

First common beam test of the CBM STS, RICH and TRD subsystems at the CERN Proton Synchrotron

D. Emschermann and C. Bergmann

IKP, Münster, Germany

A first common beam test of the CBM Transition Radiation Detector (TRD), Ring Imaging CHerenkov (RICH) and Silicon Tracking System (STS) subsystems was performed for one week at the CERN Proton Synchrotron in November 2010 [1]. The measurements were carried out at the T10 beamline in an electron/pion beam with momenta of 2 to 5 GeV/c. The beamline setup is presented in Fig. 1.

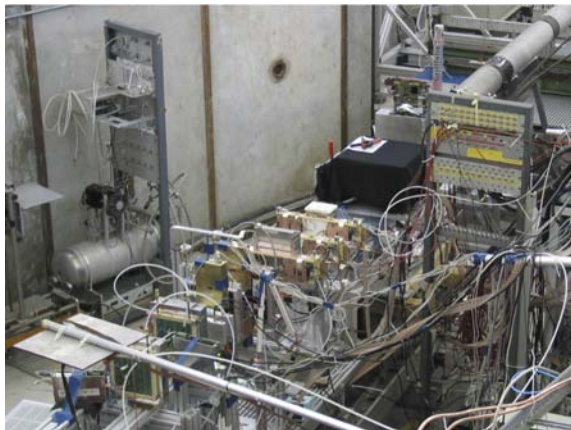
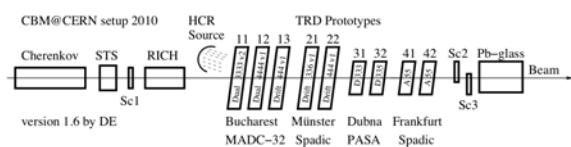


Figure 1: Setup of the prototypes along the T10 beamline

Upstream, at the beginning of the setup the STS station was mounted, followed by a RICH prototype, then came nine TRD prototypes from the four laboratories in Bucharest [2], Münster, Dubna and Frankfurt [3]. Besides the above mentioned prototypes, the setup comprised a Cherenkov detector and a Pb-glass calorimeter for e/π identification (see Fig. 2), as well as three beam trigger scintillators.

The STS station was commissioned in beam at CERN to prepare for the following December beam time at COSY. The RICH was based on a proximity focussing setup with a solid (plexiglass) radiator and four Hamamatsu MAPMTs allowing to reconstruct Cherenkov ring segments [4]. The readout of the STS and RICH subsystems was based on the nXYTER front-end, read out by the CBM readout controller (ROC).

For the TRD, various MWPC geometries were under test, and two complementary approaches for the signal

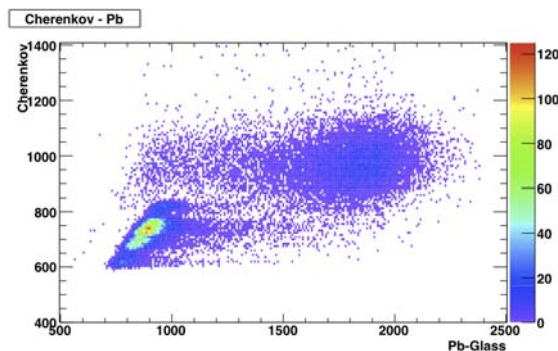


Figure 2: e/π separation for a run at 2 GeV/c

processing were investigated: The TRDs from Münster and Frankfurt were readout with the custom SPADIC [5], a self-triggered sampling ADC, while the detectors from Bucharest and Dubna used a VME-based peak sensing ADC. Part of the test program were high voltage scans, Ar-CO₂ and Xe-CO₂ gas mixtures, variation of the incident beam angle and momentum, and different versions of radiators.

A hybrid DABC/MBS setup was prepared allowing to read the beam monitoring detectors and all (self-)triggered prototypes in a common data acquisition system [6]. The analysis of the beam time data, e.g. pion efficiency and position resolution for the TRDs, is still ongoing.

In autumn 2011 the tests will be iterated with another common CBM beam time at the CERN PS/T9 beam line, giving access to higher momenta.

References

- [1] D. Emschermann, CBM Testbeam 2010 Website, <http://cbm.uni-hd.de/testbeam2010>
- [2] M. Petris *et al.*, *Two-dimension position sensitive Transition Radiation Detector in beam-tests using new Fast Analog Signal Processor (FASP)*, this report
- [3] W. Yu *et al.*, *First beam test of the Frankfurt prototype for the CBM-TRD*, this report
- [4] J. Eschke *et al.*, *Single Cherenkov photon measurements with multi-anode photomultipliers for the CBM-RICH photodetector*, this report
- [5] T. Armbruster, The SPADIC Project Website, <http://spadic.uni-hd.de>
- [6] S. Linev, J. Adamczewski-Musch and J. Frühauf, *DABC as data acquisition framework for CBM*, this report

Two-dimension position sensitive Transition Radiation Detector in beam-tests using new Fast Analog Signal Processor (FASP)

M. Petriș¹, M. Petrovici¹, V. Simion¹, D. Bartoș¹, G. Caragheorgheopol¹, V. Cătănescu¹, F. Constantin¹, C. Bergmann², D. Emschermann², S. Linev³, W. Mueller³, and J.P. Wessels²

¹NIPNE, Bucharest, Romania; ²University of Münster, Germany; ³GSI, Darmstadt, Germany

The new two-dimension position sensitive TRD prototype architecture for CBM experiment developed by us is based on diagonally split rectangular pads of the read-out electrode [1]. The choice of triangular-pad geometry allows for position determination in both coordinates: across and along the pads, respectively. The TRD prototype used in the present tests has a readout electrode of 25 μm thickness kapton foil having on both sides evaporated Al/Cr layers with the mentioned pad structure.

The first version of the prototype was built with an anode-cathode distance of 3 mm (DSTRD-V1) and a read-out electrode with a double sided pad structure [2, 3] similar with small size double sided TRD prototype which showed that such a geometry preserves the performance up to $2 \times 10^5 \text{ part} \cdot \text{cm}^{-2} \cdot \text{s}^{-1}$ counting rate. In order to improve the charge sharing between the pads for position reconstruction, the second version was built with a 4 mm anode-cathode distance (DSTRD-V2).

Both detectors were tested with the 5.9 keV X-ray ^{55}Fe source using both the anode and pad signal, respectively. 80% Ar + 20% CO₂ gas mixture was flushed through the counter. For pad signal processing we used the new FEE - Fast Analog signal Processor (FASP) [4] developed in our group. It has 8 input/output channels and can provide two type of outputs: a fast output with a semi-Gaussian shape (Fig.1, blue line) and a flat top output (Fig. 1, red line) [5].

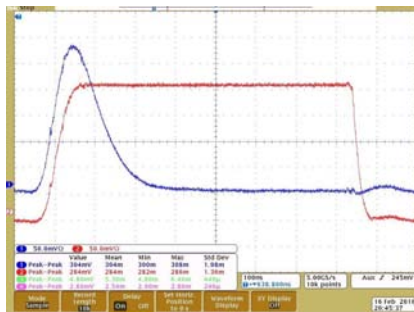


Figure 1: Fast output (blue line) and flat top output (red line) of the Fast Analog signal Processor (FASP)

The obtained pulse height spectrum (10% energy resolution in sigma) for the pad signal of DSTRD-V2, processed by the FASP fast output is presented in Fig. 2 (left). The applied anode voltage was 1750V. The right side of Fig. 2 shows the obtained pulse height spectrum (10.4% energy resolution in sigma) for the flat-top output and 1800 V anode voltage. Both FASP outputs were digitized with an AD811 converter, the fast output via a main amplifier with

300 ns shaping time, the flat top output directly.

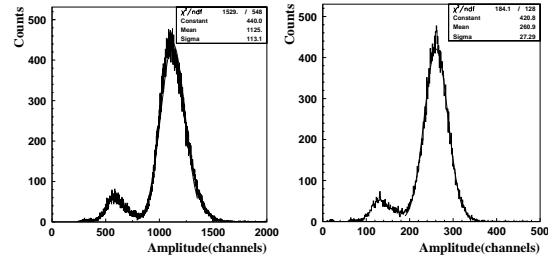


Figure 2: Pulse height spectrum of the (FASP) fast output, anode voltage 1750 V (left side), as well as of the flat-top output (right side), anode voltage 1800V

The detectors were tested with electron and pion beam of 1 - 5 GeV/c momenta at the T10 beam line of the CERN PS accelerator in a joint measurement campaign of the CBM Collaboration. The signals delivered by 16 triangular pads were processed by the FASP using the flat top output. They were digitized by a 32 channels peak sensing Mesytec ADC (MADC-32).

Figure 3 shows the pulse height distributions of electrons and pions for 2 GeV/c momentum, a gas mixture of 80% Xe + 20% CO₂ and operating the DSTRD-V1 counter with 1700 V anode voltage. A detailed analysis is in progress.

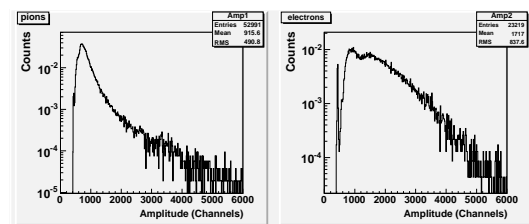


Figure 3: Pulse height distributions of electrons and pions for 2 GeV/c momentum

References

- [1] D. Bartoș *et al.*, *CBM Progress Report 2009*, Darmstadt 2010, p. 31
- [2] M. Petrovici *et al.*, *Nucl. Instrum. Meth. A* **579** (2007) 961
- [3] M. Klein-Bösing *et al.*, *Nucl. Instrum. Meth. A* **585** (2008) 83
- [4] V. Cătănescu *et al.*, *CBM Progress Report 2009*, Darmstadt 2010, p. 47
- [5] A. Caragheorgheopol *et al.*, *Front-end electronics for high counting rate TRD*, this report

First beam test of the Frankfurt prototype for the CBM-TRD

W. Yu, H. Appelshäuser, A. Arend, M. Hartig, P. Dillenseger, and P. Reichelt

Goethe University, Frankfurt am Main, Germany

As one of the key components in the CBM experiment, the Transition Radiation Detector (TRD) will play a significant role in the particle identification. A fast detector with double sided readout chambers [1] and a ALICE type of detector with both drift and amplification regions were designed for the circumstance of high particle rates. We propose to build a fast detector with an amplification region only. Simulation studies combining dE/dx and transition radiation show that such a simple detector can fulfill the requirement of particle identification [2]. If such design can be realized and verified by more sophisticated studies and beam tests, it will noticeably reduce the cost and simplify the construction.

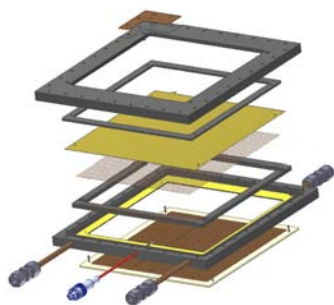


Figure 1: Sketch of the readout chamber

The IKF group in Frankfurt participated in the beam test in November 2010 at CERN and tested its two prototype detectors. Both detectors are equipped with a readout chamber, which has an amplification region of 1 cm. A sketch of the readout chamber is shown in Fig. 1. The chamber size is $15 \times 15 \text{ cm}^2$ and it is enclosed by an aluminized kapton foil and a simple PCB for the charge sensitive readout.

Inside the readout chamber a plane of anode wires is located in the centre for gas amplification. The pitch between anode wires is 5 mm for one chamber and 2.5 mm for the other. The anode wires are made of Au plated W, $20 \mu\text{m}$ in diameter. Rectangular pads with a conservative size of $5 \times 50 \text{ mm}^2$ are chosen to read out particle-induced signals. In the beam test, eight neighbouring pads in the middle column grouped together from each chamber are read out by the 8-channel SPADIC chip, developed to be a self-triggered pulse amplification and digitization ASIC [3]. The radiator is a sandwich construction of Rohacell HF71 foam and polypropylene fibres. Figure 2 displays one of the prototype detectors during the beam test.

The setup of the Frankfurt prototypes can be found in the overview of this CERN beam test [4]. Both detectors were tested at beam momenta of 2, 3, 4 and 5 GeV/c respectively.

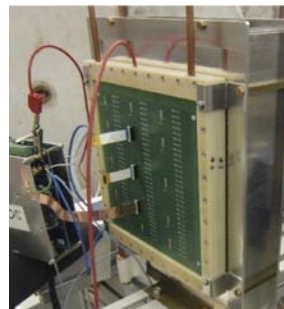


Figure 2: Prototype detector in the beam tests

Two gas mixtures were used in the test: Xe-CO₂ and Ar-CO₂, with a ratio of 80:20 in both cases. Figure 3 shows a very preliminary result of the integrated ADC spectra from pions (blue line) and electrons (red line) separately. Here the data was collected by the chamber of 2.5 mm wire pitch at the beam momentum of 5 GeV/c and with the gas mixture of Xe-CO₂.

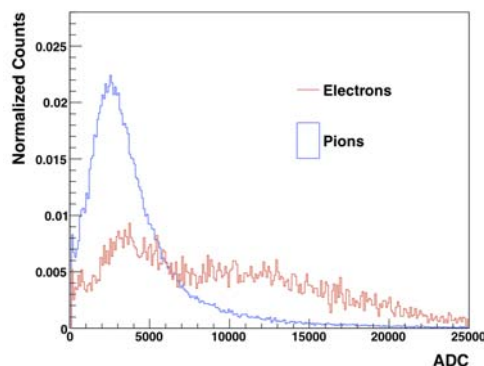


Figure 3: Integrated ADC spectra from pions (blue line) and electrons (red line)

References

- [1] M. Klein-Bösing *et al.*, Nucl. Instrum. Meth. **A 585** (2008) 83
- [2] P. Reichelt *et al.*, *Study on electron-pion discrimination with the CBM Transition Radiation Detector*, this report
- [3] T. Armbruster *et al.*, *CBM-TRD readout with the SPADIC amplifier / digitizer chip*, this report
- [4] D. Emschermann and C. Bergmann, *First common beam test of the CBM STS, RICH and TRD subsystems at the CERN Proton Synchrotron*, this report

CBM-TRD readout with the SPADIC amplifier / digitizer chip

T. Armbruster, P. Fischer, and I. Perić

University of Heidelberg, Germany

The SPADIC chip is being developed for the readout of the CBM Transition Radiation Detectors (TRD). The basic readout concept is to perform both the amplification and the digitization of the (charge) pulses from the CBM TRD in a single front-end ASIC. It is intended to continuously digitize the whole shaper pulses which allows for a flexible subsequent feature extraction (amplitude, time, etc.) either directly on the chip or in some FPGA (both options are currently subject of discussion). The group in Heidelberg started the development of the SPADIC (Self triggered Pulse Amplification and Digitization asIC) chip in 2008. The latest prototype SPADIC 0.3 contains 26 channels with input protection and different amplifier versions, out of which 8 are equipped with pipelined 9 Bit ADCs running at 25 MHz.

The system noise including the ADC was measured to $\approx 800 e^-$ at a peaking time of 80 ns and a capacitive input load of 30 pF while consuming 3.6 mW for the front-end and 4.5 mW for the ADC per channel. Using static input signals the resolution of the ADC is close to 8 Bit (INL slightly larger than 0.5 LSB).

The prototype chip also contains an on-chip digital memory which can record snapshots of up to 42 ADC data samples that can be read out later at slower speed. The architecture is self-triggered so that an amplitude above a programmable threshold triggers data storage on a per channel basis.

The final chip will also include a digital IIR filter to eliminate long ion tails as well as a fast serial interface compatible to the CBM DAQ data format. With the help of measured detector pulses the optimal filter structure (filter order, topology, word widths, etc.) is presently being evaluated. A first iteration of the filter will already be realized in the next ASIC prototype. A web page about the SPADIC chip has been created at <http://spadic.uni-hd.de>.

In order to read out several SPADIC chips when mounted on the test chambers, a versatile fast data acquisition board and a suited SPADIC interface board (see Fig. 1) were developed and tested. The SUSIBO ('SuS Interface BOard') contains a USB 2.0 interface, a large Xilinx FPGA, memory, Ethernet IO and a differential interface to the trigger logic. It is controlled by custom software running under Linux. The interface board houses a SPADIC chip (wire bonded to the PCB), interface and biasing circuitry and a ZIF connector to connect TRD chamber prototypes to the amplifier inputs. Eight units have been assembled for use mainly in the 2010 TRD beam test. A 2nd generation interface board with improved interfacing and better signal routing is presently being prepared.

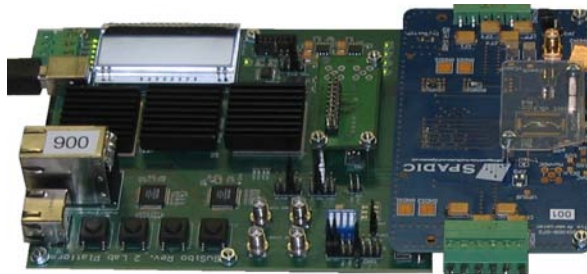


Figure 1: SUSIBO readout board (left) and interface board with SPADIC chip (right)

The readout system was successfully used in the 2010 CBM test beam campaign at CERN to read out TRD prototype detectors from Frankfurt and Münster. A screenshot of the online event display with two detector pulses is shown in Fig. 2. The data are presently being analyzed.

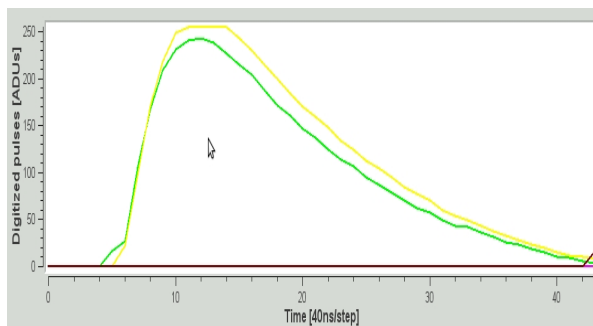


Figure 2: Online display of detector pulses digitized with the SPADIC chip (Self triggered Pulse Amplification and Digitization asIC)

Front-end electronics for high counting rate TRD

A. Caragheorghopol¹, D. Bartoş¹, V. Catanescu¹, V. Văleanu², and V. Vasiliu²

¹NIPNE, Bucharest, Romania; ²ISS, Bucharest, Romania

Fast Analog Signal Processor FASP-0.1 [1, 2] is a prototype ASIC designed at NIPNE for HCR-TRD having in mind the CBM experiment at FAIR. In this contribution we report on relevant measured parameters of ASIC analog channels and a FEE based on FASP, designed and built for in-beam tests of our HCR-TRD prototypes [3].

- The measured ASIC parameters [4, 5] are:
- quiescent supply current ($V_D = 3.3V$): $30mA \pm 1mA$.
 - output baseline shift :
 - with power supply ($V_D = 3.0- 3.6V$): $< 0.07\%$;
 - with detector leakage current ($I_L = \pm 50nA$): $< 9\mu V/nA$.
 - conversion gain G vs. C_{det} (for FAST outputs):

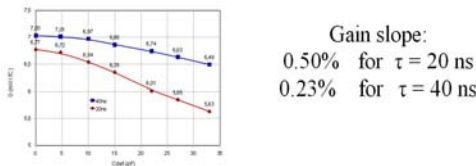


Figure 1: Conversion gain G vs. C_{det}

- integral nonlinearity (INL)(0-1V linear range):
 - INL = 1.0% for $\tau = 20ns$, FLAT output;
 - INL = 0.2% for $\tau = 40ns$, FAST output.
- overload recovery (for FAST outputs, $\tau = 40 ns$): first pulse: $\times 10$ overload ; second pulse: after 400ns (corresponding average pulse rate $> 300kcps$).

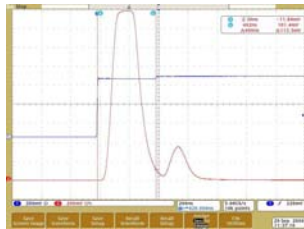


Figure 2: Overload recovery

- electronic noise charge ENC vs. C_{det} for FAST outputs:

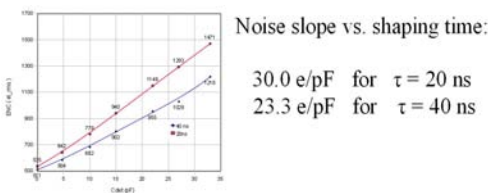


Figure 3: ENC vs. C_{det}

Front End Electronics (FEE) was designed to cope with the requirements for in-beam test of 3 different HCR-TRD prototypes. The requirements are:

- acceptable immunity to the "pick-up" noise;
 - long transmission line of detector signals to ADC;
 - NIM logic standard for request/grant protocol;
 - 16 analog signal channels for each detector (48 total).
- FEE is splitted in two units (Fig.4). The first one, motherboard, houses one FASP ASIC for wich it provides power supply, all DC references voltages (THRESHOLD, BASELINE, etc.), 8 analog buffers with differential outputs (each buffer can be switched to handle FAST or FLAT TOP signal), and NIM logic standard interface (EVT, REQ, RDY, RST signals). Motherboard is a three layers PCB of $100 \times 120mm^2$ size. The second one, adapter board, has two identic sections. Each section has 8 differential input channels providing single-ended outputs. DC output levels can be adjusted to match ADC inputs. Adapter board is three layers PCB of $78 \times 74mm^2$ size.

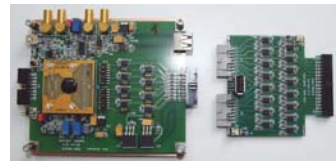


Figure 4: ASIC MB (Left) and Adapter (Right)



Figure 5: Experimental set-up used in the in-beam test

HCR-TRD prototypes, the described FEE (48 channels) and geometry control mechanism (Fig.5) were successfully tested at T10 beam line of the CERN PS accelerator, last November .

References

- [1] V.Catanescu, CBM 10th Colaboration Meeting, Sept. 25-28,2007, Dresden
- [2] V.Catanescu, et al., DPG,Bochum, March 18,2009
- [3] M.Petris et al., contribution to this Sci.Rep.
- [4] A. Caragheorghopol et al., 14th CBM Colaboration Meeting, Split,Oct.6-9,2009.
- [5] A. Caragheorghopol et al., CBM FEE/DAQ Workshop, Feb. 22-23,2010,GSI

Development and test of fast readout chambers for the CBM-TRD

S. Chernenko, G. Cheremukhina, O. Fateev, S. Razin, Yu. Zanevsky, and V. Zryuev

Joint Institute for Nuclear Research, Dubna, Russia

A three-stage GEM detector with two-dimensional strip readout [1] was tested with FEE based on the nXYTER chip (FEB, D revision) in the laboratory (Fig. 1). The active area of the detector is $10 \times 10 \text{ cm}^2$. The strip pitch of the 2-D readout board amounts to $800 \mu\text{m}$, while the width of upper and bottom strips are $160 \mu\text{m}$ and $640 \mu\text{m}$, respectively. The total number of readout channels was 256. The detector test was performed with a ^{55}Fe r/a source applying a gas mixture of Ar/CO₂ (85/15). The counting plateau of the tested detector is shown in Fig. 2. The profile of the collimated ^{55}Fe source along the x direction is displayed in Fig. 3; the profile in y direction is similar.



Figure 1: A three-stage GEM detector (back side view) with FEE electronics (based on the nXYTER) at the laboratory test stand

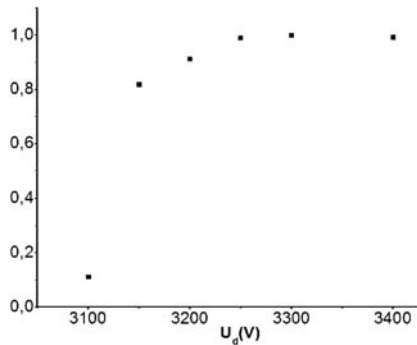


Figure 2: Counting plateau measured with the ^{55}Fe source

Two Dubna-type TRD prototypes were in addition tested in beam at the CERN-PS in November 2010 [2] using a pion-electron beam. These detectors are based on MWPC ($10 \times 10 \text{ cm}^2$) with pad readout, 2 mm anode wire pitch and an anode-cathode gap of 3 mm. The drift gaps are 2 mm and 5 mm respectively, the active area of the detector is $40 \times 40 \text{ mm}^2$ with a pad size of $5 \times 20 \text{ mm}^2$. Fiber radiators of 4.8 cm thickness were used, the same as for the ALICE TRD [3]. The detectors were operated with a gas mixtures of Ar/CO₂ (80/20) and Xe/CO₂ (80/20). To

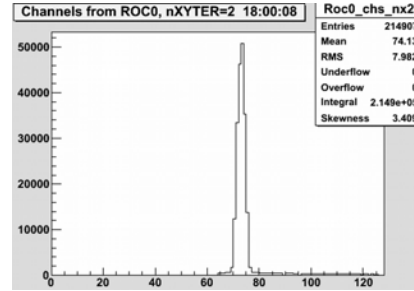


Figure 3: Profile of collimated ^{55}Fe source

identify pions as well as electrons, Čerenkov and Pb-glass counters were used.

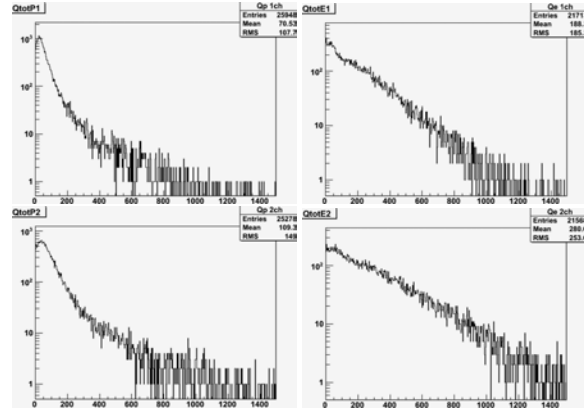


Figure 4: Total charge distribution for MWPC with 3 mm (top row) and 5 mm (bottom row) drift gap for 4 GeV/c pions (left column) as well as electrons (right column)

Preliminary result of the data analysis are presented in Fig. 4. One can see that the pion-electron separation can be performed by these prototypes for beam energies of 4-5 GeV/c. The preliminary value of spatial resolution measured along the wires is better than $300 \mu\text{m}$. Further data analysis is in progress.

References

- [1] S. Chernenko *et al.*, *CBM Progress Report 2009*, Darmstadt 2010, p. 34
- [2] D. Emschermann and C. Bergmann, *First common beam test of the CBM STS, RICH and TRD subsystems at the CERN Proton Synchrotron*, this report
- [3] ALICE TRD, TDR CERN/LHCC 2001-21

High granularity, symmetric differential readout - timing multigap RPC

*M. Petriş¹, M. Petrovici¹, V. Simion¹, D. Bartoş¹, G. Caragheorgheopol¹, F. Constantin¹,
I. Deppner², N. Herrmann², P. Loizeau², K. Doroud³, and M. C. S. Williams⁴*

¹NIPNE, Bucharest, Romania; ²University of Heidelberg, Germany; ³CERN, Geneva, Switzerland; ⁴INFN, Bologna, Italy

We report about results of a R&D activity concentrated on the development of a multigap RPC (MRPC) prototype with strip readout for high counting rate and high multiplicity environments as it is required by the low polar-angle region of the CBM-TOF detector. In order to cope with the challenging counting rate requirements at the inner part of the CBM-TOF wall ($\sim 2 \times 10^4$ part. \cdot cm $^{-2}$ \cdot s $^{-1}$), we built a few prototypes using as resistive electrodes a special low-resistivity glass with a resistivity of the order of 10^{10} Ω cm [1, 2].

The obtained results showed that operating a MRPC with very good time resolution at high counting rate environments (up to 16,000 part. \cdot cm $^{-2}$ \cdot s $^{-1}$) is feasible. Nevertheless, the low polar-angle region requires not only a high counting rate performance, but also a high granularity detector to meet the multiplicity challenge (up to 1000 tracks/event at 25A GeV Au+Au collisions). For this particular region of the TOF wall, we designed and built a RPC prototype using a readout electrode with short length strips (46 mm).

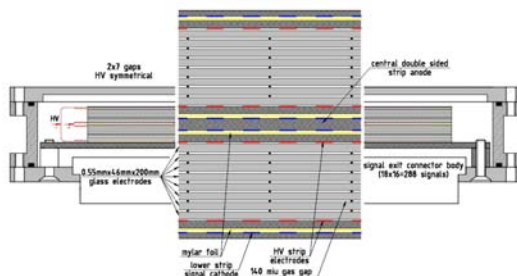


Figure 1: Sketch of the RPC configuration

A cross section through this configuration is shown in Fig. 1. It is a completely symmetric two stack structure, with high voltage electrodes for both positive and negative polarities. Each high voltage electrode has an identical strip structure as the readout electrodes. Each stack has seven gaps of $140 \mu\text{m}$ each, defined by eight resistive electrodes made from a normal high resistivity float glass ($\sim 10^{12}$ Ω cm). The strips of the high voltage electrodes were in contact with a resistive layer painted on the last glass electrode. The readout electrodes (the cathodes and central double-sided anode) have a strip structure of 2.54 mm pitch and 1.1 mm strip width. The anode and cathode signals are connected by twisted pair cables and sent to the differential FEE based on the NINO chip [3].

The detector was tested in beam at T10 beam line of the CERN PS accelerator with a 6 GeV/c momentum beam of

negative pions. A 90% C₂F₄H₂ + 5% SF₆ + 5% iso-C₄H₁₀ gas mixture was used.

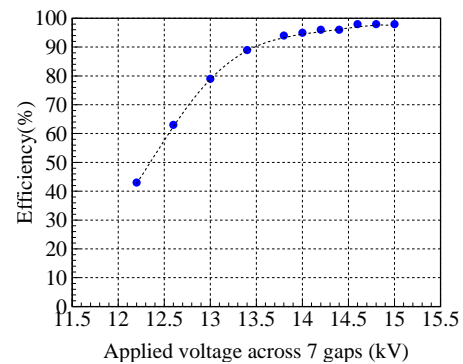


Figure 2: Efficiency as function of applied voltage

Applying a HV larger than 2kV/gap, an efficiency of 95% to 98% was measured, where the efficiency was determined by the number of RPC hits with valid time and time over threshold information divided by the number of triggers. The time of flight distribution was obtained as the mean of the time information recorded at both ends of the used strip relative to the reference signal delivered by a plastic scintillator. We performed for each measured strip a time walk correction and subtracted quadratically the contribution of the scintillator reference counter (61 ps) and an electronics jitter (33 ps). The resulting time resolution was determined to 57 ps (Fig. 3) at 2.09 kV/gap.

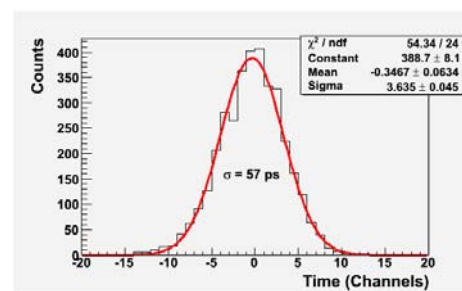


Figure 3: Time of flight spectrum

References

- [1] D. Bartoş *et al.*, 2008 NSS/MIC, Vols. 1-9 Book Series: IEEE Nuclear Science Symposium - Conf. Rec. Pg: 1933-1935
- [2] M. Petriş *et al.*, Rom. Journ. Phys. (2010), in press
- [3] F. Anghinolfi *et al.*, Nucl. Instrum. Meth. A **533** (2004) 183

Crosstalk free multi-strip Resistive Plate Chambers?

D. Gonzalez-Diaz^{1,2}, H. Chen², and W. Yi²

¹GSI and TU, Darmstadt, Germany; ²Tsinghua University, Beijing, China

Because of its highly-quenched operating mode, a gaseous detector of the Resistive Plate Chamber type (RPC) can work at constant fields in excess of 100 kV/cm at ambient conditions. The very fast avalanche dynamics can thus result in exponential signal rise-times down to $t_{rise} = 100$ ps, when not space-charge limited. The associated time resolution $\sigma_t = 50 - 100$ ps is a consequence of this fact.

A most intriguing technological problem is the routing of such signals out of the RPC detector itself, usually made of densely packed multi-strip electrodes. Next generation RPCs (CBM, NeuLAND-R3B, iTOF-R3B) aim at doing it over up to 2 m with little signal shaping and, as much as NeuLAND and CBM are concerned, with little or no crosstalk also. Present ‘state-of-the-art’, 1 m long multi-strip RPCs (from the ‘4-pi’ experiment at GSI) show, indeed, a fairly large cluster size of 4.5 strips/track.

The problem of signal transmission can be tackled through a N-conductor transmission line simulation. However, the structure of the solutions is complicated enough that no simple analytical estimates can be obtained in general. We have introduced in [1, 2] an analytical technique for obtaining the complete lossy solution, that is suited for RPC structures and allows for simple solutions in several practical cases. As a result, some approximate RPC characteristics can be deduced (see [2] for details):

1. The low-frequency/short-distance crosstalk is proportional to the capacitive coupling C_{mutual}/C_{ground} .
2. The high-frequency/long-distance crosstalk is approximately proportional to the unbalance between the capacitive and the inductive coupling $C_{mutual}/C_{ground} - L_{mutual}/L_{self}$, the detector length, and the inverse of the signal rise time.
3. Losses are dominated by the glass loss-tangent and the counter length D , largely independent from phenomena 1, 2. Typical glass-based counters have a cutoff frequency of ~ 1 GHz for 2 meters (Fig. 1 bottom).
4. In a high-frequency/long system, the best transmission properties are obtained by accurate balance of the inductive and capacitive coupling.
5. Such a situation can be achieved through a compensation scheme (hereafter ‘electrostatic compensation’) based on the fine adjustment of the system dielectrics.
6. As long as the coupling to the over-next neighbour is small, typical RPCs can be electrostatically compensated in general. We show in Fig. 1 the experimental verification of such a procedure for 2-strip RPCs in both the time and frequency domain.

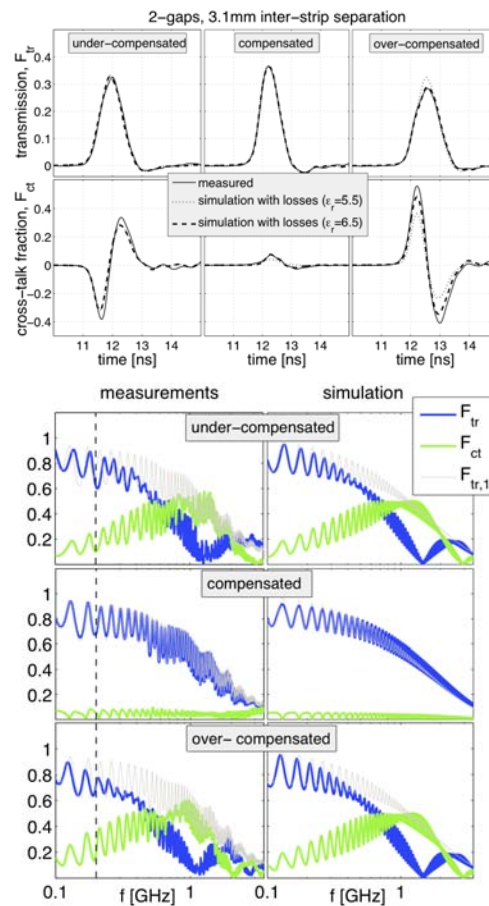


Figure 1: (Top) Transmission characteristics for a 2 m long 2-strip RPC in the time domain. Shown is the measured transmission F_{tr} and crosstalk fraction F_{ct} (—) for different degrees of compensation. Simulations overlaid as ··, ——. (Bottom) Transmission characteristics in the frequency domain (measurements: left column, simulations: right column). $F_{tr,1}$ is the transmission for a single strip, that approximately represents the theoretical limit of a compensated system. See [2] for details.

This development opens the way to the construction of timing RPCs of virtually unlimited size, with performances similar to those achievable in small cells in terms of resolution, efficiency and crosstalk.

References

- [1] D. Gonzalez-Diaz, Nucl. Instrum. Meth. A (2010), doi:10.1016/j.nima.2010.09.067
- [2] D. Gonzalez-Diaz, H. Chen and Yi Wang, submitted to NIM, arXiv:1102.1389v1

Performance of low resistive glass

Yi Wang, J. Wang, W. Ding, and H. Chen

Department of Engineering Physics, Tsinghua University, Beijing, China

The counting rate capability of MRPCs is strongly dependent on the resistivity of glass. A kind of low resistive silicate glass with bulk resistivity of the order of $10^{10} \Omega\text{cm}$ were produced in Tsinghua University. The architecture of melting, annealing and polishing is very important to get high quality glass. Fig. 1 shows the bulk resistivity as a function of position. Although the resistivity changes a little in different position, it is still of the order of $10^{10} \Omega\text{cm}$.

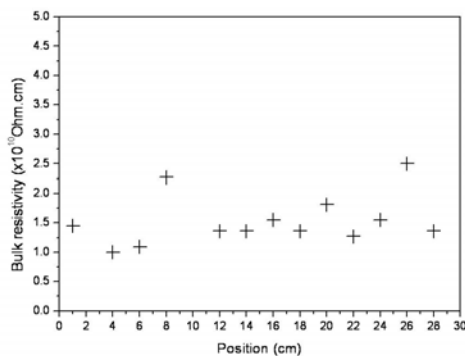


Figure 1: Bulk resistivity as a function of position. The dimension of the glass is $20 \text{ cm} \times 30 \text{ cm} \times 1.1 \text{ mm}$.

Temperature and high voltage tests are shown in Fig. 2, which shows that this kind of glass has very good performance.

In order to get the surface quality of the glass, 2-D and 3-D scanning were done. Because the glass was polished by precise machines, the surface is very smooth and its roughness is less than 10 nm.

The stability with respect to time and integrated charge of the electrical properties of the electrode materials was shown to be a drawback in some previous attempts, so we have focused on this aspect. Fig. 3 shows the stability test of the glass resistivity with respect to the charge integrated across it. The test was done at 28°C for 34 days, with an applied voltage of 1 kV. The accumulated charge was 1 C/cm^2 , roughly corresponding to the CBM life time over 5 years of operation at the maximum particle flux of about 20 kHz/cm^2 . Despite the main conductivity being electronic, an increase of the bulk resistivity with time/charge can be seen, not exceeding a (tolerable) factor of 2, even for such large integrated charges.

The specifications of the low resistivity glass are shown in Table 1.

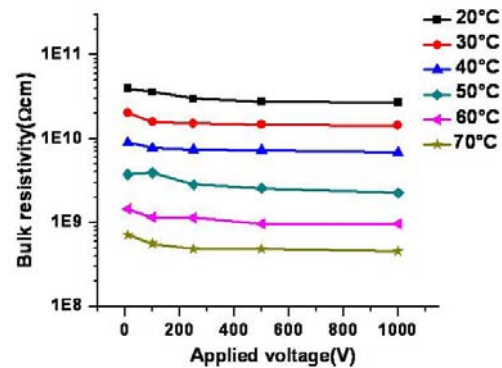


Figure 2: Bulk resistivity of the low resistive silicate glass as a function of applied voltage at various temperatures

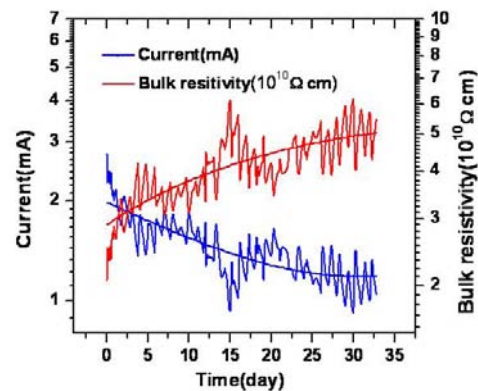


Figure 3: Long term stability test of the low-resistive silicate glass for 34 days: current (lower line) and bulk resistivity (upper line) as a function of time at 28°C , for an applied voltage of 1 kV. The total integrated charge across the material was 1 C/cm^2 .

Table 1: Specification of glass

Maximal dimension	50 cm x 50 cm
Bulk resistivity	$\approx 10^{10} \Omega\text{cm}$
Standard thickness	0.5 mm - 2 mm
Thickness uniformity	$\pm 0.02 \text{ mm}$
Dielectric constant	≈ 10
Surface roughness	$< 10 \text{ nm}$
DC measurement	very stable

Performance test of MRPC with different pad size

Y. Sun, C. Li, H. Chen, S. Yang, and L. Xu

USTC, Hefei, China

The multi-gap Resistive Plate Chamber (MRPC), a technology with excellent timing performance, is proposed to be the most promising candidate for the CBM-TOF. In the CBM-TOF wall, there are four regions with different rate and multiplicity requirements [1]. For the two central regions, not only plates with low resistivity are necessary to cope with the high particle flux, but also the granularity is an important issue because of the high particle multiplicity.

To improve the understanding of the performance dependence on the pad size, two MRPC prototypes with variable pad size and different readout method were constructed and tested.

Both prototypes are twelve-gap modules with 0.22 mm gap size, as shown in Fig. 1 (a). These gaps are arranged in two stacks to relax the high voltage (HV) requirement. Normal floating glass is used as the resistive plate. The HV electrodes are made of graphite tape with surface resistivity of about 200 kΩ/□. The shape and size of the two prototypes are the same but with different readout pads (see Fig. 1 (b)). Prototype I has single-end readout pads while prototype-II has a double-end readout. The pad width is 2.5 cm and the gaps between pads are 4 mm.

The prototypes were tested with a 600 MeV proton beam in July 2010 on the E3 line at the Institute of High Energy Physics (IHEP), Beijing, China. The setup of the test is shown in Fig. 2. The gas mixture used during the test consists of 90% Freon (R-134a) + 5% SF₆ + 5% iso-C₄H₁₀. The time reference given by four PMTs is ~ 40 ps.

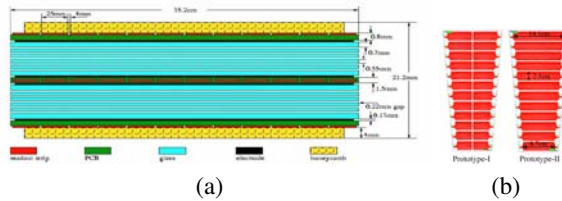


Figure 1: (a) Side view of the MRPC structure. (b) The readout pattern of the two prototypes.

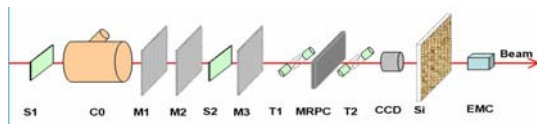


Figure 2: The setup at the E3 line at IHEP

Figure 3 (a) shows efficiency and time resolution as functions of the applied differential HV for one selected pad (the third shortest pad) of prototype I. The efficiency is higher than 98% for HV ≥ ± 6.8 kV, and the time reso-

lution is around 55 ps. The time distribution after slewing correction is shown in Fig. 3 (b).

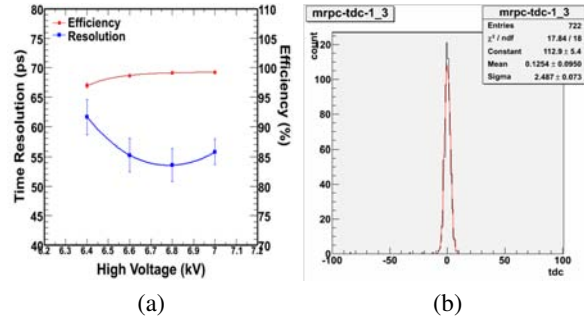


Figure 3: (a) Efficiency and time resolution as functions of the applied HV for the third shortest pad on prototype I. (b) A typical time distribution of MRPC after slewing correction (25 ps/TDC bin).

To investigate the performance dependence on the pad size, a position scan was performed in the test. Figure 4 shows the time resolution of each pad, from the shortest (4.3 cm) to the longest (7.0 cm) of the prototype I under HV = ± 6.8 kV. For most of the pads, the time resolution varies between 50-60 ps.

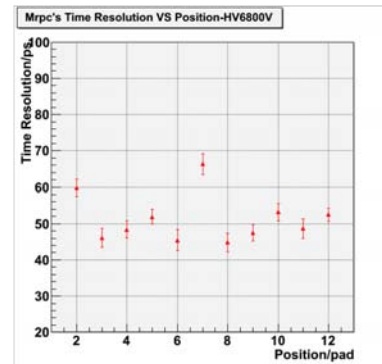


Figure 4: Time resolution of different pads of prototype I. A lower pad number corresponds to shorter pad length.

Prototype II was not tested because of the limited beam time. From the results of prototype I, we found no dependence of MRPC timing performance on the pad size in this range.

References

[1] I. Deppner *et al.*, Nucl. Instrum. Meth. A (2010), doi:10.1016/j.nima.2010.09.165

Development of ceramics RPC for high rate capability timing detector application

*L. Naumann, R. Eißmann, B. Kämpfer, R. Kotte, A. Laso Garcia, R. Peschke, D. Stach, C. Wendisch,
and J. Wüstenfeld*

Helmholtz-Zentrum Dresden-Rossendorf, Germany

The installation of timing Resistive Plate Chambers (RPC) is under consideration for the very forward, high rate environment of the Compressed Baryonic Matter (CBM) experiment [1]. For that purpose prototype timing RPC were developed at Helmholtz-Zentrum Dresden-Rossendorf (HZDR). Electrodes with a volume resistivity of about $10^9 \Omega\text{cm}$ [2, 3] are considered for detectors with high rate capability $\leq 2 \cdot 10^4 \text{ s}^{-1}\text{cm}^{-2}$. Special ceramics composites were developed and processed.

In 2010 two prototypes with dimensions of the ceramics electrodes of $10 \times 10 \text{ cm}^2$ and one prototype with $20 \times 20 \text{ cm}^2$ were exposed at the electron accelerator ELBE at HZDR to 32 MeV single-electron beam pulses. The flux of the primary beam is tunable from few electrons/s to 10^7 electrons/s. The exposed region amounts to about 10 cm^2 . Position-dependent efficiency and time resolution distributions (Fig. 1) were measured over the full detector area by moving the RPC perpendicular to the beam axis.

The behaviour of both small RPCs is very similar, even

though the surface roughness differs by one order of magnitude (40 nm resp. 400 nm). A four times larger RPC was assembled as a more realistic demonstrator for the innermost CBM-TOF segment. The construction differs in few details only. No additional inner support structure was provided, although both linear dimensions increased by a factor of two. A two-dimensional efficiency plot is shown in Fig. 2 for a beam flux of $4.2 \cdot 10^4 \text{ s}^{-1}\text{cm}^{-2}$. For all RPCs the highest applied field amounts to 105 kV/cm in the four gas gaps of $300 \mu\text{m}$ width.

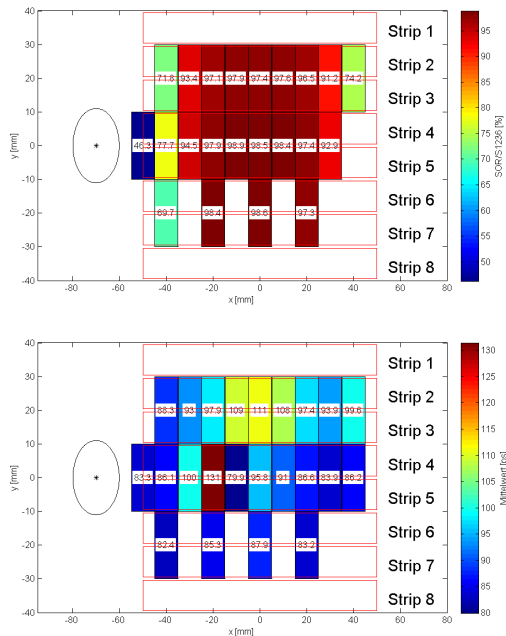


Figure 1: Efficiency (top) and time resolution (bottom) of the $10 \times 10 \text{ cm}^2$ RPC as a function of the beam position for an electron flux of $2 \cdot 10^5 \text{ s}^{-1}\text{cm}^{-2}$

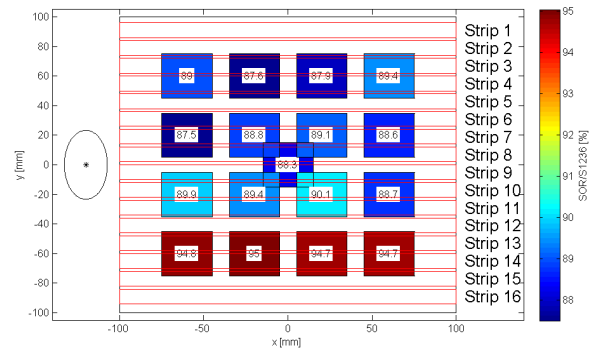


Figure 2: Efficiency of the $20 \times 20 \text{ cm}^2$ RPC as a function of the beam position for an electron flux of $4.3 \cdot 10^4 \text{ s}^{-1}\text{cm}^{-2}$

References

- [1] I. Deppner *et al.*, Nucl. Instrum. Meth. **A** (2010), doi:10.1016/j.nima.2010.09.165
- [2] L. Naumann *et al.*, Nucl. Instrum. Meth. **A** **628** (2011) 138
- [3] L. Naumann *et al.*, Nucl. Instrum. Meth. **A** (2010), doi:10.1016/j.nima.2010.09.121

Performance of a differential CBM-TOF demonstrator

I. Deppner¹, N. Herrmann¹, P.-A. Loizeau¹, K. Wisniewski¹, C. Xiang¹, Y. Zhang¹, M. Ciobanu², and J. Friihauf²

¹Physikalisches Institut, Universität Heidelberg, Germany; ²GSI, Darmstadt, Germany

Currently multi-gap Resistive Plate Chambers (MRPC) are the optimal choice to fulfill the CBM-TOF requirements [1]. For the low rate region ($< 1 \text{ kHz/cm}^2$) a MRPC in multi-strip configuration with thin standard float glass can be considered. Here we report on results obtained during a test experiment at COSY/Jülich with an fully differential MRPC prototype developed at Physikalisches Institut in Heidelberg (more details regarding this prototype see [2]). In addition a high granularity MRPC prototype from Bucharest with electrodes made of low resistive glass delivered from China [3] was tested.

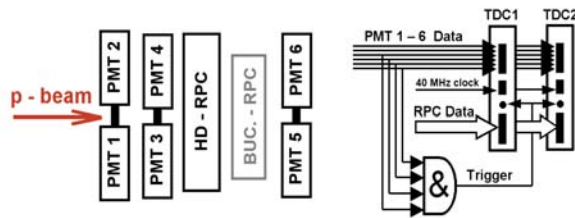


Figure 1: Experimental setup. Left: detector arrangement; right: trigger and data processing.

Figure 1 shows the experimental setup as used in the test experiment. The trigger was formed by coincidence between two plastic scintillators read out by two photomultiplier tubes (PMT) each (PMT 3 - 6 see fig.1 right). An additional pair of PMTs (PMT 1,2) was used for time resolution measurement. All PMTs and the HD-MRPC were connected to customized designed preamplifier cards called PADI [4]. In order to extract the time over threshold information the LVDS signals from PADI output were split and fed into two different TDCs (Caen V1290A). One of them measured the rising edge and the other the falling edge of the signal. Both TDCs were synchronized by a external 40 MHz clock. The time over threshold information of each contributing channel was used to correct the pulse height dependencies (walk) of the measured time difference between the average of the PMT and the RPC times. Additional corrections on the nonlinearities of the TDC were done in order to minimize the electronics time resolution.

Figure 2 displays the time resolution of one strip of the RPC (only two strips were covered by the trigger scintillator) as a function of the applied high voltage (HV) for two thresholds settings at 30 mV and 50 mV including the electronics resolution estimated to be about 30 ps. At the nominal operation voltage (HV = 11.7 kV), the time resolution is in the order of 50 ps, whereas for the higher thresholds

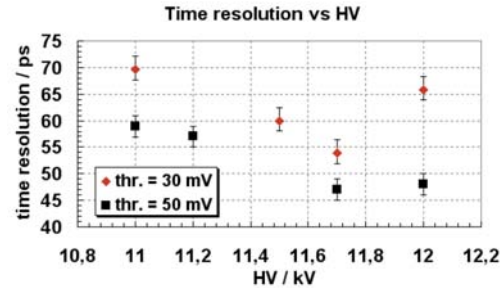


Figure 2: Time resolution as a function of high voltage for different preamplifier thresholds

small signals are not detected, and therefore a better time resolution is obtained as compared to a lower threshold. The efficiency, which is about 93% for $thr. = 30 \text{ mV}$ at nominal operation voltage, drops by 3% for $thr. = 50 \text{ mV}$.

In Figure 3 the average cluster size, i.e. the number of neighboring strips that fire simultaneously, is depicted as a function of the high voltage. The average cluster size depends on the threshold. For both thresholds the dependence on the HV is nearly linear with a similar slope of about 0.46 kV^{-1} . At HV = 11.7 kV, the cluster size reaches values between 1.4 and 1.6.

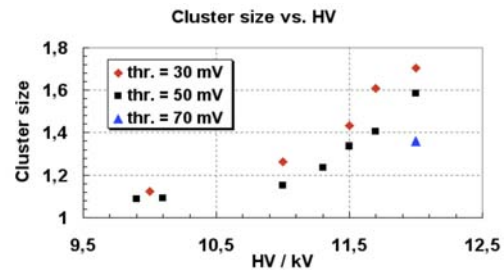


Figure 3: Cluster size as a function of high voltage for different preamplifier thresholds

References

- [1] I. Deppner *et al.*, Nucl. Instrum. Meth. A (2010), doi:10.1016/j.nima.2010.09.165
- [2] I. Deppner *et al.*, CBM Progress Report 2009, Darmstadt 2010, p. 40
- [3] Y. Wang *et al.*, Performance of low-resistivity glass, this report
- [4] M. Ciobanu *et al.*, IEEE NSS, Dresden 2008, 2018

Status of the CBM-TOF readout chain

J. Friihauf¹, N. Herrmann², I. Deppner², P.-A. Loizeau², C. Xiang^{2,3}, K. Wisniewski², M. Ciobanu¹, H. Flemming¹, H. Deppe¹, K. Koch¹, and S. Manz⁴

¹GSI, Darmstadt, Germany; ²Physikalisches Institut, Universität Heidelberg, Germany; ³Institute of Particle Physics, Huazhong Normal University, China; ⁴Kirchhoff-Institut für Physik, Heidelberg, Germany

The current CBM-TOF readout chain consists out of six different modules. A board with two preamplifier and discriminator ASICs [1] (FEET-PADI) with four channels each and a digitizer board with two event-driven TDC ASICs [2] (FEET-GET4) are used as front-end electronic. These ASICs are specially developed for the CBM-ToF detector. An adapter board (R2F-Board) is used as an interface between the readout controller and the front-end cards, and an FPGA based readout controller (ROC) transfers then the data to the data acquisition (DAQ) hosted on a computer. A very precise clock-generator [3] (CLOSY2) provides the two used system frequencies. There is a 250 MHz frequency for the ROC and in addition a phase-coupled 156.25 MHz frequency, which is needed by the TDC. A third signal is send out by the CLOSY2 for synchronization of the two provided clocks and to create epoch markers. A clock distribution is needed to spread out these three signals in a tree. This is realized by a 1:10 splitter for each CLOSY2 signal.

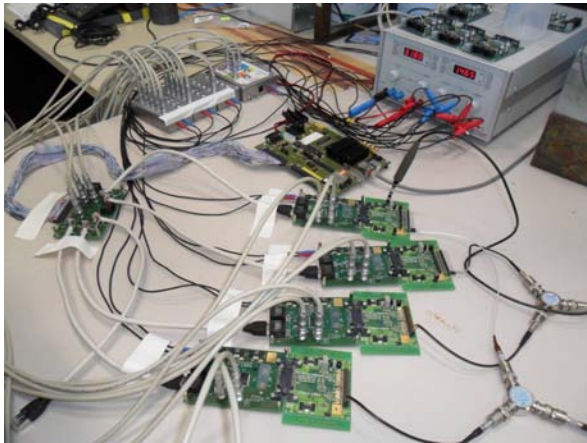


Figure 1: Readout Chain

The test setup in the laboratory is shown in Fig. 1. There are four FEET-PADI directly connected to the FEET-GET4. The same input pulse is used for all 32 channels. The signal is split into four and injected into the parallel input of the FEET-PADI board. There they are getting amplified and discriminated and are afterwards led into the FEET-GET4 to mark each rising and falling edge with a timestamp. With this setup it is possible to measure the time resolution of the complete readout chain. In order to characterize the system, the combined resolution of two

channels is measured when they belong: a) to the same chip (chip-level) b) to 2 chips on the same pcb (pcb-level) and c) to 2 different pcbs (pcb-pcb-level). In Fig. 2 the resolution plot for the chip-level is shown. The results of the different time resolutions obtained by a Gaussian fit are listed in Table 1.

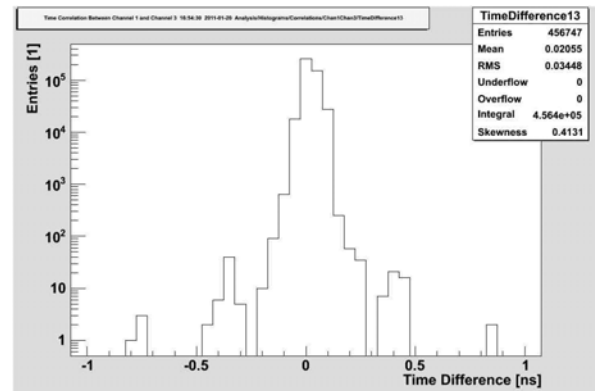


Figure 2: Resolution of the chip-level

Table 1: Resolution of the readout chain

	σ [ps]
chip level	36.94
PCB level	38.94
PCB-PCB level	40.22

This setup was used in a beam time to read out an RPC [4] with 16 strips (32 channels) and a reference system which consists of 8 photomultipliers. Preliminary results of the achieved data as well as the ongoing work on the analyzing tool for this system are presented in [5].

References

- [1] M. Ciobanu *et al.*, IEEE-NSS, Dresden (2008), 2018
- [2] H. Flemming and H. Deppe, IEEE-NSS, Orlando (2009), 1082
- [3] K. Koch, *CBM Progress Report 2009*, Darmstadt 2010, p. 51
- [4] I. Deppner *et al.*, *Performance of a differential CBM-TOF-Demonstrator*, this report
- [5] P.-A. Loizeau *et al.*, *Status of the analysis chain for CBM-TOF demonstrator data*, this report

Status of the analysis chain for CBM-TOF demonstrator data

P.-A. Loizeau¹, N. Herrmann¹, I. Deppner¹, K. Wisniewski¹, C. Xiang^{1,2}, M. Ciobanu³, H. Deppe³, H. Flemming³, J. Frühauf³, K. Koch³, and S. Manz⁴

¹Physikalisches Institut, Universität Heidelberg, Germany; ²Institute of Particle Physics, Huazhong Normal University, China; ³GSI, Darmstadt, Germany; ⁴Kirchhoff-Institut für Physik, Heidelberg, Germany

The CBM experiment will apply for the first time a data driven data acquisition concept for all subsystems. We develop the TOF part of this system and present here the analysis chain of the CBM-TOF demonstrator. Testing is done using self-triggered data acquired last November at COSY, Jülich.

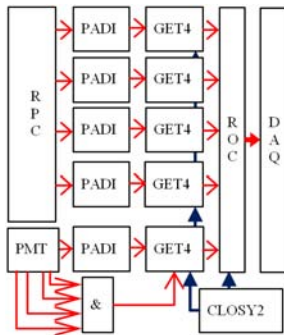


Figure 1: Setup used at COSY in Nov. 2010. RPC = Resistive Plate Chamber, PADI = pre-amplifier, GET4 = time digitizer, ROC = readout controller, CLOS2 = Clock generation, PMT = 4 plastic scintillators read out by 2 photomultipliers each.

The setup used to take the test data is sketched in Fig. 1 and consists of a fully differential, 16-strips MMRPC [1], the full CBM-TOF readout chain [2] and the DABC DAQ. In total 40 channels were connected: 32 for the double-ended detector strips and 8 for the PMTs used as reference system. Additionally, a logic signal of the coincidence of the four main PMTs was fed into the external synchronization input (ExtSync) of one TDC, giving a reference point in the data stream. Three runs were recorded, amounting for 40 GB of data and around 1.5M “events” (ExtSync).

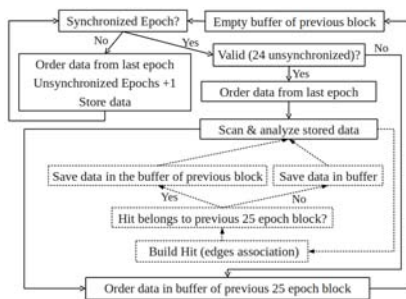


Figure 2: Cleaning and hit building procedure

The analysis procedure on data produced by this setup is organized in three steps: hit building, event building and calibration. The first step is realized inside a GO4 unpacker and consists itself of three operations described in Fig. 2: data are cleaned, reordered and used to build hits. Cleaning the data is required because the ROC transfers all data to the DABC DAQ system. This means that unsynchronized

data are still present, which are useless in a multi-chip environment. Those data messages are also not time ordered because there is a token ring readout system in the digitizer chip. Finally the rising and falling edges provided by the TDC have to be matched to produce full hits with time and Time over Threshold (ToT) information.

The cleaning is done by rejecting chip by chip invalid epochs blocks, i.e. groups of 26.2144 μ s periods called epochs. An epoch block is invalid when the TDC loses its synchronization with the common clock system, which can be checked every 25 epochs. The data messages must be time ordered inside each valid 25 epochs block for each chip, before being able to associate rising and falling edges in hits. As those hits are saved when the falling edge is found but must be ordered by their rising edges for event building, a buffer of two blocks and a second time ordering are necessary. The data are finally saved in a ROOT tree used by the next steps.

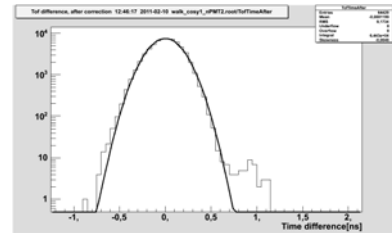


Figure 3: Time difference between reference system and one RPC strip, after partial calibration, with a Gaussian fit

The second step is done in a ROOT macro. Two options are available to build events. (i) A narrow time window is searched for the occurrence of signal coincidences. When one is found, all signals in a wider time window are associated. (ii) The ExtSync is used as reference. The data in a time window around it are put together as event. This speeds up the data analysis. The same macro can be used for both as ExtSync is saved in data as an additional “fake” channel.

The third step is also done by a ROOT macro. The calibration consist of the walk correction on the 4 main PMTs and the 2 RPC channels corresponding to one strip. Figure 3 shows an example obtained with beam test data.

References

- [1] I. Deppner *et al.*, *Performance of a differential CBM-TOF demonstrator*, this report
- [2] J. Frühauf *et al.*, *Status of the CBM-TOF readout chain*, this report

CBM calorimeter located at 1.5 meters from the target

I. Korolko¹, A. Kurepin², A. Maevskaya², M. Prokudin¹, and Yu. Zaitsev¹

¹ITEP, Moscow, Russia; ²INR RAS, Moscow, Russia

We investigated the possibility to use the innermost section of the standard ECAL for photon reconstruction and electron identification with a very first CBM setup at SIS-100. The smaller momenta and multiplicity of produced particles permits the reconstruction in a calorimeter located at only 1.5 m from the target. The total acceptance of the calorimeter was chosen to coincide with the acceptance of the magnet. The size of the calorimeter wall is $2.0 \times 2.5 \text{ m}^2$ with a module size of $12.5 \times 12.5 \text{ cm}^2$. Each module is divided into 25 (5×5) light-isolated cells. A module stack consists of 70 layers of 1.5 mm thick scintillator plates interlaid by 1.0 mm thick tungsten plates. The total thickness of a calorimeter module is 17.5 cm (~ 20 radiation lengths). The number of readout channels (taking into account a hole for the beam pipe) is 7900.

This calorimeter design differs significantly from the one used in the standard CBM setup – it has a constant transverse segmentation and covers a wider angular acceptance. The reconstruction algorithms for such a calorimeter required considerable developments. Cluster finding, calibration and fitting with shower shape library procedures were revisited and improved.

A calorimeter cluster should be large enough to maximize the measured photon (electron) energy fraction; on the other hand, it should be small enough to minimize the energy contamination from neighbour tracks. The new cluster finding procedure consists of the determination of local maxima (hottest calorimeter cell); the determination of the 2×2 cell array (including the hottest cell) with maximum energy deposit; the calculation of its centre of gravity, the construction of an ellipse with centre located at distance r from this centre of gravity and major semi-axis coinciding with the direction from the center of gravity to the calorimeter center, the ellipse semi-axes (a and b) and the distance r being parameters of the algorithm; the computation of the intersection area of the ellipse with all related calorimeter cells; the construction of a pre-cluster consisting of n cells with maximum intersection area; and the definition of a cluster as a set of neighbouring pre-clusters.

The parameters a , b and r were determined by minimization of the signal width for 16 GeV photons entering the ECAL at 25° and 35° impact angles. The best pre-cluster size n depends on the photon impact angle and varies from 4 to 9.

Calibration is necessary for a precise matching of the measured energy deposition to the incoming particle energy. The calorimeter response to photons in a wide range of energies and impact angles was simulated to determine the calibration constants. The dependence of the incoming particle energy on the energy deposition in the scintillators

was fitted with $c_0 \log x + c_1$ and $c_0 \log x + c_1 + c_2 x$ for all incoming angles. The dependence of parameters c_0 , c_1 and c_2 on impact angle was then fitted with a parabola.

The reconstruction algorithms should be able to unfold two neighbour photons hitting the calorimeter in close proximity, which requires the precise knowledge of the shape of the photon energy deposition. There are two different approaches for the shower shape calculation: a shower library or an analytical function [1, 2]. While a shower library has a huge size ($> 50 \text{ Mb}$), an analytical formula does not provide enough precision. We united the two methods by fitting the shower library shapes with a neural network (multilayer perceptron). A similar approach can be used not only for the determination of the average cell response but also for calculation of dispersion and correlation coefficients for the energy deposition in neighbouring calorimeter cells. The latter would allow us to use a more precise χ^2 formula for the cluster fitting procedure.

An implementation of the detector layout and the reconstruction algorithms outline above was used to study the feasibility of a measurement of $J/\psi \rightarrow e^+e^-$ in p+C collisions at 30 GeV beam energy. A background of 10^6 UrQMD events for p+C and J/ψ generated by HSD were transported through the STS and calorimeter setup. Tracks with transverse momentum larger than 1.2 GeV/c were selected as J/ψ daughter candidates. The background was determined by the mixed-event method [3]. Figure 1 shows the resulting invariant-mass spectrum of electron pairs. At an assumed J/ψ multiplicity of $5.12 \cdot 10^{-8}$, about 3,000 signals are reconstructed with a signal-to-background ratio of 0.99 and an efficiency of 15%.

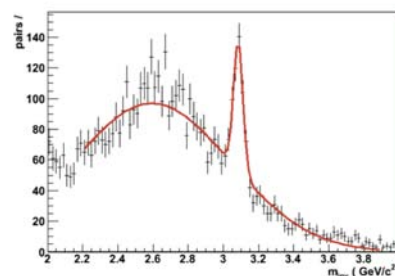


Figure 1: Invariant-mass spectrum of electron pairs after a p_t cut at 1.2 GeV/c on the electrons

References

- [1] F. Berger *et al.*, Nucl. Instrum. Meth. **A 321** (1992) 152
- [2] A. Bazilevsky *et al.*, IEEE Trans. Nucl. Sci. **47** (2000) 1982
- [3] A. B. Kurepin *et al.*, CBM-PHYS-note-2007-001

SC dipole magnet for CBM

E. A. Matyushevskiy, P. G. Akishin, V. S. Alfeev, V. V. Ivanov, and A. I. Malakhov

JINR, Dubna, Russia

The dipole magnet is an essential constituent of the planned CBM experiment [1]. The magnet should host the target, the Micro-Vertex Detector (MVD), and the Silicon Tracking System (STS). It is located in immediate proximity to the RICH detector, where the magnetic field should not exceed 250 Gs. A field integral of 1.0 - 1.1 Tm over a distance of about 1 m is required. The angular acceptance of the magnet should cover 50° in the vertical and 60° in the horizontal direction. The magnet gap must be large enough to permit installation and maintenance of the STS (not less than $1.3 \times 1.3 \text{ m}^2$).

The engineering design of the dipole magnet is presented in Fig. 1. The magnet is supplied with a yoke of magnetically soft steel with low carbon content. The upper and bottom beams form the poles of the magnet. Magnetic shields, reducing the field in the RICH, are installed on the yoke.

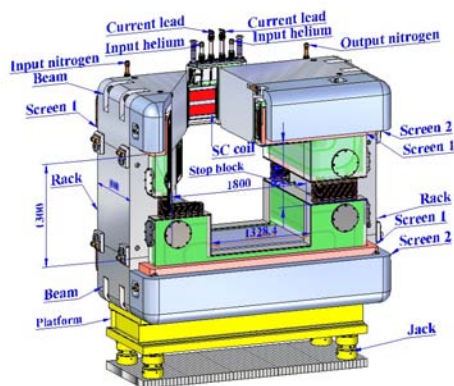


Figure 1: Superconducting dipole magnet

The superconducting (SC) coils have the "Cossack saddle" form, which allows to create a magnet with a minimal size along the beam. The coils are reeled up by a cable with a cross-section of $2 \times 3 \text{ mm}^2$. The cable consists of eight SC wires of 0.5 mm diameter and ten copper wires of 0.75 mm diameter. It is insulated by polyamide film and fibreglass tape. The cross-section ratio of superconductor to copper is 1:6.5. The enhanced copper content in the SC cable allows to overheat the cable up to 35 K at evacuation of the energy stored in the magnet if the SC cable passes to a normal state.

The excitation coils are hosted in the cryostat (Fig. 2) composed of a helium vessel, a nitric screen and a vacuum casing. The helium vessel is fastened in the vacuum casing by supports of fibrous and plastic materials. It is cooled by liquid helium. The thermal flow through the supports (36 pieces) amounts to 3.8 W, the thermal losses through radiation to 0.22 W.

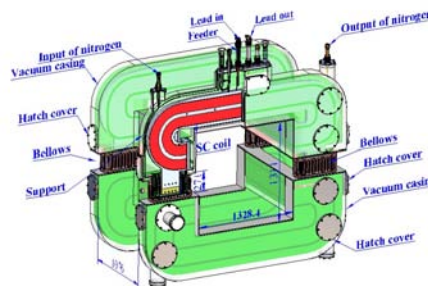


Figure 2: Cryostat of the excitation coils

The nitric screen is cooled down below 70 K. It is fixed on the support of the helium volume. The thermal losses by radiation are 35 W. Inspection plates and hatches of the vacuum casing provide access to the equipment inside. Pump-down of the casing is provided by oil-free vacuum pumps.

The upper cryostat is equipped by a feeder with two current leads (1.5 kA each) for in- and output of the excitation current. The feeder has ports for incoming and outgoing liquid and gaseous helium. The pipelines and the elements of communications going to the helium vessel create thermal losses at the level of 1.8 W [2, 3].

Calculation of the field by the computer codes RADIA and TOSCA showed that a current of 1.0 kA creates a field of 1.15 T. The field distribution along the z axis is presented in Fig. 3. The field does not exceed 250 Gs in the photo-detector plane of the RICH [3, 4].

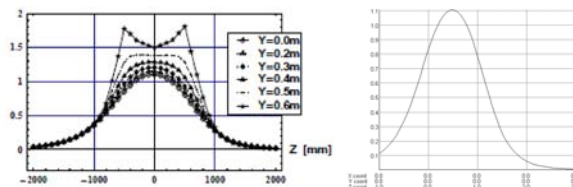


Figure 3: Left: $|B|$ along the beam axis calculated with RADIA. Right: B_y along the beam axis calculated with TOSCA.

References

- [1] *CBM Experiment - Technical Status Report*, Darmstadt 2006
- [2] E. Litvinenko, *Dipole magnet for CBM*, CBM collaboration meeting, October 2008, Dubna
- [3] E. Matyushevskiy, *Superconducting dipole magnet for CBM*, CBM collaboration meeting, October 2009, Split
- [4] A. Malakhov, *CBM superconducting dipole magnet*, CBM collaboration meeting, April 2010, Darmstadt

Design justification of the STS section of the CBM beam pipe

S. Belogurov, A. Chernogorov, and A. Semennikov

ITEP, Moscow, Russia

The tracking setup of the CBM experiment consists of two principal subsystems: the micro-vertex detector (MVD) and the silicon tracking system (STS). The MVD is placed in the same vacuum volume as the target. The boundary of the vacuum volume has two parts crossed by an appreciable flux of the measurable particles, namely the window and the first section of the beam pipe connected through welding.

The beam pipe serves for the transport of the ion beam, scattered in the target without nuclear interactions, to the beam dump. The acceptable probability of an ion interaction with the beam pipe walls is not more than 10^{-4} .

It is important for the physical performance of the tracking system to minimize the number of secondaries produced by the measurable particles and their deflection in the pipe and window. For this reason the amount of the material in these elements should be minimized, and their shape and position should be optimized.

A figure of merit for vacuum chamber materials can be established from the elastic modulus E and the radiation length X_0 [1, 2]. For the case of a chamber under external pressure, this has been shown to be $X_0 E^{1/3}$. Beryllium is the best material by this criterion and is used in the most critical parts of the beam pipes of many experiments (LHCb Atlas, CMS, Alice, Belle, CDF, etc.). As a backup option, aluminium with stiffening pattern is considered.

The best shape of the beam pipe is a trade-off between minimum interference with measurable particles and low probability of ion interactions with walls. Several levels of analysis were performed for the optimization of the beam pipe shape, taking into account

- the integrated range (IR) of all the charged particles from one central UrQMD event in the bulk of the beam pipe wall $IR = \sum l_i \cdot q_i^2 \cdot n_e$, where l_i is the range of i -th particle, q_i its charge and n_e the electron concentration in the medium. This value is proportional to the total ionization losses in the material of the beam pipe;
- the number of hits per central event in the STS stations. This value allows to check effects of the position of welds and bellows position w.r.t. the STS stations;
- the momentum-dependent reconstruction efficiency for primary and secondary tracks, the number and momentum distribution of ghost tracks and the processing time per event;
- the parameters of reconstructed particles, e.g. $\Lambda \rightarrow p\pi^-$ and $K_s^0 \rightarrow \pi^+\pi^-$.

It was found that at each level of the analysis, the best configuration of the beam pipe is a narrow cylindrical tube connected to a thin spherical window. An important difference with respect to the results reported in e.g. [3] is that a cylindrical tube is better than a conical one. This is due to the presence of the magnetic field. Without a field, the best solution is a cone.

On the other hand, the ion beam downstream the target has a certain size and angular divergence. The beam pipe should be sufficiently wide for letting most of ions pass through without interactions. The relevant parameters are the beam emittance, the bending of the beam in the magnetic field and multiple scattering of beam particles in the target. The expected beam emittance at SIS-300 is 0.8 mm-mrad horizontal and 0.27 mm-mrad vertical. The tails of the spatial distribution can be reduced if a system of collimators is employed. For 8A GeV/c gold ion scattered in the 0.25 mm thick gold target, only $4.5 \cdot 10^{-5}$ ions are outside the angle of 1° . The maximum bending of the beam particles in the magnetic field will be observed at the minimum extraction rigidity. In this case the angle after the passage of 1 Tm field is 0.9° .

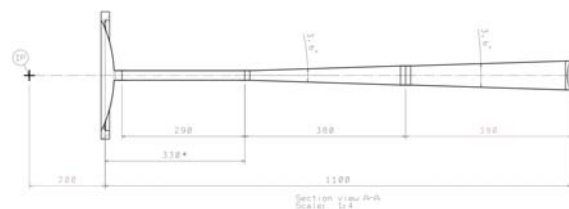


Figure 1: Tentative design of the STS beam pipe

On the basis of MC simulations, a shape composed of a spherical window, a cylindrical tube, and a cone was chosen. The dimensions of segments and welds were implemented according to the technical feasibility at JSC Kompozit, Moscow Region. The structure was subjected to mechanical analysis, and some parameters were iterated. The tentative design of the beam pipe is shown in Fig. 1. If the wide end of the beam pipe is supported, the safety factor against buckling is more than 4 for both the spherical window and the tube part.

References

- [1] C. Hauviller, *Design of Vacuum Chambers for Experimental Regions of Colliding Beam Machines*, Particle Accelerator Conference, Washington DC, May 1993
- [2] R. Veness *et al.*, *Vacuum* **64** (2002) 467
- [3] The LHCb collaboration, *Beam pipe portrait*, CERN-Poster-2008-050

A First-level Event Selector for the CBM experiment

J. de Cuveland and V. Lindenstruth

FIAS Frankfurt Institute for Advanced Studies, Goethe-Universität, Frankfurt am Main, Germany

The First-level Event Selector (FLES) is the central physics selection system in CBM. It receives all hits and performs online event selection on the 1 TByte/s input data stream. The event selection process requires high-throughput event building and full event reconstruction using fast, vectorized track reconstruction algorithms. The current FLES architecture foresees a scalable supercomputer. To achieve the high throughput and computation efficiency, all available computing devices will have to be used, in particular FPGAs at the first stage of the system and heterogeneous many-core architectures such as GPUs for efficient track reconstruction. A high-throughput network infrastructure and flow control in the system are other key aspects.

The FLES system will contain approximately 1000 input nodes with fast PCIe interfaces receiving data from the detector at a total rate of 1 TByte/s. Online event analysis will be performed by processing nodes estimated to require in total approximately 60000 cores. A high-throughput network infrastructure will connect all nodes and enables interval building at the full input data rate. The FLES architecture is summarized in Fig. 1.

The interface between the custom data acquisition network and the FLES PC farm is implemented as an add-on card to the host PC (see Fig. 2). This add-on card has to feature high-bandwidth links both from the readout electronics to the host PC and a large and high-bandwidth buffer memory. The current baseline assumption is to use a custom FPGA-based add-on card with a PCIe interface at the maximum achievable PCIe data rate. The FPGA design implements the data acquisition protocol for receiving data, merges input links, performs memory management and controls the PCIe transfer. To allow for efficient time-indexed data access, it additionally analyzes the incoming data's time stamp information and builds corresponding look-up tables.

While there are CBM running scenarios that require full event building prior to selection, other selection scenarios are feasible with a reduced load on the event building network. This is especially important during the early building phases of the experiment. Therefore, the FLES implements

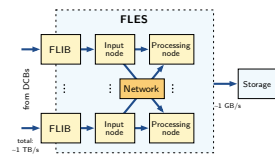


Figure 1: Architecture of the FLES

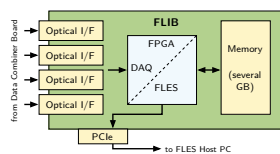


Figure 2: The FLES interface board (FLIB)

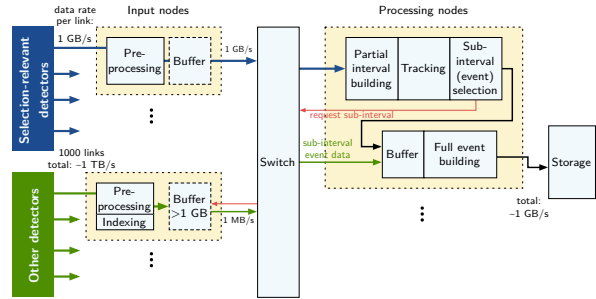


Figure 3: Data flow in the First-level Event Selector

a two-staged event building and event selection scheme. The main data flow in the FLES is illustrated in Fig. 3. Data from all detectors that contribute to the initial stage of event selection are forwarded to the interval-building network between input nodes and processing nodes. The goal here is to concentrate data that have a similar time stamp from all detector links in a single processing node. For that reason, the input nodes package all input data corresponding to fixed time intervals (containing, e. g., 1000 events). Each processing node receives data for a different time interval. This interval building corresponds to the event building process commonly used in other experiments. To optimize for maximum throughput, several routing concepts are currently under investigation. Using a network technology such as InfiniBand QDR, FLES implements high-throughput event building at the full data rate of 1 TByte/s.

For each time interval, the associated processing node performs the required feature extraction and online analysis. At an average event rate of 10 MHz, discarding all events that cannot be cleanly separated in time would result in a considerably reduced efficiency. To avoid this, the track reconstruction algorithm applied by the processing node directly matches tracks not only in the three spatial dimensions, but also in time as an additional dimension. After interesting events have been identified, the two-staged event building process allows the processing node to request a corresponding sub-interval from additional detectors not participating in the initial interval building. The challenge in online event reconstruction is the high event rate of 10 MHz in combination with non-trivial trigger criteria requiring partial or full event reconstruction. To fully exploit the hardware potential of heterogeneous many-core systems, reconstruction codes have to be rewritten with respect to efficient parallel processing. To efficiently utilize resources, the FLES building network is also used as an interface to the mass storage system.

Demonstrator beam time results for the clock distribution and synchronization of the CBM-DAQ system

F. Lemke, S. Schenk and U. Bruening

University of Heidelberg, Mannheim, Germany

Because of new requirements for the DAQ system, the previously planned hierarchical CBM network structure using Read-Out Controllers (ROC) for detector readout, Data Combiner Boards (DCB) for data combining and Active Buffer Boards (ABB) for data buffering and First Level Event Selection (FLES) attachment was extended. The usage of a unified link for three different data types such as Data Transport Messages (DTM), Detector Control Messages (DCM), and Deterministic Latency Messages (DLM) and the communication principles and packet structures will not be changed, because it has proven its reliability [1, 2]. But new detector readout chips and high-level data flow handling concepts generated new feature requests. Therefore, a new CBMnet V2.0 was designed and will be implemented supporting lane handling with different bandwidth in up- and down-link direction, large messages, an adapted data loss strategy in cases of overloads, easy meta data detection, and a fully reliable communication for data streams. The new planned CBM network structure using the CBMnet V2.0 is shown in Fig. 1. The detector readout ASICs can now be connected to the CBM network via a HUB ASIC which provides data aggregation and rate conversion and drives the opto-converter boards. Within the inner network part, the DCB was replaced by a Data Processing Board (DPB), which serves also as a bridge to the Experiment Central System (ECS). The back-end part using ABBs attached to FLES within computing clusters will stay the same. For the HUB ASIC chip and the opto-converter, the analysis and conception has already started; its implementations will be major parts within future work packages.

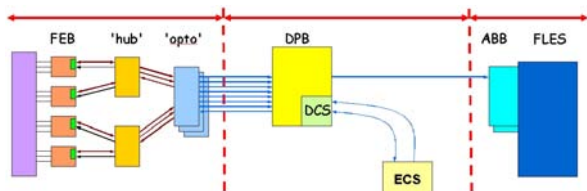


Figure 1: The planned CBM network structure

For the proof of concept and to enable the readout over optics for the detectors used during beam time, a readout chain consisting of the previously developed prototypes was created. The demonstrator build-up used during the beam time tests in December 2010 is presented in Fig. 2. It shows the two DCBs used as DPB prototypes. They were connected to an ABB that served as emulation for

the ECS providing the clock and a system synchronization with DLMs via the CBM protocol V1. Both DCBs have four bidirectional connections to the front-end for attachment of four ROCs using the unified CBM protocol for synchronization and data acquisition. The received data is combined to a single data stream within the DCBs and sent to an ABB plugged into a workstation running the current version of the DABC software for data collection. During the complete COSY test beam time from 13th to 19th December, the optical readout demonstrator was used. The data acquisition ran problem-free. The ECS emulation providing the control system and the clock distribution was reliable. The network synchronization worked without errors and delivered the targeted bit-clock synchronization, so that a synchronization with less than 400 ps was guaranteed. The concept of using the unified link providing DLMs for synchronization has now shown its valuable improvement for future detector system solutions.



Figure 2: DCBs used in the demonstrator build-up

References

- [1] F. Lemke, S. Manz and W. Goa, *Time synchronization and measurements of a hierarchical DAQ network*, Spring meeting of the Deutsche Physikalische Gesellschaft, Bonn, Germany, March 15-19, 2010
- [2] F. Lemke et al., *A Unified DAQ Interconnection Network with Precise Time Synchronization*, IEEE Trans. Nucl. Sci. **57**, No. 2 (2010)

DABC data acquisition input for slow control variables

J. Adamczewski-Musch, B. W. Kolb, and S. Linev

GSI, Darmstadt, Germany

The Data Acquisition Backbone Core (DABC) is a software framework to run DAQ with distributed event building on high performance Linux clusters [1]. There are several use cases, especially in test beam times where the setup during data taking is intentionally changed very often, and the interpretation of the acquired detector data depends on the experimental set-up. Usually, the set-up is managed by a slow control system like EPICS [2], which has powerful tools to archive the set-up values. For online analysis, however, a direct access to such values in the DAQ data stream can be very useful, e.g. for a conditional analysis depending on certain settings. Moreover, it is possible to perform a fast scan of detector properties with the control system and record simultaneously the measured data in the same file. Because of this an EPICS data input for DABC was developed.

DABC data input for EPICS

The DABC framework has plug-in interfaces to attach any kind of data sources to the DAQ [3]. Such data-input interface was implemented as Epics-input plug-in for reading a set of slow control process variables from an EPICS IOC server. This implementation is based on the existing Easy Channel Access (ezca) extension library [4], featuring basic C functions to request named variables from any EPICS IOC.

This DABC ezca-plugin can be configured by XML file which contains the names of the process variables to be fetched. Currently an expandable set of integer or double values can be treated, other EPICS records may be implemented in future versions. One special EPICS record defines a "flag" variable which is polled by DABC with a configurable repetition time, e.g. 100ms. Only if this flag variable shows a specific value, e.g. 0, the complete set of the defined records is acquired from the IOC. Thus by setting this variable, the IOC can decide the refresh rate of the data recorded to the DAQ stream. This can be done by an EPICS timer, or when a change of the set-up is significant for the DAQ.

The ezca::DataInput instance puts each acquired set of EPICS process variables into an MBS event/subevent structure. The order of the EPICS records in the subevent data field is currently defined by the order of records in the DABC configuration file. Additionally, the MBS event identifiers can be specified in the DABC set up.

The processing DABC module, connected to the ezca::DataInput transport, may combine this EPICS subevent with MBS subevents of the DAQ data stream from other data sources, e.g. an external MBS system, or the CBM readout controller (ROC). Since the EPICS data rate

is much lower than the usual DAQ data rate, synchronization between EPICS records and the other event data can be done in the subsequent analysis software by means of the system time stamp which is recorded in the ezca subevent payload, and should be also available in the subevents of other data sources.

Application for the CBM test beam at COSY

A CBM test beamtime was performed at COSY in December 2010 [5]. The set-up of detector voltages and motor positions was controlled by one EPICS IOC. The DABC DAQ was configured with the ezca plug-in such that all variables of the IOC were recorded with the full data stream every 10 s. Thus it was possible in the attached Go4 online monitoring analysis [6] to visualize these EPICS variables together with the detector display: for instance, the motor controlled positions of the GEM detectors were shown; also the settings of a beam enclosing "ROLU" scintillator frame.

During the voltage scan of the STS detectors, the recorded EPICS data allow to directly correlate the detector signals with the settings in the final analysis.

Besides the EPICS data, the DABC data stream also contained a "spill-on/spill-off" message from a signal directly fed into the ROCs by a beam trigger sensor. This allowed an automatic baseline calibration of the ROCs in the Go4 online analysis whenever the synchrotron beam was paused. Although the mechanism of getting the set-up state was different here, the principle of a conditional analysis steered by slow control variables within the DAQ data stream would be the same for the EPICS records.

References

- [1] J. Adamczewski-Musch *et al.*, *Data Flow Engine in DAQ Backbone DAB*, IEEE Trans. Nucl. Sci. **57**, No.2 (2010), p. 614
- [2] <http://www.aps.anl.gov/epics/>
- [3] J. Adamczewski-Musch, H. G. Essel and S. Linev, *The DABC Framework Interface to Readout Hardware*, Proceedings of the 17th IEEE Real-Time Conference, Lisboa 2010, to be published in IEEE Trans. Nucl. Sci.
- [4] <http://www.aps.anl.gov/epics/extensions/ezca>
- [5] J. M. Heuser *et al.*, *Test of prototype modules of the CBM Silicon Tracking System in a proton beam at COSY*, this report
- [6] <http://go4.gsi.de>

Radiation tolerance of the Universal Read Out Controller

N. Abel, H. Engel, J. Gebelein, D. Gottschalk, S. Manz, A. Oancea, and U. Kebschull

Kirchhoff Institute of Physics, Heidelberg University, Heidelberg, Germany

Since 2007 our contribution focused on the Silicon Tracker's FEE (Front End Electronic), consisting of the nXYTER, an ADC (Analog Digital Converter) and a ROC (Read Out Controller). Since 2009 we are also designing and implementing readout logic for the GET4 chip [1] and the TRD FEE. To keep the re-usability as high as possible, we split the ROC into two fully independent modules: the readout logic and the transport logic. This modularization of the Read Out Controller and the consequential separation of the control software into different layers, enabled us to provide a Universal ROC, which offers quick access to a long-run tested transport logic and allows us to easily add a new readout logic for further FEE setups [2].

Radiation Tolerance

The heart of the Universal ROC is an SRAM based FPGA, since FPGAs provide the best combination of performance and long-term flexibility. However, there is a crucial problem regarding FPGAs: the radiation which is inevitable in high energy physics experiments can cause the FPGA's doped silicon to change its electrical properties, depending on its Linear Energy Transfer (LET). This physical separation of electron-hole pairs results in spontaneous Single Event Effects (SEE) as well as long-term Total Ionizing Dose (TID) cumulation within the material. SEEs, especially Single Event Upsets (SEU) and Single Event Transients (SET), show up as permanent, but non-destructive binary bit flips within logic memory or as short glitches on the routing network. This becomes extremely critical for latches or flip-flops at clock signal setup/hold times. TID effects are not that critical for short-term applications, but preponderantly problematic for long-term considerations. They increase the number of stuck charges resulting of the electron-hole pair separation, leading to modification of the chips doped semiconductor properties. Overall, hardware failures may occur in nonrelevant circuits or may lead to spontaneous unexpected system behavior, but most critical they can lead to a total system halt, known as Single Event Functional Interrupt (SEFI) [3].

According to this problem, very specialized shielded radiation hard materials have been and currently are developed for military and space grade FPGAs, realized within the Xilinx Virtex QPro II, 4 and 5 series, complemented by a configuration refresh feature called "scrubbing". As some of these chips are not available for commercial applications due to military export restrictions, common devices are provided with special TID mitigation techniques and SEE failsafe combinations of logic blocks. Basically, such

ambitions in securing the logical hardware design layer can be realized by three different approaches: spatial redundancy, temporal redundancy and various combinations of both. Spatial redundancy features synchronous data sampling of combinational logic at multiple routes to mitigate SEUs. The addition of adjacent voters is required to analyze processed data values. Well known candidates using this principle are Dual and Triple Modular Redundancy (DMR/TMR), mostly accompanied by Error Detection and Correction Codes (EDAC). Temporal redundancy enables a single combinational logic circuit to be sampled at multiple times. Additional voter circuitry compares all of the results and decides whether an error occurred or not. The combination of both spatial and temporal redundancy leads to SEU and SET immunity.

Conclusions

The usability of FPGAs in radiation environments highly depends on the usage of mitigation technologies such as scrubbing, spatial or temporal redundancy. This has a strong influence on the board design as well as on the FPGA design: the Universal ROC is implemented on a board (namely the SysCore Board) which provides an external FLASH memory and an additional radiation hard flash-based FPGA which are required to realize the scrubbing technology [4]. Furthermore the modules (transport logic as well as readout logic) are using a combination of spatial and temporal redundancy. The implemented architecture layers and methods have been practically tested under experimental conditions within different particle accelerator beams. The Universal ROC had been directly placed into the center of the particle beam line to get comprehensible results at a maximum ionization impact. These tests will be continued in 2011 and will be used to develop a radiation tolerant Universal ROC.

References

- [1] S. Manz, *GET4 readout chain*, CBM Collaboration Meeting, 2009, Split, Croatia
- [2] N. Abel *et al.*, *CBM Progress Report 2009*, Darmstadt 2010, p. 53
- [3] J. Gebelein *et al.*, *FPGA Fault Tolerance in Particle Physics Experiments*, Information Technology 52 (2010) Heft 4 Schwerpunktthema, Oldenbourg Wissenschaftsverlag
- [4] D. Gottschalk, *Concept and Status of the SysCore 3 Board*, CBM FEE/DAQ Workshop 2010, Frankfurt, Germany

Design and implementation of an object-oriented framework for dynamic partial reconfiguration

N. Abel, A. Beyer, F. Grüll, N. Meier, and U. Kebschull

Kirchhoff Institute of Physics, Heidelberg University, Heidelberg, Germany

Nowadays, two innovative future trends regarding embedded hardware development and hardware description can be found. The first trend concerns the hardware itself. Modern FPGAs (Field Programmable Gate Arrays) provide the possibility that parts of the configuration can be exchanged while the rest of the circuit is running untouched – which is called dynamic partial reconfiguration (DPR).

The second trend concerns the way hardware is described. Currently, the most important hardware description languages (HDLs) are VHDL and Verilog. Although they allow to describe hardware on a very high level, the developer still has to handle registers, clocks and clock domains. Using an HDL operating on the algorithmic level, this is not necessary any longer – the corresponding synthesis process is called high level synthesis (HLS).

Although both, DPR and HLS are very important future trends regarding hardware design, they develop rather independently. Most of today's software-to-hardware compilers focus on conventional hardware and therefore have to remove dynamic aspects, such as the instantiation of calculating modules at runtime. On the other hand, DPR tools work on the lowest possible layer regarding FPGAs: the bitfile level. Thus, currently the use of DPR leads to a struggle with architectural details of the FPGAs and the corresponding synthesis and implementation tools.

Our workgroup focuses on a combination of DPR and HLS, since DPR can change the programming paradigm in future HDLs with regard to dynamic instantiations. Dynamic aspects would not be a problem any longer, but could be realized on the target FPGA using DPR. Beyond that, a high level language support of DPR could help it to become a commonly used method. The aim of our work is to find a solution how HDLs on algorithmic level and DPR can

be combined, solely using language constructs which are already well-known to software-developers.

As a first step, the typical structure and behavior of reconfigurable hardware has been analyzed. Thereby it turned out that the best way to describe such hardware is to make use of the object-oriented paradigm combined with multi-threading. In consequence, an enriched subset of Java, forcing the programmer to make use of multiple objects running in parallel, has been defined: POL (Parallel Object Language).

The specification of POL comes with a set of requirements. The most challenging part is the high degree of flexibility regarding object instantiation and inter-object communication. POL allows the user to instantiate and to destroy objects as well as to establish and to dissolve their connection at *any* position in the code. Beyond that, POL allows an overmapping of the FPGA.

In order to enable the evaluation of the possibilities and limitations of POL, a development framework has been implemented. This framework includes an emulator which allows the execution of POL in software [1], a compiler which is responsible for the translation from POL to VHDL [2], a so called Communication Matrix which serves as fast and flexible communication structure on the FPGA [3], and a scheduler (running on an embedded processor) that decides which hardware module is loaded (Fig. 1).

For performance analysis, an audio filter has been implemented. It shows that overmapping can be used in environments with a data rate of $\sim 100\,000$ samples/s, while scenario-based scheduling algorithms can be used in streaming applications with data rates of $\sim 100\,000\,000$ samples/s. These maximum data rates are solely possible due to the usage of object-orientation in POL and the corresponding optimizations of the reconfiguration times [4].

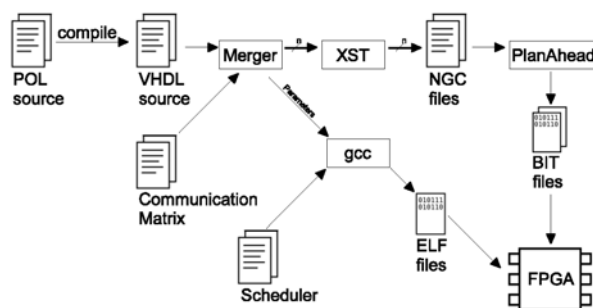


Figure 1: The implementation toolflow of the framework

References

- [1] A. Beyer, *Development of an Emulator for the execution of POL-Code inside a Java-Environment*, bachelor thesis, University of Heidelberg, Germany, 2008
- [2] F. Grüll, *The Parallel Object Language*, diploma thesis, University of Heidelberg, Germany, 2009
- [3] N. Meier, *Development of a Framework for Dynamic Partial Reconfiguration serving the Object Oriented Hardware Programming Language POL*, diploma thesis, University of Heidelberg, Germany, 2008
- [4] N. Abel, *Design and Implementation of an Object-Oriented Framework for Dynamic Partial Reconfiguration*, PhD thesis, University of Heidelberg, Germany

DABC as data acquisition framework for CBM

S. Linev, J. Adamczewski-Musch, and J. Friühauf

GSI, Darmstadt, Germany

Optical transport for ROC

For development of the different software components for the CBM readout controller (ROC) [1], the Data Acquisition Backbone Core (DABC) [2] was used. The ROC board was primarily developed to read out data from nXYTER-based frontends. With a new FPGA firmware the readout of GET4/FEET frontends is also possible [3]. In addition to the existing Ethernet based data transport, an optical fibre data transport via a special PCIe board (AVNET) was implemented to the ROC software and tested. The optical protocol [4] was designed to transport data, control and clock information over the same media. Data rates up to 200 MB/s can be achieved here. Additionally, the optical connections allow clock synchronization between many ROCs. Usage of the optic transport in ROCLib is absolutely transparent and does not require any changes in user software compared to the Ethernet case.

Synchronisation with MBS

The ROC produces a time-stamped data flow and does not require external triggers for signal measurements. On the other hand, there is a lot of existing hardware, useful for different detector tests, which is read with trigger-based MBS DAQ. To synchronize the data taken by MBS with the data taken by ROC, a special SYNC-sender module was developed based on the VULOM board. This module sends a SYNC message to all ROCs every time the MBS trigger is produced. A DABC software module was implemented to search for such SYNC messages in the ROC data, and to associate subsequent data messages with the corresponding MBS trigger. The data combined together by such software can be analyzed in a Go4 analysis.

SPADIC readout

The SPADIC is a prototype chip for TRD readout, developed in Uni Heidelberg [5]. It allows to read out detector signal shapes with external trigger. Trigger signal input is compatible with ROC SYNC message, therefore MBS with a SYNC-sender module can be used as a trigger producer for SPADIC. Based on a library for USB readout of SPADIC [5], a DABC plugin was developed to acquire SPADIC data with DABC; this plugin was integrated into ROCLib. Data from SPADIC are represented as MBS events. These can be combined together with ROC and MBS data, synchronized by the SYNC message number.

TRD/RICH/STS beamtime at CERN In this beamtime in November 2010, 4 different TRD prototypes were read out: two with MBS, another two with DABC with 6 SPADICs. In addition, one STS station and a RICH setup were read out with 3 ROCs. A DABC application was implemented to combine data from all these inputs together.

STS/GEM beamtime at COSY Figure 1 shows the DAQ setup of the COSY beamtime in December 2010: all 8 ROCs were optically connected via special Data Combiner Boards (DCB) to the AVNET PCIe board, read out by the DABC application. An additional connection for each DCB provides a clock distribution. Thus all ROC clocks were running synchronously. An MBS system was used to read out beam monitor scintillators; synchronization with ROC data was done via a SYNC sender module.

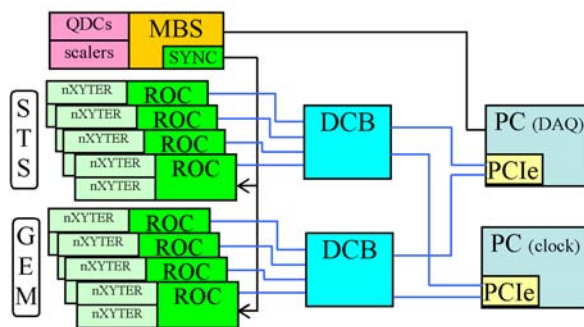


Figure 1: COSY beamtime setup

Status and outlook

Current software shows good stability and robustness in all beam tests performed up to now. Further developments are planned for closer integration of the DAQ with the experiment control system EPICS.

References

- [1] S. Linev, J. Adamczewski-Musch and H. G. Essel, *CBM Progress Report 2009*, Darmstadt 2010, p. 56
- [2] J. Adamczewski *et al.*, *Data Acquisition Backbone Core DABC*, IEEE Trans. Nucl. Sci. **55**, No.1 (2008) 251
- [3] S. Manz and U. Kebschull, *CBM Progress Report 2009*, Darmstadt 2010, p. 52
- [4] F. Lemke, S. Schenk and U. Bruening, *CBM Progress Report 2009*, Darmstadt 2010, p. 54
- [5] T. Armbruster, <http://www.spadic.uni-hd.de>

Memory kernel development of the Active Buffer

A. Wurz, W. Gao, A. Kugel, and A. Männer

Informatik V, ZITI, University of Heidelberg, Germany

Originally the Active Buffer Board (ABB) for the CBM experiment used an elasticity buffer based on the internal RAM blocks of the Xilinx FPGA, limiting the size to 128 kB. To increase the size of the buffer we completed in 2010 the large-size DDR2 SDRAM FIFO project on the AVNET Virtex5 board [1]. An additional data count module was added and verified. The buffer has been used during last beam tests and worked properly.

Block diagram

We use a 64-bit DDR2 SDRAM module of 256 MB as kernel memory. Figure 1 shows the block diagram of the large-size FIFO. The DDR2 SDRAM module is outside the FPGA. Inside the FPGA we use two smaller built-in FIFOs, 4KB each, as the interface module, which qualifies the entire FIFO to behave as a standard FIFO.

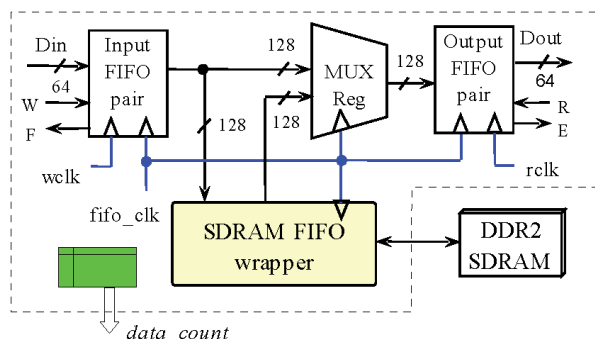


Figure 1: Large-size FIFO block diagram

Development notes

1) Data into and out of the SDRAM module are aligned to the row boundary, to have a better and simplified management over the SDRAM module. Only when the data amount in the small input FIFO block reaches a row size of the DDR2 SDRAM, is the data transfer into the FIFO wrapper executed. And on the other side, only after the output FIFO is able to accommodate a row-size data, is the data directed from the SDRAM to the output FIFO. The advantage lies in minimized row-open and row-close operation for the SDRAM module.

2) Internal data run in double-width data bus, i.e. 128 bit bus, which suffices the possibly full data rate, even if the SDRAM overhead, such as auto refresh and row recharge, have to be taken into account.

3) The PAD delays are variable and calibratable, so that the design has a general application scope to variety

of boards. On the Xilinx Virtex5 LX110T FPGA board, IODELAY is used with variable delay value adjustment.

4) The clock frequency for the SDRAM module is some percent higher than the external FIFO clock frequency, to compensate the SDRAM operation overhead such as refresh, recharge. In the ABB2 system, we use 166 MHz as the the kernel clock rate and accordingly, the PCIe DMA fabric logic clock rate is 125 MHz.

5) The data count must be additionally built. Data count is for DMA read logic to determine when to issue the request and for software to know how many data are ready in the Active Buffer.

Test and verification

Timing performance can go easily to over 125 MHz for Virtex5 FPGA with speed grade -1. The numbers of flip-flops and (4-input) look-up-tables used for this FIFO wrapper are both under 1000 and the number of 18Kb RAM blocks is 4. For the adjusting of data bus arrival of the SDRAM module, 4 IDELAYCTRLs are used. Simulation and real test work very well. Additionally we make a stand-alone test design intensely targeting the FIFO behavior. In a long and sustained test with manual button presses, the FIFO behaves very well in terms of performance and stability. The peak bandwidth goes to $125\text{MHz} \times 2 \times 32\text{bit} = 8\text{ Gbps}$ in the system. Figure 2 is an example snapshot from ChipScope analyzer.

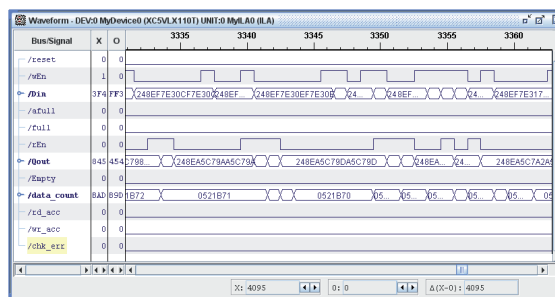


Figure 2: DDR2 SDRAM FIFO behavior

The newer version logic of PCIe DMA integrated with this large-size FIFO works well in system and is verified in the COSY beam test at FZ Jülich in December 2010.

References

[1] W. Gao *et al.*, *CBM Progress Report 2008*, Darmstadt 2009, p. 58

A SIMD implementation of the Deterministic Annealing Filter for the CBM experiment

R. Frühwirth¹, H. Gjersdal², I. Kisel³, A. Strandlie^{2,4}, and M. Zyzak^{5,6}

¹HEPHY, Austria; ²University of Oslo, Norway; ³GSI, Darmstadt, Germany; ⁴Gjøvik University College, Norway;
⁵Goethe University, Frankfurt, Germany; ⁶University of Kyiv, Ukraine

The main challenge of the CBM experiment is an extremely high track density. This leads to overlapping of the hits and the distortion of their position. In order to reduce an influence of the attached distorted or noise hits on the reconstructed track parameters the Deterministic Annealing Filter (DAF) [1] is under development within the Kalman filter (KF) package.

The idea of DAF is to introduce “temperature” depending weight to each hit and perform several filtration iterations gradually “cooling” the system. With “cooling” weights for noise hits are gradually decreasing to zero, while for true hits they are remaining high. After the first pass of the Kalman filter based smoother with equal weights the track position is predicted at every layer of the detector. Based on these predictions the probability, that a hit belongs to the track, and the weight of a hit are calculated. Decreasing the temperature the influence of noise hits is suppressed with each next iteration. On each iteration weights are recalculated using smoothed track parameters from the previous iteration.

Most modern CPUs has SIMD units, which currently can give speedup of factor 4 for single-precision floating-point calculations. In the nearest future speedups of 8 and 16 will be available. Therefore in order to utilize the whole potential of CPU the implementation of DAF should be based on the SIMD instruction set.

Currently the DAF implementation is based on the SIMD KF track fitter [2]. The Kalman filter mathematics has been modified in order to include weights of hits. Since DAF needs smoothed track parameters, the KF based smoother has been added to the KF package. The smoother is implemented as two Kalman filters processing in opposite directions: forward and backward. Parameters and covariance matrices of the track, that are calculated by these filters, are merged at the hit position. During the iteration in DAF the same hit weights are used both for the forward and backward filters. Weights are calculated by:

$$p = \frac{1}{1 + \exp((\chi^2 - \chi_{\text{cut}}^2)/(2T))},$$

where p is a weight of the hit on the station; T — “temperature” of the current iteration, the values of $T = 9, 4, 1$ and 0.1 are used in the algorithm; χ^2 is a squared distance between the hit and a smoothed track position normalized on the hit and track parameters errors; χ_{cut}^2 is a threshold, which determines the region, where the hit is accepted (the value of $\chi_{\text{cut}} = 4$ has been used, that provides the probability of 99,995% to attach a correct hit for the normal distribution).

Tests for time and fit quality of the algorithm have been performed on the Ixir039 computer with 2 Xeon X5550 processors at 2.7 GHz and 8 MB L3 cache, one core has been used. A setup of 2 stations of the Micro-Vertex Detector (MVD) and 8 stations of the Silicon Tracking System (STS) has been used. For tests 20000 long reference primary tracks, reconstructed with the CA track finder, have been used. The tracks could have on average up to 0.5% incorrectly attached hits.

To test the algorithm the hit on the 4th STS station has been displaced by a certain amount of the hit error ($\sigma_{\text{hit}} = 17 \mu\text{m}$) along the X direction from the Monte-Carlo position. The percentage of rejected hits has been calculated on all stations of the detectors. The obtained results are given in Table . As one can see, the current implementation gives good noise hits rejection for distant hits. The execution time of DAF is 14 μs per track.

Table 1: Percentage of rejected hits depending on the distance from the shifted hit on the 4th STS station to its Monte-Carlo position

Hit displacement	unshifted	$5 \sigma_{\text{hit}}$	$10 \sigma_{\text{hit}}$	$20 \sigma_{\text{hit}}$
MVD	1	0.4	0.4	0.4
	2	0.7	0.7	0.7
STS	1	0.3	0.3	0.3
	2	0.4	0.4	0.4
	3	0.4	0.7	0.8
	4	0.5	43.9	85.0
	5	0.5	1.6	1.6
	6	0.6	0.6	0.6
	7	0.6	0.6	0.6
	8	0.1	0.1	0.1

The DAF algorithm will be further investigated within the CA track finder.

References

- [1] R. Frühwirth and A. Strandlie, Track fitting with ambiguities and noise: a study of elastic tracking and nonlinear filters. *Comp. Phys. Comm.* **120** (1999) 197
- [2] S. Gorbunov *et al.*, *Comp. Phys. Comm.* **178** (2008) 374

CA-based track finder with STS detector inefficiency

I. Kisel¹, I. Kulakov^{2,3}, I. Rostovtseva⁴, and M. Zyzak^{2,3}

¹GSI, Darmstadt, Germany; ²Goethe University, Frankfurt, Germany; ³University of Kyiv, Ukraine; ⁴ITEP, Moscow, Russia

The CBM experiment at FAIR is being designed to study heavy-ion collisions at high track densities up to 1000 tracks per central collision in the Silicon Tracking System (STS). Double-sided strip detector modules will be used in STS, that leads to up to 85% additional combinatorial space points. The Cellular Automaton (CA) based algorithm [1] is used for track reconstruction in the STS detector of the CBM experiment. The algorithm creates short track segments (triplets) in each three neighboring stations, then links into track-candidates and selects according to the maximum length and minimum χ^2 criteria.

To handle real experimental conditions the track reconstruction algorithm has to cope with detector inefficiencies. Therefore the stability of the algorithm has been investigated with respect to detector inefficiencies. In order to improve the stability new features have been added to the algorithm: (i) triplets can skip one station with a missing hit, (ii) gathering individual hits by track-candidates and (iii) merging separate parts of the same track.

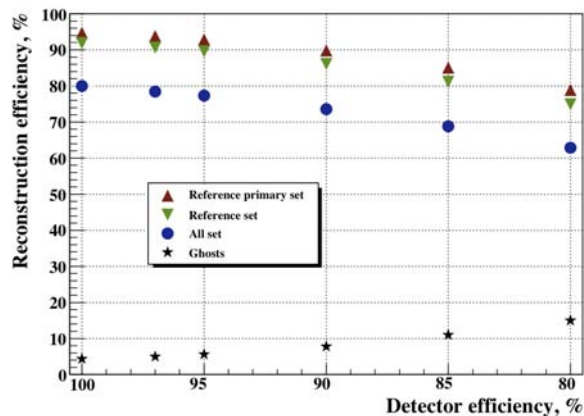


Figure 1: Reconstruction efficiencies and ghost rate versus the detector strip efficiency

For tests 100 central Au+Au UrQMD events at 25 AGeV have been simulated. The track reconstruction with the detector strip efficiencies of 100, 97, 95, 90, 85 and 80 per cent has been investigated. The track reconstruction efficiency and track fitting quality were monitored.

Track reconstruction efficiency is defined as the number of reconstructed tracks assigned to generated particles divided by the number of all reconstructible tracks. Reconstructible tracks are those, which have momentum greater than 0.1 GeV/c and intersect the sensitive regions of at least four consecutive stations. A reconstructed track is assigned

to a particle, if at least 70% of its hits have been caused by this particle. A reference track should have a momentum greater than 1 GeV/c in addition. The reference set of tracks can also include tracks of particular physics interest: secondary tracks from interesting decays or primary tracks coming from the target region. If a reconstructed track is not assigned to any particle it is called a ghost.

The dependence of the track reconstruction efficiency on the detector strip efficiency is shown in Figure 1. The efficiencies for all reconstructible tracks, reference tracks and primary reference tracks and ghost rate are presented. As one can see, the algorithm is robust and shows a slight reconstruction efficiency degradation with respect to the detector inefficiency. In particular, decreasing of the detector efficiency from 100% to 95% leads to decreasing of the track reconstruction efficiency only by 3%.

Table 1: Residuals of track parameters versus the detector strip efficiency

Detector strip efficiency, %	100	97	95	90	85	80
x , μm	12	13	13	14	14	15
y , μm	57	60	61	65	69	73
t_x , mrad	0.35	0.36	0.37	0.38	0.40	0.42
t_y , mrad	0.60	0.61	0.61	0.63	0.64	0.66
p , %	1.22	1.25	1.28	1.34	1.41	1.48

Track fit quality at the first track point has been investigated with respect to the detector inefficiency as well. Resolutions become slightly worse due to the smaller number of hits in a track (see Table). Resolutions and pulls (resolutions normalized on estimated errors) of all track parameters are unbiased.

Summarizing, the algorithm of track reconstruction has been improved and shows stability with respect to the STS detector inefficiency.

References

- [1] I. Kisel, Nucl. Instrum. Meth. A **566** (2006) 85

L1 CA track finder with realistic STS clusterization

I. Rostovtseva¹, D. Golubkov¹, I. Kisel², and Yu. Zaitsev¹

¹ITEP, Institute for Theoretical and Experimental Physics, Moscow, Russia; ²GSI, Darmstadt, Germany

In a realistic process of strip clusterization some loss of information inevitably occurs due to merging of clusters. A merged cluster is a group of strips, fired by more than one MC point. For Au+Au collisions at 25 AGeV simulated with `cbmroot` version Jun10, about 12% of hits are created from merged clusters (at least in one projection) and more than $\sim 50\%$ of tracks contain hits from merged clusters. This may affect the tracking performance and the present work considers this influence on L1 Cellular Automaton Track Finder (CA) [1].

The “removal procedure” of the CA, which removes from further consideration hits attached to found track candidates, does not allow tracks to have hits in common and thus by default does not take into account possible merging of the clusters. Therefore it is able to remove true hits together with fakes if the corresponding cluster (at least in one projection) has been included in some other track.

This particular source of loss in the track finding efficiency was considered in our talk [2]. To recover the efficiency without significantly increasing the clone and ghost rates we tried to optimize the removal procedure (in order to remove maximum of non-merged and minimum of merged clusters), using the information about: the total cluster charge, the mean charge of the clusters on the track, and the size of the cluster. The charge distributions significantly differ for single- and many-strip clusters, so we considered them separately. Figure 1 shows the dependence of the efficiency, the ghost and clone rates after the first step of the algorithm on the cut on the minimal cluster charge.

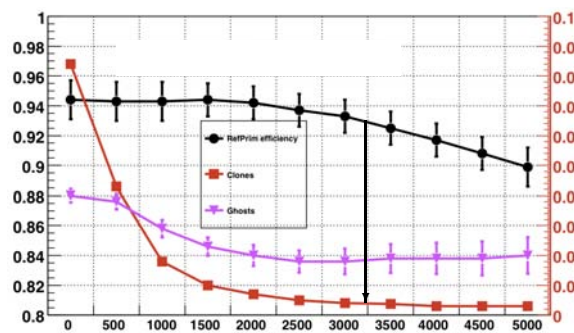


Figure 1: RefPrim efficiency (circles), clones (squares), ghosts (triangles) versus cut on the total cluster charge

We chose to cut on the minimal total cluster charge for many-strip clusters below 2500 to remove clusters with low charge which are more likely to be non-merged. The effect of the difference in charge distribution between merged and

non-merged single-strip clusters is less pronounced.

Because the cluster charge depends on the type of the particle, its momentum and angles, one can expect to achieve some improvement by cutting on “normalized charge” obtained by dividing the charge of the cluster by $\text{mean}(\{c_i\})$, the mean value of cluster charges on the track. We have also studied different truncated mean definitions: $\text{mean}(\{c_i\} \setminus c_{\max})$, and $\text{mean}(\{c_i\} \setminus \{c_{\max}, c_{\min}\})$ to increase robustness. No significant difference could be found between the results obtained using the cut on total cluster charge or cutting on any of the studied normalized cluster charges.

Table 1: Comparison of CA performance with default and modified removal procedure

Track category	Jun10	charge < 2500
	%	%
RefSet (> 1 GeV/c)	89.0	94.1
RefPrim	90.4	95.1
RefSec	80.2	87.8
All set	82.5	87.6
Extra set (< 1 GeV/c)	66.2	71.2
Clone	0.6	1.0
Ghost	3.4	3.3

As listed in Table 1 (taken from [2]), using the optimal cut on the total charge of many-strip clusters at the first step of the CA algorithm, it was possible to recover the tracking efficiency for the reference set of tracks to about 94% while keeping low clone and ghost rates.

It is necessary to underline that the amount of merged clusters significantly depends on the properties of the detector and on the digitization algorithm as well as the local track occupancy. So, it will be subject to keep step with the development of the detector design and changes in operational conditions. Due to the reported strong dependencies we have decided not to include the described modifications in the official release of the L1 CA. Nevertheless, the presented study may be used at a later phase of adjusting the tracking algorithm to the performance of the real detector.

References

- [1] I. Kisel, Nucl. Instrum. Meth. A **566** (2006) 85
- [2] I. Rostovtseva *et al.*, *Status of L1 Track Finder*, 16th CBM collaboration meeting, Mamaia, Romania, 28 September 2010

Scalability of the CA-based track finder in the CBM experiment

I. Kisel¹ and I. Kulakov^{2,3}

¹GSI, Darmstadt, Germany; ²Goethe University, Frankfurt, Germany; ³University of Kyiv, Ukraine

The main challenge of the CBM experiment is to cope with high interaction rates up to 10^7 collisions per second. The average track density is about 1000 particles per central Au+Au collision. The tracking system of CBM is positioned within a dipole magnet and is build of double-sided silicon strip detectors. In addition to such high input rate and complicated event topology, the full event reconstruction and selection will be done at the First Level Event Selection (FLES) stage. This requires utilization of the full potential of modern many-core CPU/GPU architectures. Since developments of modern processors tend to increase a number of cores rather than a CPU frequency, a good scalability of the event reconstruction is essential.

The core of the track reconstruction for the CBM experiment is the Cellular Automaton (CA) based reconstruction [1] in the Silicon Tracking System (STS). It is the most sophisticated and time consuming part of the event reconstruction. Therefore it should have a good scalability with respect to the number of cores.

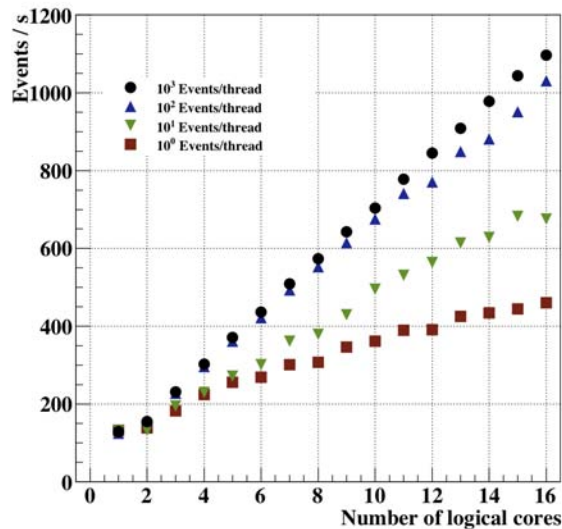


Figure 1: Scalability of the CA track finder for minimum bias events

A stand-alone package [2] was used for the investigation of the CA track reconstruction scalability. Tests were performed with a two Xeon X5550 processors computer having 8 cores in total at 2.7 GHz and with 8 MB L3 cache (GSI lxir039). Each physical core has two logical cores due to the hyper-threading technology. In order to investigate

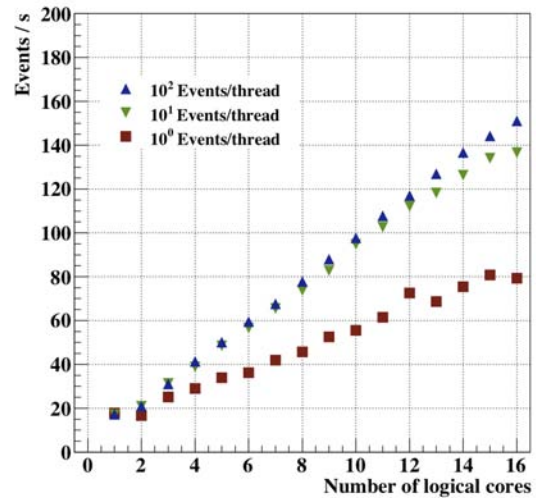


Figure 2: Scalability of the CA track finder for central events

the scalability, track finding was run on various numbers of cores. The Intel Threading Building Blocks (TBB) software package [3] was used for parallel execution between cores.

In Fig. 1 the scalability on the logical cores is shown for minimum bias events. Here, the track reconstruction was parallelized by execution of one thread per (one) logical core. Reconstruction of 1, 10, 100 and 1000 events was executed for each thread. In the same way the track reconstruction was executed for 1, 10 and 100 central events (see Figure 2). The figures show a good linear scalability for large groups of events, while for small groups of events an overhead is observed.

In conclusion, running on a computer with 8 cores the CA based track finder demonstrates the maximum throughput of 150 central or 1100 minimum bias events per second using the Intel Threading Building Blocks. The strong many-core scalability of the CA track finder makes it possible to keep the reconstruction at the event-level parallelism.

References

- [1] I. Kisel, Nucl. Instrum. Meth. A **566** (2006) 85
- [2] I. Kisel et al., *CBM Progress Report 2008*, Darmstadt 2009, p. 79
- [3] <http://www.threadingbuildingblocks.org>

Towards parallel track reconstruction with Intel ArBB

I. Kisel¹, I. Kulakov^{2,3}, H. Pabst⁴, and M. Zyzak^{2,3}

¹GSI, Darmstadt, Germany; ²Goethe University, Frankfurt, Germany; ³University of Kyiv, Ukraine; ⁴Intel, Germany

The Intel Array Building Blocks (ArBB) software [1] is a data-parallel programming environment designed to effectively utilize the power of existing and upcoming throughput-oriented features on modern processor architectures, including Intel's multi-core and many-core platforms. Intel Array Building Blocks provides a generalized vector parallel programming solution that frees application developers from dependencies on particular low-level parallelism mechanisms or hardware architectures. It is comprised of a combination of standard C++ library interface and powerful runtime. It produces scalable, portable, and deterministic parallel implementations from a single high-level source description. It allows to parallelize on both data and task levels in an easy way.

The track reconstruction is a task, which needs a lot of computational power. At the same time all modern high energy physics experiments operate with huge data rates and require fast reconstruction procedures. In order to operate effectively in such difficult conditions the full utilization of CPU is required. Parallel programming is considered now as the only way to utilize the full power of CPU, since all modern CPUs have more than one core and contain a SIMD unit. All the characteristics of ArBB make it perfectly suitable for fast track reconstruction and fitting tasks.

The SIMDized Kalman filter track fitter [2] has been modified using ArBB. Results obtained with the ArBB version have been compared with results of the SIMD version [3]. Tests for time and track fit quality of the algorithm have been performed on a 8-cores computer (GSI Ixir039) with two Xeon X5550 processors at 2.7 GHz and 8 MB L3 cache. The computer has 16 logical cores due to the hyper-threading technology.

For time tests two types of calculations using 1 logical core only as well as all 16 logical cores have been performed. The former is to compare the level of the code vectorization using SIMD instructions, the latter in order to compare parallelization level between cores and utilization of the full potential of the CPU. The ArBB version shows practically the same time results, as the SIMD one (see Table).

Table 1: Fitting time per track of the SIMD and ArBB versions executed on one core and all cores

	SIMD		ArBB	
Cores	1	16	1	16
Time, μ s	0.42	0.05	0.43	0.06

Residuals and pulls (residuals normalized on the estimated errors) of the estimated track parameters have been calculated at the production vertex in order to test the track fit quality. In Figure 1 residuals and pulls for the track position x , the track slope in the XZ plane t_x and the inverse particle momentum, signed according to charge, q/p are shown. Obtained results are the same as in the SIMD version.

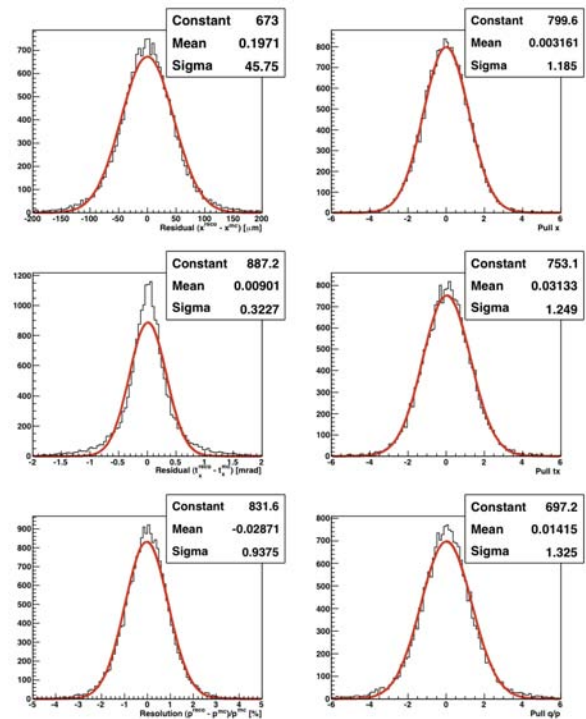


Figure 1: Residuals and pulls of the estimated track parameters calculated with the ArBB version of the Kalman filter track fitter

Subsequently we consider modifications of the Cellular Automaton (CA) based track reconstruction algorithm using ArBB.

References

- [1] <http://software.intel.com/en-us/articles/intel-array-building-blocks>.
- [2] S. Gorbunov *et al.*, *Comp. Phys. Comm.* **178** (2008) 374
- [3] I. Kisel, M. Kretz and I. Kulakov, *CBM Progress Report 2009*, Darmstadt 2010, p. 75

A new cluster-based CbmRoot reconstruction chain for the TRD

C. Bergmann¹, D. Emschermann¹, F. Uhlig², and J. P. Wessels¹

¹Institut für Kernphysik, Münster, Germany; ²GSI, Darmstadt, Germany

A new track position reconstruction chain with a realistic cluster charge induction algorithm was implemented in CbmRoot. This algorithm is based on the induced charge distribution described by Mathieson [1] and implemented for rectangular pad geometries. The full chain consists of three classes; CbmTrdClusterizer, CbmTrdClusterFinderFast and CbmTrdHitProducerCluster.

CbmTrdClusterizer

The Clusterizer is used to approximate the induced charge on the pad plane created by the primary MC-particle. To describe this charge distribution, one needs only one parameter $K3$, which is a function of characteristic chamber parameters. Let $\rho(r)$ represent the induced charge density distribution on the cathode pad plane in a chamber with equal distance of the cathode planes with respect to the anode wire plane. The x-coordinate can either be parallel or normal to the anode wire direction. One can write the formula for two dimensions with $r = \sqrt{x^2 + y^2}$ and a given net anode charge q_a :

$$\rho(r/h) = q_a \cdot \frac{\pi/2 \cdot (1 - \sqrt{K_3/2}) \sqrt{K_3}}{4 \arctan(\sqrt{K_3})} \cdot \frac{1 - \tanh^2(\pi/2 \cdot (1 - \sqrt{K_3/2})r/h)}{1 + K_3 \tanh^2(\pi/2 \cdot (1 - \sqrt{K_3/2})r/h)}$$

Values of $K3$ have been taken from [1]. The algorithm implemented in CbmRoot has a static $K3$ value of 0.525 which corresponds to an anode wire radius of 25 μm , an anode-cathode separation of 3 mm and an anode wire pitch of 3 mm. This fixed value can be replaced by a parameterization to cope with variable detector geometries. The Mathieson-formula is calculated along the particle track at periodical positions which provide for MC-particles with a large impact angle. The induced charge is given by the integral of the charge density on the pad plane. The information of each fired pad is stored in a so called TrdDigi.

CbmTrdClusterFinderFast

The CbmTrdClusterFinderFast re-sorts the chronological TrdDigis into spatial order and associates TrdDigi accumulations with TrdClusters. This is done by using the so called combiID. This ID provides the combined row and column information of each pad by a unique number within each module. They get a spatial order by sorting the TrdDigis by the combiID. TrdDigis with a continuous combiID are combined to rowClusters, row by row. Rows are separated by an artificial dummy column. Subsequently,

overlapping rowClusters in consecutive rows are merged to final TrdClusters. The merging step is skipped for chambers within a certain radius around the beam pipe, since the probability for row overlapping TrdClusters is correlated to the impact angle and the path length of the particle track through the chamber volume. The TrdClusters are CbmRoot data objects like TrdDigis. Due to the high hit density, especially for the detectors close to the beam pipe, a separation mechanism for neighbouring TrdClusters was implemented. This is realised by a minimum charge threshold for TrdDigis which has been optimized.

CbmTrdHitProducerCluster

The CbmTrdHitProducerCluster is used to reconstruct particle positions from TrdCluster information provided by the CbmTrdClusterFinderFast. The Hitproducer use the charge information of each TrdDigi within the TrdClusters. First, the TrdDigi with the maximum charge per TrdCluster is searched. From this information the TrdHit position is reconstructed by applying a center-of-gravity method.

Conclusion

After optimizations of the method MC simulations yield an overall reconstruction efficiency between 75% and 90%. The position resolution along the wire direction is around 300 microns averaged over all hits in the TRD (see Fig.1) which meets the technical design goal of 300 - 500 microns for the CBM TRD.

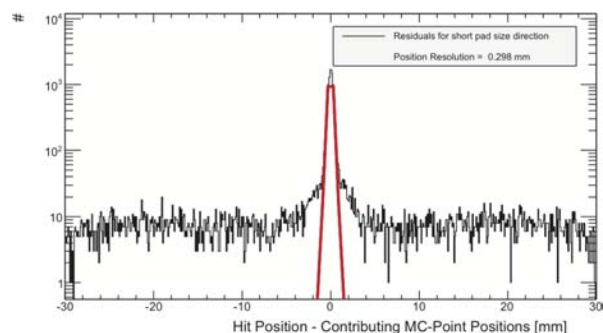


Figure 1: Position resolution of the reconstructed hits relative to the MC-positions for short pad size direction

References

- [1] E. Mathieson, Nucl. Instrum. Meth. **A 270** (1988) 602

Status of tracking in the TRD and MUCH detectors of the CBM experiment

A. Lebedev^{1,2}, C. Höhne³, I. Kisel¹, and G. Ososkov²

¹GSI, Darmstadt, Germany; ²LIT JINR, Dubna, Russia; ³Justus Liebig University, Giessen, Germany

In this report the status of the track reconstruction in the Transition Radiation Detector (TRD) and muon system (MUCH) of the CBM experiment is presented. Global track reconstruction in the electron and muon setup of the CBM detector, i.e. with either TRD or MUCH system, is based on track following using reconstructed tracks in the STS as seeds. In the STS the track reconstruction is based on the cellular automaton method and provides initial track parameters as starting point for the following track prolongation. This ray tracing is based on the standard Kalman filter technique and is used for the trajectory recognition and estimation of track parameters in the TRD and MUCH. Tracks are prolonged subsequently from one detector station to the next adding hits in the detector stations.

The detailed layout of the detectors is still under investigation. In the high track density region of the TRD and MUCH stations, a pad layout is foreseen based on MWPC or GEM technology. For the downstream detector stations in MUCH, where track densities are low, straw tube chambers are under discussion. The first TRD station can be used as tracking station after the last MUCH absorber.

In the performed studies the algorithms were tested using central Au+Au collisions at 25 AGeV beam energy from UrQMD. In addition, for the reconstruction in TRD, 5 primary e^+ and 5 primary e^- with momenta $1 \text{ GeV}/c \leq p \leq 10 \text{ GeV}/c$ were embedded in each event. The performance inside the muon system was evaluated by embedding 5 primary μ^+ and 5 primary μ^- per event with momenta $2.5 \text{ GeV}/c \leq p \leq 25 \text{ GeV}/c$.

Table 1: Track finding efficiency for muon tracks for five different MUCH geometries in %. NN – nearest neighbour algorithm; branch – branching algorithm

	MUCH geometry				
	MUCH1	MUCH2	MUCH3	MUCH4	MUCH5
NN	93.8	94.4	93.8	92.8	92.8
Branch	94.0	94.7	94.1	94.9	94.9

The tracking efficiency for five different MUCH layouts was compared: 1) MUCH1 is the standard layout with 6×3 detectors including pad readout, 2) MUCH2 has 13 detectors with pad readout, 3) MUCH3 has 3×3 detectors with pad readout and straw tube detectors in the last 3×3 stations, 4) MUCH4 is the same as MUCH2 but with TRD after the last absorber, 5) MUCH5 is the same as MUCH3 but with the TRD after the last absorber, i.e. MUCH5 is currently the preferred layout. Table 1 lists the track finding efficiencies for these 5 MUCH geometries using two algorithms: the nearest neighbour as well as the branching. The reconstruction

efficiencies differ slightly with respect to the MUCH layout option.

Concerning the TRD layout, the influence of the TRD detector position resolution on the tracking efficiency was studied. The position resolution for the x coordinate was fixed to $300 \mu\text{m}$. In y direction it has been varied from $100 \mu\text{m}$ to 30 cm . Nearest neighbour tracking was used in this study. The track finding efficiency is presented in Fig. 1. The efficiency stays acceptable up to a position resolution of several centimeters. For larger polar angles, where track densities are lower, the detector resolution can be up to 6–7 cm.

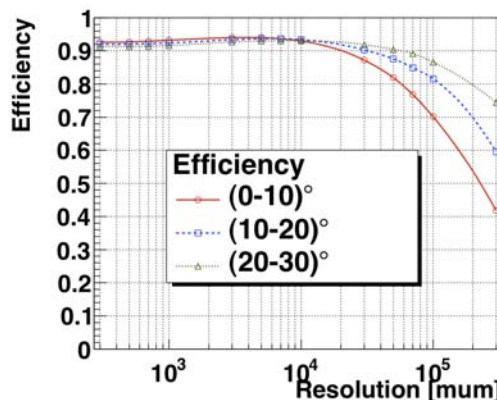


Figure 1: Track finding efficiency for TRD in dependence on position resolution for different polar angles

The speed of the tracking software is extremely important for data analysis in CBM. A fast parallel track reconstruction algorithm which uses available features of modern processors was further investigated. The algorithm uses two features of modern CPUs: a SIMD instruction set and multithreading. The results of the algorithm speedup for the MUCH system are presented in Table 2.

Table 2: Speedup of the track fitting (time is shown per track in μs) and track finding algorithm (time is shown per event in ms) for track reconstruction in MUCH

	Track fitting		Track finding	
	Time	Speedup	Time	Speedup
Initial	1200	-	730	-
Optimization	13	92	7.2	101
Vectorization	4.4	3	4.9	1.5
Multithreading	0.5	8.8	1.5	3.3
Final	0.5	2400	1.5	487

Status of the electron identification algorithm for the RICH and TRD detector systems of the CBM experiment

S. Lebedev^{1,2}, C. Höhne³, and G. Ososkov²

¹GSI, Darmstadt, Germany; ²JINR, Dubna, Russia; ³Justus Liebig University, Giessen, Germany

RICH detector

In the ring reconstruction algorithm [1] a further speedup optimization and the event level parallelism was investigated. In order to test the ring reconstruction algorithm, central UrQMD Au+Au collisions at 25 AGeV beam energy with 10 embedded primary e^+ and e^- were simulated. The test computer has two Intel Core i7 CPUs with 4 cores each at 2.67 GHz (16 logical cores in total).

The ring reconstruction efficiency is the same for the scalar and parallel version and equals to 93% integrated over momentum. The number of fake rings is 2.7 per event, the number of clone rings is 0.9 per event, which has to be compared to a total number of 80 rings per event. A speed up factor of 74 is achieved by the optimization of the algorithm. Using SIMDization and multithreading the speed of the algorithm was increased further by a factor of 2. In total a speed up factor of 143 was achieved (from 357 ms/event to 2.5 ms/event) for the optimized parallel version in comparison to the initial algorithm.

Event level parallelism was studied as well. Events are accumulated in a buffer, then groups of events are reconstructed in parallel in different threads (different CPU cores). A thread scheduler was developed in order to control the creation and life cycle of threads. It allows to run threads on a certain CPU core. The scalability of the event level parallelism was investigated: N events were read from the event buffer, an individual thread was created for this group of events and the reconstruction was executed. The first thread executes on the first logical core of the first CPU, the second thread executes on the second logical core of the first CPU. The next two threads execute on the second core, and so on. Our tests show that the performance increased linearly in dependence on the number of running threads. Using the computer CPUs at a maximum (16 running threads) algorithm reconstructs more than 1800 central events per second (500 μ s/event) and roughly 8000 mbias events per second (125 μ s/event).

Table 1: Pion suppression in the RICH detector for two different algorithms

	ANN	Cuts
π suppression ($p < 6\text{GeV}/c$)	500	200
π suppression ($p > 6\text{GeV}/c$)	260	130

Two algorithms for electron identification in the RICH detector were implemented: 1) standard ring radius cut method, 2) method based on the ANN [2]. The comparison of the pion suppression results assuming 93% electron identification efficiency is presented in Table 1.

TRD detector

In addition to previous studies [3] further investigations of the electron identification algorithm in the TRD were performed. To calculate the pion suppression factor 10^6 electrons and 10^6 pions were simulated with the following parameters $\theta = (2.5^\circ, 25^\circ)$, $\phi = (0^\circ, 360^\circ)$ and a momentum of 1.5 GeV/c. A set of radiator parameters was used which was tuned to describe the experimental results (3rd set in [3]). The BDT method was applied for this study [4].

Due to the high track multiplicity and density, the track reconstruction algorithm sometimes assigns fake hits to a track. For example, from 12 hits of an electron track 11 hits were found correctly and one hit was wrongly substituted by a pion hit. This effect has been studied in two ways (see Table 2): 1) assign fake pion hits to an electron track, 2) assign fake electron hits to a pion track.

Table 2: Pion suppression in the TRD detector in dependence on the number of wrong hits per track

Number of wrong hits	0	1	2	3	4	5
π supp., variant 1	660	225	89	37	17	9
π supp., variant 2	660	215	74	30	13	7

The BDT method was adapted to identify electrons which have 6 to 12 hits in the TRD. This is necessary because 1) different geometries with different number of layers have to be investigated; 2) detector inefficiency; 3) tracks which do not pass through all layers should also be identified; 4) the track reconstruction algorithm might find only a part of a track. The dependence of the pion suppression on the number of hits per track is presented in Table 3. The gain of the pion suppression due to the additional hit is presented too. The gains are calculated as pion suppression for tracks with N hits divided by the pion suppression for tracks with (N-1) hits.

Table 3: Pion suppression in the TRD detector in dependence on the number of hits per track

# of hits	12	11	10	9	8	7	6
π supp.	660	500	334	215	132	85	54
Gain	1.33	1.55	1.50	1.63	1.55	1.6	—

References

- [1] S. Lebedev *et al.*, CBM Progress report 2009, p. 79
- [2] S. Lebedev *et al.*, CBM Progress report 2008, p. 84
- [3] S. Lebedev *et al.*, CBM Progress report 2009, p. 81
- [4] G. Ososkov *et al.*, e^-/π separation with TRD, <https://www.gsi.de/documents/DOC-2009-Oct-232-1.pdf>

First steps towards a time-based simulation and reconstruction for the CBM experiment

V. Friese¹ and E. Kryshen²

¹GSI, Darmstadt, Germany; ²PNPI, Gatchina, Russia

Simulation, reconstruction and analysis for the CBM experiment are performed using the FAIRROOT software framework. The feasibility studies performed so far include the transport of events through the CBM geometry, the simulation of the detector response according to the present knowledge on detector and read-out electronics properties, and full hit, track and vertex reconstruction. With these tools, the feasibility of the measurement of all major observables of the CBM physics programme was demonstrated.

However, the framework, and consequently all simulation results, are based on event-by-event processing, i.e. the association of hits in the detector to physical events is given *a priori*. This corresponds to a conventional experiment where events are defined by a hardware trigger before readout. The data acquisition concept of CBM, in contrast, will not employ a latency-limited trigger, but foresees autonomous, self-triggered read-out electronics which will send time-stamped hit information into the DAQ chain whenever the corresponding detector channel is activated. The association of the hit information to physical events must thus be performed in software.

In order to demonstrate the feasibility of such a read-out concept, in particular for event rates as high as envisaged for CBM, the following tasks arise:

- The detector response simulation shall consider the Monte-Carlo time information and, in turn, provide a time tag for the produced detector hit, taking into account the anticipated behaviour of the detector and, in particular, of the front-end electronics. This means for instance that a double hit in a detector channel is not defined by two tracks in this channel within one event, but within a given time interval (detector dead time).
- Based on this time-based hit information, an algorithm for “event building”, i.e. the association of hits to physical events must be developed. In the simplest case (low interaction rates), when the average time between two subsequent events is large compared to the variation of hit times within one event, this can be done using the time information alone. The already developed event-based reconstruction can then proceed as before.
- For high interaction rates, events will overlap in time. The association of hits to events is thus no longer trivial. Then, space-time correlations must be employed,

such that track and event reconstruction will operate in four dimensions (instead of the common three ones).

As a first step towards these developments, the software framework was extended to facilitate the treatment of data based on time and not on events. A dedicated task class (`CbmMCStreamer`) regroups the Monte-Carlo hits delivered by the event-by-event transport according to their hit time into time slices (*epochs*), thus destroying the correlation of the MC hits to the input events from the generator. The format for this new data level is still a ROOT TTree, but now with one entry per epoch instead of one entry per event. The size of the epoch is adjustable to the user’s convenience. It should be noted that the epoch on the MC level need not coincide with any time scale defined by the read-out and DAQ system, but is in first place just a mean to discretise a continuous data stream. Parameters for the MC-Streamer are the average interaction rate and a model of the time profile of the beam.

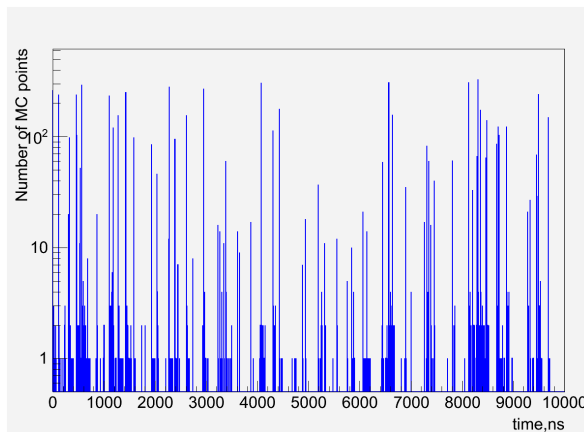


Figure 1: Time sequence of MC hits in the CBM silicon tracking system, assuming an average interaction rate of 10 MHz and a white beam, for Au+Au collisions at 25.4 GeV

As a simple application of the new data format, Fig. 1 shows the time sequence of MC hits in the CBM-STC detector system, assuming an average interaction rate of 10 MHz with a white beam. With the new data format as input, the development of advanced, time-based digitisers for the different detector systems will be the next steps towards the full simulation and reconstruction of the data flow in CBM.

Software development infrastructure for the FAIR experiments

F. Uhlig

GSI, Darmstadt, Germany

Beside the framework itself the FairRoot core team also provides software development tools for the experimental groups using FairRoot as base for their own developments. This tools should help the developers to concentrate on his main topic, the development of the experiment specific simulation and analysis software, which includes also the independence of a specific code development tool. Each user can work with the tool he is used to. The tools used by the developers ranges from a simple editor like *vi* to IDE (Integrated Development Environments) like *XCode*. The CMake [1,2] based build system will created the native build files for each environment out of simple configuration files which are stored in a portable text format.

The main components of the software development infrastructure are the source code repository as well as the test and build system. The so called software testing server is used to store and view the information produced by instances of the test and build system. The project management software provides a web interface to the source code repository, a bug tracking, and a wiki system which are tightly integrated. This makes it for example possible to link bug tickets directly to the problem in the code, which allows the user to move from the description of a problem to the erroneous code block with one click inside the web browser.

Some components will be described in more detail below. A detailed description of most of the components can be found at [3].

Source Code Revision Control System

As revision control system we use Subversion (SVN) [4] which is the de facto standard for central revision control systems. The main SVN repository at GSI hosts beside the FairRoot framework also the source code of all supported experiments. This somewhat complicated repository structure has some advantages. First of all it is easily possible to couple the experiment specific code with the base framework without having the need to copy the code of the FairRoot framework. The base framework is included to the experiment specific code (CbmRoot, PandaRoot etc.) as external packages. This setup is completely transparent for the user so he will not see that some of the code comes from a different repository. Another benefit of this SVN setup for the experiments is that we can provide features like continuous integration and backup of the source code on every commit to the repository. This support is triggered by the repository itself.

Project Management

We use *trac* [5] as project management software which combines the advantages of a wiki and a bug tracking system with a powerful web front end to our subversion repository. Any of these tools alone is very useful and may be even needed to manage a larger software project but the tight connection of these tools under one hood even enhances the value of the single tools. All tools use a wiki markup language that allows to easily create hyperlinks. This simplifies the connection from a bug report to a line of code in a specific revision of the software or make it possible to create a hyperlink from the commit message to a closed feature request.

The source code browser allows to navigate in the source tree, check older revisions or commit messages. This includes also as diff-like comparison between different code revisions.

The issue *tracking system* is absolutely necessary to keep track of the development process. This includes also the ability to report software problems or request new features in a well defined and traceable way. I also makes sure that the request is assigned to the correct developer.

trac also allows to define milestones which define states of the project like a stable version or the implementation of a feature. The tickets can be assigned to such a milestone and the roadmap shows the milestones together with the open and closed tickets, which shows by this means the progress towards the milestone. The timeline shows all events like new commits to the repository or new tickets in the project ordered in time.

The wiki allows to create and organize a collection of linked information without great affords. Due to the easy creation of cross links the complete system becomes a valuable source of information. If there are still features missing they can be added using a plugin mechanism. There are already many plugins like support for other version control systems or a spam filter available.

References

- [1] K. Martin and B. Hoffmann, *Mastering CMake. A Cross-Platform Build System*, Kitware Inc., 2007
- [2] <http://www.cmake.org>
- [3] F. Uhlig and M. Al-Turany, PoS(ACAT2010)043
- [4] <http://trac.edgewall.org/>
- [5] <http://subversion.apache.org/>

Study of high p_T pion emission in central Au+Au collisions at CBM

V. P. Ladygin, A. I. Malakhov, and T. A. Vasiliev

LHEP-JINR, Dubna, Russian Federation

The suppression of particle emission at high transverse momenta p_T in central heavy ion collisions is interpreted as a sign of parton energy loss in strongly interacting matter at RHIC and top SPS energies [1, 2]. Therefore it seems to be worthwhile to study high p_T pions at the energy domain of SIS100/300 [3]. Fig. 1 displays the transverse momentum

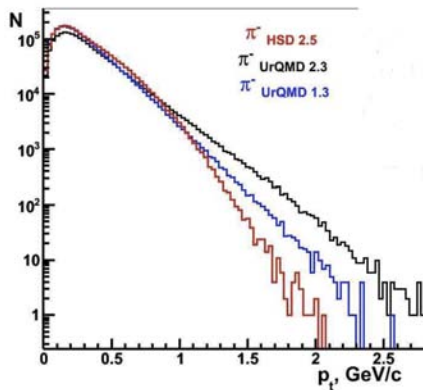


Figure 1: Negatively charged pions transverse momentum spectra from Au+Au central collisions at 10 A-GeV for UrQMD 2.3 (black), UrQMD 1.3 (blue) and HSD 2.5 (red)

spectra of negatively charged pions from central $Au + Au$ collisions at 10 A-GeV for UrQMD 2.3, UrQMD 1.3 [4] and HSD 2.5 [5] generators given by the black, blue and red lines, respectively. One can observe significantly different behavior of the pion spectra at $p_T > 1 \text{ GeV}/c$ for different models [4, 5].

The simulation has been performed for 10000 $Au + Au$ UrQMD 2.3 central events at 10 A-GeV using the standard STS geometry and the magnetic field map for the electron version of CBM, release JUN10. The pions have been selected using $m^2 - p$ correlation, where momentum and time-of-flight were reconstructed from STS and RPCs information, respectively. This method unavoidably leads to the contamination of misidentified kaons and protons, especially at high momenta [3]. To improve the purity of the particle identification procedure the $m^2 - p$ plot was divided into several momentum slices. In each slice the contamination of pions, kaons and protons were estimated by a multi-Gaussian fit of the m^2 - axis projection (see Fig. 2). The graphical cut was modified in the way that the pion border next to kaon was shifted to the left getting equivalent numbers of pions and kaons in a certain bin. This procedure improves the purity for the π^+ identification.

The π^-/π^+ ratio for $Au + Au$ collisions at 10 AGeV as a function of transverse momentum p_T for symmetrical [3]

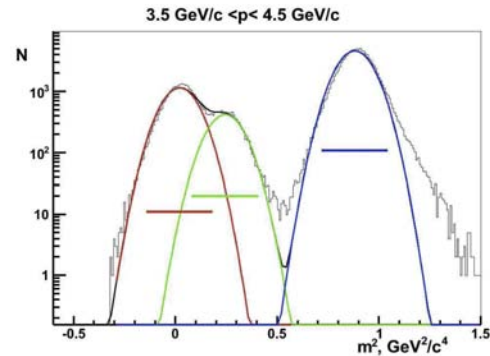


Figure 2: Result of the minimization procedure for reconstructed momentum slice for three Gaussian function. The horizontal lines show the 2σ intervals (95% events).

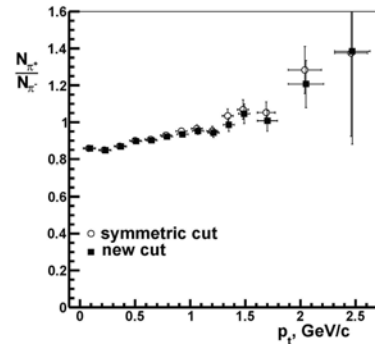


Figure 3: The π^-/π^+ ratio for $Au + Au$ collisions at 10 AGeV as a function of p_T for different graphical cuts

and new graphical cuts is shown in Fig. 3 by the open and closed symbols, respectively. The ratio at large p_T obtained with the new cut is closer to the expected value of ~ 0.8 [4, 5]. However, additional criteria (for instance, the use of RICH information) is required to improve the purity of the π^+ identification.

References

- [1] C. Alt *et al.*, Phys. Rev. **C 77** (2008) 034906
- [2] S. S. Adler *et al.*, Phys. Rev. **C 69** (2004) 034910
- [3] V. P. Ladygin, A. I. Malakhov and T. A. Vasiliev, *CBM Progress Report 2009*, Darmstadt 2010, p.58.
- [4] S. A. Bass *et al.*, Prog. Part. Nucl. Phys. **41** (1998) 225; M. Bleicher *et al.*, J. Phys. **G 25** (1999) 1859
- [5] W. Cassing and E. L. Bratkovskaya, Phys. Rep. **308** (1999) 65

Study of $C_2(\Delta\phi)$ azimuthal correlation in central Au+Au collisions at CBM

V. P. Ladygin, A. I. Malakhov, and T. A. Vasiliev

LHEP-JINR, Dubna, Russian Federation

One of the signatures of a hot dense medium is the modification of properties of jets originating from hard scattering of partons. The study of two-particle azimuthal correlations allows to extract the jet signal from the soft background because the jet particles are strongly correlated in azimuth. Recent RHIC results [1, 2] on high p_T di-hadron correlations confirmed that this approach can be used to study the properties of the nuclear medium. At CERN SPS energies the so called hole-jet transition in di-hadron correlations has been observed [3]. Such investigations can be performed at CBM at SIS-100 energies.

The simulation were performed for 10000 central Au + Au UrQMD 2.3 events at 10 A-GeV. The standard STS geometry and the magnetic field map for an electron version of CBM as well as the Kalman filter procedure for momentum reconstruction in the STS were used (release JUN10). Particle identification was done using time-of-flight information from the RPCs.

Pions were selected using the $m^2 - p$ correlation with a symmetrical graphical cut [4]. The pion with the highest transverse momentum p_T (larger 1.5 GeV/c) in the event is considered as a "trigger" particle. Its direction in the transverse momentum plane is defined as ϕ_0 . All other pions in the event are considered as the "associated" particles. $\Delta\phi$ is the difference between the angle of the "associated" pion ϕ_{ass} and the angle of the "trigger" pion ϕ_0 : $\Delta\phi = \phi_{ass} - \phi_0$. The distribution on the angle difference

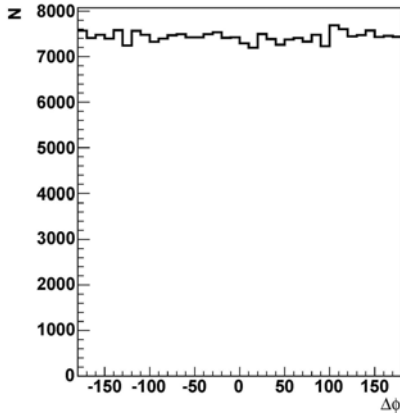


Figure 1: Number of "associated" particles (pions) as a function of $\Delta\phi$

$\Delta\phi$ for the selected pions is shown in Fig. 1. The shape of the distribution is flat as expected from UrQMD 2.3.

The azimuthal correlation $C_2(\Delta\phi)$ is defined a ra-

tio of the normalized $\Delta\phi$ distributions of the "associated" particles in the events with the "trigger" pion, $N_{corr}(\Delta\phi)/\int N_{corr}(\Delta\phi')d(\Delta\phi')$, and obtained from the mixing procedure, $N_{mix}(\Delta\phi)/\int N_{mix}(\Delta\phi')d(\Delta\phi')$:

$$C_2(\Delta\phi) = \frac{N_{corr}(\Delta\phi) \cdot \int N_{mix}(\Delta\phi')d(\Delta\phi')}{N_{mix}(\Delta\phi) \cdot \int N_{corr}(\Delta\phi')d(\Delta\phi')} \quad (1)$$

For the mixing procedure the ϕ_0 is defined from the event with the "trigger" pion, while the "associated" particles are taken from the next event.

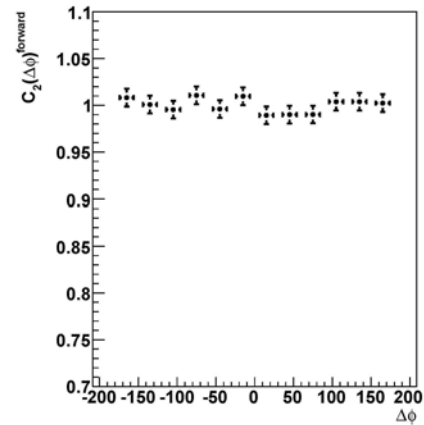


Figure 2: Azimuthal correlation C_2 for pions for Au + Au UrQMD 2.3 central events at 10 A-GeV as a function of $\Delta\phi$

The azimuthal correlation $C_2(\Delta\phi)$ for the selected pions obtained for 10k central Au + Au UrQMD 2.3 events at 10 A-GeV is presented in Fig. 2. The $C_2(\Delta\phi)$ distribution is close to the unity. One can expect the away-side enhancement for systems with smaller size (for instance, Si + Si [3]). The feasibility studies for the energy dependence of $C_2(\Delta\phi)$ (hole-jet transition) at CBM require the improvement of the π^+ identification at high momenta.

References

- [1] A. Adare *et al.*, Phys. Rev. C **78** (2008) 014901; Phys. Rev. C **77** (2008) 011901(R)
- [2] M. M. Aggarwal *et al.*, Phys. Rev. C **82** (2010) 024912; H. Agakishiev *et al.*, arXiv:1010.0690v1 [nucl-ex]
- [3] M. Szuba *et al.*, arXiv:0805.4637 [nucl-ex]; M. Szuba *et al.*, arXiv:0809.5210v1 [nucl-ex]
- [4] V.P. Ladygin, A.I. Malakhov and T.A. Vasiliev, *CBM Progress Report 2009*, Darmstadt 2010, p. 58

Fast Ξ^- reconstruction in Au+Au collisions at 10A GeV with the CBM experiment

I. Vassiliev^{1,2} and V. Akishina³

¹Goethe University, Frankfurt, Germany; ²GSI, Darmstadt, Germany; ³Moscow State University, Moscow, Russia

The main goal of the CBM experiment is to study the behaviour of nuclear matter at high baryonic densities. At these extreme states of strongly interacting matter, the transition to a deconfined quark gluon plasma phase is expected. As a signature of the deconfined phase the enhanced production of multi-strange particles is predicted. At CBM, multi-strange hyperons such as the double-strange Ξ^- will be identified by their decay into charged hadrons, which are detected with the Silicon Tracking System (STS).

To study the feasibility of the (fast) reconstruction of Ξ^- as well as Λ and K_s^0 with CBM, a set of 5k central Au+Au UrQMD events at 10A GeV was simulated. Such an event contains on average 12 K_s^0 , 20 Λ and 0.18 Ξ^- . The Ξ^- decays into $\Lambda + \pi^-$ with a branching ratio of 99.9% and $c\tau = 4.91$ cm.

The STS geometry with 8 double-sided segmented strip detectors was used for tracking. No kaon, pion or proton identification is applied. In order to reconstruct the $\Lambda \rightarrow p\pi^-$ decay, the proton mass was assumed for all positively charged tracks and the pion mass for all negatively charged ones. K_s^0 is reconstructed assuming the pion mass for both tracks. The combination of single track cut ($\chi_{prim}^2 > 3\sigma$) and geometrical vertex cut ($\chi_{geo}^2 < 3\sigma$) allows to see a clear signal (see Figs. 1 and 2) of K_s^0 and Λ .

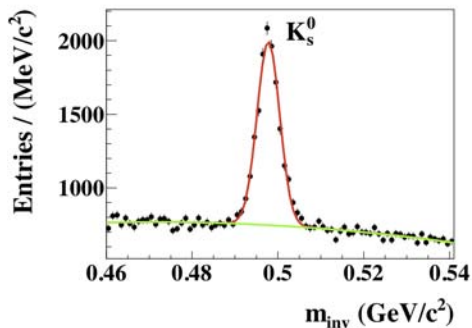


Figure 1: The $\pi^+\pi^-$ invariant-mass spectrum. About 1.6 K_s^0 per event were reconstructed. The red line shows a Gaussian fit to the signal, the green line the polynomial background.

The Ξ^- reconstruction includes several steps: tracks with $\chi_{prim}^2 > 3\sigma$ are selected for a Λ search, where oppositely charged tracks were paired to form a Λ -candidate; a good quality geometrical vertex ($\chi_{geo}^2 < 3\sigma$) was required to suppress combinatorial background. The invariant mass of the reconstructed pair is compared with the

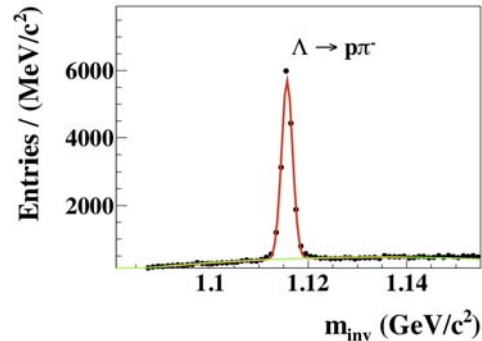


Figure 2: The proton π^- invariant-mass spectrum. About 2.8 Λ per event were reconstructed. The red line shows a Gaussian fit to the signal, the green line the polynomial background.

Λ mass value; only pairs inside $1.116 \pm 6\sigma = 10$ MeV were accepted; primary Λ rejection, where only Λ with $\chi_{prim}^2 > 5\sigma$ and z-vertex greater than 4 cm are chosen. The selected Λ s were combined with secondary π^- tracks ($\chi_{prim}^2 > 3\sigma$) and Ξ^- -KFParticle were created. A Ξ^- -KFParticle was accepted as a Ξ^- candidate if it had good quality geometrical and topological vertex reconstructed more than 3 cm downstream the target plane.

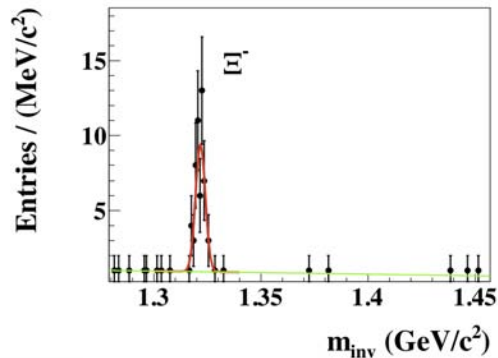


Figure 3: Reconstructed invariant-mass spectrum of $\Lambda\pi^-$ candidates. 51 Ξ^- were reconstructed. The S/B ratio is about 17, the reconstructed mass value is $1.321 \text{ GeV}/c^2$

The resulting invariant-mass spectrum is shown in Fig. 3. The signal reconstruction efficiency is about 5.5%. The reconstructed mass value of $1.321 \pm 0.0023 \text{ GeV}/c^2$ agrees well with the simulated one.

Feasibility study of Ω^- reconstruction with the CBM experiment at SIS-300

I. Vassiliev^{1,2}, I. Kisel², and V. Akishina³

¹Goethe University, Frankfurt am Main, Germany; ²GSI, Darmstadt, Germany; ³Moscow State University, Moscow, Russia

One of the predicted signatures of a phase transition from nuclear matter to a deconfined quark gluon plasma phase is the enhanced production of multi-strange particles. Also, the yield of particles carrying strange quarks is expected to be sensitive to the fireball evolution. Consisting of 3 strange quarks, the Ω^- hyperon is one of the most interesting objects. It will be identified by its decay into charged hadrons, which are detected by the Silicon Tracking System (STS) and the Time-of-Flight detector (TOF) of the CBM experiment.

To study the feasibility of the Ω^- decay reconstruction with CBM, a set of 10k central Au+Au UrQMD events at 25A GeV were simulated. The Ω^- decays into $\Lambda + K^-$ with a branching ratio of 67.8% and $c\tau = 2.46$ cm. Since the Ω^- is rare at 25A GeV central Au+Au UrQMD events (0.022 per event), in each UrQMD event a Ω^- decay into $\Lambda + K^-$, generated by PYTHIA, was embedded.

The STS geometry with 8 double-sided segmented strip detectors was used for track reconstruction; TOF is applied for proton identification. Λ decays most often happen inside the STS detector. In order to reconstruct the $\Lambda \rightarrow p\pi^-$ decay, each identified proton track was combined with every negatively charged track assuming the pion mass for the latter.

The Ω^- event reconstruction includes the usual steps de-

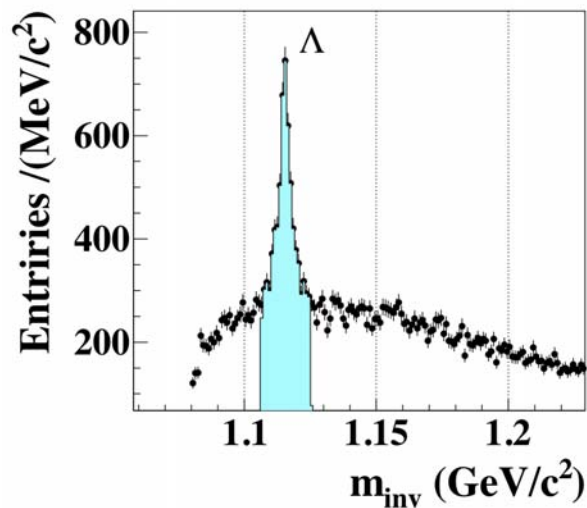


Figure 1: Secondary Λ ($\chi^2_{prim} > 5\sigma$) candidates inside a $1.116 \pm 6\sigma$ window were used for the Ω^- reconstruction

scribed in [1]: fast track finding and fitting [2, 3], Λ search and selection of secondary Λ .

The selected secondary Λ candidates (Fig. 1) were combined with secondary negatively charged tracks assuming the kaon mass, K^- ($\chi^2_{prim} > 7\sigma$), and Ω^- -KFParticle were created. An Ω^- -KFParticle was accepted if showing a reasonable quality of the geometrical and topological detached vertex: ($\chi^2_{geo} < 3\sigma$, $\chi^2_{topo} < 3\sigma$) and z-vertex > 3 cm downstream the target plane.

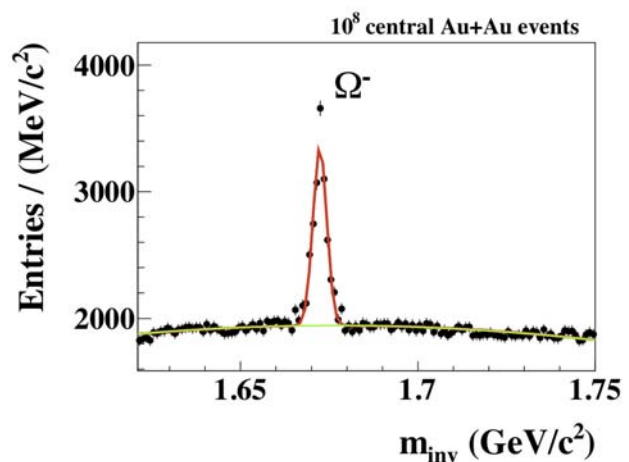


Figure 2: Reconstructed invariant-mass distribution of ΛK^- pairs. The Ω^- reconstruction efficiency is 0.55% at a S/B ratio of 0.4. The reconstructed mass value is $1.672 \text{ GeV}/c^2$. The red line shows a gaussian fit to the signal, the green line the polynomial background fit.

The invariant-mass spectrum is shown in Fig. 2. The Ω^- reconstruction efficiency is about 0.55% for central and about 2% for minimum bias events. The reconstructed mass value of $1.672 \pm 0.003 \text{ GeV}/c^2$ is in good agreement with the PDG's data used for the simulation. The invariant-mass resolution accounts for $2.3 \text{ MeV}/c^2$.

References

- [1] I. Vassiliev, I.Kisel and M. Zyzak, *CBM Progress Report 2009*, Darmstadt 2010, p. 59
- [2] I. Kisel, *Nucl. Instrum. Meth. A* **566** (2006) 85
- [3] S. Gorbunov *et al.*, *Comp. Phys. Comm.* **178** (2008) 374
- [4] M Zyzak and I. Kisel, *Vertexing status*, 14. CBM Collaboration Meeting, October 6-9, 2009, Split, Croatia

D^0 , D^+ and Λ_c decay feasibility study in the CBM experiment

I. Vassiliev^{1,2} and I. Kisel²

¹Goethe University, Frankfurt am Main, Germany; ²GSI, Darmstadt, Germany

One of the major experimental challenges of the CBM experiment is to trigger on the displaced vertex of the D-meson or Λ_c decay via hadronic modes in the environment of heavy-ion collisions. This task requires a fast and efficient track reconstruction algorithm and high resolution of the secondary vertex determination. Particular difficulties in identifying the displaced vertex of the rare open charm decays are caused by weak K_S^0 and hyperon decays which produce displaced vertices downstream the target, very low multiplicities of the rare open charm production, the small branching ratios as well as multiple scattering in the beam pipe and detector systems.

To study the feasibility of D^0 , D^+ and Λ_c decay reconstruction in the CBM experiment, a set of 10^4 central Au+Au UrQMD events at 25A GeV were simulated. The D^0 , D^+ or Λ_c decay to hadrons was forced (BR = 1) and added to each event in order to simulate a signal in the environment of background hadrons. A realistic STS geometry with 2 MAPS at 5 cm (thickness 300 μm) and 10 cm (thickness 500 μm) and 8 double-sided (thickness 400 μm , different z-position of the stations) segmented strip detectors was used. Assuming a 0.1 MHz interaction rate and 30 μs read-out time of the MAPS detectors, δ -electrons produced by 300 gold ions and 3 minimum bias interactions were added to each central event in order to simulate additional background hits in the MAPS detectors. The cluster finding method described in [1] was used for the STS. The primary vertex was reconstructed with high accuracy (6 μm in z direction, 1 μm in x and y) from about 450 tracks reconstructed in the STS in a non-homogeneous magnetic field by the SIMDized Kalman filter procedure described in [2].

A fast track finder was used to reconstruct D^0 , D^+ or Λ_c decays. The algorithm first finds the primary vertex using all reconstructed tracks, and then the open charm particle is reconstructed from its two or three daughter particles using the primary vertex as the production point. The vertex resolution for D^0 , D^+ or Λ_c is 52 μm , 56 μm and 69 μm , respectively. Because of originating from a displaced decay vertex, D^0 , D^+ or Λ_c daughter tracks have a non-vanishing impact parameter at the target plane. Since the majority of the primary tracks have very small impact parameter, a large fraction (99%) of the background tracks was rejected using a cut on their χ^2 distance to the primary vertex.

The combinatorial background is suppressed mainly by the geometrical and topological vertex cuts. Multiplicities, cut efficiencies, acceptance, z -vertex resolution, mass resolution, signal to background ratios and yields per 10^{12} minimum bias interactions are calculated by using the Hadrons String Dynamics (HSD) and Statistical Model (SM), as

presented in Table 1. The shape of the background in the signal invariant-mass region was estimated using the event mixing technique. The invariant-mass distributions of the resulting background plus \bar{D}^0 and D^0 signal are shown in Fig. 1.

Table 1: Acceptance, efficiencies, mass resolution and signal-to-background ratio (S/B, $\pm 2\sigma_m$) of D^0 , D^+ , and Λ_c decay reconstruction in central Au+Au collisions at 25A GeV. The total efficiencies result from the product of geometrical acceptance, reconstruction efficiency and cut efficiencies.

	$D^0 + \bar{D}^0$	$D^+ + D^-$	Λ_c^+
decay channel	$K^\pm \pi^\mp$	$K^\pm \pi^\pm \pi^\mp$	$p K^- \pi^+$
HSD multiplicity	$1.5 \cdot 10^{-4}$	$4.2 \cdot 10^{-5}$	-
SM multiplicity	$8.2 \cdot 10^{-4}$	$8.4 \cdot 10^{-5}$	$4.9 \cdot 10^{-4}$
branching ratio	3.8%	9.5%	5.0%
acceptance	29.2%	40.1%	71.0%
z -resolution [μm]	52	56	69
total efficiency	3.95%	4.75%	0.05%
σ_{im} [MeV/c^2]	11.0	11.0	11.0
SM $S/B_{2\sigma}$ ratio	2.1 (6.4)	1.1 (2.4)	0.6
HSD $S/B_{2\sigma}$ ratio	0.16 (0.5)	0.55 (1.2)	-
SM yield/ 10^{12} mb	225k+78k	95k+179k	3.2k
HSD yield/ 10^{12} mb	41k+14k	47k+89k	-

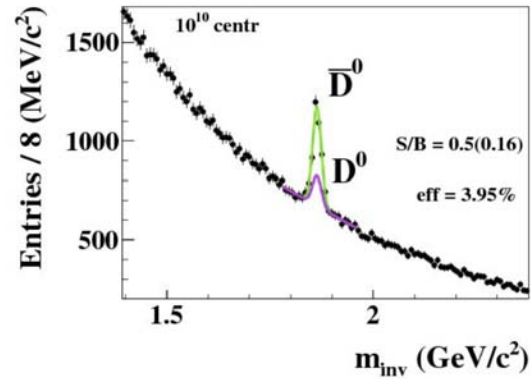


Figure 1: Reconstructed \bar{D}^0 -mesons in 10^{10} central Au+Au collision at 25A GeV. The green line shows the \bar{D}^0 signal, the magenta one the D^0 .

References

- [1] A. Kotynia *et al.*, *CBM Progress Report 2009*, Darmstadt 2010, p. 7
- [2] I. Kisel *et al.*, *Comp. Phys. Comm.* **178** (2008) 374

D^\pm decay reconstruction in p+C collisions at SIS-100 energies with CBM

I. Vassiliev^{1,2} and I. Kisel²

¹Goethe University, Frankfurt am Main, Germany; ²GSI, Darmstadt, Germany

The investigation of p+A collisions up to 30 GeV and A+A collisions from 4A to 11A GeV beam energies is considered as part of the CBM research program and will be performed in the first phase of FAIR with a start version of the CBM detector at the SIS-100 accelerator. This start version consists presumably of two detector systems: the Silicon Tracking System (STS) mounted in a magnetic field to the measurement of momenta and vertices and a Time-Of-Flight (TOF) wall placed 10m downstream of the target for hadron identification.

To study the feasibility of D^\pm decay measurement in the CBM experiment, a set of 10^5 p+C events ($b = 0$ fm) at 30 GeV was simulated. The D^\pm decay to $K^\mp \pi^\pm \pi^\pm$ was used in order to simulate a signal. A realistic STS geometry with 2 MAPS at 5 cm (thickness $300 \mu\text{m}$) and 10 cm (thickness $500 \mu\text{m}$) and 8 double-sided segmented strip detectors (thickness $400 \mu\text{m}$) was tested. δ -electrons produced by 15k protons and 50 minimum bias interaction (assuming up to 5MHz interaction rate) simulated additional background hits in the MAPS detectors. The primary vertex was reconstructed with high accuracy ($60 \mu\text{m}$ in z direction, $10.0 \mu\text{m}$ in x and y) from about 4.5 tracks (on average) fitted in the STS with a non-homogeneous magnetic field by the SIMDized Kalman filter procedure described in [1].

A fast track finder was used to reconstruct the D^\pm decay. The D^\pm particle is reconstructed from its three daughter particles assuming the geometrical target center as the production point. The resulting D^\pm z -vertex resolution is $51 \mu\text{m}$. The 3-prong vertex was considered as a D^\pm decay candidate if it was found more than $450 \mu\text{m}$ downstream the target. The primary vertex was constructed from all non D^\pm tracks and D^\pm -particle. The combinatorial background is suppressed mainly by the vertex cut χ_{geo}^2 and χ_{topo}^2 for good quality detached vertices.

The shape of the background in the signal invariant-mass region was estimated using the event mixing technique. The resulting background plus D^+ and D^- signal spectra calculated using the Hadrons Strin Dynamics (HSD) model are shown. The predicted multiplicities are $2.7 \cdot 10^{-8}$ for D^+ and $5.7 \cdot 10^{-8}$ for D^- . The branching ratio is 9.5%. Two sets of cuts were studied. Relatively soft single track cuts ($\chi_{primary}^2 > 3\sigma$) allowed to keep the total reconstruction efficiency of about 13.2%. Applying this set of soft cuts, we expect to collect about 335 D^+ and 712 D^- per 10^{12} p+C collisions ($b = 0$ fm), with a signal-to-background ratio of about 0.6 and 1.2 respectively. A set of strong single track cuts ($\chi_{primary}^2 > 4\sigma$) decreases the total reconstruction efficiency to 11.6%, but increases the signal-to-background ratio to 1.4 and 3.0, respectively. The expected statistics accounts for 290 D^+ and 617 D^- per 10^{12} p+C collisions ($b = 0$ fm).

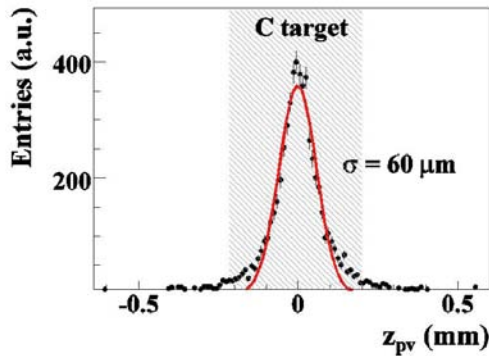


Figure 1: Z-distribution of the reconstructed primary vertex. The dashed region corresponds to the carbon target. The 3-prong vertex was considered as a D^+ decay candidate if it was found more than $450 \mu\text{m}$ (7.5σ) downstream the target.

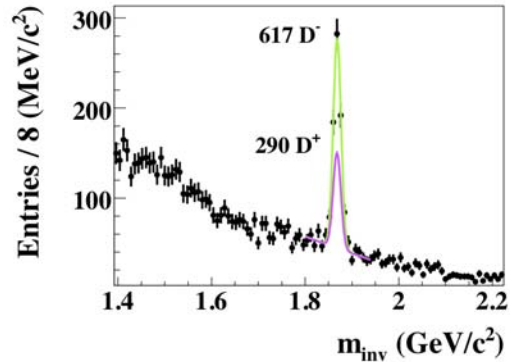


Figure 2: Reconstructed D^- and D^+ -mesons in 10^{12} p+C collision ($b = 0$ fm) at 30 GeV using hard cuts. The green line represents the D^- signal plus exponential background, the magenta one the estimated D^+ signal.

References

- [1] I. Kisel *et al.*, Comp. Phys. Comm. **178** (2008) 374

Reconstruction of Σ^+ in p+C collisions at 30 GeV with ECAL

S. M. Kiselev

ITEP, Moscow, Russia

The feasibility of the Σ^+ reconstruction by the decay $\Sigma^+ \rightarrow p\pi^0$ was studied on a sample of 10^6 p+C ($b=0$ fm) events from UrQMD at the SIS-100 energy 30 GeV (cbmroot trunk MAY09, reconstructed in ECAL by M.Prokudin). The ECAL wall with a size of $X \times Y = 12 \times 9.6$ m² containing a beam hole of 0.8×0.8 m² is distanced from the target at 12 m downstream.

PID information is not used in the analysis. A positively charged track is named by "accepted" if it has MC points in at least four STS stations (placed at 30, 35, 40, 50, 60, 75, 95, 100 cm from the target) and by "reconstructed" if it has the reconstructed track (≥ 70 % of track hits belong to the same MC track). The impact parameter cut > 5 (in σ) is used to reject primary tracks with positive charge (~ 12 per event).

In [1] the reconstruction of π^0 was analyzed. About 50 % of "vertex" photons are lost in the detector systems placed before the ECAL (RICH, TRD and TOF). For the current analysis reconstructed photons with $p > 0.7$ GeV/c were used. Invariant mass distributions for $\gamma\gamma$ pairs with $p_{\gamma\gamma} > 0.2$ GeV/c are displayed in Fig 1. For π^0 candidates

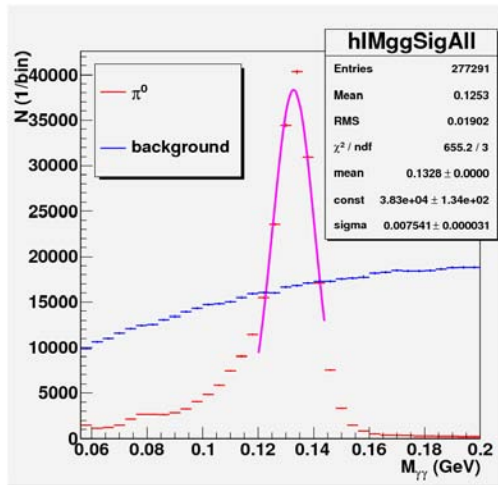


Figure 1: Invariant mass spectra of $\gamma\gamma$ pairs for p+C at 30 GeV

the pairs with $0.12 < M_{\gamma\gamma} < 0.14$ GeV were selected.

Fig. 2 shows the invariant mass distributions of $p\pi^0$ pairs. We obtain a signal-to-background ratio (S/B) of about 8 % with a significance of 1.8. In order to achieve a reasonable significance level of about 10 an event statistics of the order of 10^7 is required.

The main characteristics of the analysis are summarized in Table 1. With the current statistics (43 reconstructed signal pairs) it is not possible to study the dependence of the

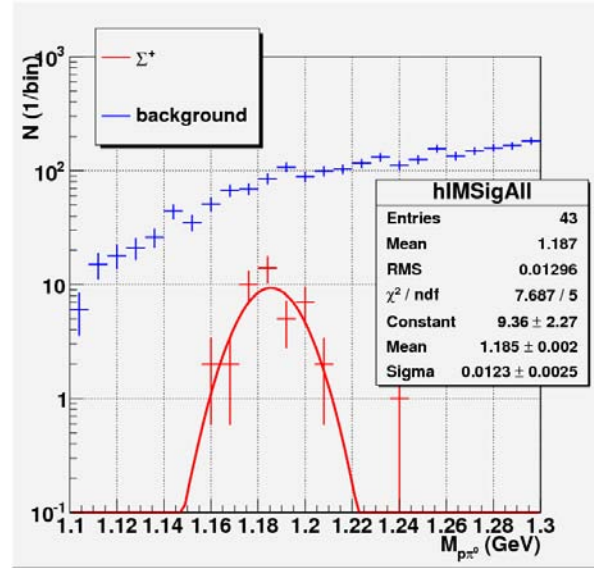


Figure 2: Invariant mass spectra of signal and background $p\pi^0$ pairs for p+C at 30 GeV

Table 1: Main characteristics of the Σ^+ analysis for p+C at 30 GeV

characteristic	value
statistics (events)	10^6
yield/event	0.03
acceptance efficiency	2.3 %
reconstruction efficiency	43 %
cut efficiency	14 %
total efficiency	0.14 %
σ (MeV)	12.3
S/B _{2σ}	8.0 %
significance	1.8

S/B on transverse momentum. The physical motivation for the presented study as well as more analysis details can be found in [2].

References

- [1] S. M. Kiselev, *CBM Progress Report 2009*, Darmstadt 2010, p. 69
- [2] S.M. Kiselev, *Reconstruction of hyperons with ECAL in p+C at SIS100*, 15th CBM collaboration meeting, April 12-16, 2010, GSI, Darmstadt, <https://www.gsi.de/documents/DOC-2010-Apr-64-1.pdf>

Reconstruction of ω in p+C collisions at 30 GeV with ECAL

S. M. Kiselev

ITEP, Moscow, Russia

The feasibility of ω reconstruction by its decay $\omega \rightarrow \pi^0\gamma$ using the ECAL was studied on a sample of 10^6 p+C (b=0 fm) events from UrQMD at 30 GeV (geometry and release as provided in [1], previous page). The invariant mass spectrum of $\gamma\pi^0$ tracks is displayed in Fig. 1. $\gamma\pi^0$ pairs within an invariant mass interval of $0.77 < M_{\gamma\pi^0} < 0.79$ GeV are taken as "primary" ω .

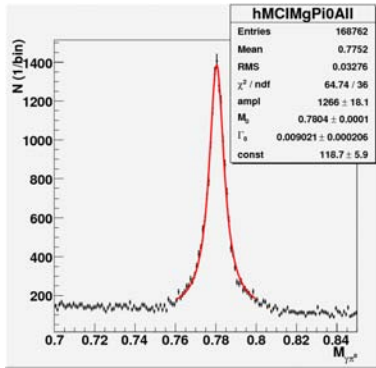


Figure 1: Invariant mass distribution of $\gamma\pi^0$ pairs for p+C at 30 GeV, fitted by a Breit-Wigner function (red line).

About 50 % of "vertex" photons are lost in the detector systems placed before the ECAL (RICH, TRD and TOF) [2]. In case of the ω reconstruction photons above 1 GeV/c momentum were used. The resulting $\gamma\gamma$ invariant mass distribution is shown in Fig. 2. For π^0 candidates the pairs with $m_{\pi^0} - 2\sigma < M_{\gamma\gamma} < m_{\pi^0} + 2\sigma$ were selected, $\sigma=7.2$ MeV.

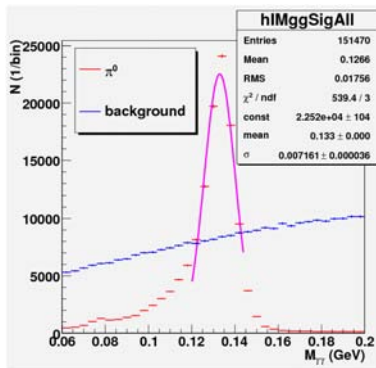


Figure 2: Invariant mass distributions of signal (red) and background (blue) of $\gamma\gamma$ pairs for p+C at 30 GeV

Fig. 3 depicts the invariant mass distributions of $\gamma\pi^0$ pairs. We obtain a signal-to-background ratio (S/B) of about 0.7 % with a significance of 0.9. In order to achieve

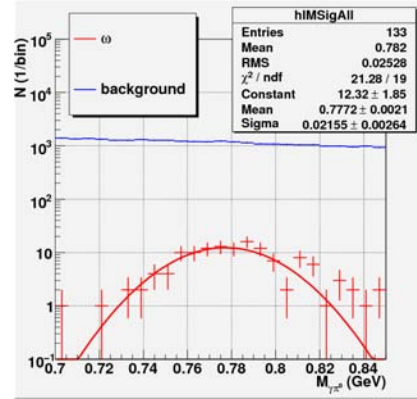


Figure 3: Invariant mass spectra of signal (red) and background (blue) $\gamma\pi^0$ pairs for p+C at 30 GeV

a reasonable significance level of about 10, event statistics of the order of 10^8 is required. The main characteristics of the analysis are summarized in Table 1. With the current statistics (133 reconstructed signal pairs) it is not possible to study the dependence of S/B on transverse momentum. The physical motivation for the presented investigation as well as more analysis details can be found in [3].

Table 1: Main characteristics of the ω analysis for p+C at 30 GeV

characteristic	value
statistics (events)	10^6
yield/event	0.015
acceptance efficiency	4 %
reconstruction efficiency	73 %
cut efficiency	30 %
total efficiency	0.9 %
σ (MeV)	22
S/B $_{2\sigma}$	0.7 %
significance	0.9

References

- [1] S. M. Kiselev, *Reconstruction of Σ^+ in p+C collisions at 30 GeV with ECAL*, this report
- [2] S. M. Kiselev, *CBM Progress Report 2009*, Darmstadt 2010, p. 69
- [3] S. M. Kiselev, *Reconstruction of $\omega \rightarrow \pi^0\gamma$ with ECAL in p+C at SIS100*, 16th CBM collaboration meeting, September 27- October 1, 2010, Mamaia, Romania

Subthreshold J/ψ production in Au+Au collisions at SIS-100 studied with a start version of the CBM muon detector

A. Kiseleva¹, C. Höhne², E. Kryshen³, A. Lebedev^{4,5}, M. Ryzhinskiy³, and P. Senger⁵

¹Goethe University, Frankfurt, Germany; ²Justus Liebig University, Giessen, Germany; ³PNPI, Gatchina, Russia; ⁴JINR-LIT, Dubna, Russia; ⁵GSI, Darmstadt, Germany

The CBM experiment at FAIR will measure the leptonic decay of vector mesons both in the di-electron and the di-muon channel. A particular challenge is the identification of the soft muons from ρ , ω , and ϕ mesons produced in nucleus-nucleus collisions at beam energies between 15 and 45 AGeV. To perform these measurements an instrumented hadron absorber system has been designed which comprises 6 iron plates of variable thickness (see first column in table 1) and 18 gaseous tracking chambers located in triplets behind each iron slab [1]. The detector layers are segmented into read-out pads with a minimum size of $0.28 \times 0.28 \text{ cm}^2$, and a maximum size of $4.48 \times 4.48 \text{ cm}^2$, corresponding to a total of 560000 channels.

The identification of energetic muons from charmonium decays is less demanding. We developed a start version of the CBM muon detection system which can be used for the measurement of J/ψ mesons already at SIS100 beam energies. As a first step, we have simulated the reconstruction of J/ψ mesons in 25 GeV $p + Au$ collisions at using the LIT global tracking package for full track reconstruction [2]. It turned out that a setup consisting of 2 iron absorber layers (thickness 20 cm and 205 cm) and 2 detector stations with 3 detector layers each would be sufficient to identify J/ψ mesons with an efficiency of 13% and a signal-to-background ratio of above 100 [3].

In a second step we have investigated the possibility to identify J/ψ mesons in nucleus-nucleus collisions at SIS100 energies. We have used the UrQMD event generator to calculate the background for Au+Au collisions at 10 A GeV, and calculated the corresponding J/ψ multiplicity with the HSD code. Please note, that the threshold energy to produce J/ψ mesons in p+p collisions is 11.3 GeV. The muon detector start version which was optimized for proton-nucleus collisions turned out to be insufficient because of many track mismatches resulting in a large combinatorial background (see last column in Table 1). In order to improve the track reconstruction we have inserted one more detector triplet after an iron absorber of 70 cm thickness while keeping the overall absorber thickness constant (225 cm). The result is very promising: J/ψ mesons can be identified with an efficiency of 3.3 % and a signal-to-background ratio of 0.6 (see second column in Table 1).

These simulations demonstrate that a start version of the muon detection system for charmonium measurements can be built with 3 detector stations as illustrated in figure 1: a highly granulated detector triplet consisting of Gas-Elektron-Multipliers (GEM) behind the first hadron absorber (20 cm iron), a second detector triplet optionally

based on Micromegas technology behind the second absorber (70 cm iron), and a large-area low-granularity detector triplet behind the last absorber (135 cm iron). The last triplet consists either of straw-tube detectors, or the first TRD station will be used. The different detector options are under investigation.

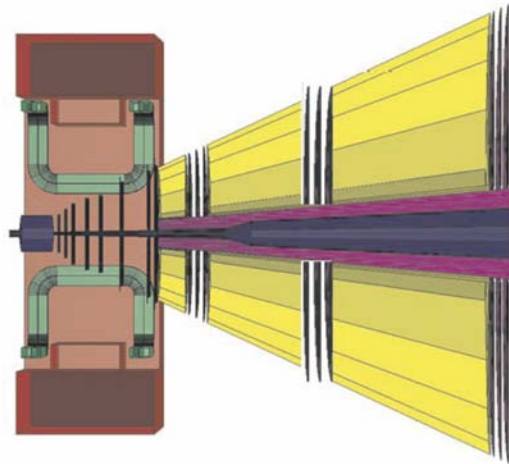


Figure 1: Start version of the CBM muon detection system for J/ψ meson measurements in nucleus-nucleus collisions at SIS-100 beam energies

Table 1: Efficiency and signal-to-background (S/B) ratio for J/ψ mesons from central Au+Au collisions at 10A GeV for three different absorber/detector combinations

detectors	18	9	6
Fe (cm)	3x20+30+35+100	20+70+135	20+205
$\varepsilon(J/\psi)$	7%	3.3%	1.3%
S/B	0.5	0.6	0.08

References

- [1] A. Kiseleva *et al.*, *CBM Progress Report 2008*, Darmstadt 2009, p. 27
- [2] A. Lebedev *et al.*, *CBM Progress Report 2009*, Darmstadt 2010, p. 77
- [3] A. Kiseleva *et al.*, *CBM Progress Report 2009*, Darmstadt 2010, p. 27

CBM publications 2010

- N. Abel *et al.*:
[Increasing Design Changeability Using Dynamical Partial Reconfiguration](#)
 IEEE Trans. Nucl. Sci. **57** (2010) 602
- J. Adamczewski-Musch *et al.*:
[Dataflow Engine in DAQ Backbone DABC](#)
 IEEE Trans. Nucl. Sci. **57** (2010) 614
- J. Adamczewski-Musch *et al.*:
[Data Acquisition Backbone Core DABC release v1.0](#)
 J. Phys. Conf. Ser. **219** (2010) 022007
- M. Al-Turany, F. Uhlig and R. Karabowicz:
[GPU's for event reconstruction in the FairRoot framework](#)
 J. Phys. Conf. Ser. **219** (2010) 042001
- T. Armbruster, P. Fischer and I. Peric:
[SPADIC- A Self-Triggered Pulse Amplification and Digitization ASIC](#)
 IEEE Nuclear Science Symposium 2010 Conference Record
- A. Bubak *et al.*:
[TRD Tracking Using the Cellular Automaton Algorithm for Compressed Baryonic Matter Experiment](#)
 Act. Phys. Pol. **B 41** (2010) 3
- S. Chatterji *et al.*:
[Development of radiation hard silicon sensors for the CBM Silicon Tracking System using simulation approach](#)
 IEEE Nuclear Science Symposium 2010 Conference Record
- M. Deveaux *et al.*:
[Radiation tolerance of CMOS monolithic active pixel sensors with self-biased pixels](#)
 Nucl. Instrum. Meth. Phys. Res. **A 264** (2010) 428
- M. Deveaux *et al.*:
[Status of the Micro Vertex Detector of the Compressed Baryonic Matter Experiment](#)
 PoS(Bormio2010)041
- C. Dritsa *et al.*:
[A detector response model for CMOS Monolithic Active Pixel Sensors](#)
 PoS(Bormio2010)015
- V. Friese:
[Prospects for strangeness and charm measurements in the CBM Experiment](#)
 J. Phys. **G 37** (2010) 094025
- A. Fülöp and G. Vesztergombi:
[Highly parallel algorithm for high-pT physics at FAIR-CBM](#)
 J. Phys. Conf. Ser. **219** (2010) 022032
- J. Gebelein, H. Engel and U. Kebschull:
[FPGA Fault Tolerance in Radiation Susceptible Environments](#)
 Proceedings of *11th European Conference on Radiation and its Effects on Components and Systems (RADECS-2010)*, September 2010, Langenfeld, Austria
- J. Heuser:
[The Compressed Baryonic Matter Experiment at FAIR](#)
 Proceedings of *3rd International Conference on Current Problems in Nuclear Physics and Atomic Energy (NPAE-Kyiv2010)*, June 2010, Kiev, Ukraine
- A. Lebedev *et al.*:
[Track reconstruction algorithms for the CBM experiment at FAIR](#)
 J. Phys. Conf. Ser. **219** (2010) 032048
- S. Lebedev, C. Höhne and G. Ososkov:
[Ring recognition and electron identification in the RICH detector of the CBM experiment at FAIR](#)

- J. Phys. Conf. Ser. **219** (2010) 032015
- S. Lebedev *et al.*:
[Fast Parallel Ring Recognition Algorithm in the RICH Detector of the CBM Experiment at FAIR](#)
PoS(ACAT2010)060
 - F. Lemke *et al.*:
[A Unified Interconnection Network with Precise Time Synchronization for the CBM DAQ-System](#)
IEEE Trans. Nucl. Sci. **57** (2010) 412
 - S. Manz *et al.*:
[An universal read-out controller](#)
JINST **5** (2010) C11017
 - C. Schrader *et al.*:
[A demonstrator for the Micro-Vertex-Detector of the CBM experiment](#)
PoS(Bormio2010)017
 - P. Staszal:
[CBM experiment at FAIR](#)
Act. Phys. Pol. **B 41** (2010) 341

CBM presentations 2010

<http://cbm-wiki.gsi.de/cgi-bin/view/Public/PublicPresentations2010>

Doctoral, diploma, master and bachelor theses 2010

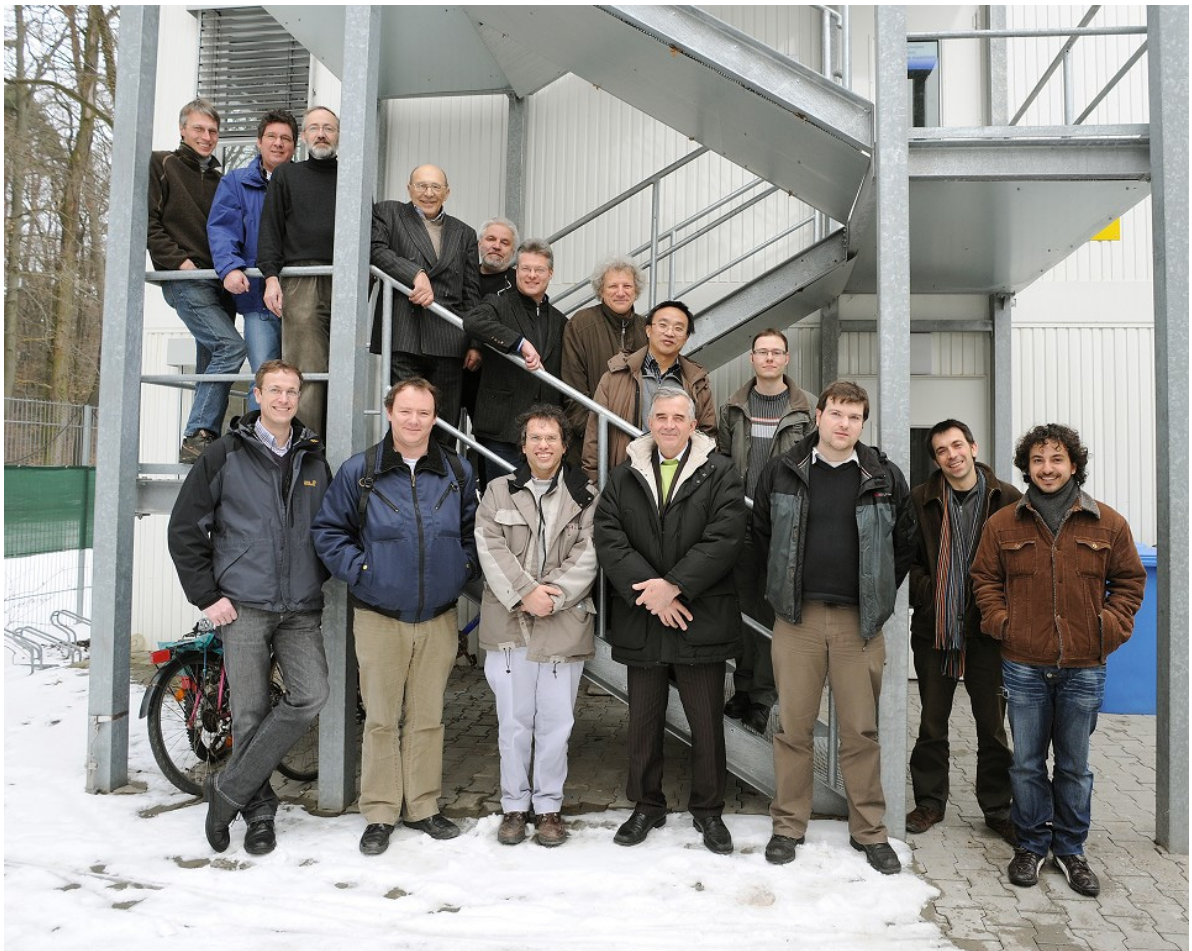
<http://cbm-wiki.gsi.de/cgi-bin/view/Public/Thesis2010>

1st Workshop on Ultra-light Silicon Tracking and Vertex Detection Systems

February 17-18, 2010, GSI, Darmstadt

The exploration of novel technologies towards thin systems is the aim of Joint Research Activity ULISI (short for "Ultra-light Silicon Detector Systems") taking place within the EU-FP7 Project "HadronPhysics2". Participants in ULISI met at GSI on February 17-18, 2010 for a common overview of the started developments. Three work packages were discussed, focusing on an innovative microstrip tracking system with ultra-thin aluminum-polyimide cables (CBM Silicon Tracker), an optimized hybrid pixel detector with low-power chip and thin epitaxial sensor (PANDA Micro Vertex Detector), and an ultra-thin monolithic pixel detector embedded in polyimide flexible circuit board foils (CBM Micro Vertex Detector). The research benefits from synergies in several fields, including vertical integration and space technologies and their application to hadron and particle physics.

Further information on the research activity is available at <http://ulisi-wiki.gsi.de>.



ULISI workshop participants from GSI, INFN Torino, CNRS-IPHC Strasbourg, Univ. Frankfurt, FZ Jülich, Univ. Bonn, SE SRTIIE Kharkov, INR Kiev and CiS Erfurt

Physics with FAIR: Indian Perspective

March 8 – 10, 2010, VECC Kolkata, India

Members of the Indian scientific community are steadily gearing up towards formulating details of their participation at FAIR. One very important aspect, being discussed in India, is that of human resources to be engaged in FAIR related activities. A dedicated meeting, sponsored by EU-FP7-programme, was held at VECC-Kolkata on March 8-10, 2010, where about 135 scientists and engineers from 35 institutions showed up. Also a large team from Germany, consisting of members from FAIR joint core team, CBM and NUSTAR collaborations, participated, together with the representatives of Indian funding agencies such as the Department of Atomic Energy (DAE) and the Department of Science and Technology (DST).

Dr. R. K. Bhandari, Director-VECC welcomed the delegates and also participated in the discussions. Dr. Y. S. Mayya, Managing Director of the Electronics Corporation of India Limited (ECIL), constituting the nodal Indian company in the FAIR-India collaboration, reviewed the technological capabilities of ECIL for FAIR. Dr. Bikash Sinha, Home Bhabha Professor, DAE, presented the keynote address. Peter Senger, Spokesperson of the CBM collaboration, and Reiner Krücken, former chairman of the NUSTAR collaboration, were among the delegates present in the meeting.

During the days detailed discussions were held on the status and challenges being faced by the Indian institutions with e. g. developing the LEB magnets, beam stopper, CBM muon chambers, PANDA luminosity monitor and various possible contributions to NUSTAR. With some developments here, considerable progress has already been made. Another key feature was an extensive discussion on the physics programmes to be addressed within the FAIR experiments. It was felt that the formation of the FAIR Company at the earliest would speed up further progress here. Therefore, the participants appreciated the official announcement on the Russian Prime Minister having signed the agreement on the Russian contribution to FAIR. The top scientific community agreed on holding such meetings more regularly.



15th CBM Collaboration Meeting
 April 12-16, 2010, GSI, Darmstadt



15th CBM Collaboration Meeting
 April 12-16, 2010

Compressed Baryonic Matter Physics Workshop
 April 14, 2010, GSI, Darmstadt
 Lecture Hall, 9 a.m.

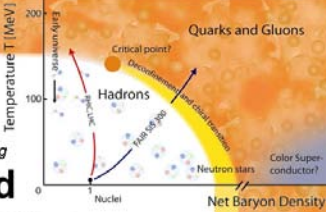
Further information:
 Ms. A. Zimbelius
 Tel.: +49-6159-711581
 Fax: +49-6159-713916
 E-Mail: A.Zimbelius@gsi.de













in the context of the 15th CBM Collaboration Meeting

Compressed Baryonic Matter Physics Workshop
 April 14, 2010, GSI, Darmstadt
 Lecture Hall, 9 a.m.

- The QCD phase diagram
- Quarkyonic Matter
- Parton/Hadron Transport in Relativistic Nucleus-Nucleus Collisions
- Lattice QCD calculations
- Explore the QCD Phase Diagram in High-Energy Nuclear Collisions
- Antimatter with Heavy-Ion Beam
- Hadron production of chemical freeze-out
- The Dilepton Probe - from SIS to RHIC
- Results from HADES
- STAR analysis of K_s0(892)
- First collisions at LHC seen with ALICE

Speakers include:
 A. Andronic, Darmstadt
 H. Appelshäuser, Frankfurt
 W. Cassing, Giessen
 H. van Hees, Giessen
 R. Holzmann, Darmstadt
 K. Redlich, Wrocław
 H.-G. Ritter, Berkeley
 P. Salabura, Krakow
 C. Sasaki, Frankfurt
 C. Schmidt, Frankfurt
 N. Xu, Berkeley
 Z. Xu, Brookhaven




Workshop for Future Challenges in Tracking and Trigger Concepts

June 7-11, 2010, GSI, Darmstadt

The 1st *International Workshop for Future Challenges in Tracking and Trigger Concepts* has been organized in June 7-11, 2010 at GSI. Almost 50 participants from 10 countries discussed different topics of fixed-target and collider experiments, reconstruction methods, computer and software architectures. Two days were devoted to trainings on vector classes and SIMD, multi-threading, Intel's Ct, CUDA and OpenCL parallel languages. The follow-up workshop is planned on July 7-8, 2011 at CERN.



The poster features a dark blue background with a complex network of white lines and circles, resembling particle tracks or data points. The text is in yellow and white. Logos for HIC for FAIR and Hadron Physics 2 are visible in the top right corner.

Workshop for Future Challenges in Tracking and Trigger Concepts

June 7-11, 2010, GSI, Darmstadt, Germany

Topics:

- Fixed-Target Experiments (CBM, HADES, PANDA)
- Collider Experiments (ALICE, STAR)
- Reconstruction Methods (Finding/Fitting)
- Computer Architectures (CPU/GPU)
- Software Architectures (Framework/Standalone)

Training:

- Vector Classes/SIMD
- Multi-Threading
- Intel's Ct
- CUDA/OpenCL

HIC for FAIR
Heinrich Heine International Center

Hadron Physics 2

16th CBM Collaboration Meeting
 September 27 - October 1, 2010, Mamaia, Romania

16th CBM Collaboration Meeting
 27 September – 1 October 2010
 Mamaia, Romania

Topics

R&D, Monte Carlo Simulations:
 Electromagnetic Calorimeter
 Micro-Vertex Detector
 Muon Chambers
 Resistive Plate Chambers
 Ring Imaging Cherenkov Detector
 Silicon Tracking Detector
 Spectator Detector
 Transition Radiation Detector

Physics:
 Equation of State
 Phase Transitions
 Critical Point

Front-End Electronics

Data Acquisition, Fast Online Event Selection

Organizing Committee:
 Dan Cozma
 Jürgen Eschke
 Volker Friese
 Walter F.J. Müller
 Mihai Petrovici
 Peter Senger

Online and Offline Software, Computing Model

Sponsors:


<http://niham.nipne.ro/cbm2010>



4th Workshop of the CBM-MPD STS Consortium

October 25-28, 2010, Hirschhorn am Neckar, Germany

The GSI Helmholtz Center for Heavy Ion Research GmbH, Darmstadt, Germany, the Joint Institute for Nuclear Research, Dubna, Russia and the V. G. Khlopin Radium Institute, St. Petersburg, Russia organized the 4th Work Meeting of the CBM-MPD Silicon Tracking System Consortium at Castle Hotel Hirschhorn am Neckar, Germany from 25 to 28 October 2010.

The STS Consortium was established in 2007 by GSI, Darmstadt and JINR, Dubna with the aim of bringing together institutes and specialists to work in joint effort on novel ultra-thin detector systems for accurate particle track identification in the planned experiments CBM at FAIR and MPD at NICA. Its members come from Germany, Russia, Ukraine and Belarus.

The retreat, supported by GSI, EU-FP7 HadronPhysics2 and ISTC, continued a series of meetings previously held in Russia at JINR, at IHEP Protvino and in Sortavala, Karelia. With 25 participants, the agenda focused on reviewing progress with work packages on the development of radiation hard silicon microstrip detectors for the CBM experiment, engineering of low-mass mechanical supports, readout electronics, and the development and test of demonstrator systems. The meeting concluded with an outline of the roadmap towards the production of components for the CBM STS and their system integration. Distinguished guest speaker was Prof. G. Nooren from the University of Utrecht, The Netherlands, who elaborated on the making of the Silicon Strip Detector of the ALICE Inner Tracking System.

For further information see

https://indico.gsi.de/conferenceOtherViews.py?confId=1067&view=cbm_conference.



CBM FEE/DAQ Workshop

February 22-23, 2010, GSI, Darmstadt

November 29 - December 1, 2010, FIAS, Frankfurt, Germany

The international workshops covered the front-end electronics and read-out chain of the CBM experiment, especially:

- Front-end ASICs,
- Front-end boards (FEBs),
- Data transport chain from detector to CBM annex building, and
- Hit-level data pre-processing

of all CBM detector systems. They focused also on the DAQ system aspects, especially

- Data formats and
- Flow control (dead-time handling).



Workshop participants in front of the FIAS building at Frankfurt, Germany.

The CBM Collaboration

Aligarh, India, Department of Physics, Aligarh Muslim University

N. Ahmad, M.D. Azmi, M. Irfan, E.M. Kashif, M.M. Khan

Beijing, China, Department of Engineering Physics, Tsinghua University

Jianping Cheng, Zhi Deng, Jin Li, Yuanjing Li, Yulan Li, Yi Wang, Qian Yue, Xianglei Zhu

Bergen, Norway, Department of Physics and Technology, University of Bergen

D. Röhrich, K. Ullaland, S. Yang

Bhubaneswar, India, Institute of Physics

D.P. Mahapatra, P.K. Sahu,

Bucharest, Romania, National Institute for Physics and Nuclear Engineering (NIPNE)

C. Andrei, I. Berceanu, V. Cătănescu, G. Caragheorgheopol, D. Cozma, A. Herghelegiu, M. Petriș, A. Petrovici, M. Petrovici, A. Pop, C. Schiaua

Bucharest, Romania, Atomic and Nuclear Physics Department, University of Bucharest

D. Argintaru, V. Baban, C. Besliu, M. Calin, V. Covlea, T. Esanu, A. Jipa, A. Jinaru, I. Lazanu, A. Scurtu, S. Velica

Budapest, Hungary, Eötvös Loránd University

B. Bozsogi, M. Csanád, Á. Fülöp, A. Kiss

Budapest, Hungary, KFKI Research Institute for Particle and Nuclear Physics (KFKI-RMKI)

L. Boldizsar, E. Denes, Z. Fodor, E. Futo, J. Kecskemeti, T. Kiss, A. Laszlo, T. Tolyhi, G. Vesztergombi

Chandigarh, India, Department of Physics, Panjab University

M.M. Aggarwal, A.K. Bhati, Manjit Kaur

Darmstadt, Germany, GSI Helmholtzzentrum für Schwerionenforschung GmbH

J. Adamczewski, M. Al-Turany, A. Andronic, E. Badura, T. Balok, E. Berdermann, S. Biswas, P. Braun-Munzinger, S. Chatterji, M. Ciobanu, H. Deppe, J. Eschke, H. Flemming, V. Friese, C. Garabatos, D. González-Díaz, J. Heuser, R. Holzmann, I. Kisel, A. Kiseleva, V. Kleipa, K. Koch, P. Koczoń, B. Kolb, A. Lebedev (JINR-LIT, Dubna), S. Lebedev (JINR-LIT, Dubna), S. Linev, S. Löhner, W.F.J. Müller, W. Niebur, J. Pietraszko, C.J. Schmidt, R. Schmidt, P. Senger, C. Sturm, O. Torheim, F. Uhlig

Dresden, Germany, Institut für Strahlenphysik, Forschungszentrum Dresden-Rossendorf (FZD)

A.L. Garcia, E. Grosse, K. Heidel, J. Hutsch, B. Kämpfer, R. Kotte, L. Naumann, R. Peschke, C. Wendisch, J. Wüstenfeld

Dubna, Russia, Veksler and Baldin Laboratory of High Energies, Joint Institute for Nuclear Research (JINR-VBLHE)

Yu. Anisimov, S. Avdeyev, V. Chepurinov, S. Chernenko, O. Fateev, V. Golovatyuk, A. Ierusalimov, V. Karnaukhov, V. Kirakosyan, V. Ladygin, A. Malakhov, J. Manjavidze, E. Matyushevskiy, E. Plekhanov, V. Pozdnyakov, S. Razin, O. Rogachevsky, T. Vasiliev, Yu. Zanevsky, V. Zrjuev

Dubna, Russia, Laboratory of Particle Physics, Joint Institute for Nuclear Research (JINR-LPP)

K. Davkov, V. Davkov, Ju. Gousakov, G. Kekelidze, V. Lucenko, V. Mialkovski, D. Peshekhonov, V. Peshekhonov, A. Zinchenko

Dubna, Russia, Laboratory of Information Technologies, Joint Institute for Nuclear Research (JINR-LIT)

P. Akishin, E. Akishina, T. Akishina, S. Baginyan, O. Derenovskaya, Victor Ivanov, Valery Ivanov, E. Litvinenko, G. Ososkov, A. Raportirenko, W. Scheinast, P. Zrellov

Frankfurt, Germany, Institute for Computer Science, Frankfurt Institute for Advanced Studies, Goethe Universität Frankfurt

M. Bach, J. de Cuveland, S. Gorbunov, D. Hutter, S. Kalcher, M. Kretz, V. Lindenstruth

Frankfurt, Germany, Institut für Kernphysik, Goethe Universität Frankfurt

S. Amar-Youcef, H. Appelshäuser, A. Arend, M. Deveaux, P. Dillenseger, D. Doering, M. Domachowski, C. Dripta (IPHC, Strasbourg), I. Fröhlich, T. Galatyuk, M. Hartig, A. Kotynia, I. Kulakov, E. Lebedeva, A. Lymanets (KINR, Kiev), B. Neumann, B. Milanovic, C. Müntz, P. Reichelt, C. Schrader, S. Seddiki, M. Singla, I. Sorokin (KINR, Kiev), J. Stroth, T. Tischler, C. Trageser, I. Vassiliev, B. Wiedemann, Weilin Yu, M. Zyzak

Gatchina, Russia, Petersburg Nuclear Physics Institute (PNPI)

V. Baublis, V. Dobyryn, V. Golovtsov, V. Ivanov, A. Khanzadeev, L. Kochenda, B. Komkov, E. Kryshen, L. Kudin, N. Miftakhov, V. Nikulin, V. Poliakov, E. Rostchin, Y. Riabov, M. Ryzhinskiy (St. Petersburg State Univ.), V. Samsonov, O. Tarassenkova, S. Volkov, E. Vznuzdaev, M. Zhalov

Giessen, Germany, II. Physikalisches Institut, Justus-Liebig-Universität Gießen

C. Höhne, D. Kresan, T. Mahmoud

Guwahati, India, Department of Physics, Gauhati University

B. Bhattacharjee, K. Dey K.J. Nath, R. Talukdar

Hefei, China, Department of Modern Physics, University of Science & Technology of China (USTC)

Hongfang Chen, Cheng Li, Ming Shao, Yongjie Sun, Zebo Tang, Ziping Zhang, Xiaolian Wang

Heidelberg, Germany, Kirchhoff-Institut für Physik, Universität Heidelberg (KIP)

N. Abel, S. Böttger, T. Breitner, H. Engel, J. Gebelein, U. Kebschull, C. Lara, S. Manz, P. Zelnicek

Heidelberg, Germany, Physikalisches Institut, Universität Heidelberg

M. De Gaspari, I. Deppner, D. Gottschalk, N. Herrmann, P. Loizeau, K. Piasecki (Warsaw University), K. Schweda, H.K. Soltveit, K. Wisniewski (Warsaw University), Yapeng Zhang

Heidelberg, Germany, Zentrales Institut für Technische Informatik, Universität Heidelberg, Standort Mannheim

T. Armbruster, U. Brüning, P. Fischer, C. Kreidel, A. Kugel, F. Lemke, R. Männer, M. Nüssle, I. Peric, C. Steinle, Wenxue Gao, D. Wohlfeld, A. Wurz

Jaipur, India, Physics Department, University of Rajasthan

R. Raniwala, S. Raniwala

Jammu, India, Department of Physics, University of Jammu

P.V.K.S. Baba, A. Bhasin, A. Gupta, S. Mahajan, S.S. Sambyal, M. Sharma

Katowice, Poland, Institute of Physics, University of Silesia

A. Bubak, A. Grzeszczuk, S. Kowalski, M. Krauze, E. Stephan, W. Zipper

Kharagpur, India, Indian Institute of Technology

P. Banerjee, T.K. Bhattacharyya, A.K. Singh

Kolkata, India, High Energy Physics Division, Saha Institute of Nuclear Physics

Sukalyan Chattopadhyay, D. Das, I. Das, A.K. Dutt-Mazumdar, L. Pal, S. Pal, P. Roy, T. Sinha

Kolkata, India, Department of Physics and Department of Electronic Science, University of Calcutta

A. Bhattacharya, S. Bandyopadhyay, A. Chakrabarti, Sanatan Chattopadhyay, G. Gangopadhyay

Kolkata, India, Variable Energy Cyclotron Centre (VECC)

Z. Ahmad, P. Bhaduri, Subhasis Chattopadhyay, M. Dey, A. Dubey, M.R. DuttaMajumdar, S.A. Khan, B. Mohanty, G.S.N. Murthy, T. Nayak, S. Pal, A. Roy, Y. Saini, R.N. Singaraju, V. Singhal, P. Trivedy Y.P. Viyogi

Kraków, Poland, Faculty of Electrical Engineering, Automatics, Computer Science and Electronics, Department of Measurement and Instrumentation, AGH University of Science and Technology

J. Gajda, P. Gryboś, M. Kachel, K. Kasinski, P. Maj, R. Szczygieł, M. Żołądź

Kraków, Poland, Marian Smoluchowski Institute of Physics, Jagiellonian University

Y. Ali, J. Brzychczyk, Z. Majka, P. Staszal

Kyiv, Ukraine, Department of Nuclear Physics, National Taras Shevchenko University of Kyiv

O. Bezshyyko, I. Kadenko, Y. Onishchuk, V. Plujko, V. Shevchenko

Kyiv, Ukraine, High Energy Physics Department, Kiev Institute for Nuclear Research (KINR)

M. Borysova, A. Chaus, A. Kovalchuk, A. Melnik, V. Militsija, Ya. Panasenko, V. Pugatch, D. Storozhyk

Moscow, Russia, Institute for Nuclear Research (INR)

M. Golubeva, F. Guber, A. Ivashkin, O. Karavichev, T. Karavicheva, E. Karpechev, A. Kurepin, A. Maevskaya, V. Marin I. Peshenichnov, A. Reshetin, A. Sadovsky, V. Tiflov, N. Topil'skaya E. Usenko

Moscow, Russia, Alikhanov Institute for Theoretical and Experimental Physics (ITEP)

A. Akindinov, A. Arefiev, S. Belogurov, A. Chernogorov, D. Golubkov, A. Golutvin, F. Khasanov, S. Kiselev, I. Korolko, I. Kudryashov, V. Maiatski, K. Mikhailov, P. Polozov, M. Prokudin, I. Rostovtseva, A. Semennikov, G. Sharkov, A. Stavinskiy, Y. Zaitsev

Moscow, Russia, Skobeltsyn Institute of Nuclear Physics, Lomonosov Moscow State University (SINP-MSU)

N. Baranova, D. Karmanov, M. Korolev, M. Merkin, V. Popov, A. Voronin

Moscow, Russia, Kurchatov Institute

D. Blau, A. Kazantsev, V. Manko, I. Yushmanov

Moscow, Russia, National Research Nuclear University MEPhI

E. Atkin, Y. Bocharov, A. Kluev, O. Malyatina, A. Petrovskiy, V. Shumikhin, A. Silaev, A. Simakov, M. Strikhanov, Y. Volkov

Münster, Germany, Institut für Kernphysik, Westfälische Wilhelms Universität Münster

R. Berendes, C. Bergmann, D. Emschermann, N. Heine, Ch. Klein-Bösing, A. Wilk, J. Wessels

Obninsk, Russia, National Research Nuclear University

N. D'Ascenzo, A. Galkin, V. Galkin, D. Ossetski, V. Saveliev

Prag, Czech Republic, Czech Technical University (CTU)

V. Petráček, V. Pospisil, L. Skoda

Protvino, Russia, Institute for High Energy Physics (IHEP)

A. Artamonov, V. Dyatchenko, Yu. Gilitsky, S. Golovnya, S. Gorokhov, Yu. Kharlov, D. Konstantinov, I. Lobanov, E. Lobanova, A. Ryazantsev, V. Rykalin, S. Sadovsky, A. Semak, A. Soldatov, Y. Sviridov, Yu. Tsyupa, M. Ukhanov, V. Victorov, A. Vorobiev

Pusan, Korea, Pusan National University (PNU)

Kunsu Oh, Jihye Song, Jun-Gyu Yi, In-Kwon Yoo

Řež, Czech Republic, Nuclear Physics Institute, Academy of Sciences of the Czech Republic

D. Adamova, A. Kugler, P. Tlustý

Seoul, Korea, Department of Physics, Korea University

Byungsik Hong, Tae Im Kang, Kwang-Souk Sim

Split, Croatia, University of Split

I. Carević, M. Anđelić, M. Dželalija

Srinagar, India, Department of Physics, University of Kashmir

S. Ahmad, S.A. Khan, M.F. Mir,

St. Petersburg, Russia, V.G. Khlopin Radium Institute (KRI)

M. Chubarov, S. Igolkin, V. Jakovlev, V. Karasev, S. Lashaev, Y. Murin, L. Solin

St. Petersburg, Russia, St. Petersburg State Polytechnic University (SPbSPU)

A. Berdnikov, Y. Berdnikov

Strasbourg, France, Institut Pluridisciplinaire Hubert Curien (IPHC), IN2P3-CNRS and Université Louis Pasteur Strasbourg

N. Chon-Sen, G. Claus, R. De Masi, A. Dorokhov, W. Dulinski, A. Himmi, K. Jaaskelainen, M. Koziel, F. Rami, I. Valin, M. Winter

Varanasi, India, Department of Physics, Banaras Hindu University

A. Prakash, B.K. Singh, C.P. Singh, V. Singh

Warsaw, Poland, Institute of Experimental Physics, Warsaw University

M. Kirejczyk, P. Gasik, T. Matulewicz, J. Rożynek (Soltan Institute for Nuclear Studies, Warsaw), B. Sikora, K. Siwek-Wilczynska

Wuhan, China, Institute of Particle Physics, Hua-zhong Normal University

Xu Cai, Yaping Wang, Zhongbao Yin, Daicui Zhou

Wuppertal, Germany, Fachbereich Physik, Bergische Universität Wuppertal

K.-H. Becker, K.-H. Kampert, J. M. Kopfer, C. Pauly, J. Pouryamout, S. Querchfeld, J. Rautenberg

Zagreb, Croatia, Rudjer Bošković Institute

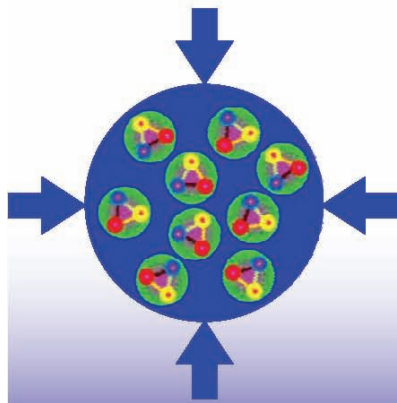
Z. Basrak, R. Čaplar, I. Gašparić, M. Kiš

Contacts

Chairman of the Collaboration BoardYogendra P. Viyogi
viyogi@veccal.ernet.in**Spokesman**Peter Senger
p.senger@gsi.de**Deputy Spokesman**Yuri Zaitsev
zaitsev@itep.ru**Deputy Spokesman**Subhasis Chattopadhyay
sub@veccal.ernet.in**Physics Coordinator**Volker Friese
v.friese@gsi.de**Technical Coordinator**Walter Müller
w.f.j.mueller@gsi.de**Ressource Coordinator**Jürgen Eschke
j.eschke@gsi.de**Management Board**

S. Chattopadhyay, N. Herrmann, F. Rami, D. Röhrich, J. Stroth, J. Wessels, Y. Zaitsev

<http://www.gsi.de/fair/experiments/CBM>



CBM

FAIR



GSII



HIC for **FAIR**
Helmholtz International Center

